

Human Cervix In Vitro Models of Healthy, Neoplastic and Cancerous Tissues Based on Organ-on-Chip Technology

Dissertation

der Mathematisch-Naturwissenschaftlichen Fakultät
der Eberhard Karls Universität Tübingen
zur Erlangung des Grades eines
Doktors der Naturwissenschaften
(Dr. rer. nat.)

vorgelegt von
Elena Christina Kromidas
aus Wuppertal

Tübingen
2024

Gedruckt mit Genehmigung der Mathematisch-Naturwissenschaftlichen Fakultät der
Eberhard Karls Universität Tübingen.

Tag der mündlichen Qualifikation:	08.05.2024
Dekan:	Prof. Dr. Thilo Stehle
1. Berichterstatter/-in:	Prof. Dr. Peter Loskill
2. Berichterstatter/-in:	Prof. Dr. Ulrich Rothbauer

Contents

ABSTRACT	I
KURZFASSUNG	III
CANDIDATE'S PUBLICATIONS	V
LIST OF PUBLICATIONS	V
CANDIDATE'S CONTRIBUTION TO PUBLICATIONS	V
LIST OF ABBREVIATIONS	VII
LIST OF FIGURES	VIII
LIST OF TABLES	VIII
1. INTRODUCTION	2
1.1. THE CERVIX UTERI AND IT'S ASSOCIATED (PRE)CANCEROUS LESIONS.....	2
1.1.1. <i>The Cervix</i>	2
1.1.2. <i>Human Papilloma Virus</i>	3
1.1.3. <i>The Ectocervical Epithelium</i>	4
1.1.4. <i>Cervical Intraepithelial Neoplasia, an HPV-Induced Premalignant Disorder</i>	4
1.1.5. <i>Cervical Carcinoma</i>	5
1.2. TRADITIONAL MODELS OF THE ECTOCERVIX.....	6
1.3. THE ORGAN-ON-CHIP TECHNOLOGY	8
2. OBJECTIVE OF THE THESIS	12
3. RESULTS	14
3.1. DEVELOPMENT OF MICROPHYSIOLOGICAL PLATFORMS FOR CERVICAL TISSUES	14
3.1.1. <i>Concept of the Microphysiological Platforms</i>	14
3.1.2. <i>First Platform Generation: Laser-Cut Thermoplastic Layers Thermally Fused to a Single-Well Platform</i>	15
3.1.3. <i>Second Platform Generation: Integration of Flexible Thermoplastic Elastomer Layers into a 4-Well Platform Enables Tissue Retrieval</i>	17
3.1.4. <i>Third Platform Generation: Microscope Slide-Sized 8-Well Platform with Two Fluidically Independent Systems</i>	19
3.2. CHARACTERIZATION OF HUMAN ECTOCERVICAL TISSUE AND ISOLATION OF KERATINOCYTES, FIBROBLASTS AND ENDOTHELIAL CELLS.....	19
3.3. TISSUE ENGINEERING OF ECTOCERVICAL TISSUES IN THE CERVIX-ON-CHIP	22
3.3.1. <i>Generation of Ectocervical Tissue Using Collagen Matrices</i>	23
3.3.2. <i>Semisynthetic HyStem®-C Hydrogel is Stable During Long-term Culture of Ectocervical Tissue</i>	25
3.3.3. <i>Synthetic Dextran Hydrogel is Mechanically Robust and Supports Ectocervical Keratinocytes</i> ..	26
3.3.4. <i>Scaffold-Assisted Stromal Layer</i>	28
3.4. GENERATION OF A PRECANCEROUS TISSUE IN THE CIN-ON-CHIP	30
3.5. ENDOTHELIAL CELL LINING OF THE VASCULATURE-LIKE CHANNEL OF THE CIN-ON-CHIP	32
3.6. REPLICATION OF CANCEROUS TISSUE IN THE CERVICAL CANCER-ON-CHIP WHICH RESPONDS TO CISPLATIN TREATMENT AND INTEGRATES NEUTROPHILS.....	33
4. DISCUSSION AND OUTLOOK	38
4.1. ROBUST PDMS-FREE MICROFLUIDIC PLATFORMS ARE TAILORED TO THE CULTIVATION OF ECTOCERVICAL TISSUES.....	38
4.2. ECTOCERVICAL CELL ISOLATION, CULTIVATION AND CHARACTERIZATION	39
4.3. DONOR-DERIVED 3D TISSUES EMULATE THE ECTOCERVIX IN THE CERVIX-ON-CHIP	40
4.4. ABERRANT EPITHELIA EMULATE PRECANCEROUS TISSUE IN THE CIN-ON-CHIP	41
4.5. ENDOTHELIAL CELL LINING OF VASCULATURE-LIKE CHANNELS ADVANCE DISEASE MODELS	42

4.6.	RESPONSE TO CHEMOTHERAPY AND IMMUNE CELL INTEGRATION HIGHLIGHT CRUCIAL FEATURES OF THE CANCER-ON-CHIP.....	43
4.7.	STRUCTURAL AND FUNCTIONAL CHARACTERIZATION OF CERVICAL TISSUES	44
4.8.	USE OF ANIMAL COMPONENTS WAS REDUCED IN CELL AND TISSUE CULTIVATION	45
5.	CONCLUSION	48
6.	EXPERIMENTAL PROCEDURES	50
6.1.	FABRICATION OF THE MICROFLUIDIC PLATFORMS.....	50
6.2.	TISSUE ENGINEERING AND ON-CHIP CULTIVATION	51
6.2.2.	<i>Primary Cell Isolation and Cell Cultures</i>	51
6.2.3.	<i>Generation of the Stromal Layer</i>	51
6.2.4.	<i>Generation of a Keratinocyte Epithelium</i>	53
6.2.5.	<i>Endothelial Cell Seeding in CInoC</i>	53
6.3.	CELL & TISSUE CHARACTERIZATION	54
6.3.1.	<i>Histology</i>	54
6.3.2.	<i>Staining</i>	55
7.	REFERENCES.....	57
8.	ACKNOWLEDGEMENTS	69
9.	DECLARATION	70
10.	ENCLOSED PUBLICATIONS	71
	PUBLICATION [1].....	71
	PUBLICATION [2].....	83
	PUBLICATION [3].....	108

Abstract

Women's health has received little attention in biomedical research, leading to an insufficient understanding of gynecologic diseases and sex-specific differences in the efficacy and safety of drug treatments. The cervix uteri is part of the female reproductive system and numerous women worldwide suffer from infections and disorders of the cervix, including the precancerous lesion cervical intraepithelial neoplasia (CIN) and cervical cancer (CC), that may arise upon persistent infection with the human papillomavirus (HPV). Given the absence of adequate drugs for CIN and the frequent recurrence, side effects and complications after CC treatment, there is a pressing need to develop optimized therapies. To address this issue, this thesis aimed to develop complex human in vitro models of the cervix as a tool to advance basic research and to facilitate the exploration of novel treatment options in an academic context.

In vitro tissue models were generated by employing Organ-on-Chip (OoC) technology, which integrates microfabrication techniques and tissue engineering. A microfluidic platform was developed iteratively, resulting in three generations of platforms, each of which benefited from insights gained from concurrent tissue engineering experiments. The third version comprises two fluidically independent systems within a microscope slide-sized platform, each featuring four open-top tissue wells for cervical tissues.

The normal ectocervix consists of a multilayered squamous epithelium covering a stromal layer. Donor-derived keratinocytes, fibroblasts, and endothelial cells were isolated, characterized, and utilized as species- and tissue-specific cell sources for the engineering of normal and diseased ectocervical tissues. In the Cervix-on-Chip (CXoC), the combination of a hydrogel mimicking the extracellular matrix, and a mechanically robust scaffold proved to be the most promising method for generating a fibroblast-rich stromal layer. By generating a multilayered, differentiated ectocervical epithelium on top of the stroma using primary keratinocytes, a physiological tissue architecture of normal ectocervical tissue was closely emulated. This model can be applied for basic research as well as for infection studies.

A diseased tissue model was generated in the CIN-on-Chip (CINoC), incorporating a stromal layer covered with an aberrant epithelium generated from the SCC cell line SiHa to emulate the pathophysiological tissue architecture. In a more complex model, the perfused microchannels of the CINoC were lined with cervical endothelial cells to more closely mimic the vasculature.

In the CC-on-Chip (CCoC), SiHa spheroids were embedded in a fibroblast-spiked stromal environment to mimic infiltrating cancerous nests. Tissue engineering allowed for dissecting the effects of co-cultivation, demonstrating enhanced viability and proliferation of the cancerous nests in the presence of fibroblasts. Treatment with the chemotherapeutic agent cisplatin at clinically relevant routes of administration and dosing resulted in reduced tissue viability, highlighting the platform's applicability for drug testing. Furthermore, the model allows for the integration and recruitment of donor-derived neutrophils from the microvasculature-like channel into the tissue, all while maintaining their ability to form neutrophil extracellular traps.

In the future, these models can advance our understanding of disease mechanisms, including studies involving the microbiome and pathogens related to sexually transmitted infections, as well as the development of improved drugs and (immune)therapeutic options.

Kurzfassung

Die Gesundheit von Frauen hat in der biomedizinischen Forschung wenig Beachtung gefunden, was zu einem unzureichenden Verständnis gynäkologischer Erkrankungen und geschlechtsspezifischer Unterschiede in der Wirksamkeit und Sicherheit von Medikamenten geführt hat. Weltweit leiden zahlreiche Frauen an Erkrankungen der Zervix, einem Teil des weiblichen Reproduktionssystem. Diese umschließen Infektionen, präkanzerösen Läsion (Cervical Intraepithelial Neoplasia, CIN) und Zervixkarzinome (Cervical Cancer, CC), welche durch eine anhaltende Infektion mit dem Humanen Papillomavirus (HPV) entstehen können. Angesichts des Mangels an geeigneten Medikamenten zur Behandlung von CIN und der Rezidiven und Komplikationen nach der Behandlung von CC, besteht ein dringender Bedarf an der Entwicklung optimierter Behandlungsoptionen. Als Werkzeug für die Grundlagenforschung und die Entwicklung neuer Behandlungsmöglichkeiten wurden in dieser Dissertation humane in vitro Gewebemodelle der Zervix entwickelt.

Für die Herstellung der in vitro Modelle wurde die Organ-on-Chip (OoC) Technologie eingesetzt, einer Kombination aus Mikrofabrikationstechnologie und Gewebekonstruktion. Es wurde eine mikrofluidische Plattform entwickelt, welche über drei Generationen hinweg iterativ optimiert wurde. Dabei profitierte jede Version von den Erkenntnissen der begleitenden Experimente zur Gewebekonstruktion. Die endgültige Plattform hat die Größe eines Objektträgers und umfasst zwei fluidisch unabhängige Systeme mit jeweils vier Vertiefungen für die Zervix-Gewebe.

Die gesunde Ektozervix besteht aus einem mehrschichtigen Plattenepithel auf einem fibroblastenreichen Stroma. Zur Herstellung des gesunden sowie der erkrankten Zervix-Gewebe wurden Keratinozyten, Fibroblasten und Endothelzellen von Gewebespenden isoliert und charakterisiert. Die Kombination eines mechanisch robusten Gerüsts mit einem Hydrogel, welches die extrazelluläre Matrix imitiert, erwies sich als die vielversprechendste Methode um ein Stroma in dem Cervix-on-Chip (CXoC) zu erzeugen. Mit dem auf dem Stroma befindlichen ektozervikalen Epithel aus primären Keratinozyten konnte die physiologische Gewebearchitektur eines gesunden Ektozervix-Gewebes nachgeahmt werden. Dieses spezies- und gewebespezifische CXoC kann zukünftig sowohl für die Grundlagenforschung als auch für Infektionsstudien eingesetzt werden.

Im CIN-on-Chip (CINoC) wurde die pathophysiologische Gewebearchitektur nachgebildet, indem das Stroma mit einem entarteten Epithel aus der Zervixkarzinom-Zelllinie SiHa bedeckt wurde. In einer Erweiterung des Modells wurden die blutgefäßähnlichen Kanäle mit zervikalen Endothelzellen ausgekleidet.

Im CC-on-Chip (CCoC) wurden SiHa-Sphäroide in einem mit Fibroblasten angereichertes Stroma eingebettet, um infiltrierende Tumore nachzuahmen. Die Gewebekonstruktion ermöglichte es, die Auswirkungen der Co-Kultivierung zu analysieren und zeigte auf, dass die Anwesenheit von Fibroblasten die Lebensfähigkeit und die Vermehrung der Tumore verbesserte. Eine Behandlung mit dem Chemotherapeutikum Cisplatin in einer klinisch relevanten Darreichungsform und Dosierung führte zu einem erhöhtem Gewebesterben, was die Anwendbarkeit der Plattform für Medikamententests demonstriert. Darüber hinaus ermöglicht das Modell die Integration und Rekrutierung von Neutrophilen aus dem blutgefäßähnlichen Kanal in das Gewebe hinein. Ihre Fähigkeit zur Produktion von „Neutrophil Extracellular Traps“ blieb dabei erhalten.

In Zukunft können diese Modelle unser Verständnis von Krankheitsmechanismen vertiefen. Ferner ermöglichen sie Studien, die das Mikrobiom, sowie Pathogene einschließen, die an sexuell übertragbaren Infektionen beteiligt sind. Des Weiteren können sie zur Entwicklung optimierter Medikamente und (immun)therapeutischer Behandlungen beitragen.

Candidate's Publications

List of Publications

= authors contributed equally

Publication [1]:

Rogal, J., Binder, C., Kromidas, E., Roosz, J., Probst, C., Schneider, S., Schenke-Layland, K., & Loskill, P. (2020). WAT-on-a-chip integrating human mature white adipocytes for mechanistic research and pharmaceutical applications. *Scientific Reports*, 10(1), Article 1. <https://doi.org/10.1038/s41598-020-63710-4>

Publication [2]:

Maulana, T. I.#, Kromidas, E.#, Wallstabe, L., Cipriano, M., Alb, M., Zaupa, C., Hudecek, M., Fogal, B., & Loskill, P. (2021). Immunocompetent cancer-on-chip models to assess immuno-oncology therapy. *Advanced Drug Delivery Reviews*, 173, 281–305. <https://doi.org/10.1016/j.addr.2021.03.015>

Publication [3]:

Kromidas, E., Geier, A., Weghofer, A., Liu, H.-Y., Weiss, M., & Loskill, P. (2023). Immunocompetent PDMS-Free Organ-on-Chip Model of Cervical Cancer Integrating Patient-Specific Cervical Fibroblasts and Neutrophils. *Advanced Healthcare Materials*, e2302714. <https://doi.org/10.1002/adhm.202302714>

Candidate's Contribution to Publications

R = Review

Publication No.	1	2	3
Accepted publication yes/no	yes	yes	yes
Number of authors	8	9	6
Position of candidate in list of authors	3	1	1
Scientific ideas by the candidate (%)	10	40	60
Data generation by the candidate (%)	10	R	70
Analysis and interpretation by the candidate (%)	0	R	75
Paper writing done by the candidate (%)	5	40	80

List of Abbreviations

2D/3D	two-/three dimensional
ALI	air-liquid interface
BF	brightfield
CAF	cancer-associated fibroblast
CC	cervical cancer
CCoC	Cervical Cancer-on-Chip
CIN	cervical intraepithelial neoplasia
CINoC	Cervical Intraepithelial Neoplasia-on-Chip
CK	cytokeratin
Coll	collagen
CXoC	Cervix-on-Chip
dex	Dextran
EC	endothelial cell
E-Cad	E-Cadherin
ECGM	Endothelial Cell Growth Media
ECM	extracellular matrix
FDA	fluorescein diacetate
FFPE	Formalin-fixed paraffin embedded
FN	fibronectin
HE	hematoxylin and eosin
HPV	human papillomavirus
HUVEC	human umbilical vein endothelial cells
iPS	induced pluripotent stem cells
K-SFM	Keratinocytes Serum-Free Media
LEEP	loop electrosurgical excision procedure
NETs	neutrophil extracellular traps
P/S	penicillin and streptomycin
PBS	phosphate-buffered saline
PC	polycarbonate
PDA	polydopamine
PDMS	polydimethylsiloxane
PEG	polyethylene glycol
PET	polyethylene terephthalate
PI	propidium iodide
PMMA	poly(methyl methacrylate)
PMN	polymorphonuclear leukocytes
SCC	squamous cell carcinoma
SEBS	styrene-ethylene-butylene-styrene
TME	tumor microenvironment
TPE	thermoplastic elastomer
VE-Cad	VE-Cadherin
VEGF	vascular endothelial growth factor
vim	vimentin
VWF	von Willebrand factor
IHC	immunohistochemistry
LDH	lactate dehydrogenase
FCS	fetal calf serum
ICC	immunocytochemistry

List of Figures

Figure 1. The Cervix Uteri is Part of the Female Reproductive System.....	3
Figure 2: Ectocervical Changes from Normal Ectocervical Epithelium to Neoplasia and Carcinoma.	4
Figure 3: Development of an Organ-on-Chip.	9
Figure 4: Concept of the Microfluidic Platforms.	14
Figure 5: A Single-Well Thermoplastic Module Represented the First Generation of the Microfluidics Platforms.....	16
Figure 6: A 4-Well Module Integrating Thermoplastic Elastomers as the Second Generation of the Microfluidic Platforms.....	18
Figure 7: An 8-Well Module with Two Independent Fluidic Systems Represents the Third Generation of the Microfluidic Platforms.....	19
Figure 8: Keratinocytes, Fibroblasts and ECs Were Isolated from Human Cervical Tissues.....	21
Figure 9: Comparison of Animal-free and Animal-Derived Antibodies.....	22
Figure 10: Process for the Generation of a Normal Ectocervical Tissue in the CXoC.....	23
Figure 11: Collagen I Shrinks in the Presence of Fibroblasts and Supports Epithelial Differentiation in the CXoC.....	24
Figure 12: HyStem®-C is a Robust Hydrogel in a Long-Term Cultivated Model of Ectocervical Tissue in the CXoC.....	25
Figure 13: Dextran Hydrogel Serves as a Robust ECM Substitute and Supports Keratinocyte Adhesion in the CXoC.....	27
Figure 14: MatriDerm® Represented a Robust Scaffold for Creating a Stromal Layer and Supported a Multilayered Epithelial Differentiation when Combined with a Hydrogel in the CXoC.	29
Figure 15: Precancerous Tissues Generated With a SiHa Epithelium Replicated Pathophysiological Features in the CINoC.	31
Figure 16: Cervical Endothelial Cells Covered the Vasculature-Like Channel in a Triple-Cultivation with CIN Tissue.....	32
Figure 17: The Cervical Cancer-on-Chip Allowed for the Investigation of Co-Culture Effects, Response to Cisplatin and Neutrophil Migration.	34
Figure 18: Advancing Cervical Cancer-on-Chip with Epithelia and Cisplatin-Sensitive CC7 Tumor Spheroids.	35
Figure 19: Removal of the Bottom PC-layer.	54
Figure 20: OCT-Embedding.....	54
Figure 21: Schematic of the Process for Tissue Retrieval and Generation of FFPE Tissue Sections.	55

List of Tables

Table 1: Conditions for Creating the Stroma and Epithelium of the Ectocervical Tissue Models.....	52
---	----

CHAPTER 1

Introduction

1. Introduction

Women's health has received little attention in biomedical research, resulting in an insufficient study of gynecologic diseases and an incomplete understanding of sex-specific differences in drug treatment efficacy and safety, as well as disease incidence and symptoms¹. Both psychosocial and biological differences between the sexes, such as drugs interactions with reproductive hormones and their associated receptors, contribute to an elevated susceptibility to adverse drug reactions in women. It has been postulated, that the representation of females in preclinical research may have prevented the oversight of crucial adverse reactions¹, emphasizing the need for sex-specific in vitro models. The cervix uteri is part of the female reproductive system and numerous women worldwide suffer from cervical diseases, including infections and potential sequelae such as cervical intraepithelial neoplasia (CIN) and cervical cancer (CC). Therefore, there is an urgent need for more (preclinical) research on the cervix and its associated diseases.

1.1. The Cervix Uteri and It's Associated (Pre)Cancerous Lesions

1.1.1. The Cervix

The cervix is part of the female reproductive system, encompassing the lower part of the uterus and protruding into the vagina² (**Figure 1.A**). The cylindrical structure measures approx. 3 cm in length and 2.5 cm in diameter and connects the vagina to the uterine cavity through a narrow channel². The cervix contains three distinct anatomical regions, including the ectocervix, the transformation zone, and the endocervix, each of which is covered by different epithelia (**Figure 1.B**). The mucin-producing columnar epithelium lines the endocervical canal and transitions superiorly into the uterine epithelium. Inferiorly, the endothelial epithelium meets the ectocervical epithelium at the squamocolumnar junction in the metaplastic transformation zone. The ectocervix, which encompasses the outer surface of the vaginal portion, is covered by a squamous epithelium, that transitions into the vaginal epithelium². The squamous epithelium is completely replaced by a new population of cells every 4 to 5 days through tissue renewal: The lower, basal cells divide either symmetrically to generate more basal cells, or asymmetrically, with one of the daughter cells moving upward toward to the surface. As the cells move upward, they progressively acquire characteristics of differentiation in the parabasal and intermediate layer until they ultimately exfoliate from the superficial cell layer^{2,3}.

The cervix represents a barrier between the vagina as the "external" environment and the uterus. It acts as a gatekeeper to the uterus by facilitating the migration of spermatozoa from the vagina while maintaining sterility by preventing the passage of pathogens, thereby mitigating ascending infection of the uterus. In addition, the cervix plays a central role in pregnancy, particularly in the delivery of the fetus from the uterus, which occurs only once the cervix is dilated. The cervix is exposed to the vaginal microbiome, which comprises 20-140 bacterial species in an individual, with *Lactobacillus* as the most dominant species⁴. A healthy microbiome plays a crucial role in preventing vulvo-vaginal infections and inflammatory conditions. An imbalanced microbiome, on the other hand, can affect the rate of pathogen clearance. For instance, evidence suggests that a vaginal infection with *Chlamydia trachomatis* may predispose individuals to a human papillomavirus (HPV) infection by altering the microbiome, thereby linking the microbiome to HPV-associated diseases⁴.

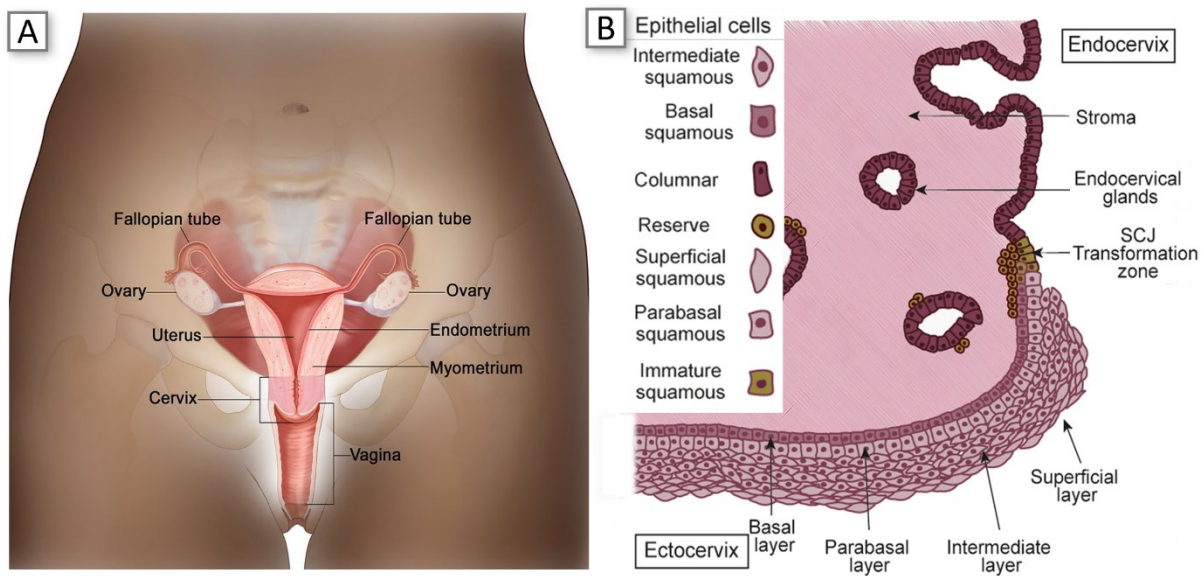


Figure 1. The Cervix Uteri is Part of the Female Reproductive System.

A) Schematic of the female reproductive system illustrates the cervix as the lower part of the uterus that extends into the vagina. Adapted from © 2021 Terese Winslow LLC, U.S. Govt. has certain rights. B) The cervix is divided into several distinct anatomic regions, including the endocervix, the inner part of the cervix that is lined by columnar epithelium. The ectocervix, the outer part of the cervix, is covered by a squamous epithelium that consists of basal, parabasal, intermediate and superficial keratinocyte layers. Both epithelia meet at the squamocolumnar junction (SCJ) in the transformation zone. Schematic adapted from⁵, CC BY 4.0.

1.1.2. Human Papilloma Virus

HPV is a common sexually transmitted virus, with >80% of sexually active people acquiring an infection at least once by the age of 45⁶. The vast majority of HPV infections are asymptomatic and transient, with 80% of infections being naturally cleared by the immune system within two years⁷. However, around 4.5% of all diagnosed human malignant neoplasms are attributable to HPV, including cervical, anal, vaginal, vulvar, penile, and oropharyngeal cancers, with cervical cancer (CC) being the most prevalent among them⁸. Of the >400 HPV genotypes, approx. 12 are considered to be high-risk cancer-causing types or potentially high-risk^{8,9}. While a persistent infection with high-risk HPV is considered the primary etiologic factor for CC, low-risk genotypes can cause benign tumors such as warts (papillomas)¹⁰.

The small, double-stranded DNA virus of approx. 55 nm in size, comprises approx. 8,000 base pairs and exhibits a strict tropism for cutaneous or mucosal epithelial cells¹¹. In the squamous epithelium, HPV gains access through microabrasions in the epithelium and specifically infects the basal cells. Thereafter, expression of the extrachromosomal HPV genome is regulated by the keratinocyte differentiation status, involving an early and late transcriptional program^{3,6,12}. Initial DNA amplification in the infected basal cells is regulated by the early genes E1 and E2, maintaining a range of 50-100 copies of the episomal viral genome. Copy number and viral protein expression is sustained at low levels as long as the basal cells divide. As the cells progress through differentiation, viral DNA increases to thousands and all genes are activated. Among them, the viral oncoproteins E6 and E7 inactivate the tumor suppressor genes p53 and pRB, disrupting apoptotic pathways and promoting cell proliferation and genomic instability¹³. The expression of the late genes L1 and L2, which encode structural components for genome encapsidation and virion assembly, occurs in the superficial cell layers of the epithelium, facilitating the shedding and distribution of infectious particles. This regulation of the viral life cycle enables HPV to evade detection by the immune system by restricting high levels of viral gene expression and virion production to the uppermost layers of the epithelium, which are not subject to immune surveillance^{3,14}.

1.1.3. The Ectocervical Epithelium

The ectocervix is composed of multiple cell layers (**Figure 2**), which can be distinguished by hematoxylin and eosin (HE) staining and further identified by specific markers. The epithelium is separated from the underlying stroma by the basement membrane, a specialized extracellular matrix (ECM). The basal layer of the ectocervical squamous epithelium consists of a single row of small cylindrical epithelial cells (10 μm in diameter), expressing high levels of cytokeratin (CK) 19, with large oval nuclei that are arranged perpendicular to the basement membrane. Above them, the parabasal cells form four to five cell layers, exhibiting a polyhedral shape and a larger size compared to the basal cells, with slightly more cytoplasm rich in CK14^{2,15}. The intermediate or suprabasal layer, located above the parabasal layer, consists of more mature, flattened cells with increased cytoplasm, positive for CK10 and CK13 and smaller nuclei than those in the basal layer. These cells are arranged with their long axis parallel to the basement membrane. The superficial layer is characterized by cells 50 μm in diameter with abundant and clear cytoplasm due to glycogen accumulation, and a small, centrally located round nucleus. The cells in the superficial layer become flat and elongated, have a large amount of cytoplasm, and exfoliate physiologically. Keratinization can occasionally occur in both the intermediate and superficial layers and serves to protect the underlying epithelial cells and the subepithelial vascularization from trauma and infection^{2,15,16}.

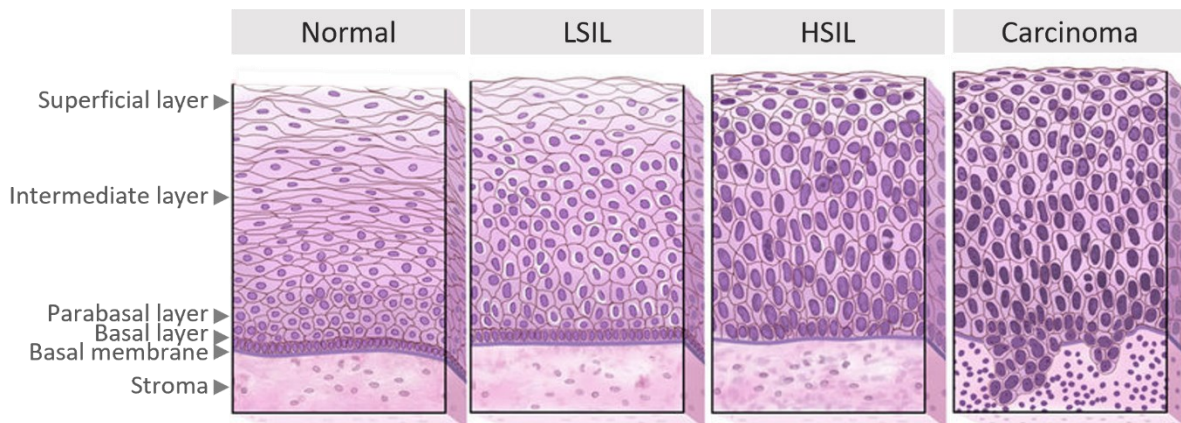


Figure 2: Ectocervical Changes from Normal Ectocervical Epithelium to Neoplasia and Carcinoma.

In the normal ectocervical epithelium, basal cells proliferate and differentiate as they ascend to the surface, exhibiting distinct cell morphology and protein expression profiles in the basal, parabasal, intermediate, and superficial layers. HPV can gain access to basal cells through microabrasion and initiate abnormal epithelia. As the disease progresses from low-grade to high-grade squamous intraepithelial lesions (LSIL/HSIL), the likelihood of developing invasive carcinoma increases, involving the infiltration of transformed cells through the basement membrane into the underlying cervical stroma. Adapted from © 2014 Terese Winslow LLC, U.S. Govt. has certain rights.

1.1.4. Cervical Intraepithelial Neoplasia, an HPV-Induced Premalignant Disorder

Ectocervical epithelia harboring a high- or low-risk HPV infection may develop abnormalities and are clinically identified as CIN or Low/High-Grade Squamous Intraepithelial Lesions (LSIL/HSIL), if not cleared by the immune system^{17,18} (**Figure 2**). These proliferative lesions exhibit abnormal cytologic and histologic differentiation resulting from viral replication and include dedifferentiation, disrupted epithelial architecture, increased mitotic activity, presence of atypical mitoses, cellular pleomorphism and nuclear atypia¹³. The degree of cellular aberration and the extent of epithelial involvement vary with the severity of the lesion, graded from mild dysplasia (CIN 1/LSIL) to moderate (CIN 2) and severe dysplasia (CIN 3), where dysplastic changes extend to the lower, middle, and upper thirds of the epithelium, respectively. CIN 2 and CIN 3 are collectively known as HSIL due to the challenge in distinguishing between these stages, given the poor inter-observer reproducibility for this specific diagnosis, and both stages are typically treated similarly¹³.

These lesions are considered precancerous because they are thought to progress slowly over time from LSIL (CIN 1) to HSIL (CIN 2 and 3) and eventually to invasive carcinoma. The progression from HPV infection to viral persistence, then to dysplasia and finally to invasive CC takes approx. 15 years¹⁹. Detection of dysplasia is the primary focus of cervical screening programs, which involve collection and examination of exfoliating cells from the superficial layers, commonly known as Papanicolaou or "Pap" smears. The goal is to identify abnormal cells and initiate treatment at an early stage to prevent the development of an invasive disease¹⁷. Since 90% of CIN 1 spontaneously regresses within three years due to immune surveillance²⁰, CIN 1 does not require medical intervention and is instead monitored regularly²¹. While 18% of CIN 2 cases will progress to CIN 3, 50% of CIN 2 will regress within two years²² and the likelihood of regression for CIN 3 is 33-50%, with 12% progressing to invasion^{19,23}. Although only a subset of CIN 3 patients will progress to cancer, the standard approach to treating CIN 2 and 3 is to surgically remove the affected tissue by loop electrosurgical excision procedure (LEEP). In some cases, dysplasia is treated with ablation techniques such as cryosurgery or CO₂ laser ablation, but these procedures have a higher recurrence rate when compared to LEEP²⁴. Despite treatment, patients with CIN 3 are at increased risk of developing CC^{25,26}. Due to the lack of diagnostic tests that can reliably distinguish between regressing and progressing lesions, cases of HSIL cases are often overtreated²⁷. Therefore, the goal is to prevent potential progression to cancer while avoiding overtreatment, as lesions may spontaneously regress, and treatment may have adverse effects. Established standard therapies are invasive and tissue-destructive, potentially leading to cervical incompetence and preterm birth²⁵. Research is ongoing to explore non-invasive alternatives, including herbal regimens²⁸, physical plasma^{29,30}, therapeutic vaccines³¹, and immunotherapy¹⁰.

1.1.5. Cervical Carcinoma

With approximately 600,000 new cases diagnosed in 2020, CC is the fourth most common cancer in women globally, accounting for 6.5% of all female cancers³². A significant advance in the control of HPV-related disease was the introduction of Gardasil in 2006, a prophylactic vaccine targeting high-risk HPV strains HPV 16 and 18³³. The subsequent release of the nonavalent vaccine Gardasil 9 in 2014 extended its protection to HPV 6, 11, 31, 33, 45, 52 and 58³³, covering both low- and high-risk HPV types to prevent both malignant and benign epithelial transformation. Although HPV vaccination has been recommended in Germany since 2007 and gender-neutral vaccination since 2018, the rates of prophylactic HPV vaccination rates remain below 50% in both sexes³⁴. The highly effective primary (vaccine) and secondary (screening) preventive measures have rendered CC almost preventable. Unfortunately, incomplete adoption of these preventive measures, lack of disease awareness and poor health infrastructure facilities contribute to CC remaining a pressing global health concern as the leading cause of cancer death in 36 countries, particularly in low- and middle-income countries³³.

The two dominant histologic subtypes of CC are squamous cell carcinoma (SCC) and adenocarcinoma, accounting for over 70% and nearly 20% of all CC, respectively³⁵. Structurally, invasive SCC is characterized by a population of neoplastic cells arranged in irregular nests infiltrating the stroma³⁶. Infection with an oncogenic HPV is a necessary yet insufficient cause of cervical carcinogenesis³⁷. HPV 16 and 18 are the most clinically significant drivers, underlying approx. 70% of all SCC³⁸. Additional risk factors include first sexual intercourse at an early age, multiple sexual partners, immunosuppression (e.g. HIV/AIDS), parity, oral contraceptive use, other sexually transmitted infections, active cigarette smoking and exposure to second hand smoke^{18,39}.

A considerable number of patients are still diagnosed only at an advanced stage with a poor prognosis, particularly in low and middle income countries³³. In Germany as well, the prognosis and survival rate of patients with advanced CC remains a challenge, with age-adjusted five-year relative survival rates of 84.6% for localized, 48.2% for regional, and 17.9% for distant stage cases⁴⁰. Therefore, receiving

timely and effective therapy is critical. Surgery or radiotherapy are recommended for early stages, while advanced stages may require combined therapy with radiation and cisplatin-containing chemotherapy. In instances of metastasis and locally advanced malignancies, targeted therapy with bevacizumab and immunotherapy with immune checkpoint inhibitors have been recently employed⁴¹. Frequent recurrence, along with associated adverse effects and complications, emphasize the need for alternative CC treatment options⁴²⁻⁴⁵. Currently, therapeutic HPV vaccines hold promise for expanding therapy options, and ongoing research is investigating additional immune checkpoint inhibitors, adoptive cell transfer with tumor-infiltrating lymphocytes selected for the HPV oncogenes E6 and E7^{10,21} and the use of mathematical (artificial intelligence supported) models to guide screening and medical treatment decisions⁴⁶⁻⁴⁹.

1.2. Traditional Models of the Ectocervix

Due to the high clinical relevance of cervical infections and transformed epithelial disorders, various models have been developed, and reviews are available on animal models^{50,51} and bioengineered in vitro models⁵²⁻⁵⁵, some of which focus specifically on cervical spheroids/organoids^{5,9,56,57}. While multiple animal studies involved rhesus macaques^{48,58-60}, most animal studies have used mouse models. Several transgenic mice have been developed^{50,61,62}, most of which express the HPV-oncogenes E6 and/or E7 under the CK14 promoter⁵⁰. Despite the advantages of studying the effect or carcinogenic contribution of individual proteins in transgenic mice, species-related differences between human and mouse biology must be considered, including telomerase activity, pathways to prevent cancerous changes, and required genetic alterations required for malignant transformation^{50,63}. In the context of CC, a notable difference between mice and humans revolves around the pathways of the two key oncogenes E6/E7. In mice, the p53 pathway, which is inhibited by HPV-E6, plays a critical role in triggering senescence, whereas in humans the pRb pathway, which is inhibited by HPV-E7, dominates⁶⁴.

Xenograft mouse models, particularly patient-derived xenograft (PDX) models, have emerged as an advanced approach to mimic human cancer by transplanting human cancer cell lines or biopsies into genetically modified mice with suppressed immune systems. While human cell lines in xenograft models capture the human genetic background, they reduce tumor cell heterogeneity due to in vitro cell culture, which favors less differentiated and more virulent clones⁵⁰. PDX models, on the other hand, better recapitulate the diversity of cell types in human cancers, preserving the heterogeneity, histology, the tumor microenvironment (TME) and overall metastatic patterns associated with each disease^{9,50}. PDXs are widely used in preclinical models of various tumors and to date ten PDX models have been developed for CC⁵¹, often by subcutaneous tissue transplantation to study chemotherapy toxicity and drug delivery efficacy. Additional transplantation methods, such as subrenal capsule transplantation and orthotopic CC models, have been employed to investigate tumor metastasis and cancer signaling pathways in order to identify potential therapeutic targets^{9,51}. Although orthotopic CC PDXs show promise with good correlation in transcriptomic landscapes and similar histologic, metastatic, and stromal patterns compared to donor tissues⁵⁵, their widespread application is hindered by ethical concerns, required surgical skills, long latency periods, variability in transplantation rates, and high costs. Moreover, immunosuppression in mice limits the study of tumor interactions with the specific immune system, a critical component of the TME and of immunotherapy^{9,50}.

As an alternative to animal models, in vitro models have been developed that include both two- and three dimensional (2D/3D) cell cultures using single cells or co-cultures. Human ectocervical epithelial cells have been isolated and cultivated, including primary ectocervical (immortalized) keratinocytes⁶⁵⁻⁶⁷ and 52 CC cell lines⁶⁸, with primary CC cells proving particularly challenging to cultivate⁹. Although low infrastructure and expertise requirements render cost-effective 2D cultures appealing for large-

scale drug screening, the absence of 3D environmental cues from the surrounding matrix affects cell behavior⁵. Changes in cell morphology, cytoskeletal organization, cell-cell communication, accumulation of mutations, and altered protein expression patterns have been observed in 2D culture, affecting cell viability, differentiation, and proliferation processes. When CC cells were cultured as monolayers on plastic dishes⁵⁵ or in a 3D adenocarcinoma model, the 3D models exhibited spheroid formation and increased cell proliferation compared to conventional 2D monolayer cell sheets⁵⁹. In a model incorporating the ectocervical cancer cell line SiHa, viral transcripts were more highly expressed in the 3D multilayer model than in the 2D culture⁶⁹. In summary, there is a consensus that 2D (tumor) cell cultures significantly deviate from *in vivo* and are often inadequate models⁹. Addressing these challenges requires the establishment of tumor models that serve as a bridge between cell culture and animal models, and more accurately reflect *in vivo* pathophysiology. The past decade has witnessed a transformative period in the development of 3D tumor models⁹. Various strategies have emerged to create 3D models of the human ectocervix, including organotypic raft cultures, spheroid/organoid models, tumor explants, and microfluidic systems.

Organotypic raft cultures, commonly used to study skin, have been adapted to generate 3D cervix models⁵². Seeding keratinocytes on a gel followed by subsequent differentiation at the air-liquid interface (ALI) marked a breakthrough in achieving keratinocyte differentiation *in vitro*⁵⁵. This approach has been widely employed to model the human ectocervix⁶⁹⁻⁷⁷, and has allowed mimicry of 3D tissue architecture, co-culture with various cell types, and significant advances in understanding cervix biology and infectiology. While some *in vitro* models have mistakenly utilized preputial keratinocytes due to their greater availability, it is important to note that epithelia from different organs exhibit distinct differentiation programs, with or without keratinization, and varied CK expression in the epithelial layers⁵³. Despite the progress made with organotypic raft cultures, the limitations in studying direct virus-host interactions, the short lifespan of the models and a missing vasculature have led to the development of more intricate 3D models⁵⁵.

Patient-derived organoids (PDOs), the second most commonly employed 3D tumor model, arise from the proliferation and self-organization of cells isolated directly from patient tumor tissue⁹. In contrast to spheroids, which result from facilitated cell aggregation, PDOs spontaneously form 3D structures based on their genetic programming, closely resembling the actual development of tumors. Due to their uniform shape and size, spheroids are well-suited for high-throughput testing in multiwell plates and are particularly advantageous for identifying potent drug candidates. Cancer spheroid models have been shown to recapitulate outcomes commonly observed in solid tumors and to exhibit greater resistance to treatment compared to 2D cultures. In contrast, the development of more physiologically relevant cancer organoids has improved the preservation of the natural cancer cell heterogeneity, along with the genetic and phenotypic characteristics of the native tissue. Organoids, being more cost-effective and, in certain instances, more physiologically relevant than PDX models, have emerged as a valuable tool. However, the establishment of human ectocervical organoid models remains a challenging endeavor, with only a limited number established successfully⁹. Adult ecto- and endocervical organoids have been derived from hysterectomy or Pap smear specimens and embedded in a matrix simulating a basement membrane^{78,79}. While normal ectocervical organoids were maintained for more than 6 months and spontaneously generated stratified squamous epithelia that closely resembled *in vivo* tissue architecture, morphology and transcriptional profiles, cancerous organoids recapitulated cancer-associated gene expression patterns, gene alterations, and HPV integration patterns^{9,57}. A recent study confirmed the similarity of histopathology and gene profiles between the organoid and the original tumor⁸⁰. Limitations of current cervical organoid models include the frequent absence of the underlying stromal compartment, as well as the lack of immune cells and vasculature⁵⁷. Another limitation is that squamous epithelial organoids have the superficial layer on

the inside, making them inaccessible to direct medical therapies such as physical plasma^{29,30}. A promising approach to mimic physiological tissue architecture, including vasculature and immune cells, is the Organ-on-Chip (OoC) technology.

1.3. The Organ-on-Chip Technology

Species-specificity contributes to a high failure rate in translating drugs from animal testing to human treatment. This, along with ethical concerns about animal experimentation, is driving the use of more human-relevant tools that promise to be more predictive of human disease and response⁸¹. Among the “non-animal methods” or “new approach methodologies” (NAMs), OoC technology has emerged as a revolutionary approach in the field of biomedical research to generate complex human tissue models and improve translatability in drug development⁸². This innovative technology involves the integration of microfabrication techniques with cell culture systems to create microscale devices that mimic the structural and functional aspects of specific tissues. The ORCHID (Organ-on-Chip In Development) Consortium defines it as a “fit-for-purpose microfluidic device, containing living engineered organ substructures in a controlled microenvironment, that recapitulates one or more aspects of the organ’s dynamics, functionality and (patho)physiological response in vivo under real-time monitoring”⁸³. OoC promises to combine the advantages of in vivo experiments, including complex 3D tissues in a physiological microenvironment and circulation, with the benefits of in vitro models, including the human genetic background, cost efficiency and potential for automation and standardization.

A key feature of these in vitro models is the perfusion through vasculature-mimicking microchannels, allowing continuous delivery and removal of molecules and cells. This facilitates the integration of (circulating) immune cells, making OoC suitable for investigating the impact and involvement of immune components in various diseases and for the development of drugs targeting the immune system, a promising approach being pursued in oncology (**Publication [2]**).

The development of organ-on-chip models constitutes an interdisciplinary process that combines technologies and concepts from microfabrication, microfluidics, biomaterials, pharma/toxicology, and medicine, among others⁸⁴ (**Figure 3**). The human body serves as a structural blueprint and cell source for the creation of human-relevant in vitro models in a microfluidic platform. Rogal and colleagues have outlined this development as a journey, starting with the initial idea/specific scientific question and progressing to the design/concept phase. Subsequently, the simultaneous work on engineering (fabrication, materials, sensor integration) and biological questions (cell sources, biomaterials/scaffolds) allows for an iterative process. This process is followed by the establishment of cell injection and tissue assembly, assay development, and functional validation, ultimately leading to the final applications in the (pharmaceutical) industry, clinical research or for addressal of mechanistic biomedical studies.

One of the pioneering OoC systems that received global attention was a lung-on-chip that applied mechanical stimuli to the cells through a stretch mechanism⁸⁵. This platform introduced a concept, used in many succeeding platforms, featuring a tissue-specific culture compartment separated from the perfusable vasculature-like channel by a porous membrane. Since then, platforms integrating various tissues have been developed, including brain, blood-brain barrier, eye, kidney, liver, pancreas, heart, adipose, intestine, colon, uterus, placenta, blood vessel, and skin⁸².

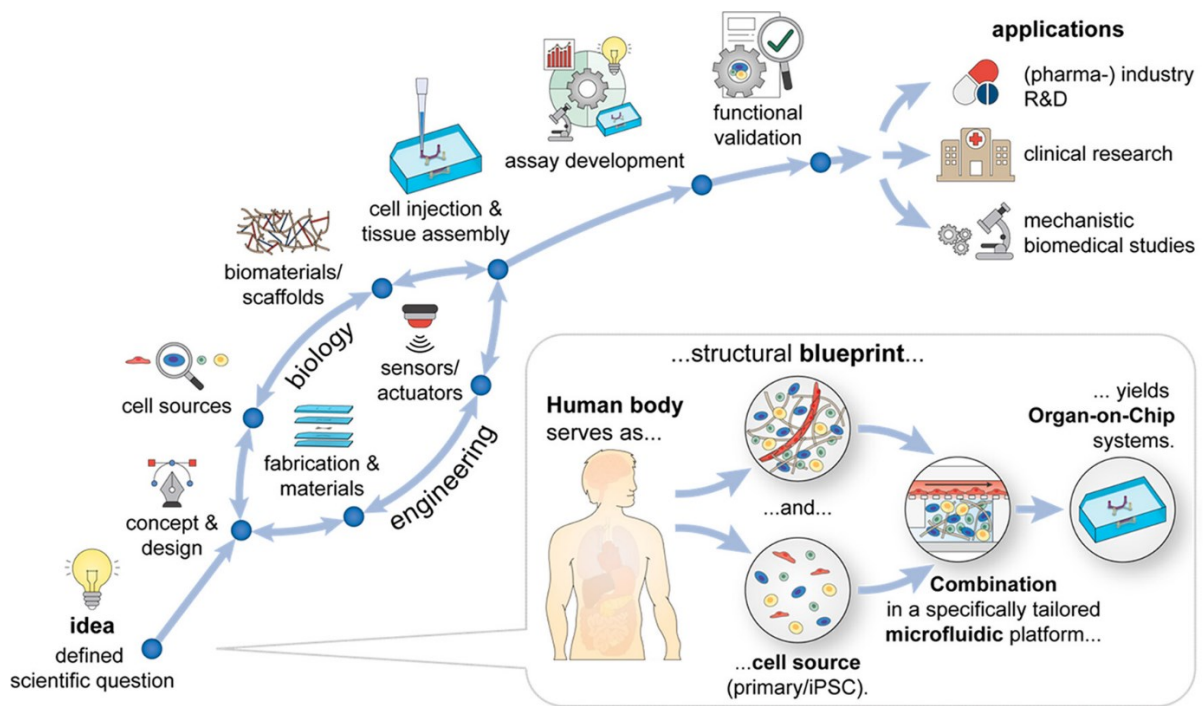


Figure 3: Development of an Organ-on-Chip.

The scientific question is the basis for conceptualizing and designing a platform using the human body serving as the structural blueprint and cell source for the OoC. From there, the biology (including cell sources and biomaterials/scaffolds, and their injection) goes hand in hand with the engineering (including materials and fabrication processes and potentially sensor/actuator integration), with feedback from each branch contributing to adjustments in the other, resulting in an iterative process. Appropriate assays are developed to allow functional validation of the tissue, which can then be applied in (pharmaceutical) industry, clinical research and mechanistic biomedical studies. Reproduced from⁸⁴, CC BY 4.0.

To date, four OoC platforms have been developed incorporating ectocervical cells, two of which feature adjacent compartments containing 2D cell cultures connected by microchannels. The first platform comprised the SCC cell line CaSki and human umbilical vein endothelial cells (HUVECs) in the two adjacent channels to study the interaction between tumor and endothelial cells (ECs)⁸⁶. The second study included immortalized ecto- and endocervical cells in the two compartments to investigate intercellular interactions and their contributions in maintaining cervical integrity in response to LPS and TNF α stimulation⁸⁷. In a recent preprint, a platform with two stacked microchannels separated by a porous membrane was employed to culture a commercially available mixture of primary human endo- and ectocervical keratinocytes along with primary human cervical fibroblasts on each side of the membrane⁸⁸. The epithelial and stromal layers generated a tissue several layers thick and allowed the study of cervical mucus physiology and its role in human host-microbiome interactions. All of these platforms share the widely used material polydimethylsiloxane (PDMS), which is known to absorb hydrophobic molecules⁸⁹. This aspect is particularly important for women's health models, where future applications may require controlled exposure to (hydrophobic) hormones and drugs. These models lack similarity to the in vivo tissue, including the 2D cultivation of cell lines and the lack of perfusion in the first two studies, as well as the non-physiological mixture of epithelial cells in the last model and the exposure of the epithelial cells to media perfusion in all models.

The integration of a tissue explant ensures the exact replication of the tissue, as opposed to the bottom-up approach, which allows the engineered tissue to be adapted to the research question and contribution of each player to be dissected. Despite the drawback of limited availability of replicates, explants have been incorporated into traditional cell culture systems^{90,91}. Xiao et al. (2017) utilized the microfluidic 'EVATAR' platform, which can support five interconnected organs, and incorporated human liver spheroids, mouse ovarian explants, human fallopian tube epithelium, human

endometrium, and human ectocervical explants. The cervical explants, obtained by 3 mm biopsy punches, maintained viability, hormonal responsiveness and stratified squamous epithelial tissue architecture for 28 days. The ability to study inter-organ communication demonstrates an important feature of compartmentalized OoC platforms.

In summary, various animal and in vitro models of the ectocervix have been developed. 3D human ectocervical tissue models are required for research questions related to HPV infection, as HPVs exhibit species- and tissue-specific properties with a high tropism for stratified squamous epithelia⁵⁵. The inclusion of immune components in these models is crucial because the immune system plays a central role in combating HPV infections and the progression of malignancies, both of which are processes that are not yet entirely understood. The development of more effective therapies is hampered by the lack of in vitro cancer models that adequately capture the complexity of human tumors, particularly with respect to the TME and the immune response. Despite treating patients according to defined guidelines, individual responses vary due to the heterogeneity of patients and their tumors. While certain prognostic factors have been identified, there are still many unknown factors that lead to differential therapeutic success⁹². Therefore, there is an urgent need for patient-specific in vitro models for basic research, drug development and to accurately stratify and predict the efficacy of available treatments. OoC technology offers the opportunity to generate sophisticated in vitro models that include perfusion and multicellular 3D tissues and can be well adapted to the use of patient- or donor-derived cells.

CHAPTER 2

Objective of the Thesis

2. Objective of the Thesis

The overall aim of this thesis was to develop a **human in vitro model** based on OoC technology, integrating **normal and diseased ectocervical tissues** to advance knowledge in basic research and explore novel therapeutic approaches in an academic context. To accomplish this overarching goal, the following **specific objectives** were pursued:

1) Development of a **microfluidic platform**

The aim was to design and fabricate a microfluidic platform specifically tailored to ectocervical tissues. This involves the integration of advanced microfabrication techniques and biocompatible materials with tissue engineering, to create a microenvironment that supports complex ectocervical tissues and includes a mimicry of a perfused vasculature. The platform must consist of materials compatible with hydrophobic molecules and allow for a variety of (real-time) readout methods to facilitate comprehensive characterization and application of the OoC.

2) Isolation and characterization of **ectocervical cells from human tissues**

To create multicellular, species- and tissue-specific in vitro models, protocols must be established for the isolation of multiple cell types from resected tissues. Subsequent expansion and extensive characterization of primary cells is required prior to integration into the OoC. Primary cells are the optimal representatives of the original tissues as they contain the human genetic background and closely reflect the heterogeneous in vivo physiology of donors and patients.

3) Generation, cultivation, and characterization of **healthy and diseased ectocervical 3D tissues**

This objective focused on creating multicellular ectocervical tissues that closely emulate the human (patho)physiological tissue architecture. This requires the establishment of protocols for the generation, cultivation, and characterization of normal and diseased 3D ectocervical tissues. An integral aim has been the incorporation of peripheral immune components, specifically focusing on neutrophils (polymorphonuclear leukocytes, PMNs) and their functional structures known as neutrophil extracellular traps (NETs), to facilitate future studies of the immune system and immune-targeting therapies.

4) **Reduction of animal components**

The use of animal-derived products raises ethical concerns, and challenges such as uncertain composition, product variability, and compromised quality. This prompts the need to reduce or eliminate animal components in experimental protocols. While OoC promises to reduce the use of animals in research and drug development, reliance on animal-derived products remains common. Although not the primary focus of this study, consistent efforts to reduce animal-derived products and explore animal-free alternatives were integral to all experiments.

CHAPTER 3

Results

3. Results

3.1. Development of Microphysiological Platforms for Cervical Tissues

3.1.1. Concept of the Microphysiological Platforms

The microphysiological platforms were designed and fabricated specifically for cervical tissue generation and cultivation. The PDMS-free, compartmentalized platforms consist of stacked, transparent polymers that create cylindrical, open-top tissue wells and a microfluidic channel sandwiching a porous membrane (**Figure 4.A**). The open-top tissue well provides direct access for cell seeding and can be sealed with a gas permeable foil during cultivation. The channel mimics the vasculature and is perfused with media to deliver nutrients to the tissue and remove cell products through convective flow driven by a syringe pump (**Figure 4.C**). The membrane serves to protect the tissue from the shear forces of the perfusing media, while its pores allow for the exchange of nutrients, metabolites, cytokines, and the migration of immune cells (**Figure 4.B**). The design, materials and continuous perfusion allow on-chip monitoring through microscopy or effluent analyses for tissue characterization. While maintaining the general concept and tissue area size throughout the platform's development, the design and materials were adapted and optimized through an iterative process, resulting in three generations of microphysiological platforms.

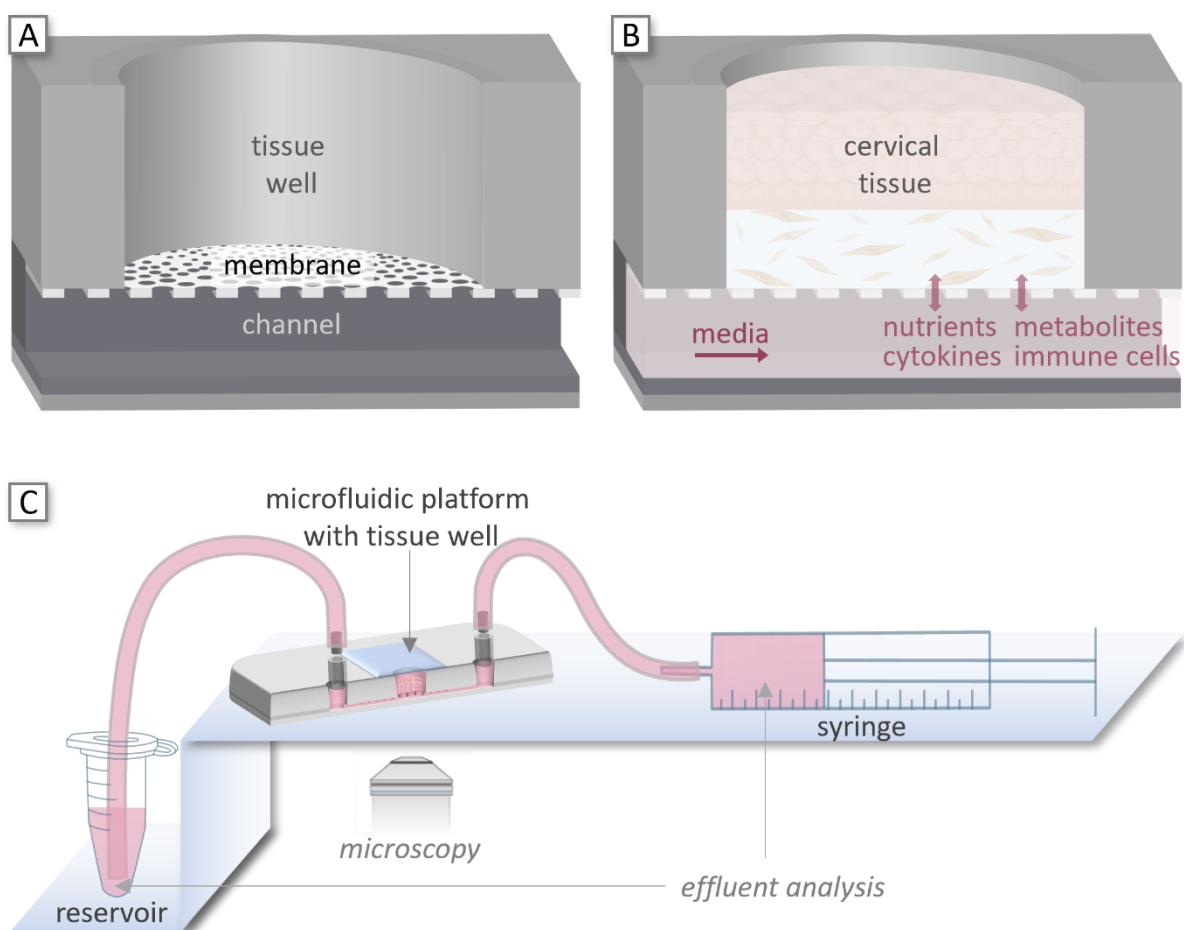


Figure 4: Concept of the Microfluidic Platforms.

A) The open-top tissue well is separated from the channel by a membrane. B) The cervical tissue is supplied by media perfusion through the channel. The porous membrane allows for diffusion of nutrients, metabolites and cytokines as well as migration of immune cells. C) Media flow is driven by a syringe pump, either by positive (“push”) or negative (“withdraw”) pressure. A media reservoir is connected to the opposite port. Platform design and media perfusion allow for real-time monitoring by microscopy and effluent analysis.

3.1.2. First Platform Generation: Laser-Cut Thermoplastic Layers Thermally Fused to a Single-Well Platform

The initial version of the platform featured a single tissue well and was fabricated by thermal fusion bonding of three laser-cut poly(methyl methacrylate) (PMMA) layers enclosing a polycarbonate (PC) membrane (**Figure 5.A,B**). When fabricated in a single bonding step, membrane sagging frequently occurred due to the large diameter of the underlying channel. Furthermore, moderate viability of cervical epithelia generated with primary cervical keratinocytes in dynamic culture was observed in preliminary experiments. To address these issues, laser cutting was employed for rapid micro-structuring, and various channel designs and configurations were explored. Eventually, a design featuring a slightly broader outlet channel, aimed at reducing media flow resistance to prevent its passage through the membrane and potential damage to the tissue, was selected for further tissue cultivation experiments. To counteract membrane sagging, a preceding thermal bonding step in the fabrication process was introduced, incorporating a PDMS support structure (**Figure 5.C**). This support structure was placed in the channel of the media layer beneath the membrane and was removed prior to the final thermal fusion with the tissue and bottom layer. Pressure was applied during the fusion process using foldback clips (**Figure 5.D**). The resulting platform was prepared for dynamic tissue cultivation by integrating adapters into the tissue layer for the connection with tubings or reservoirs (**Figure 5.E**). The platforms were placed in a drawer-like chip holder during dynamic cultivation, facilitating handling and increasing stability (**Figure 5.F**).

While the first generation of the platform demonstrated successful cultivation of primary cells as shown in **Figure 11.A**, the dense 3D tissues limited the penetration depth of microscopic analyses in the Z-direction. Despite the remarkable transparency of the platform, imaging from the side of the platform would require design modifications to decrease the distance of the tissue from the objective, and, more significantly, extensive material processing. Histology, a commonly used method for tissue characterization, could provide high resolution in the Z-direction and enable later comparisons between the engineered model and the original *in vivo* tissue or literature. However, retrieving the small and delicate tissue from the platform with a 1.2 mm biopsy punch resulted in tissue damage and loss, necessitating design and material modifications. In addition to the challenges of tissue characterization, the single tissue well design required labor-intensive fabrication of numerous platforms even for experiments with a limited number of conditions. The proximity of the tissue to the chip surface posed a risk of unintentional contact with the adhesive foil during cultivation or with pipette tips during media changes. Moreover, static cultivation by adding media on top of the platform posed the risk of media spillage, further motivating the need for design changes. Finally, imperfect bonding occasionally led to leakage during tissue generation and cultivation, motivating the search for alternative materials.

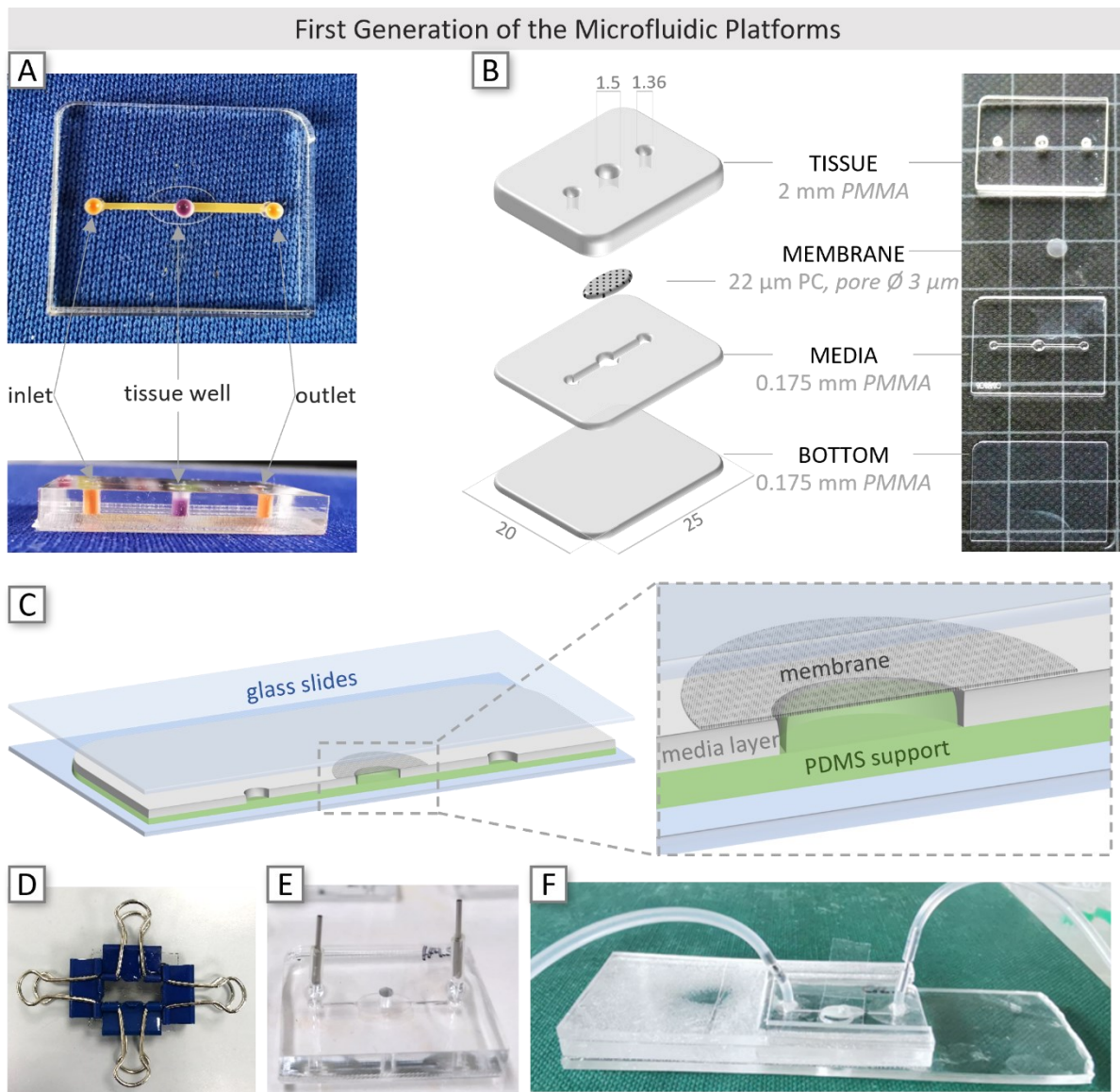


Figure 5: A Single-Well Thermoplastic Module Represented the First Generation of the Microfluidics Platforms.

A) Photographs of the platform from both top and side perspectives, highlighting the high transparency and the tissue well (purple) in the center between the inlet and outlet, which are connected by the channel (orange). The channel linked to the outlet possesses a marginally broader width of 0.8 mm in contrast to the 0.5 mm width of the channel linked to the inlet.

B) The platform was fabricated from three laser-cut PMMA layers, encompassing the tissue, media and bottom layers with a PC membrane (pore diameter 3 µm) positioned between the media and tissue layers. Dimensions are specified in mm. PMMA: poly(methyl methacrylate), PC: polycarbonate.

C) A PDMS support structure (green) was placed underneath the media layer and the membrane (gray) in the first bonding step and sandwiched between two glass slides (blue) to prevent the membrane from sagging. PDMS: polydimethylsiloxane.

D) Photograph of the platform assembly for thermal fusion bonding with pressure applied by foldback clips.

E) Photograph of the final platform including adapters consisting of small tubing and needles inserted into the ports and sealed with PDMS.

F) Photograph of a microscope slide-sized PMMA chip holder with a microfluidic platform and tubing connected to the adapters.

3.1.3. Second Platform Generation: Integration of Flexible Thermoplastic Elastomer Layers into a 4-Well Platform Enables Tissue Retrieval

The second generation addressed the challenges of the first version. The updated design integrates four tissue wells to increase replicates, with two parallel channels supplying two sequential wells each (**Figure 6.A**). Furthermore, the material composition was altered from a fully thermoplastic module to a hybrid that included a thermoplastic elastomer (TPE). This facilitated tissue retrieval and notably reduced leakage. A PMMA reservoir layer was added above the tissue layer to act as a spacer between the tissue and the adhesive foil. This addition effectively prevented media spillage and unintended contact with the tissue, as the media was contained in a large reservoir well and could be removed at a safe distance.

To fabricate the optimized platform, the channel in the media layer was microstructured by hot embossing and simultaneously thermally bonded to a PC layer (**Figure 6.B**). Due to the adhesiveness and rough surface of the TPE layer, the bottom PC foil served to optimize optical properties, robustness, and cleanliness of the platform⁹³. In an initial thermal bonding process, the membrane was sandwiched between the hot embossed media/bottom layer and the tissue layer. The PMMA reservoir layer was added on top in a second bonding step.

The material adaptation of the media and tissue layer to the rubber-like TPE styrene-ethylene-butylene-styrene (SEBS) vastly improved the tissue retrieval process. A 4 mm biopsy punch, narrow enough to pass through the hole in the reservoir layer, could cut around the well through the remaining SEBS/PC layers (**Figure 6.C**). This created a protective ring of SEBS around the delicate tissue, reducing tissue loss and facilitating handling in the histology process. Spatial orientation was maintained throughout the embedding and sectioning process by asymmetric extraction. Potential damage to the tissue cannot be ruled out due to the flexibility of the TPE material. In addition to the application of the retrieved tissue to histology for in-depth characterization, this procedure allows the application of different analyses from each of the replicates of the same module.

This improved platform was used to create various models of normal and diseased tissues (**Figure 6.B,C; Figure 12-Figure 16**). However, in terms of channel design, the bifurcated configuration presented a drawback: media flow was often not perfectly separated at the bifurcation, resulting in different flow rates in the two parallel channels. This affected media delivery to the tissues and resulted in uneven cell distribution during endothelialization of the channel and immune cell perfusion.

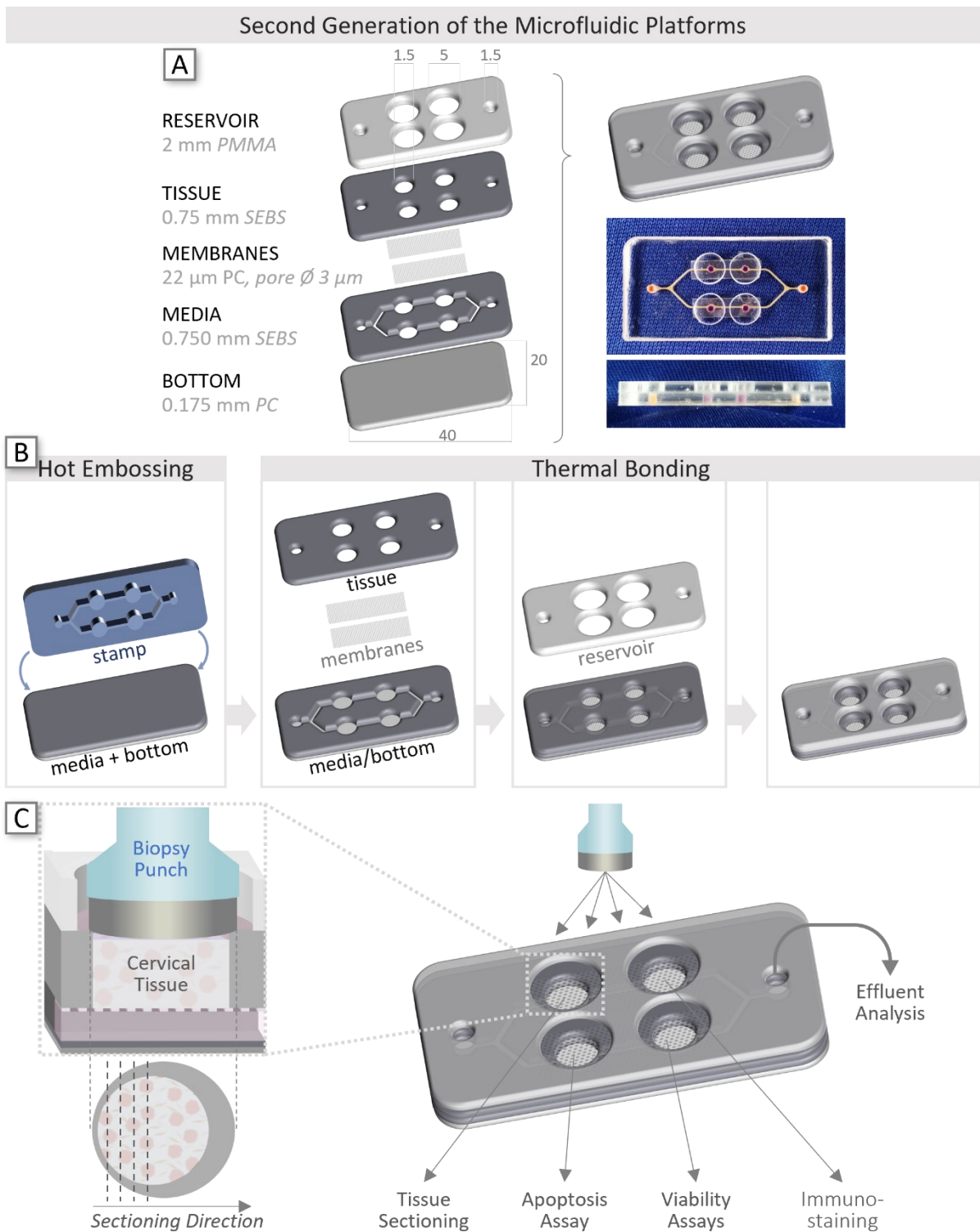


Figure 6: A 4-Well Module Integrating Thermoplastic Elastomers as the Second Generation of the Microfluidic Platforms.
 A) Illustration of the platform and the constituent layers used in its fabrication, accompanied by a photograph of the fully assembled platform. The platform consists of a PC bottom and SEBS media layer, two laser-cut PC membranes (pore diameter 3 μm), and a laser-cut SEBS tissue and PMMA reservoir layer. Dimensions are specified in millimeters. PMMA: poly(methyl methacrylate), SEBS: styrene ethylene butylene styrene, PC: polycarbonate. B) The fabrication process involved the microstructuring of the channel design into a SEBS/PC hybrid material through a combination of hot embossing and thermal fusion techniques. First, laser-structured PC membranes and SEBS tissue layers were thermally bonded to the membrane/bottom layer, followed by the addition of the reservoir layer on top. C) The integrated TPE layer facilitated tissue retrieval using a biopsy punch, enabling the application of multiple readout methods on the same system. The asymmetric removal of the tissue facilitated the maintenance of the orientation throughout the subsequent embedding and sectioning process.

3.1.4. Third Platform Generation: Microscope Slide-Sized 8-Well Platform with Two Fluidically Independent Systems

The third iteration of the platform was based on the previous version with modifications to the design and fabrication process. The latest platform implemented two independent systems with four tissue wells each, effectively increasing the number of replicates to eight wells per module (**Figure 7.A, Publication [3]**). Each system features a straight channel for optimized media supply, immune cell integration, and endothelialization (**Figure 7.B,C**). The convenient size and dimension of a microscope slide eliminated the need for chip holders, further simplifying handling. The chip fabrication process was accelerated to a single-step bonding process, and reproducibility was optimized by replacing foldback clips with weights for consistent pressure application. With this platform, an immunocompetent CCoC was established (**Publication [3]**).

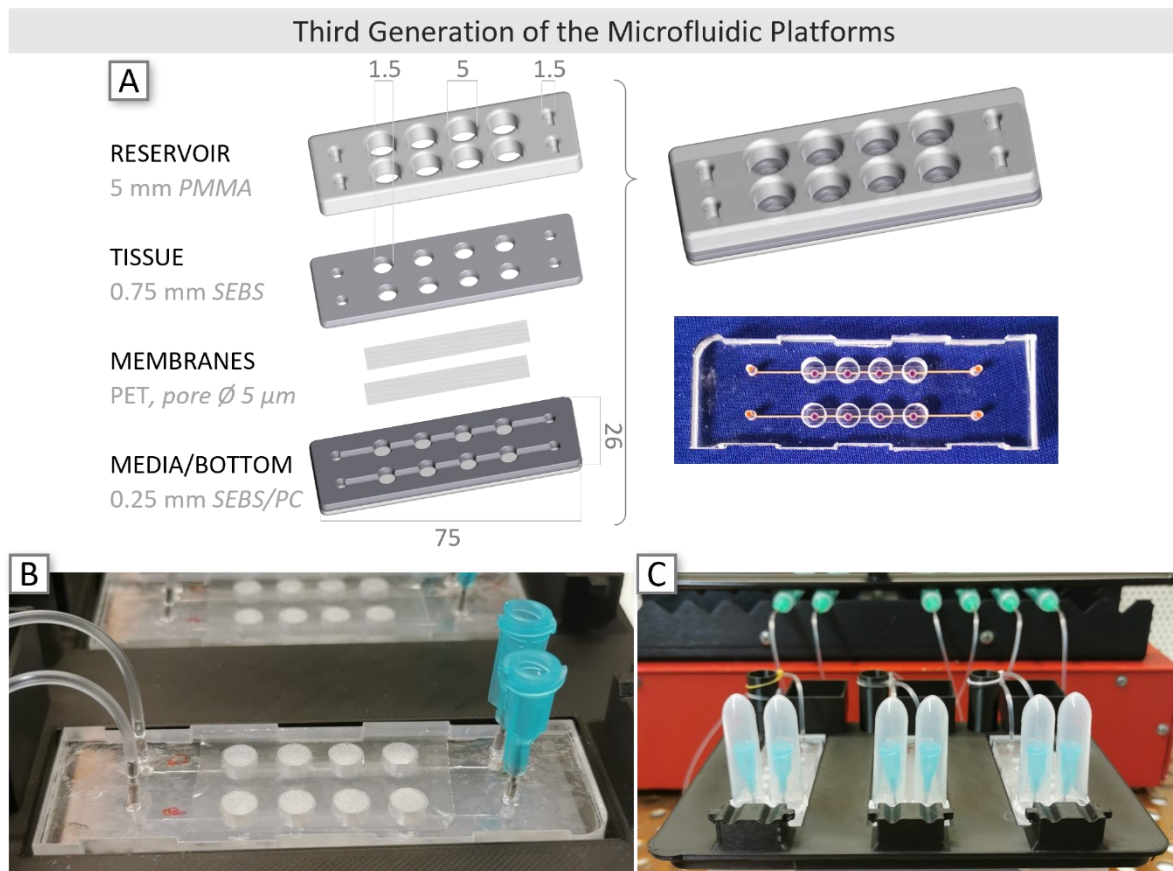


Figure 7: An 8-Well Module with Two Independent Fluidic Systems Represents the Third Generation of the Microfluidic Platforms.

A) Schematic of the platform and its component layers used for manufacturing, accompanied by a photograph of the fully assembled platform. Schematics adapted from **Publication [3]**. Dimensions are specified in mm. PMMA: poly(methyl methacrylate), SEBS: styrene ethylene butylene styrene, PET: polyethylene terephthalate, PC: polycarbonate. B) Photograph of a fully assembled platform connected to tubings and reservoirs for immune cell perfusion. C) Photograph of three platforms in a 3D-printed holder, connected to a syringe pump and reservoirs, which were covered with lids to maintain sterility.

3.2. Characterization of Human Ectocervical Tissue and Isolation of Keratinocytes, Fibroblasts and Endothelial Cells

Cervical tissues were obtained from elderly, postmenopausal women with unrelated diseases, most frequently uterus descensus and uterine fibroid. Resected tissues varied in size, with epithelial surface area of approx. 0.5-4 cm² and connective thickness of 1-2 cm. The tissues were utilized as in vivo reference and cell source.

To enable future comparisons between engineered models and clinic-derived tissues, a selection of antibodies was assembled for a comprehensive characterization panel and verified on formalin-fixed paraffin embedded (FFPE) tissue sections of the donor-tissue. The ectocervix is composed of multiple cell layers (**Figure 2**), which are distinguishable in HE stainings and further identifiable by specific markers (**Figure 8.A**). CK19 strongly stains the basal layer but is only sporadically detected in the parabasal and intermediate layers. The parabasal cells typically exhibit mitotic activity and show positive Ki67 staining, while the remainder of the normal squamous epithelium is Ki67-negative^{2,15,16}. CK14 decorates all cells of the basal and parabasal layers, along with occasional cells in the intermediate layers, but is rarely detected in the superficial layers. CK13 is a differentiation-specific CK that decorates the cells of the parabasal, intermediate, and superficial layers. E-Cadherin (E-Cad) serves as the predominant cellular adhesion molecule in the ectocervix and is located at the lateral margins of cells in the basal, parabasal and intermediate layers. In the stromal layer, collagen IV delineates the basement membrane (**Figure 8.A**), a specialized form of the extracellular matrix that provides a mechanical support for epithelial and endothelial tissues⁹⁴. Vimentin (vim), an intermediate filament present in mesenchymal cells, as well as fibronectin (FN), a glycoprotein present in the ECM, is found in the stroma of the ectocervix⁹⁵. Several markers of ECs of the vasculature were confirmed on the in vivo tissue, including von Willebrand factor (VWF), a glycoprotein involved in blood clotting, CD31 (also known as platelet EC adhesion molecule-1 (PECAM-1)), an adhesion protein crucial for leukocyte migration, and VE-Cadherin (VE-Cad), a cell adhesion molecule located exclusively at the junctions between ECs and essential for controlling vascular permeability and leukocyte extravasation⁹⁶.

Three major cell sources are commonly utilized in tissue engineering, i.e. cell lines, induced pluripotent stem (iPS) cells and primary cells isolated from tissue or liquid biopsies. By focusing on donor-derived cells, patient variability can be captured and personalized medicine advanced. Existing protocols were adapted for the isolation of three cell types from a single cervical tissue: ectocervical keratinocytes^{65,72,97}, fibroblasts^{72,97,98} and ECs⁹⁹. The cell isolation process from the cervical tissue (**Figure 8.B**) involved a combination of mechanical and enzymatic techniques. Initially, the bulk connective tissue, rich in smooth muscle cells and ECs, was removed mechanically with a scalpel. Separation of the epithelium and stroma by enzymatic digestion was followed by a separate mincing of the tissues. Keratinocytes were singularized with trypsin and digestion was stopped with trypsin inhibitor instead of Fetal Calf Serum (FCS) to reduce the use of animal components. Similarly, keratinocytes were cultured in a Keratinocyte Serum-Free Media (K-SFM) without supplementation of FCS, reducing the use of animal components and the risk of overgrowth by contaminating fibroblasts. Accumax™ was used for subcultivation as a more gentle detachment solution than trypsin. Keratinocytes in expansion culture expressed the epithelial markers E-Cad and CK13, CK14 and CK19 (**Figure 8.C**). In the cell culture, the ratio was shifted toward more cells expressing CK14 and CK19 compared to the in vivo tissue (**Figure 8.A**), where most cells were positive for CK13. The cervix predominantly consists of fibroblasts, constituting 49% of its cellular composition¹⁰⁰. They were isolated from the subepithelial stroma from which the epithelium was removed (**Figure 8.C**). Following enzymatic digestion of the minced stroma, fibroblasts were cultured in DMEM with 10% FCS and penicillin and streptomycin (P/S) and subcultured with TrypLE™ as an animal-free alternative to trypsin. During propagation, fibroblasts expressed the intermediate filament vim and the ECM component FN. ECs, the second most abundant cell type of the cervix at 24%¹⁰⁰, were isolated from the connective tissue (**Figure 8.C**). To reduce animal components, enzyme-free dissociation solution replaced trypsin to loosen ECs in the vessels of the tissue. ECs were scraped out with a scalpel into a dish containing Endothelial Cell Growth Media (ECGM) instead of phosphate-buffered saline (PBS) to increase yield

and viability, and were cultured in the presence of P/S. Primary ECs adhered and proliferated after isolation but not in secondary culture.

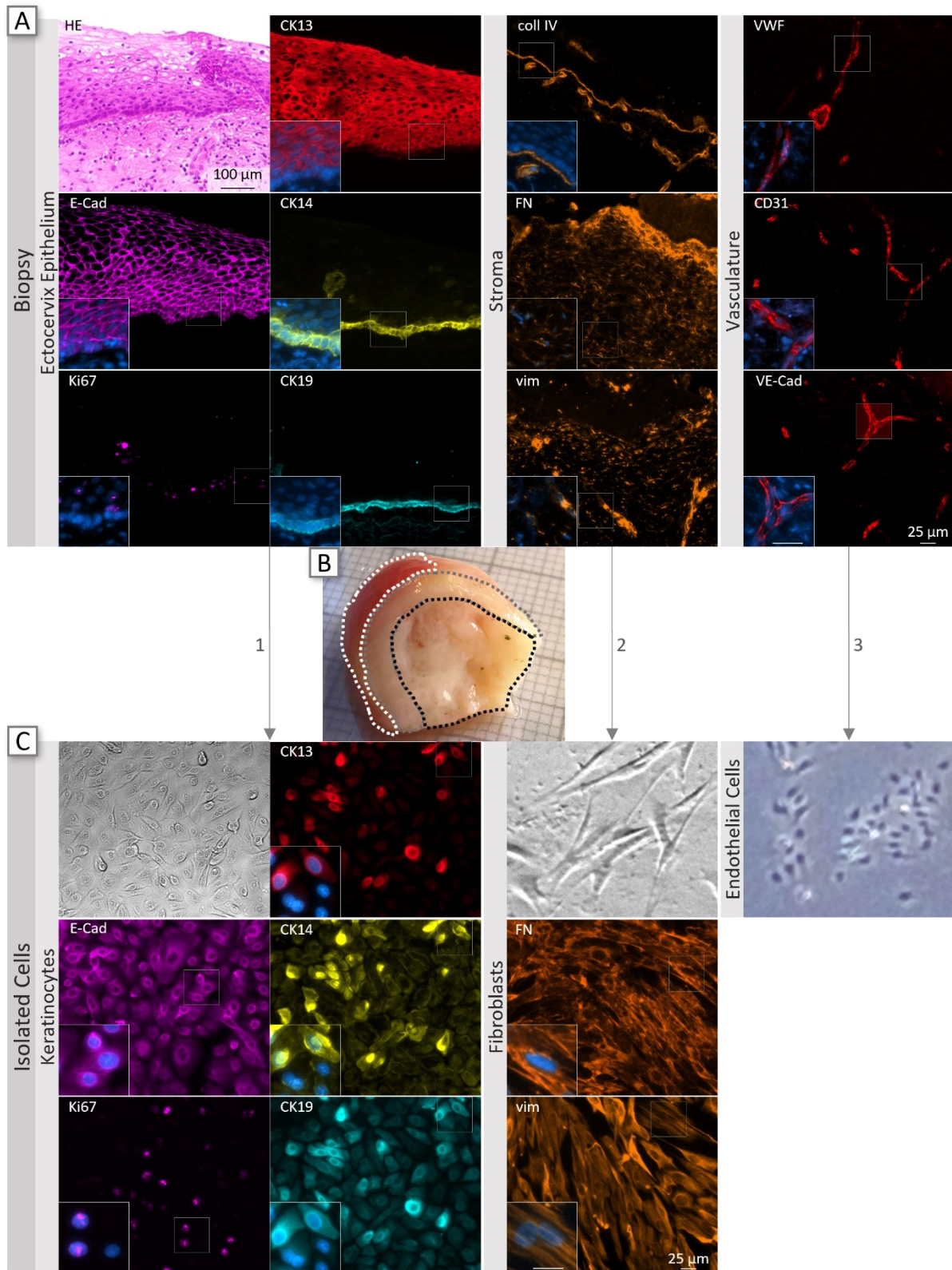


Figure 8: Keratinocytes, Fibroblasts and ECs Were Isolated from Human Cervical Tissues.

A) Sections of human cervical tissue including epithelium and stroma applied to hematoxylin and eosin (HE) and immunohistochemistry. Characterization of the epithelium by E-Cad (magenta), Ki67 (magenta), CK13 (red), CK14 (yellow), and CK19 (turquoise), the stroma by collagen IV (coll IV, orange), FN (orange) and vim (orange) and the vasculature by VWF (red), CD31 (red) and VE-Cad (red). B) Human cervical tissue with dotted lines indicating the epithelium (white), the stroma (light gray)

and the connective tissue (dark gray). C) The cells were isolated and expanded from the marked areas as shown in B), i.e. keratinocytes from the epithelium, fibroblasts from the stroma, ECs from the vasculature of the connective tissue. Cells were characterized by immunocytochemistry using the markers as described in A).

Antibody production traditionally relies on animals, but efforts to improve reproducibility and quality have led to the development of recombinant antibodies and phage display as an animal-free approach to antibody selection and maturation¹⁰¹. Immunocytochemistry (ICC) staining of primary keratinocytes with a Ki67 antibody generated with the HuCal library failed to produce a signal (**Figure 9**). In contrast, the secondary anti-mouse antibody from the HuCal library gave comparable results to the standard animal-derived polyclonal antibody.

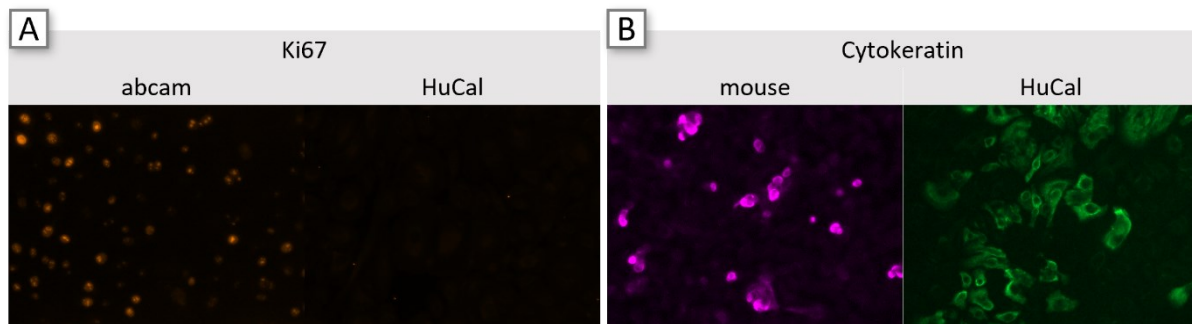


Figure 9: Comparison of Animal-free and Animal-Derived Antibodies.

A) Antibodies directed against Ki67 were used to stain cervical keratinocytes cultured in 96 well plates and derived from either a rabbit or the HuCal library. While a signal was observed with the animal-derived antibody, no signal was present with the HuCal-derived antibody. B) Primary antibody targeting CKs in cervical keratinocytes grown in a 96 well plate was applied, followed by the addition of a secondary antibody derived from either a goat or the HuCal library. The non-animal secondary antibody produced results comparable to those achieved with the animal-derived polyclonal antibody.

3.3. Tissue Engineering of Ectocervical Tissues in the Cervix-on-Chip

The ectocervical tissue of mature women in the reproductive age consists of a multilayered differentiated epithelium covering a stromal layer. While the epithelium consists mainly of keratinocytes, the stromal layer of the cervix is dominated by fibroblasts, endothelial and immune cells¹⁰⁰. Several approaches to generate a 3D tissue in the Cervix-on-Chip (CXoC) have been explored. Attempts to induce substantial ECM production in fibroblasts using the low-serum medium CnT-PR-F¹⁰², as well as efforts involving a cell accumulation technique with ECM-coated fibroblast¹⁰³ and the infiltration of a collagen membrane by fibroblasts, resulted in fibroblast aggregation. Embedding fibroblasts in transparent hydrogels emerged as a more promising approach for the consistent production of 3D stromal layers. This method offers multiple advantages, including the ability of hydrogels to mimic the human ECM, their rapid preparation, and compatibility with microscopic analyses.

To create an ectocervical tissue, hydrogel containing fibroblasts was introduced into the tissue well and allowed to equilibrate with static media supply (**Figure 10**). Subsequently, keratinocytes were seeded onto the hydrogel and allowed to reach confluency in a static co-cultivation period. To induce differentiation, the tissue was cultivated at the ALI, with media removal from the top of the tissue and the dynamic media supply through the channel.

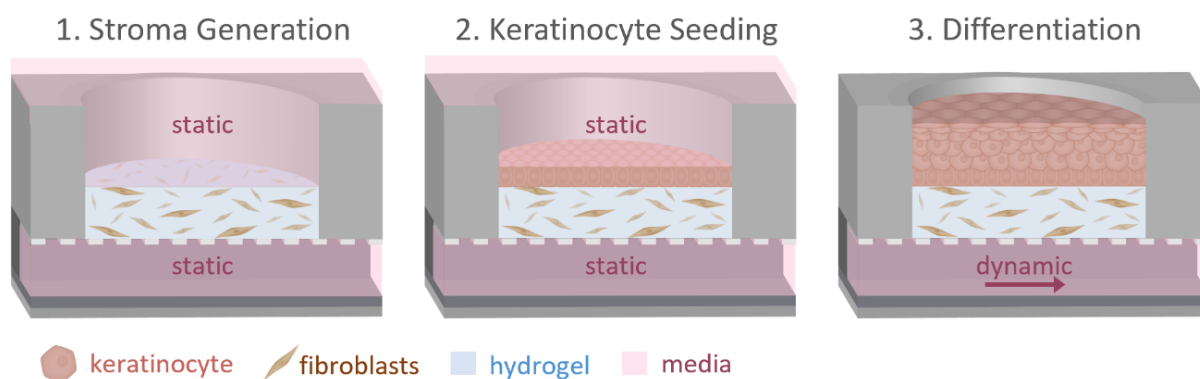


Figure 10: Process for the Generation of a Normal Ectocervical Tissue in the CXoC.

1. A stromal layer is generated in the tissue well above the membrane and equilibrated during static cultivation. 2. Keratinocytes are seeded onto the stroma and cultivated statically to achieve a confluent monolayer. 3. Epithelial differentiation is induced by cultivating the tissue at the ALI and media is supplied by dynamic perfusion in the channel.

3.3.1. Generation of Ectocervical Tissue Using Collagen Matrices

The cervical ECM is predominantly composed of collagen, which constitutes 54-77%¹⁰⁴, and is widely employed for the development of in vitro models of the cervix⁷⁰⁻⁷². Hence, the stroma in the CXoC was emulated by embedding cervical fibroblasts in collagen I. In the presence of fibroblasts, the structural integrity of the collagen hydrogel was lost, resulting in a contraction of the bovine collagen I hydrogel FibrCol® (**Figure 11.A**). Despite the observed shrinkage, the fibroblast viability remained high (**Figure 11.B**).

Next, keratinocytes were added to the surface of bovine or rat tail-derived collagen I and differentiated at the ALI. For in-depth characterization of the tissue, protocols for tissue retrieval from the platform, paraffin embedding, sectioning and staining were established as described in the experimental section (**Figure 19-Figure 21**), with the small size of the tissue and its fragility posing major challenges. The epithelial cells adhered to the bovine FibrCol® and rat tail-derived RatCol® hydrogel and formed a multilayered epithelium upon the differentiation process (**Figure 11.C,D**). While basal CK19 was present in all layers, the expression of suprabasal CK13 and parabasal CK14 indicated differentiation toward the epithelial surface. Attempts to achieve reproducible structural stability by combining the natural component collagen with the synthetic polymer polyethylene glycol (PEG)¹⁰⁵ as well as the deposition of polydopamine (PDA) on the platform, a mussel-inspired material that enhances collagen hydrogel adhesion¹⁰⁶ proved ineffective (**Figure 11.E,F**). Despite these promising features of the differentiated epithelium, the shrinkage rendered collagen gels unsuitable as an ECM substitute.

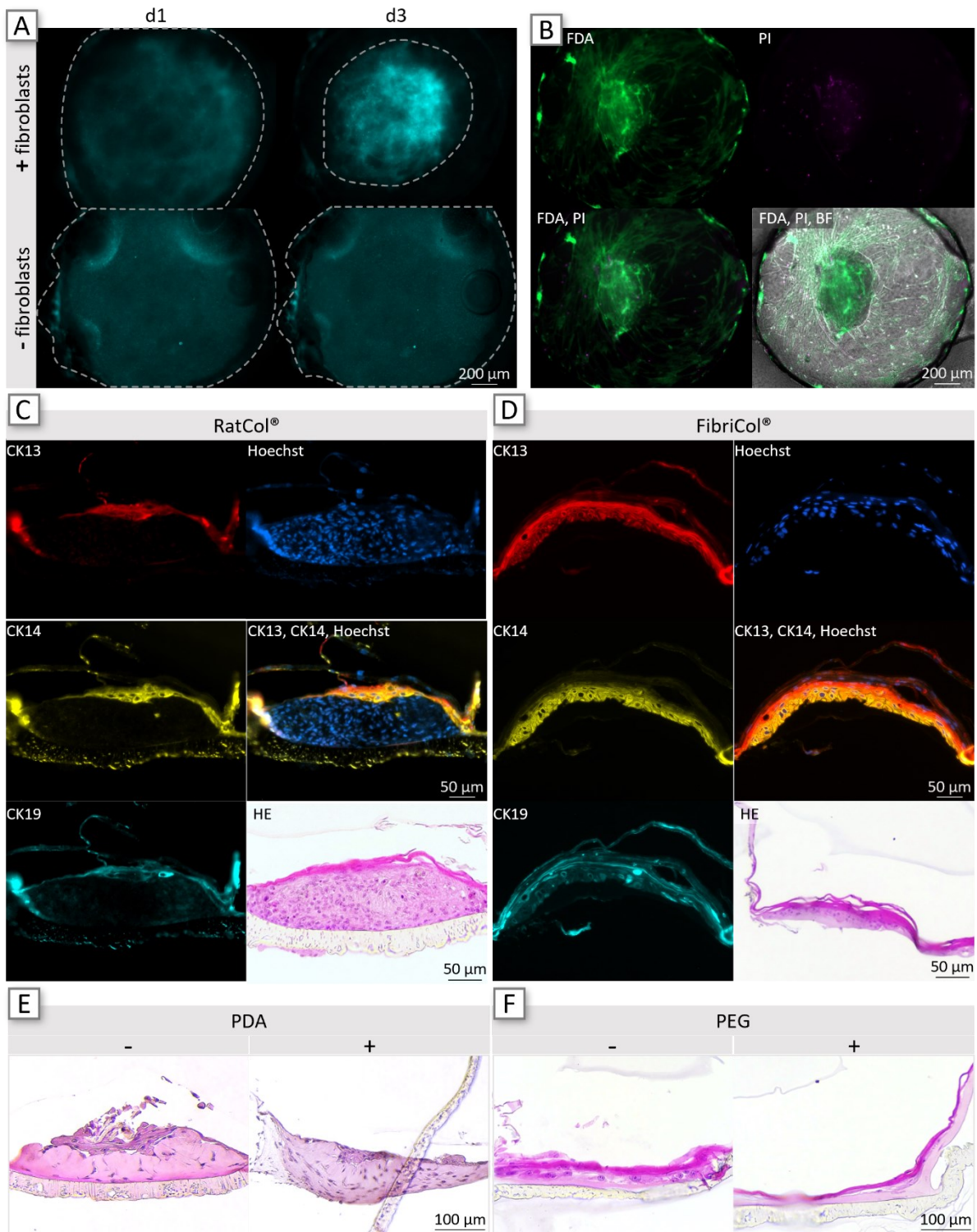


Figure 11: Collagen I Shrinks in the Presence of Fibroblasts and Supports Epithelial Differentiation in the CXoC.
 A) Collagen spiked with fluorescent beads was cultured for 3 days and showed lateral shrinkage in the presence of fibroblasts. B) Fibroblasts exhibited high viability on day 4, as displayed by fluorescein diacetate (FDA, living cells in green) and propidium iodide (PI, dead cells with magenta nuclei) staining. Collagen shrinkage is evident in the brightfield (BF) overlay, where collagen is in the center of the tissue well. C,D) In a co-culture model, stromal layers were generated using RatCol® (C) or FibriCol® (D). Shrinkage of the collagen was observed regardless of the collagen source. The keratinocytes formed a multilayered epithelium expressing CK13 (red), CK14 (yellow), and CK19 (turquoise), with *in vivo* like suprabasal CK13 and parabasal CK14 expression. E) The tissue well was coated with PDA and normal ectocervical tissue generated with RatCol®. The tissue exhibited shrinkage both in the presence and absence of PDA. F) Cervical tissue was prepared using RatCol® with the addition of PEG. The tissue showed shrinkage regardless of the presence or absence of PEG.

3.3.2. Semisynthetic HyStem[®]-C Hydrogel is Stable During Long-term Culture of Ectocervical Tissue

HyStem[®]-C is a commercially available, semisynthetic hydrogel and was explored for the generation of the stroma as an alternative to collagen hydrogels. The two thiol-modified components hyaluronan and denatured collagen were chemically cross-linked using the thiol-reactive cross-linker polyethylene glycol diacrylate. Cervical fibroblasts were embedded in the hydrogel and co-cultured with cervical keratinocytes at the ALI. With this hydrogel, no lateral shrinking of the stromal layer in the presence of fibroblasts was observed and resulted in a robust 3D tissue (**Figure 12.A**). After the differentiation process, fibroblast viability remained high, as evidenced by images focused on fibroblasts on the membrane. Inverting the CXoC for a detailed view of the keratinocytes revealed their high viability, although they did not uniformly cover the entire hydrogel surface. panCK staining of tissue sections confirmed the presence of multiple layers of keratinocytes in some areas (**Figure 12.B**). The basal cell marker CK19 was expressed in all keratinocyte layers, while only a few expressed the differentiation markers CK13 and CK14. Fibroblasts appeared elongated in vim and HE staining, although predominantly round fibroblasts were observed in replicates and disease models (**Figure 15.D**). Despite attempts in multiwell plates to improve epithelial coverage and thickness by changing the differentiation media and varying the number of keratinocytes or fibroblasts, control wells lacking the hydrogel proved superior viability and confluency compared to any other condition. Thus, despite its resistance to shrinkage, HyStem[®]-C has proved unsuitable for generating cervical tissues with ectocervical epithelia.

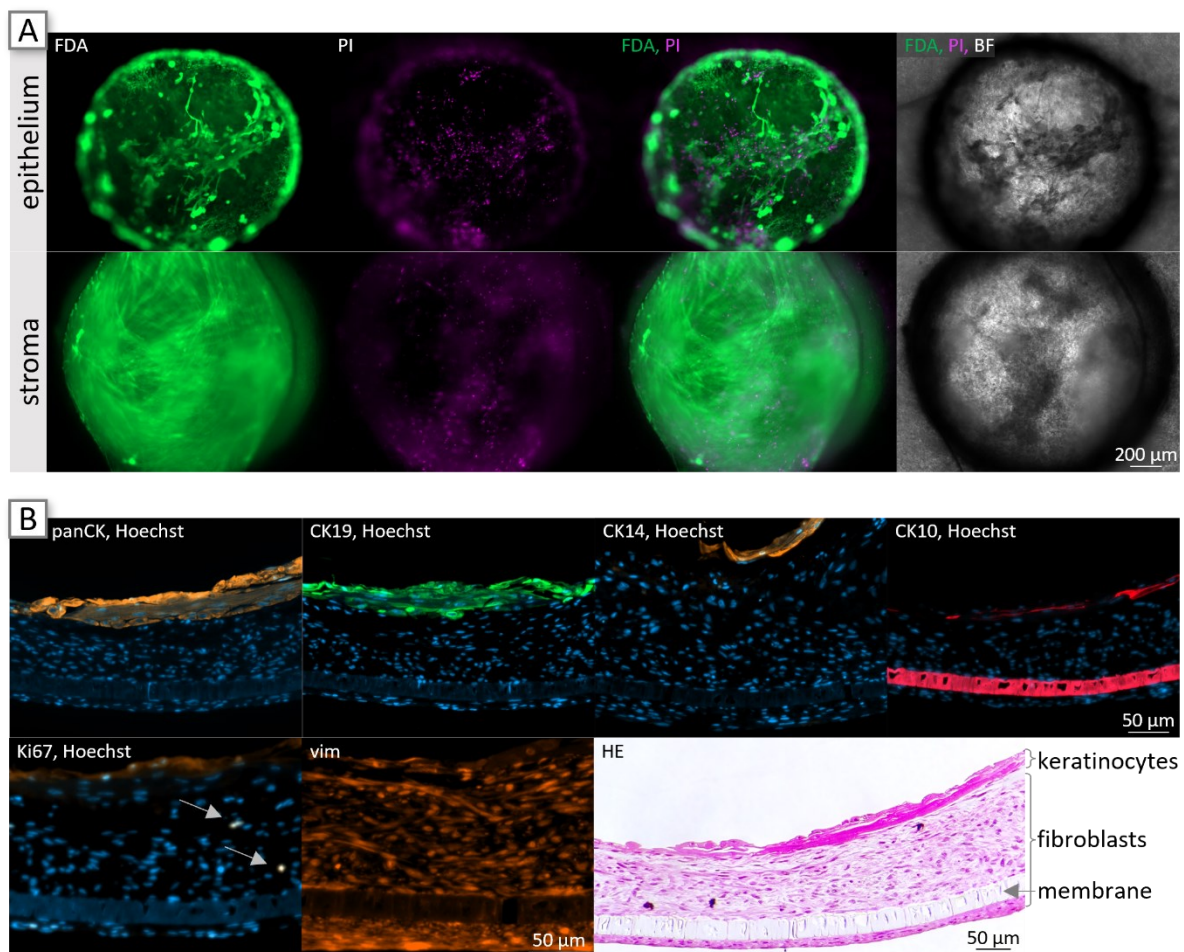


Figure 12: HyStem[®]-C is a Robust Hydrogel in a Long-Term Cultivated Model of Ectocervical Tissue in the CXoC.
 A) The stromal layer was generated with HyStem[®]-C and keratinocytes differentiated at the ALI. Both the uppermost keratinocytes and the lowermost fibroblasts of the tissue showed high viability and the tissue occupied the entire area of the

tissue well, indicating no substantial lateral shrinkage. B) Cross-sectional tissue sections revealed multiple layers of keratinocytes positive for pan-CK (panCK, orange) and CK19 (green), with a few layers of parabasal CK14 (orange) and superficial CK10. Fibroblasts were positive for vim (orange) and some of them were positive for Ki67 (orange, white arrows). HE staining demonstrated the keratinocyte epithelium atop the fibroblast-containing stromal layer on the membrane.

3.3.3. Synthetic Dextran Hydrogel is Mechanically Robust and Supports Ectocervical Keratinocytes

As a third option for generating a stromal layer with a hydrogel, a chemically defined composition based on dextran was explored, which is entirely free of animal components. The RGD-spiked, thiol-reactive dextran was chemically cross-linked with the cell degradable, thiol-modified hyaluronan CD-HyLink. This recently developed cross-linker is a modified version of the commercially available HyLink, which differs in the incorporation of an MMP-cleavable peptide. The hydrogel's stiffness is adjustable by varying the cross-linking strength and was tested at concentrations of 1.2 mM and 2.4 mM.

No lateral shrinkage was observed following cervical tissue generation and differentiation on the platform (**Figure 13.A**). Viability was moderate and remained consistent across all stiffness variations and an additional coating of the hydrogel's surface with RGD was indistinguishable from the other conditions. Keratinocytes covered the entire well with uniform viability, although epithelial coverage was not consistently reproducible. Despite the presence of all keratinocyte markers (**Figure 13.B**), the epithelium did not show differentiation toward the epithelial surface. Tissues density in BF images and marker intensity indicate a more prominent epithelial layer at lower cross-linking strengths. Fibroblasts within the hydrogel generally exhibited a spherical morphology with small pseudopod formation (**Figure 13.C**).

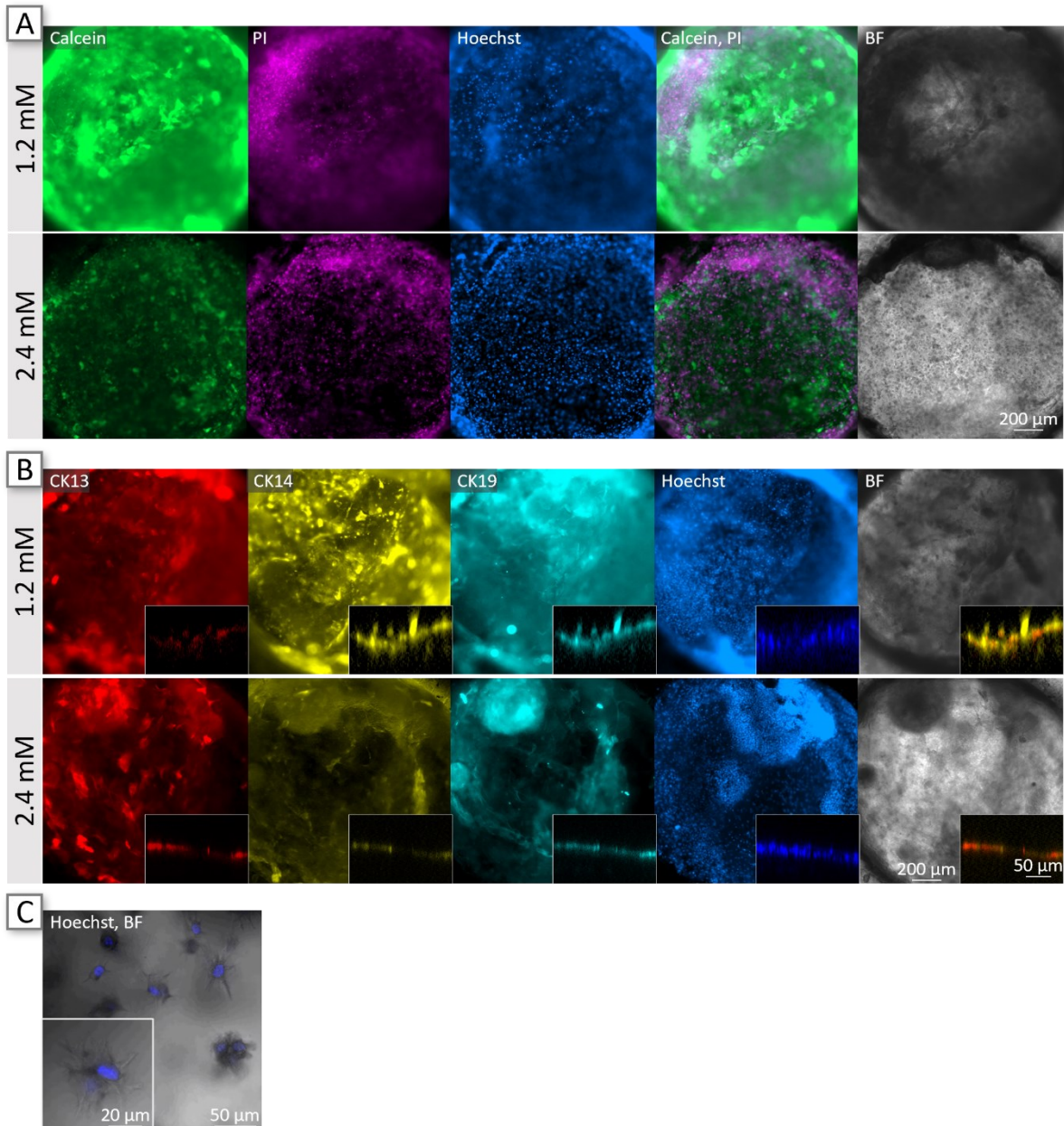


Figure 13: Dextran Hydrogel Serves as a Robust ECM Substitute and Supports Keratinocyte Adhesion in the CXoC.

A) Ectocervical tissues were generating using dextran hydrogel as an ECM substitute, and an epithelial layer differentiated at the ALI. On day 13, viability was assessed with Calcein AM (green) and PI (magenta), revealing moderate viability. Staining intensity and BF density were higher at a cross-linking strength of 1.2 mM compared to 2.4 mM. B) Differentiation markers CK13 (red), CK14 (yellow), and CK19 (turquoise) were expressed in the epithelial layer, with no observable apicobasal stratification in the orthogonal view of confocal immunofluorescence images (inset). Confocal images were acquired with adjusted imaging settings to compensate for tissue density and distance. C) Epithelial coverage was not consistently reproducible, allowing for closer imaging of the fibroblasts embedded in the hydrogel. Fibroblasts were distributed in 3D within the hydrogel and exhibited small, undirected pseudopods.

3.3.4. Scaffold-Assisted Stromal Layer

To establish a 3D stromal layer, porous scaffolds offer an alternative to hydrogels. MatriDerm® is a bovine, freeze-dried collagen-elastin matrix that serves in clinical applications as a dermal replacement scaffold for improved wound healing, and has been utilized in skin tissue engineering¹⁰⁷.

Fibroblasts were seeded onto MatriDerm® and cultivated in a 96 well plate to allow for their infiltration into the scaffold and production of ECM. After 8 days, MatriDerm® was transferred to the platform, and keratinocytes were seeded on top and differentiated until day 21 (**Figure 14.A**). HE staining of the tissue sections showed no substantial lateral shrinkage of the tissue and a thickness of approximately 400 µm. Staining of the epithelial markers CK13, CK14, and CK19 revealed keratinocytes that had permeated the scaffold (**Figure 14.B**). To prevent keratinocytes seeping into the pores, MatriDerm® was combined with collagen I to leverage the scaffold's mechanical stability and the hydrogel's rapid application and support of keratinocytes in distinct epithelial layers. Accordingly, fibroblasts were seeded onto MatriDerm® as a suspension in collagen and transferred to the platform before seeding keratinocyte the following day. After 13 days, MatriDerm® was infiltrated by fibroblasts, as indicated by Hoechst-positive and CK-negative cells, with no lateral shrinkage observed. CK-positive keratinocytes formed a distinct multilayered epithelium comparable to the condition without the scaffold, expressing suprabasal CK13 and parabasal CK14 as expected from *in vivo* tissue.

In preliminary experiments, an in-house produced electrospun polylactic acid membrane¹⁰⁸ was explored as a customizable alternative to the commercially available MatriDerm®, as it is devoid of any animal products and is tunable in terms of fiber thickness, pore size etc. A membrane with a pore size of 20 µm diameter was investigated, compared to approx. 100 µm diameter in MatriDerm®. The scaffold was placed in the tissue well and fibroblasts were seeded on top in a FibriCol® solution. Keratinocytes were added the following day and differentiated at the ALI in a dynamic culture of the tissue. Histologic examination of the tissue section revealed a thickness of 200-300 µm (**Figure 14.C**). The scaffold was infiltrated by cells, expressing high levels of FN and some of which expressed Ki67.

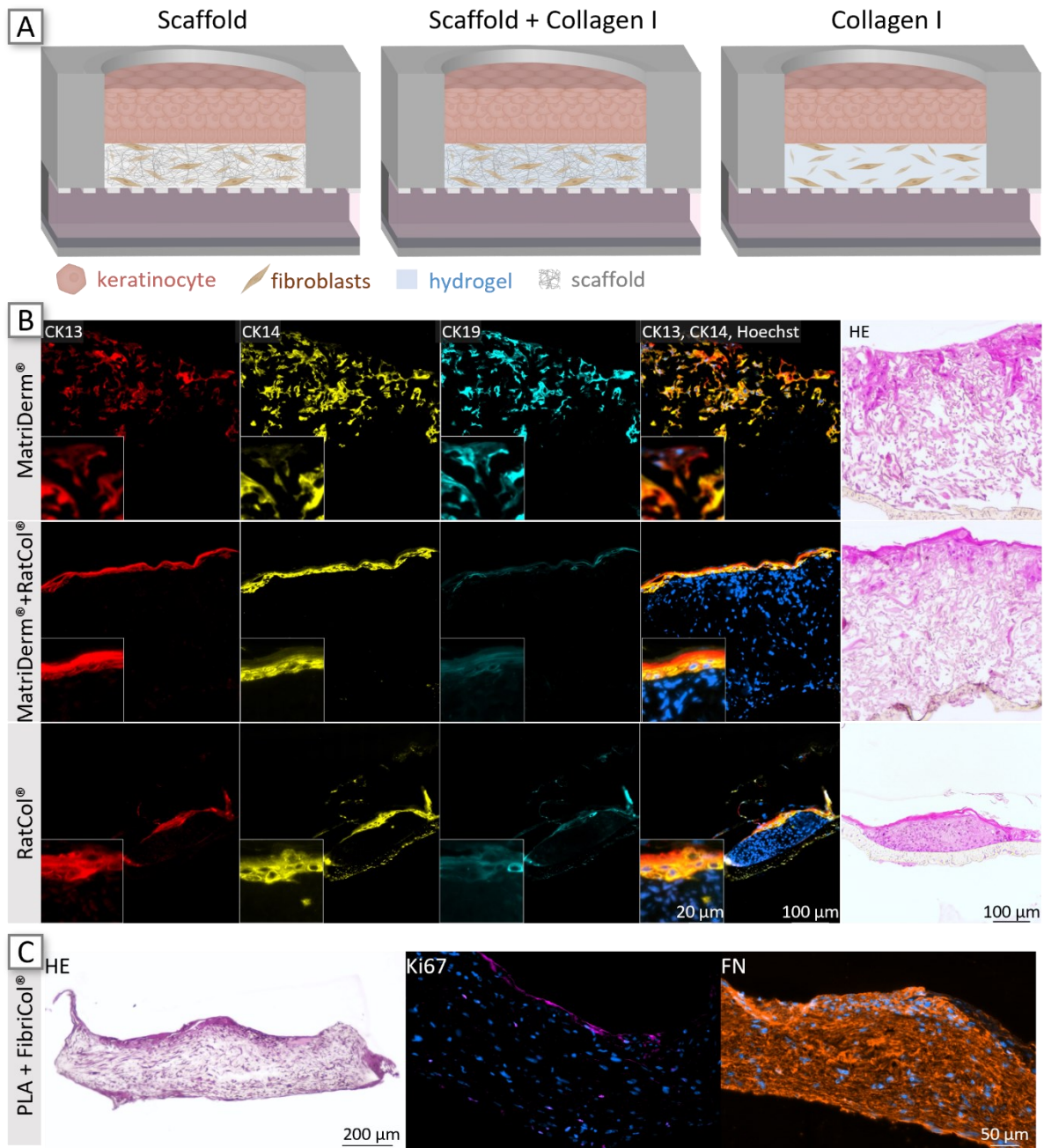


Figure 14: MatriDerm® Represented a Robust Scaffold for Creating a Stromal Layer and Supported a Multilayered Epithelial Differentiation when Combined with a Hydrogel in the CXoC.

A) The schematic depicts the use of MatriDerm® (left), collagen hydrogel (right) and their combination (middle). B) Cervical tissues were generated according to the schematic in A). With MatriDerm® as the biomatrix for the stromal layer, keratinocytes permeated the scaffold. When MatriDerm® was combined with collagen hydrogel, keratinocytes were confined to the top of the stromal layer and generated a multilayered epithelium with ubiquitous CK19 (turquoise) and an in vivo like distribution of CK13 (red) and CK14 (yellow). The use of solely collagen hydrogel revealed shrinkage of the stromal layer with a distinct epithelial layer. C) HE staining of a tissue generated with PLA, with Ki67-positive (magenta) fibroblasts that produce large amounts of FN (orange).

3.4. Generation of a Precancerous Tissue in the CIN-on-Chip

Currently, there are no established standard drugs or adequate, non-invasive treatments available for the premalignant squamous lesion or the causative HPV infection²⁸. Therefore, the primary objective of management is to prevent potential progression to cancer while avoiding overtreatment given that these lesions may spontaneously regress, and invasive treatments may have detrimental (reproductive) side effects. The development of advanced medical interventions could be vastly improved with the availability of a sophisticated human in vitro model and is particularly important for women who wish to bear children.

The second generation of platforms was employed to develop the CIN-on-Chip (CINoC). To model a tissue with a CIN 3 phenotype, which is histologically characterized by a loss of cellular differentiation within the epithelium along a high nuclear density¹⁰⁹, similar approaches to those used in the CXoC were explored to generate the stromal layer. The primary, ectocervical keratinocytes used to create the normal epithelium were replaced with SiHa, a CC cell line established from a SCC grade II¹¹⁰ (**Figure 15.A**). As in the ectocervical model, high viability and shrinkage were observed when the stromal layer was created with collagen in a PDA-coated tissue well (**Figure 15.B**). Tissues with HyStem[®]-C were robust and tissue density increased from day 4 to day 11 (**Figure 15.C**). When grown on collagen and HyStem[®]-C, the epithelial layer exhibited a multilayered structure of up to 200 μm with abundant Ki67 expression and minimal E-Cad expression (**Figure 15.D**). While FN and vim indicated elongated fibroblasts in collagen, the morphology appeared more spherical in HyStem[®]-C. On dextran, SiHa covered the entire tissue, generating a dense epithelial layer and a moderate viability on both dextran with 1.2 mM and 2.4 mM cross-linking strength (**Figure 15.E**). Histology was challenging to perform on the dextran-generated tissues because tissue sections were often lost or damaged. The HE staining shows the spherical morphology of fibroblasts in 2.4 mM cross-linked dextran and the tissue architecture of the CIN tissue with 1.2 mM cross-linked dextran, with an undifferentiated epithelium on top of the stromal layer with fibroblasts accumulated above the membrane.

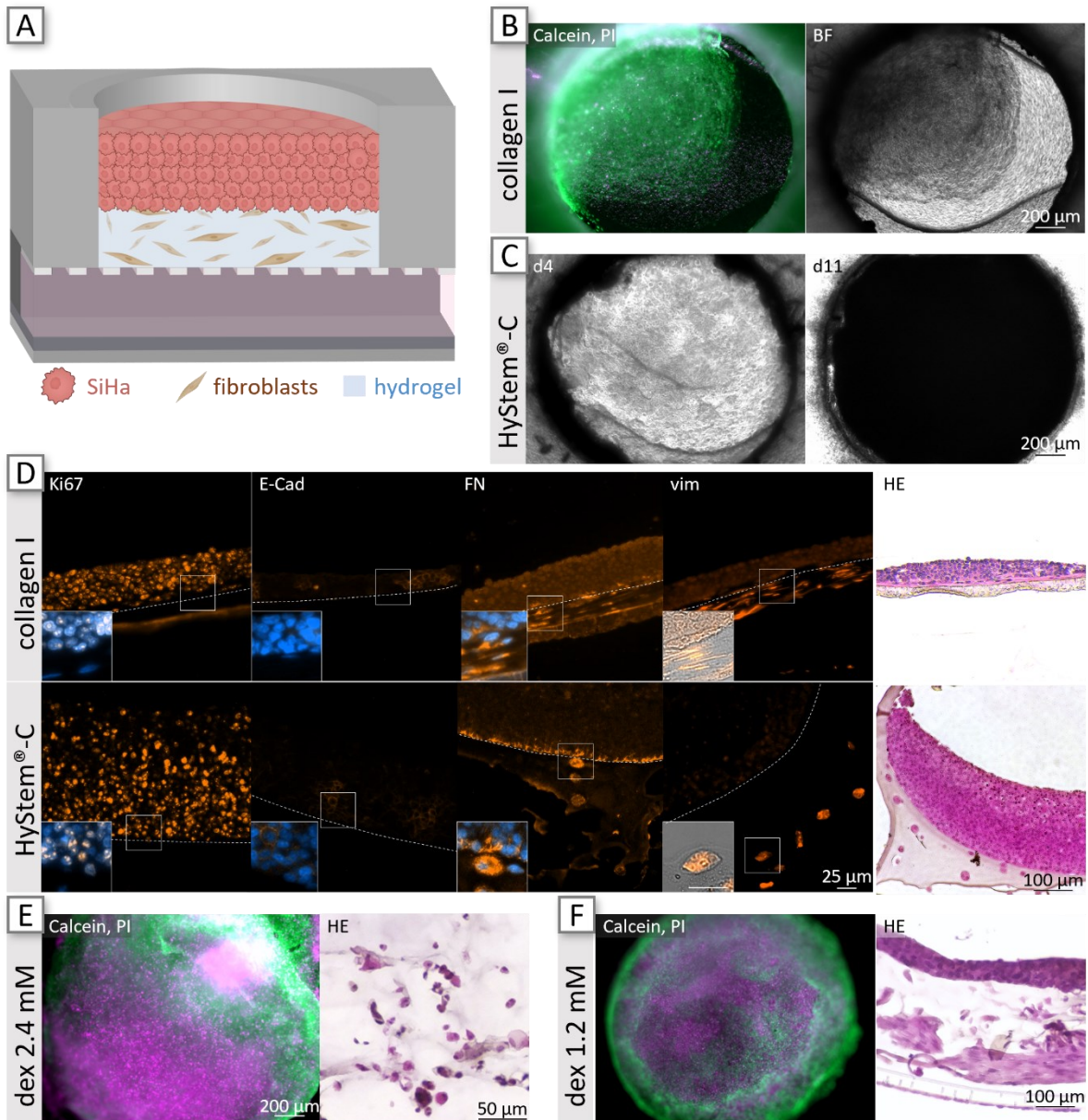


Figure 15: Precancerous Tissues Generated With a SiHa Epithelium Replicated Pathophysiological Features in the CINoC.

A) The schematic of the CINoC illustrates fibroblast embedded in a hydrogel with an undifferentiated SiHa epithelium on top.

B) CIN was generated with collagen I as illustrated in A), and viability assessed by Calcein AM (green)/PI (magenta) staining. The tissue viability was high, and shrinkage was prevalent, as confirmed in the BF image.

C) CIN tissue generated with HyStem[®]-C remained stable without lateral shrinkage, and tissue density increased from day 4 to day 11.

D) Tissue sections of collagen I- and HyStem[®]-C-based CIN tissues show Ki67 (orange) expression throughout the entire epithelium and low expression of E-Cad (orange). Fibroblasts in the hydrogels express FN (orange) and vim (orange), with an elongated morphology in collagen and a spherical appearance in HyStem[®]-C. The HE stainings depict the tissue architecture of the epithelium atop the stromal layer.

E, F) CIN was generated with dextran hydrogels at 2.4 (E) or 1.2 mM (F) cross-linking strength (dex 2.4 mM and dex 1.2 mM). Viability was assessed by Calcein AM (green)/ PI (magenta) staining, revealing moderate viability in both conditions. FFPE tissue sections stained with HE shows spherical morphology of fibroblasts in dex 2.4 mM and a multilayered, undifferentiated epithelium on dex 1.2 mM, with fibroblasts accumulating at the bottom of the hydrogel.

3.5. Endothelial Cell Lining of the Vasculature-Like Channel of the CIN-on-Chip

Blood and lymphatic vessels feature a monolayer of ECs that execute a barrier function between blood and tissue, playing a key role in regulating blood flow, maintaining tissue homeostasis, and actively controlling permeability for the extravasation of fluid and molecules^{111,112}. In the cervix, the mean vessel density increases from normal cervical tissue through low- and high-grade CIN to invasive SCC^{113,114} and there is in vitro evidence of HPV-induced angiogenesis^{115,116}. In the platforms, media is convectively transported through the vasculature-mimicking channel, which was enhanced by incorporating a channel lining composed of human cervical ECs in the CINoC.

To more closely mimic the vasculature in the CINoC, primary cervical ECs were seeded into the channel through cannula reservoirs the day after the collagen-containing stromal layer was generated. The next day, SiHa were added on top and co-cultured statically for 3 days, until the tissue was air-lifted and perfused dynamically for 10 days (**Figure 16.A**). A monolayer of ECs was present in the tissue area at the bottom of the channel as well as at the top on the membrane, as confirmed by on-chip CD31 and VE-Cad staining and HE of tissue sections (**Figure 16.B,C**). However, ECs often detached during cultivation and reproducing these results proved to be challenging, as EC expansion was unsuccessful in subsequent isolations.

During the generation of the stromal layer with dextran, the hydrogel often leaked through the membrane into the channel before solidifying. To address this issue, dermal ECs were seeded into the channel before the fibroblast-dextran solution was added to the tissue well, effectively preventing leakage into the channel (**Figure 16.D**).

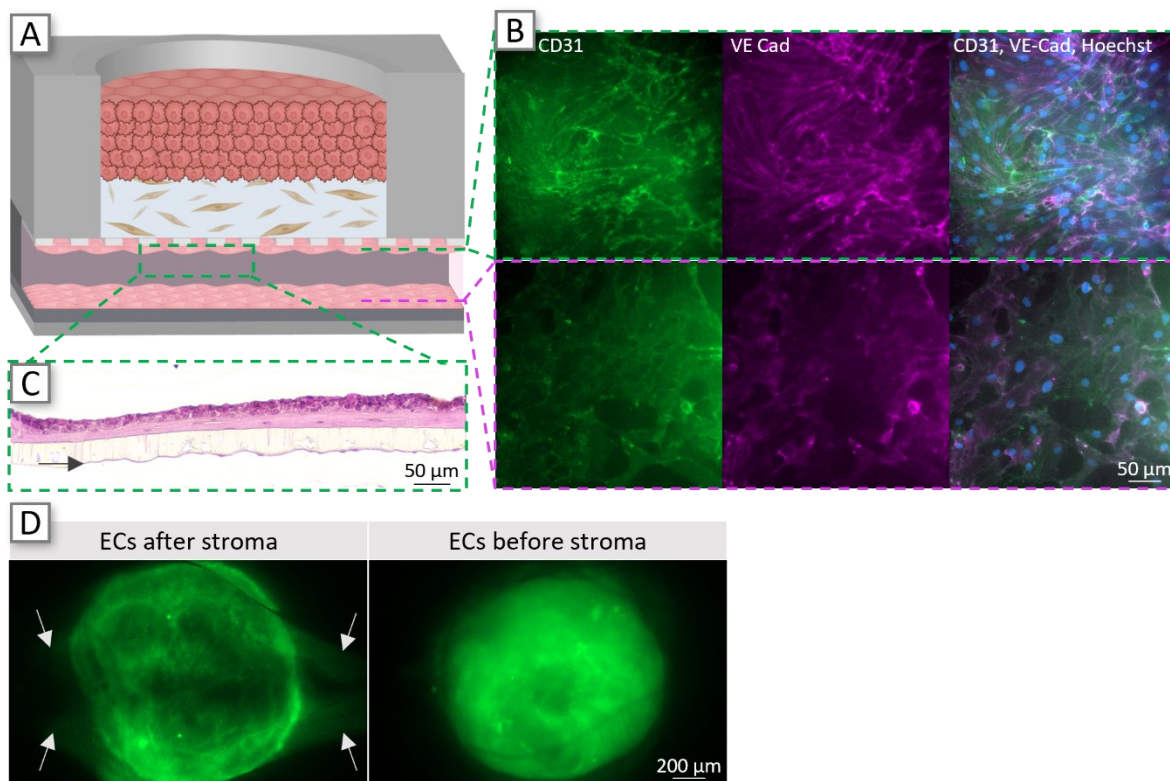


Figure 16: Cervical Endothelial Cells Covered the Vasculature-Like Channel in a Triple-Cultivation with CIN Tissue.

A) Schematic of CINoC with ECs lining the channel. B) Cervical ECs were seeded into the channel and dynamically cultivated with CIN tissue for 10 days. A CD31 and VE-Cad-positive monolayer of ECs covered the membrane at the top and the bottom of the channel. The imaging settings of immunofluorescent images were adjusted to compensate for the greater distance of the membrane from the objective. C) HE staining of the model from B), depicting CIN-like tissue with ECs beneath the membrane. D) Dextran hydrogel spiked with fluorescent microspheres was added into the tissue well and imaged the next day. Seeding ECs into the channel the day before the stroma generation prevented hydrogel leakage into the channel (white arrows).

3.6. Replication of Cancerous Tissue in the Cervical Cancer-on-Chip which Responds to Cisplatin Treatment and Integrates Neutrophils

In cases of persistent HPV infection, aberrant keratinocytes may eventually cross the basal membrane and form cancerous nests within the stroma, marking the progression to invasive CC. Surgery, radiotherapy, and chemotherapy are effective treatment strategies, and immunotherapy is emerging as a promising therapeutic option to combat advanced or recurrent malignancies.

The third generation of the platform was employed for developing an immunocompetent CC-on-Chip (CCoC) (**Figure 17**), as described in detail in **Publication [3]**. To emulate SCC including aspects of the TME, cancerous nests were recapitulated by SiHa aggregates, which were embedded alongside cervical fibroblasts in a dextran hydrogel. SiHa formed loose cell aggregates after 24 h on agarose microwells and consolidated in dextran during on-chip cultivation. The pathophysiological architecture and viability of the 3D tissue after 14 days of on-chip cultivation were verified by cell type-specific markers and live/dead staining. The effect of co-cultivating fibroblasts with tumor spheroids was investigated, revealing that fibroblasts enhanced cell viability and proliferation of the microtumors, as evidenced by live/dead staining, LDH release, and expression of the proliferation marker Ki67.

Cisplatin is the most commonly used chemotherapeutic agent in the management of CC and administered concurrently with radiotherapy¹¹⁷. To demonstrate the applicability of the CCoC model for dynamic testing of cancer therapeutics, the model was exposed to the cytotoxic agent cisplatin (**Publication [3]**). Leveraging the capability for long-term culture and perfusion of the CCoC, cisplatin was administered to the CCoC at patient-relevant doses, schedules, and route of administration, mimicking cisplatin dynamics in patient's blood after intravenous application. Cancer tissue was cultivated for a duration of up to 20 days and cisplatin treatment resulted in increased cell death.

In the TME of CC, PMNs and their functional structures NETs influence both pathogenesis and therapeutic outcomes. The suitability of the CCoC for perfusion and recruitment of functional PMNs into the tumor tissue was investigated (**Publication [3]**). PMNs were isolated from human liquid biopsies and characterized to confirm cell type and assess purity. The functionality of donor-derived PMNs by their ability to undergo PMA-induced NETosis was confirmed in well plates by immunofluorescent staining. Moreover, the compatibility of various media to allow high viability of PMNs and PMA-induced NETosis was assessed by a plate reader compatible SYTOX™ Green assay. Animal-free FTAL5 was identified as a medium compatible with all cervical cells and functional PMNs. To simulate PMN circulation through and extravasation from the blood vessels into the cancerous tissue, PMNs were introduced into reservoirs in the inlet ports (**Figure 7.B,C**) and perfused through the vasculature-like channel. PMNs migrated into the tissue and formed NET-like structures both in the channel and in the tissue.

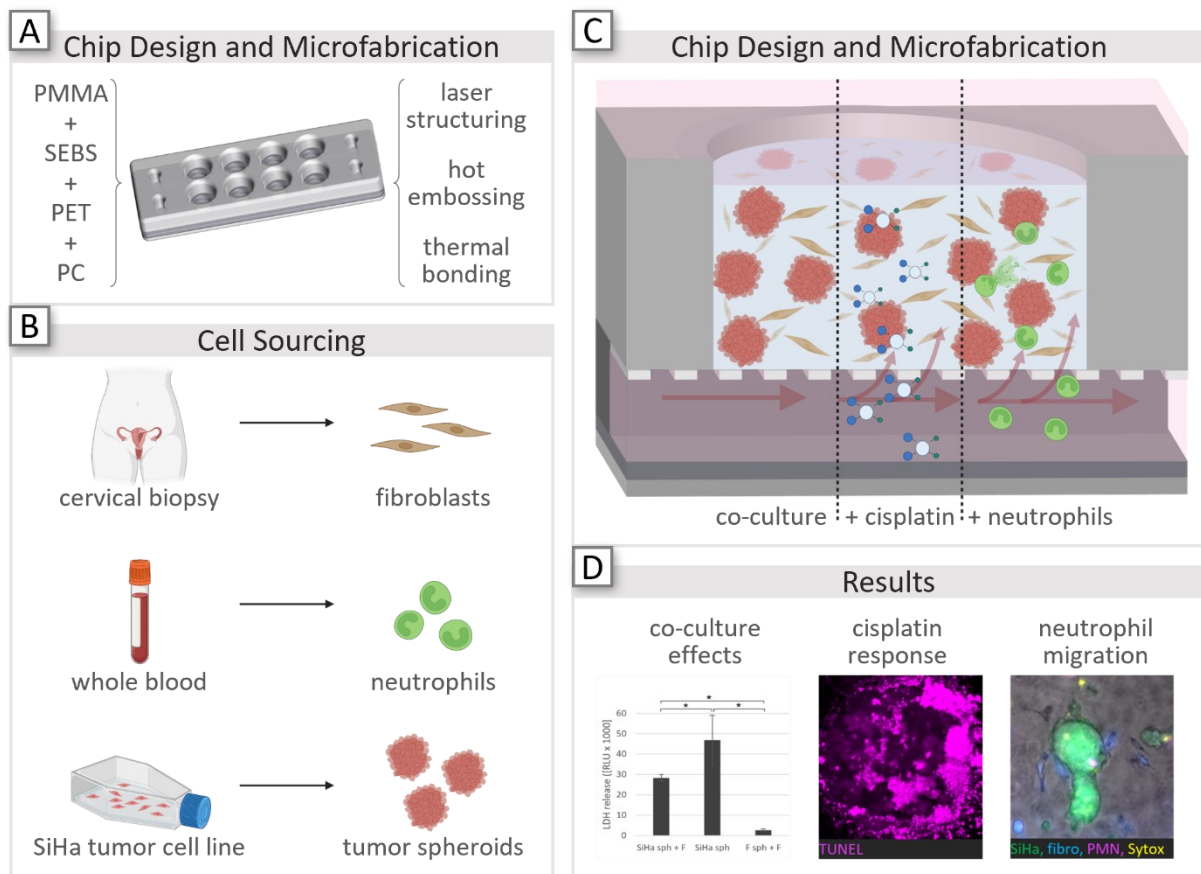


Figure 17: The Cervical Cancer-on-Chip Allowed for the Investigation of Co-Culture Effects, Response to Cisplatin and Neutrophil Migration.

Graphical abstract of **Publication [3]**: A) The third generation platform was employed for generating CC tissue in CCoC. PMMA, SEBS, PET and PC were laser cut, hot embossed and thermally bonded to fabricate the platform. PMMA: poly(methyl methacrylate), SEBS: styrene ethylene butylene styrene, PET: polyethylene terephthalate, PC: polycarbonate. B) Fibroblasts were isolated from human cervical tissues and integrated in the CCoC along with tumor spheroids generated with the SCC cell line SiHa and optionally with donor-derived neutrophils. C) The CCoC was employed to investigate co-culture effects, response to the chemotherapeutic agent cisplatin and to investigate neutrophil recruitment and their NETotic capacity on-chip. D) Tumor viability and proliferation were enhanced in the presence of fibroblasts, and cell death increased upon chemotherapy treatment. Neutrophils migrated from the channel into the CC tissue and produced NETs. Schematics in B) and C) partially created with BioRender.com.

To emulate different disease stages, an epithelialized cancer model was explored. A CIN-like epithelium was generated with SiHa on top of the CC tissue (**Figure 18.A, B**). To reduce the accumulation of SiHa spheroids above the membrane caused by hydrogel leakage during seeding, a two-step seeding process was explored: First, a thin layer of fibroblasts-embedding hydrogel was applied, followed by the addition of hydrogel containing SiHa spheroids in a second seeding. This approach prevented a "sieve effect" of the membrane on the spheroids and ensured a uniform distribution within the tissue (**Figure 18.A**). The stromal layer with cancerous nests was covered by a thick CIN 3-like epithelium (**Figure 18.B**). Moreover, a normal epithelium with ectocervical keratinocytes could be generated on a stromal layer containing SiHa spheroids without fibroblasts (**Figure 18.C**).

The CC cell line SiHa has been shown to be insensitive to CDDP, and the use of CDDP-sensitive cell lines like CC7 may provide more clinically translatable data¹¹⁸. Preliminary experiments indicate that CC7 spheroids are more compact when aggregated on agarose microwells compared to SiHa (**Figure 18.E, Publication [3]**). When co-cultured with fibroblasts in a dextran hydrogel for 14 days, CC7 spheroids showed minimal increase in size and moderate viability, while single fibroblasts remained viable (**Figure 18.D,F**).

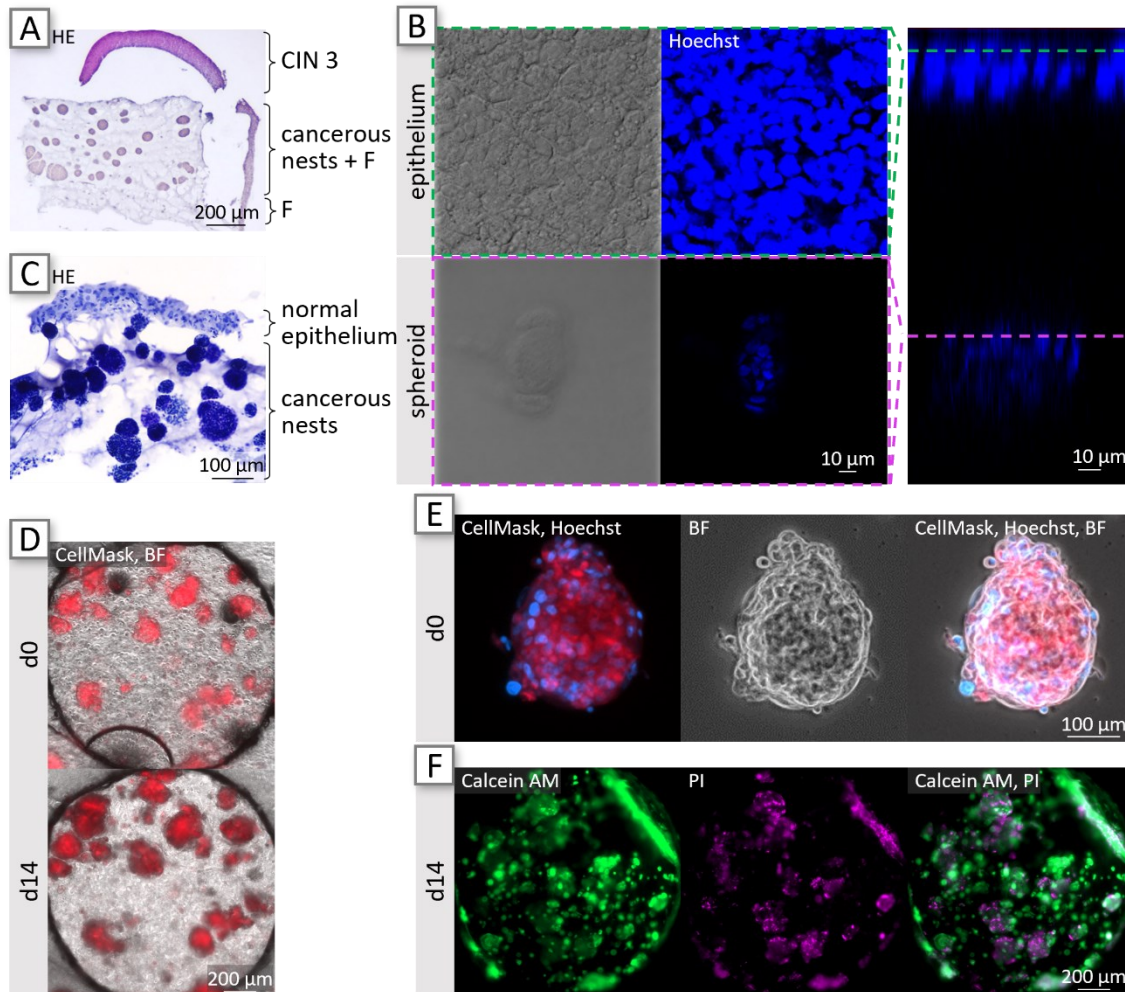


Figure 18: Advancing Cervical Cancer-on-Chip with Epithelia and Cisplatin-Sensitive CC7 Tumor Spheroids.

A) The cancer model was created by including an additional fibroblast-spiked dex 2.4 mM layer below the hydrogel containing fibroblasts (F) and spheroids. SiHa was seeded on top the cancerous stromal layer to generate an epithelium. HE staining of the FFPE section displays a homogenous distribution of spheroid in the upper stromal layer with a well-established CIN 3-like epithelium on top. B) Confocal images of a cancer model that prepared as described in A) show the epithelial surface and a spheroid approx. 125 μm below the epithelium. An orthogonal view of the tissue is included on the right. C) SiHa aggregates were co-cultured in dex 2.4 mM, with normal ectocervical keratinocytes seeded on top. The HE staining of the cryosectioned tissue displays a normal ectocervical epithelium that developed on top of a fibroblast-free stromal layer containing cancerous spheroids. D) The cancer model was generated with CellMask-stained (red) CC7 aggregates, whose size increased slightly within 14 days of on-chip cultivation. E) CellMask-stained CC7 aggregates were imaged 24 h after seeding on agarose microwells, showing a more compact appearance than SiHa spheroids (**Publication [3]**). F) Viability of the tissue from D) was assessed by Calcein AM (green)/PI (magenta) staining, revealing low viability of the spheroids and high viability of the fibroblasts.

CHAPTER 4

Discussion and Outlook

4. Discussion and Outlook

4.1. Robust PDMS-Free Microfluidic Platforms Are Tailored to the Cultivation of Ectocervical Tissues

The platform was meticulously designed for the generation and cultivation of ectocervical tissues utilizing primary cells, providing the opportunity to include immune cells and to apply various characterization and treatment options. This resulted in the following major requirements for the platform:

1. **Facilitate 3D tissue engineering with primary cells**

Donor- and patient-derived cells allow the replication of human (patho)physiology. The small diameter of the tissue well (1.5 mm) is tailored to the use of primary cells, reducing the need for time-consuming cell isolation, minimizing dependence on donor availability, facilitating extensive experimentation, and addressing inter-donor variability by enabling the generation of multiple replicates from the same donor.

2. **Enable tissue characterization**

Optical properties of the design and material must be compatible with microscopic analyses, allowing on-line monitoring and final characterization of the tissue. Tissue retrieval is beneficial for in-depth analyses with various readout methods, including histology.

3. **Compatibility with circulating immune cell integration**

Immune cells play a crucial role in tissue homeostasis. Immune cell integration requires a setup that allows switching from long-term media perfusion for tissue engineering and maintenance to immune cell perfusion. In addition, the semipermeable membrane that serves to contain the tissue in the well and to protect the tissue from shear stress is simultaneously required to incorporate pores of sufficient size to allow the passage of immune cells.

4. **Direct access to the tissue**

The open-top design facilitates cell seeding and allows for the application of innovative treatment options that require direct tissue access.

5. **Compatibility with hydrophobic molecules**

Unlike many platforms using PDMS, the selected materials must have low absorption of hydrophobic molecules to allow the application of hormones and drugs.

In an iterative process, the results of tissue engineering experiments have continually driven improvements in the platform's design, material, and fabrication process. The first version employed PMMA for its remarkable optical properties, low absorption of hydrophobic molecules¹¹⁹, and suitability for laser cutting, which enabled rapid prototyping. While primary cervical cells were successfully cultured on-chip, characterization by microscopy and histology proved challenging and this platform suffered from low throughput and leakage. In the second version, the number of tissue wells was increased to four wells per platform, increasing yield noticeably and allowing for the accommodation of multiple replicates and various conditions to be accommodated on a single platform. The inclusion of TPE reduced leakage and allowed for tissue retrieval, opening the possibility of multiple readout methods from the same platform, including histology. With this platform, multiple strategies for generating stromal layers were explored and normal and diseased models were established. However, the bifurcated design resulted in uneven flow rates in the parallel channels, impacting media delivery as well as endothelial cell and PMN integration. The latest iteration comprised two separate fluidic systems with four tissue wells each, fabricated in a single thermal bonding process, thus doubling the number of tissue wells while halving the fabrication time. Straight channels ensured uniform flow rates for all replicates. The microscopic slide size allowed for

convenient handling by fitting conventional microscopes holders, eliminating the need for adapters. While the size conforms to standard equipment in laboratories, future design adaptations may include modifying well distances for multichannel pipette use. Adapters were introduced for tubing and reservoir connection, but challenges with leakage and stability remain, prompting consideration of more efficient designs in future versions. The platform design extends its applicability to other barrier tissues, with both the second and third generation of the platform being employed in the laboratory to construct skin models.

4.2. Ectocervical Cell Isolation, Cultivation and Characterization

Human cervical tissues were utilized to establish a characterization panel as well as a cell source for tissue engineering. The established antibody panel allowed for a thorough characterization of the tissue architecture in vivo and in vitro in terms of tissue architecture, cell type (CK and E-Cad for epithelial cells; vim and FN for fibroblasts; VWF, CD31, and VE-Cad for ECs), epithelial differentiation (CK13, CK14, CK19, Ki67) and cell/tissue functionality (E-Cad, coll IV, FN, CD31, VE-Cad).

Primary cells were selected as the cell source for the generation of ectocervical tissues. Derived directly from resected tissue samples, primary cells are the optimal representatives of the original tissues, closely mirroring the heterogeneous in vivo physiology and providing excellent model systems. However, primary cell culture is dependent on donor availability, costly and time intensive, requiring more growth time than cell lines and having a limited lifespan before reaching replicative senescence. The characteristics of primary cells can undergo phenotypic shifts with each passage, further limiting their utility to early passages. Therefore, cervical keratinocytes were restricted to passage five for ectocervical engineering to preserve the original phenotype.

The isolation of three cell types from the small, resected cervical tissues required a thorough optimization of the isolation procedure to obtain a sufficient yield of all cell types. Successful isolation of keratinocytes from the epithelium, fibroblasts from the subepithelial stromal layer and ECs from the remaining connective tissue was achieved. These cells were expanded in 2D prior to on-chip cultivation, and cell types were confirmed by immunofluorescent staining of markers previously verified on tissue sections. The shift in the predominant expression of the basal and parabasal cell markers CK14 and CK19 in the keratinocyte expansion culture compared to the tissue sections indicates a preferential attachment and/or propagation of the proliferative cells, while differentiated cells expressing CK13 were nearly absent in the secondary cultures. The yield of keratinocyte could be further increased using in-house produced media as described by Chumduri et al.⁷⁸, and has been recently established in the laboratory. Fibroblast isolation was a robust process with high cell yields and successful expansion. For ECs, subcultivation posed a major challenge, as the cells did not adhere in secondary culture. A study involving EC isolation from CC patients showed a low success rate of 7% in patients ≥ 40 years of age, and the addition of vascular endothelial growth factor (VEGF) was found to be crucial for successful isolation¹²⁰. Considering that the cervical tissues for this project were obtained from elderly women, propagation of ECs may remain a challenge. Nevertheless, given the absence of VEGF and the sensitivity of ECs to P/S^{121,122}, exploring gentamycin, the addition of VEGF, and media specific for microvasculature ECs may improve cell yield and the subcultivation success.

The establishment of isolation and expansion protocols for primary cervical cells has provided a species- and tissue-specific cell source. The importance of using species-specific cervical cells was demonstrated in a study comparing HPV-immortalized cervical epithelia co-cultured on human or mouse fibroblasts in transwell models, where epithelial invasiveness was increased in the presence of human fibroblasts⁷². Donor- or patient-derived cells not only add species-specificity, but advance personalized medicine.

4.3. Donor-Derived 3D Tissues Emulate the Ectocervix in the Cervix-on-Chip

Ectocervical tissue comprises a differentiated epithelium above a fibroblast-dominated, collagen-rich stromal layer. Stromal fibroblasts have been shown to promote homeostasis in human skin models¹²³, impact differentiation in skin of mice¹²⁴ and invasion of cervical keratinocytes in an in vitro cervix model⁷² through direct contact-dependent and/or indirect paracrine signaling⁵³. The essential role of fibroblasts motivates their integration in cervical models. Three biocompatible hydrogels were explored for the generation of a 3D fibroblast-containing stromal layer, as hydrogels offer biocompatibility and optical properties beneficial for microscopy. The contractile forces exerted by cells on the ECM can cause loss of structural integrity and the contraction of collagen hydrogels¹⁰⁶, as observed in the presence of primary cervical fibroblasts. However, the collagen hydrogel supported both fibroblasts and ectocervical keratinocytes, with high fibroblast viability and evidence of epithelial differentiation as indicated by (para)basal expression of CK14 and suprabasal expression of CK13. Expression of CK19 was restricted to the basal layer in vivo and is distributed in all layers in the vitro model, consistent with findings in CCs^{125,126}. In the literature, CK19 has often not been included for the characterization of the in vitro co-culture models. In an organoid model of the ectocervix, CK19 was completely absent⁷⁸, suggesting the need for further investigation, and potentially optimized tissue culture conditions may aid to mirror in vivo-like CK19 expression.

The multilayered epithelia of the CXoC comprised fewer layers than most human in vivo tissues. Epithelial thickness and differentiation are affected by the hormonal status of women. Throughout the menstrual cycle, estrogen causes a predominance of superficial cell layers during the initial proliferative phase, whereas progesterone causes a predominance of the intermediate cell layers during the subsequent secretory phase². In young girls and elderly women with low estrogen levels, the epithelium is only a few cell layers thick (atrophic epithelium), undifferentiated, with no mitotic activity and uniform appearance of basal and parabasal cells, reduced cytoplasm and absent intracytoplasmic glycogen^{2,15}. Since cervical tissues were predominantly obtained from elderly women, achieving the thickness observed in middle-aged women may be unattainable. To increase cell layers in the ectocervical epithelium, (dynamic) estrogen supplementation can be explored in the platform, as its material was specifically selected to be compatible with the integration of (hydrophobic) hormones. However, it's important to note that the estrogen receptors expression is reduced in atrophic epithelia of postmenopausal women^{2,127}, which may limit the thickening effects on the epithelium. The large epithelial thickness achieved in the CIN model suggests that the primary cervical keratinocytes are responsible for the thin epithelium rather than an overall problematic tissue generation protocol or platform malfunction. Nevertheless, adjustments to the cultivation conditions, including exploration of increased flow rates for sufficient media delivery, should be considered in future experiments.

To achieve structural stability, the semi-synthetic hydrogel HyStem[®]-C with gelatin was investigated and resulted in robust stromal layers without substantial lateral shrinkage. Both cell types, fibroblasts and keratinocytes, exhibited high viability, contributing to the promising result. However, the epithelium on HyStem[®]-C was thinner compared to the collagen hydrogels, and epithelial coverage of the stromal layer was lower. After seeding, the entire tissue well was covered with keratinocytes, but aggregation occurred, resulting in hydrogel areas devoid of an epithelium. One explanation is the absence of matrix-binding proteins in the hydrogel, which may hinder the attachment of cell-produced ECM. The absence of basement proteins, such as laminin, could cause epithelial cells to detach and adhere to each other. Furthermore, basal cell polarization may be impaired due to the lack of essential cell-matrix interactions^{128,129}. The hydrogel may be improved by incorporating peptides that sequester and enhance interactions of the cell-produced ECM. In future studies, the fully defined hydrogel

described by Gnecco et al.¹³⁰ that incorporates matrix binding proteins and was originally designed to generate endometrial tissue, could be explored for the generation of ectocervical tissue. Since tissue architecture and differentiation is influenced by basement membrane proteins¹⁶, more *in vivo*-like expression of CK19 and improved maturation may be achieved.

Viable cells and no substantial lateral shrinkage were observed in dextran-generated cervical tissues. The epithelium covered the entire stroma, and aggregation or loss of the epithelial layer was observed to a much lesser extent than with HyStem[®]-C. The epithelia generated were sometimes multilayered and expressed the differentiation markers side by side without an obvious differentiation towards the superficial side, although closer examination with higher resolution in the Z plane is required for confirmation. Similar to HyStem[®]-C, the dextran hydrogel may benefit from the integration of ECM sequestering peptides. While dextran was the most promising hydrogel, fibroblast morphology and epithelial architecture motivated the search for alternative strategies to create the stromal layer.

MatriDerm[®] is a collagen- and elastin-rich matrix and was explored as an alternative approach to hydrogels for creating the cervical stroma. The fibroblast-derived ECM did not fill the pores of the scaffold and higher concentrations of ascorbic acid could be assessed in future experiments to increase ECM production and thereby prevent keratinocyte permeation. When combined with a collagen hydrogel, properties of both materials were combined, i.e., the mechanical stability and optical density of the scaffold, which impedes microscopy, with the hydrogel's rapid application, meniscus formation and keratinocytes support. With this approach, a robust stromal layer with 3D-dispersed cervical fibroblast and a distinct, stratified and differentiated ectocervical epithelium was achieved. The customizable PLA membrane showed promising preliminary results with proliferative, FN-producing fibroblasts distributed in the scaffold, and was further developed in the laboratory for infection studies.

To my knowledge, this is the first 3D cervical tissue within a microfluidic platform, particularly standing out for the use of species- and tissue-specific cells in a PDMS-free platform. The CXoC has the potential to deepen our understanding of the female reproductive organ, including mechanisms of infection, and the development of (therapeutic) vaccines and medications in a patient-specific setting.

4.4. Aberrant Epithelia Emulate Precancerous Tissue in the CIN-on-Chip

CIN is a precancerous condition of the ectocervix caused primarily by HPV infection. It is graded on a scale from CIN 1 (mild dysplasia) to CIN 3 (severe dysplasia), with higher grades implying a greater risk of progression to CC. High-grade lesions are characterized by the absence of maturation, exhibiting a basaloid phenotype, an elevated nucleus-to-cytoplasm ratio and enlarged nuclei¹⁸. Early detection and appropriate medical interventions, such as colposcopic examination or excisional procedures, can effectively manage and prevent the progression of CIN to CC, but may result in overtreatment of patients who may have spontaneously regressed otherwise. The availability of a CIN model could facilitate the advancement of medical interventions, aimed at reducing potential detrimental reproductive effects, which are particularly important for women who wish to have children.

To replicate a CIN tissue in the platform, primary keratinocytes were replaced with SiHa, an established cell line derived from a grade II SCC with integration of 1-3 incomplete copies of the HPV16 genome^{110,131-133}. In contrast to the normal ectocervical epithelium, SiHa created an epithelium of up to 200 μm in thickness with multiple, undifferentiated cell layers. The epithelium exhibited a CIN 3 phenotype, characterized by extensive Ki67 expression throughout the epithelium, indicating proliferating, non-differentiating cells. The minimal expression of E-Cad is consistent with *in vivo* observations, where its presence is reduced. This reduction may be attributed to the HPV infection, as the HPV 16 E6 expression has been shown to inhibit E-Cad expression in basal keratinocytes^{16,95}. Fibroblast can enhance the invasion of neoplastic epithelial cells, highlighting the importance of inter-

cellular crosstalk in disease progression⁹⁷ and therefore their importance in CIN tissue models. Characteristics of the stromal layer in the CINoC were similar to those in the normal ectocervical model, i.e. shrinkage of collagen I hydrogel, higher tissue viability on collagen I hydrogel compared to dextran, elongated morphology of fibroblasts in collagen, but spherical morphology in HyStem[®]-C and dextran. The expression of FN and vim increases with disease progression⁹⁵ and may be used in the future for characterization, when comparing models with healthy tissue. Looking ahead, scaffold assisted generation of a stromal layer may further improve this model.

Similar to the CXoC, the CINoC represents the first in vitro model including a microfluidic platform incorporating a 3D CIN tissue. With direct access to the epithelium, novel treatment options such as non-invasive physical plasma^{29,30} may be explored in the future. With the integration of patient-derived keratinocytes and PMNs, this model can be employed to investigate patient-specific effects of plasma-induced NETosis in CIN tissues¹³⁴.

4.5. Endothelial Cell Lining of Vasculature-Like Channels Advance Disease Models

Blood vessels provide a barrier function between blood and tissue, playing a key role in maintaining tissue homeostasis and controlling permeability to molecules and fluids^{111,112}. In the cervix, the mean vessel density increases from normal cervical tissue through low- and high-grade CIN to invasive SCC^{113,114}. Keratinocytes transduced with HPV 16 E6/E7 alter EC behavior^{115,116}, highlighting the importance of co-culture models that integrate vasculature-mimicking endothelial lining into HPV-associated cervical tissues. ECs exhibit species-specificity, e.g. in immune cell recruitment, organotypic and vessel type-specific heterogeneity, including cellular morphology, gene expression, ECM production, cell surface properties¹³⁵⁻¹³⁷, and considerable sex-specific heterogeneity^{136,138}. By isolating ECs from human cervical tissue, species-, organotypic- and sex-specific properties are captured in the tissue model.

ECs were seeded into the microvasculature-like channel of the CINoC, where they were triple-cultured with CIN tissue consisting of collagen-embedded fibroblasts with a SiHa epithelial layer. The EC monolayer beneath the CIN withstood long-term cultivation for a period of 10 days and perfusion in direct contact with the media. The potential of the EC lining as a means to prevent hydrogel leakage during seeding was evaluated, based on the assumption that ECs seal the pores of the membrane and confine the hydrogel in the tissue well. Leakage was successfully prevented with dermal ECs and should be confirmed with cervical ECs in the future. Further investigation is required to characterize the tightness of the EC layer, for instance as shown by Cipriano et al. and Rogal et al.^{99,139}, in particular when using FTAL5 instead of ECGM.

While a low density of lymphatic vessels has been reported in the normal cervix, the lymphangiogenic response increases during disease progression from premalignant to malignant lesions, suggesting that preneoplastic lesions are a critical point in the development of the lymphatic network vasculature and a potential target for early intervention^{120,140}, similar to blood vessels. By inducing hyperpermeability in blood vessels, VEGF contributes to tumor (lymph)angiogenesis and facilitates tumor cells extravasation, thereby promoting metastases¹⁴¹. Interestingly, the expression of VEGF is increased in HPV 16 E6/E7 transduced keratinocytes^{115,116}. To further develop drug intervention for premalignant and malignant diseases targeting the lymphatic tissue, the current models could be adapted in future studies by sorting for lymphatic ECs.

In the future, the CCoC may be further advanced to include an endothelial barrier, as this would allow a more thorough investigation of the intercellular interactions and benefit drug development. Evidence suggests that ECs stimulate the growth of CC cells¹⁴² and vice versa, cancer cells have demonstrated both pro- and anti-angiogenic effects on HUVECs¹⁴³. An early study involving co-culture of SCC cells

CaSki cells and HUVECs in a fluidic platform suggested increased resistance to the chemotherapeutic agent paclitaxel compared to single-cultured cells⁸⁶. In addition, ECs play a major role in directing inflammatory cells to the tissue by regulating leukocyte activation, adhesion and transmigration¹¹¹. Therefore, an endothelialized CCoC may facilitate the investigation of EC-mediated effects on chemotherapeutic efficacy and toxicity, as well as the impact on PMN recruitment and potentially NETosis.

4.6. Response to Chemotherapy and Immune Cell Integration Highlight Crucial Features of the Cancer-on-Chip

In SCC, the predominant form of CC, epithelial cells infiltrate the stroma and form cancerous nests. To recreate the *in vivo* cell-cell interactions, tissue architecture, and internal gradients of e.g. nutrients, oxygen and drugs, 3D tumor spheroids were generated with the SCC cell line SiHa and embedded with fibroblasts in a dextran hydrogel (**Publication [3]**). Histologically, the spheroids resembled cancerous nests of a non-keratinizing poorly differentiated SCC. Fibroblasts, as well as single SiHa cells and SiHa spheroids exhibit a spherical morphology. In a study by Zhuang et al., stiffness was reported to be a determinant of SiHa morphology¹⁴⁴ with a more elongated shape at higher stiffnesses. The Young's moduli of the dextran hydrogels are estimated to be 0.4 and 3.3 kPa for 1.2 and 2.5 mM cross-linked dextran, respectively, which is much lower than the normal cervical tissue, which was determined to be 44 and 81 kPa for CC¹⁴⁵. Despite the 10-fold difference between the two cross-linking strengths, the stiffness of a normal and cancerous cervical tissue is another 10-100 times higher, potentially affecting cell morphology and epithelial development.

Long-term cultivation allowed for prolonged observation of tumor progression and the interactions between cancer cells, stromal components, and the surrounding TME. After a two-week cultivation period, overall tissue viability was high, and the presence of fibroblasts contributed to improved viability and faster growth of tumor spheroids. The CCoC's versatility is emphasized by its ability to generate both normal and CIN-like epithelia on CC tissue, allowing for in-depth study of different disease stages and intercellular interactions. While the establishment of normal multilayered epithelia in the absence of fibroblast is challenging, preliminary results suggest that the presence of SiHa spheroids effectively compensated for their absence. These findings suggest paracrine cell-cell communication between normal and cancerous epithelial cells with fibroblasts, consistent with previous studies^{36,69,146}. Future studies could investigate fibroblast plasticity by assessing the expression of cancer associated fibroblast (CAF)-markers, including alpha smooth muscle actin, fibroblast activation protein, and transforming growth factor-beta levels in the effluent.

In vitro compound testing often involves concentrations well beyond clinical treatment regimens, due to the constraints of short culture durations and the limitations of static well plate culture. The long-term cultivation and perfusion capabilities of the CCoC allowed repeated dosing with clinically relevant drug delivery routes, schedules, and concentrations. Treatment resulted in significant tumor killing effects despite the use of lower concentrations compared to previous studies. In future investigations, it would be intriguing to treat cisplatin-sensitive cell lines, such as CC7, with the same conditions and compare the outcome with SiHa. Preliminary data indicate promising results with spheroid generation, although culture conditions need to be optimized for improved viability, such as cultivating the CC7-tissue in their expansion media instead of FTAL5. Although obtaining patient-derived organoids from SCC has proven challenging, their integration could potentially provide patient-specific estimates of minimum effective concentrations and support drug selection. However, achieving this goal requires more extensive testing and benchmarking with a variety of established compounds, including small molecules and immunomodulatory drugs.

Immune cells can influence disease progression and therapeutic outcomes and PMNs, the most abundant circulating leukocyte, exhibit both tumor-antagonistic and pro-tumorigenic functions in CC. A suitable medium was identified that maintained the viability and functionality of all cervical cell types and PMNs. When PMNs were perfused through the microvasculature-like channels of the CCoC, adherence to the membrane and migration into the tissue was observed. When NETosis was induced with PMA, critical events of NET formation were reproduced on-chip. Poly-D-Lysine coatings reduced spontaneous NETosis in static well plates and could be explored in the channels in future studies. With multiple cervical models available and the multi-tissue well design, new opportunities arise by combining normal and diseased models in a single platform. For instance, normal cervical tissue can be generated downstream of cancerous tissue to study metastasis, especially in combination with PMNs which are known to promote metastasis by trapping circulating tumor cells. Taken together, the immunocompetent CCoC presents an opportunity for in-depth mechanistic investigations into the role of NETosis in cancer and its TME and to potentially test (immune-)therapeutic options and combinations.

4.7. Structural and Functional Characterization of Cervical Tissues

Various methods were employed to characterize cervical tissues, with some being non-invasive, allowing for real-time monitoring during chip cultivation, while others were invasive, allowing for a comprehensive final examination of the tissue.

For on-line monitoring, the developed platforms were designed to be compatible with non-invasive live cell imaging, a powerful tool in conjunction with fluorescent labeling techniques such as cell-trackers, conjugated antibodies, and viability dyes. The perfusion of the microfluidic platform also enables the continuous collection of effluent, i.e. the media that has passed the tissues, providing an additional time-resolved, non-invasive method for dynamic assessment of tissue function and cellular interactions. Effluent analysis can be performed using widely available, cost-effective standard readout methods traditionally used in 2D cell culture, expanding the range of readout options available. For instance, non-invasive monitoring of the released lactate dehydrogenase (LDH) in medium effluents has allowed for long-term analysis of cytotoxicity in response to cisplatin (**Publication [3]**) or adipose tissue viability (**Publication [1]**). In addition to viability, effluent analyses allowed for in-depth investigation of tissue functionality, e.g. in adipose tissue, lipolysis was investigated by examining the adipose-associated metabolites glycerol and oleic acid, a representative of non-esterified fatty acids (**Publication [1]**). In the CCoC, effluent analyses could be extended to a comprehensive investigation of chemokines, cytokines or clinically relevant biomarkers (e.g. NETosis marker).

For final analyses, the platform was adapted to enable tissue to be removed from the chip using a biopsy punch for final analyses. This method proved beneficial for independent analysis of replicates, allowing the application of multiple characterization methods such as metabolic and proteomic analyses on a single system. Among these, histology is the most common method to evaluate cervical tissues. Despite major efforts to improve the embedding, sectioning, and staining processes, including the exploration of FFPE, cryosectioning and the uncommon embedding materials Technovit 8100, challenges persisted, particularly with semi- and fully synthetic hydrogels, leading to tissue section damage and loss. Consequently, the focus shifted to microscopy to assess structural and functional hallmarks of the tissues. Confocal microscopy, particularly when combined with immunofluorescence staining, provided a direct assessment of structural and functional aspects of the 3D model, and allowed imaging up to approx. 200 μm into the tissue. Looking ahead, tissue clearing techniques hold promise for obtaining a comprehensive view of the tissue, and flow cytometry could provide quantifiable data, albeit at the expense of losing structural information.

4.8. Use of Animal Components was Reduced in Cell and Tissue Cultivation

OoC aims at reducing animal experimentation, but the use of many animal-derived products required for in vitro model development remains a challenge. For instance, the use of the standard culture supplement fetal calf serum (FCS) was estimated at 600,000 L in 2007, corresponding to 2,000,000 bovine fetuses, and is believed to have increased since then^{147,148}. FCS remains a concern due to ethical considerations regarding its production, which leads to fetal distress and death during blood collection, as well as scientific disadvantages such as unknown exact composition, high rates of product variability, low quality, unintended interactions with test substances, viral or prion contamination etc.^{148,149}. FCS was successfully replaced with a defined soybean trypsin inhibitor to stop trypsin digestion. Despite unsuccessful attempts to replace animal-derived trypsin for keratinocyte isolation with equivalent yield, successful alternatives including TrypLE™ for fibroblast subcultivation were introduced as well as an enzyme-free dissociation solution that has been established in the laboratory for EC isolation. Cultivation of ECs in ECGM required only 2% FCS, and keratinocytes grew in serum-free K-SFM containing low amounts of animal-derived bovine pituitary extract. However, cervical fibroblasts were cultivated in media supplemented with 10% FCS, and alternative low-serum media with 2% FCS are available. Preferably, FCS could be completely replaced in the future by substitutes, human serum, human platelet lysate^{148,150} or by the use of chemically defined serum-free media. Co-cultivation of multiple cell types at high densities provides the opportunity to reduce media components and supplements, such as FCS, through intra- and intercellular signaling. In the co-cultures of fibroblasts with epithelial cells, and triple-cultures with ECs or PMNs, the chemically defined and animal-free media FTAL5 was employed at the expense of a proprietary composition. Collectively, these steps and modifications decreased the use of animal products in cell isolation and cultivation.

Next to cell cultivation, animal-derived products were used in the tissue engineering process. A reduction in animal components was sought by exploring semi- and fully synthetic hydrogels as alternatives to bovine or rat collagen, and PLA as an alternative to the bovine collagen-elastin matrix. To pursue the most promising strategy for generating normal cervical tissue, PLA in combination with a synthetic hydrogel could be explored in future studies.

Finally, there is a significant reliance on animal-derived antibodies for the specific staining of protein markers. In an attempt to find animal-free alternatives, antibodies selected by phage display were evaluated with mixed results. While a secondary anti-mouse antibody showed promising performance, Ki67-specific staining exhibited insufficient signal. The anti-mouse antibody was reported to target the IgG1 isotype exclusively, with no recognition of IgG2a or IgG2b, thus expanding the potential for multiplexing with primary antibodies of the same species and warrants further testing. While more work is needed to further minimize and replace animal use in life sciences, the use of animal-derived products was reduced in multiple processes of this project.

CHAPTER 5

Conclusion

5. Conclusion

In this study, microfluidic platforms were developed for the engineering and long-term cultivation of ectocervical tissues. Specifically, the following results were obtained:

1. PDMS-free microfluidic platforms were designed and fabricated

Through an iterative process of continuous design and material optimization, three generations of platforms were developed. While the overall concept remained the same, major advances were made in increasing the yield and incorporating flexible materials for tissue retrieval. The latest iteration resulted in a platform with two fluidically independent systems with eight open-top tissue wells. This platform is compatible with multiple treatment options and readout methods, including real-time monitoring via microscopy and effluent analysis, as well as off-chip tissue sectioning.

2. Primary cells were obtained from human donor tissues

Protocols were established for the isolation, cultivation and characterization of cervical keratinocytes, fibroblasts, and ECs from human cervical tissue. Moreover, peripheral PMNs were isolated from liquid biopsies, characterized, and functionally evaluated in various media. FTAL5 was found to be a medium that allows for co-cultivation of all primary ectocervical cells, the CC cell line SiHa, and PMNs, without compromising the capacity of the latter to produce NETs.

3. Multicellular 3D in vitro models of the ectocervix were tissue engineered

a) **CXoC**: Normal ectocervical tissues were generated with primary ectocervical cells, including a fibroblasts-containing stromal layer, covered by a multilayered epithelium of differentiating keratinocytes. The generation of a robust stroma that supported primary keratinocytes was particularly challenging, and several methods were explored until the combination of a mechanically robust scaffold with a hydrogel emerged as the most successful strategy. This model can enhance our understanding of basic research questions on ectocervical tissues, including studies of the (host's own) microbiome or infection, and can also serve as a reference tissue in drug development.

b) **CINoC**: Precancerous CIN 3 tissue was created with an undifferentiated SiHa epithelium on top of fibroblast-embedding hydrogels. While this model profited from the lessons learned in the CXoC, the integration of less demanding epithelial cells provided valuable feedback on the chip concept, design and tissue engineering process. In a triple-culture model, the vasculature-like channel was lined with ectocervical ECs, further advancing the complex donor- and tissue-specific in vitro model. With the CINoC, novel treatment strategies can be explored to eventually provide an appropriate, potentially non-invasive therapy option for CIN.

c) **CCoC**: CC tissue was generated with SiHa aggregates emulating cancerous nests in fibroblasts-containing hydrogels, with an optional normal or aberrant epithelium on top. Intercellular crosstalk resulted in enhanced viability and proliferation of the tumor spheroids. In a proof-of-concept study, CC tissue responded to cisplatin treatment at patient-relevant doses, emphasizing its potential to contribute to more translatable data. The integration of functional PMNs allowed for investigating on-chip NETosis and renders this model suitable for further immuno-oncology research.

4. Animal-derived components were reduced

The reduction and replacement of animal-derived products was successfully established in cell isolation, cultivation, and tissue engineering processes.

CHAPTER 6

Experimental Procedures

6. Experimental Procedures

The methods encompassing the design and fabrication of the third generation of the platform, including adapter integration, as well as the processes of cell isolation and cultivation for primary human cervical fibroblasts and PMNs, along with the cultivation of the SiHa, spheroid generation and seeding into dextran hydrogel, perfusion of PMNs through the platform, cisplatin treatment, flow cytometry analysis, viability staining with TUNEL, SYTOX™ Green Assay, live cell labelling with cell trackers, on-chip immunofluorescent cell staining, image acquisition and analysis, and statistical analysis, were detailed in **Publication [3]**.

6.1. Fabrication of the Microfluidic Platforms

The first generation of platforms consisted of three PMMA layers: the 175 μm thick bottom and media layer (PLEXIGLAS Resist, 99524 GT, Evonik) and the 2 mm tissue layer (0133420, Moduor), all laser-cut (VLS2.30, Universal Laser Systems) from larger sheets. The laser-assisted microstructuring of the media layer resulted in a 0.5 and 0.8 mm wide channel extending from the circular chamber towards the inlet and outlet, respectively. Inlet and outlet ports were designed with a diameter of 1.36 mm to accurately fit Tygon tubing (VERNAAD04103, VWR international GmbH) for adapter integration, as described in **Publication [3]**.

To create the PDMS support structure, a master was prepared with a media layer placed on an EtOH-wetted PMMA slide (thickness 3 mm, size 8 cm x 5 cm), and bonded for 1 h at 60° C. Subsequently, PDMS (Sylgard 184 Dow Corning) was mixed in a 10:1 ratio (base to curing agent), degassed, and poured onto the master. Two frames (height 2 mm, size 8 mm x 5 mm), fixed by foldback clips, were used to constrain the PDMS on the master. The PDMS support was cured for 3-4 h at 60° C, cut to the size of the chip, and then placed on a small glass slide.

The first generation of platforms was fabricated using a two-step thermal fusion bonding process, following a procedure akin to that detailed by Chuchuy et al.¹¹⁹. The PDMS support was cleaned with scotch tape to remove dust. The media layer and the PC membrane (thickness 22 μm , pore size 3 μm , 1000M25/610M303, it4ip S.A., Belgium) were cleaned with isopropanol and positioned atop the mold, aligning the PDMS support with the channel of the media layer and the membrane with the tissue area of the media layer. A small glass slide was then positioned on top, and the stack was secured with foldback clips and thermally fusion bonded for 8 min at 130 °C (**Figure 5.D**). Following this, the stack was allowed to cool for 5 minutes at room temperature (RT) before disassembly. In the second step, the PDMS support was removed, and the remaining layers were combined with the media-membrane layer from the initial bonding step. These layers were sandwiched between small glass slides, secured with foldback clips, and bonded for 10 minutes at 130 °C. Once again, the stack was left to cool for 5 minutes at RT before disassembly. Before use, platforms were sterilized in 70% ethanol.

The fabrication process for the second and third generation of platforms is detailed in **Publication [3]**. The second generation was manufactured with modifications, including a two-step bonding process: In the initial bonding step, a stack of the membrane, positioned between the tissue layer and the media/bottom layer, was inserted between glass slides. Pressure was applied using foldback clips, and the bonding process took place overnight at 60 °C. Subsequently, in the second bonding step, the 2 mm PMMA reservoir layer was added without pressure at 60 °C for either 7 hours or overnight. Before use, platforms were sterilized in 70% ethanol.

6.2. Tissue Engineering and on-Chip Cultivation

6.2.2. Primary Cell Isolation and Cell Cultures

The procedure for isolating cervical keratinocytes was adapted from previously published methods^{65,72,97}. Human cervical tissue was processed, and fibroblasts were isolated from the tissue as outlined in **Publication [3]**. After separating the epithelial layer from the stromal layer, tissue strips were subjected to a second enzymatic process wherein keratinocytes were singularized for 5-10 min in 0.05% trypsin/versene at 37 °C. The digestion was stopped using Defined Trypsin Inhibitor (R007100, Gibco). To reduce cell loss, it is crucial to prewet the pipette tip when resuspending or pipetting the keratinocyte solution, as these cells tend to adhere to surfaces. The cell suspension was filtered using a 70 µm cell strainer (542170, Greiner Bio-one), washed with PBS, centrifuged at 200 × g for 5 minutes, and then plated in supplemented Keratinocyte-SFM (17005042, Gibco™) in uncoated flasks. For subcultivation, Accumax (12932715, Merck) was utilized as a gentler alternative to the commonly used Trypsin. ECs were isolated from excess connective tissue as described by Rogal et al.⁹⁹, with minor adjustments: trypsin was replaced by the animal-free Enzyme Free Cell Dissociation Solution (S-014-B, Sigma Aldrich), ECs were scraped in ECGM instead of PBS and cultivated in ECGM supplemented with P/S. CC7 and mouse NIH3T3 J2 fibroblasts were cultured as described by Michnov et al.¹¹⁸.

6.2.3. Generation of the Stromal Layer

Hydrogel-based stromal layers

When specified, the platform was coated with PDA before hydrogel seeding, following the procedure outlined by Park et al.¹⁰⁶. The channels and wells were washed with both demineralized water and 10 mM Tris/HCl pH 8.5 buffer before being coating with 2 mg/mL PDA in Tris/HCl buffer for 2 hours at RT. The platform was washed twice with demineralized water and subsequently allowed to dry.

For stroma generation, the desired quantity of fibroblasts was centrifuged and then resuspended in FibrCol® (5133, Advanced BioMatrix), RatCol® (5153, Advanced BioMatrix) or HyStem®-C (GS1005, Advanced BioMatrix) according to the manufacturer's instructions. Dextran hydrogels were prepared as described in **Publication [3]**. If applicable, 4arm PEG Succinimidyl Glutarate (4ARM-SG, JenKem Technology) was dissolved in Neutralization Solution of RatCol® to a concentration of 4 mg/mL in the final hydrogel. The solidification of the hydrogel occurred in the incubator at 37 °C for a duration of 5-20 minutes before the addition of fibroblast cultivation medium. Specifics regarding cell densities and seeding volumes are listed in Table 1.

Based on the provided information from the manufacturer, the shear modulus of the dextran hydrogel is similar between HyLink and CD-HyLink cross-linked variants. Specifically, the shear moduli for 1.2 mM and 2.5 mM cross-linked dextran are measured at 0.12 kPa and 1.105 kPa, respectively. To approximate the elastic modulus, a Poisson's ratio of 0.5 for hydrogels was assumed, and the calculation followed the method outlined by Caliri and Burdick¹⁵¹: $E = 2G(1 + \nu)$, where E represents the elastic modulus, G is the shear modulus, and ν is the Poisson's ratio.

Table 1: Conditions for Creating the Stroma and Epithelium of the Ectocervical Tissue Models

	Stroma Seeding volume, concentration	Epithelium Seeding volume, density, cultivation
Figure 11.A,B	3* μ L of 5e5 cells/mL in 4 mg/mL FibrCol®	n. a.
Figure 11.C RatCol®	3 μ L of 1e7 cells/mL in 3.6 mg/mL RatCol®	0.5 μ L, 2e6 cells/cm ² , 3 days static, 10 days dynamic at ALI
Figure 11.D FibrCol®	2 μ L of 5e5 cells/mL in 8 mg/mL FibrCol®	1 μ L, 1e6 cells/cm ² , 3 days static, 10 days dynamic at ALI
Figure 11.E	1 μ L of 1e6 cells/mL in 3.6 mg/mL RatCol®	day 3: 1 μ L, 1e6 cells/cm ² , 2 days static, 5 days dynamic at ALI
Figure 11.F	2 μ L of 5e5 cells in 3.6 mg/mL RatCol®	1 μ L, 1e6 cells/cm ² , 3 days static, 10 days dynamic at ALI
Figure 12.A	2 μ L of 1e6 cells/mL in HyStem®-C	1 μ L, 0.5e6 cells/cm ² , 7 days static, 12 days dynamic at ALI
Figure 12.B	2 μ L of 2e6 cells/mL in HyStem®-C	2 μ L, 1e6 cells/cm ² , 7 days static, 12 days dynamic at ALI
Figure 13.A,B	1.4 + 1 μ L of 1e7 cells/mL in 2.4 mM dex/CD-HyLink	0.5 μ L, 1e6 cells/cm ² , 2 days static, 10 days dynamic at ALI
Figure 13.C	1.4 without cells + 1 μ L of 1e7 cells/mL in dex 2.4 mM dex/CD-HyLink	day 2: 2x 0.5 μ L, 1e6 cells/cm ² , 3 days static, 11 days dynamic at ALI
Figure 15.B,D Coll	PDA coating, 2 μ L of 1e6 cells/mL in RatCol®	day 3: 1 μ L, 1e6 cells/cm ² , 2 days static, 8 days dynamic at ALI
Figure 15.C,D HyStem®-C	2 μ L of 1e6 cells/mL in HyStem®-C	1 μ L, 1e6 cells/cm ² , 4 days static, 7 days dynamic with 5 μ L/h at ALI
Figure 15.E	1.4 + 1 μ L of 1e7 cells/mL in 1.2 or 2.4 mM dex/CD-HyLink	day 2: 0.5 μ L, 1e6 cells/cm ² , 1 day static, 10 days dynamic at ALI
Figure 18.A, BF	1.4 + 1 μ L of 0 or 1e7 cells/mL in dex 2.4 mM dex/CD-HyLink + SiHa aggregates of 1 Aggrewell/4 wells	day 2: 2x 0.5 μ L of 1e6 cells/cm ² , 3 days static, 16 days dynamic at ALI
Figure 18.A Ki67/section	1.5 + 1 μ L of 0 or 1e7 cells/mL in 2.4 mM dex/CD-HyLink + SiHa aggregates of 1 Aggrewell/4 wells	day 2: 0.5 μ L of 1e6 cells/cm ² , 1 day static, 12 days dynamic at ALI
Figure 18.B	1.4 without cells + 1 μ L of 1e7 cells/mL in dex 2.4 mM dex/CD-HyLink + SiHa aggregates of 1 Aggrewell/4 wells	day 2: 2x 0.5 μ L of 1e6 cells/cm ² , 3 days static, 11 days dynamic at ALI
Figure 18.C	1.5 + 1 μ L of 1e7 cells/mL in 2.4 mM dex/CD-HyLink + SiHa aggregates of 1 Aggrewell/4 wells	day 2: 2x 0.5 μ L of 1e6 cells/cm ² , 3 days static, 9 days dynamic at ALI
Figure 16.A-C	2 μ L of 1e7 cells/mL in 3.6 mg/mL RatCol®	day 2: 2x 0.5 μ L of 1e6 cells/cm ² , 3 days static, 10 days dynamic at ALI
Figure 16.D	1.4* without cells + 1 μ L of 1e7 /mL in dex 2.4 mM dex/CD-HyLink	n. a.
Figure 16.D	1.4* + 1 μ L of 1e7 /mL in dex 2.4 mM dex/CD-HyLink	n. a.

*FluoSpheres® (F8811, Thermo Fisher Scientific) included in some conditions

Scaffold-assisted stromal layer

MatriDerm®: Wells in a 96 well plate were coated with Anti-Adherence Rinsing Solution (07010, STEMCELL Technologies) for 5-10 min at RT and washed 3x with PBS. 3 mm discs of MatriDerm® (83404-200-1, asclepios Medizintechnik) were equilibrated in 50 µL of DMEM (41965039, Gibco) supplemented with L-ascorbic acid 2-phosphate (50 µg/mL, A8960, Sigma Aldrich) overnight in the incubator at 37 °C. The next day, bubbles were eliminated by spinning the plate for 20 min at 400 xg. Media was removed before seeding fibroblasts at a density of 628,733/cm² as described by Schimek et al.¹⁰⁷. Fibroblast-loaded scaffolds were cultivated for 7 days with media changes 3x per week until being transferred into the tissue well of the platform. In the condition involving a collagen hydrogel, fibroblasts were prepared in RatCol® as described before with 1e7 fibroblasts/mL. Subsequently, 3 µL of the fibroblast/collagen solution were seeded onto the scaffold and transferred into the tissue well of the platform.

PLA: The PLA scaffold was placed in the tissue well and 2x 1e7 fibroblasts/ml FibriCol® were seeded onto the scaffold. The next day, keratinocytes were seeded twice in 0.5 µL at a density of 1e6 keratinocytes/cm². Dynamic cultivation at the ALI was started on day 3 for a duration of 10 days.

6.2.4. Generation of a Keratinocyte Epithelium

Media was aspirated from the stromal layer after one day, and epithelial cells were seeded in their respective media. Following cell attachment, keratinocytes were submerged in FTAL5 (FTAL5, CELLnTEC) and cultured statically. For cultivation at the ALI, media was removed from the tissue well, which was then sealed with a Breath-Easy sealing membrane (Z380059, Sigma Aldrich) to reduce evaporation and keep a sterile environment. The tissue was dynamically supplied at 20 µL/h in withdraw mode. Details regarding cell density, seeding volumes, and the duration of static and dynamic cultivation are provided in Table 1.

6.2.5. Endothelial Cell Seeding in CInoC

First, fibroblasts were seeded and cultured statically for one day following the details provided in Table 1. Subsequently, cannula reservoirs were connected to the ports as shown in (**Figure 7.B**), and the channel was coated for 2 h at 37 °C with 20 µg/mL FN (F1141, Sigma Aldrich) and 100 µg/mL FibriCol® in PBS. After one wash with PBS and another with prewarmed supplemented ECGM, the channel was left filled with ECGM until seeding of ECs. Cervical ECs at a concentration of 6e6 cells/mL (passage 2) were added into the cannula and injected into the chip by withdrawing with a 2 mL syringe from the cannula reservoir at the outlet. Following this, 50 µL of ECGM with P/S was added to each cannula reservoir, and the platform was incubated in an upright position. On the subsequent day, SiHa epithelium was generated following the details provided in Table 1. A PDMS sheet stabilized with a glass slide was positioned on top of the platform and secured with a rubber band, serving as a robust lid to withstand hydrostatic pressure. FTAL5 was then added to the cannula reservoirs, and the triple-culture was cultivated according to Table 1.

To assess the barrier functionality of the endothelial channel lining, dermal ECs were isolated following the procedure outlined by Rogal et al.⁹⁹ and seeded into the channel either on the day before or after stroma generation. The stroma was generated according to the details provided in Table 1, which included the addition of FluoSpheres® (1:500, F8811, Thermo Fisher Scientific). When ECs were seeded before stroma generation, ECs were seeded twice at a concentration of 1e7/mL. First, the platform was flipped to facilitate adhesion to the top of the channel. The second seeding was performed after 45 min on an upright platform to ensure an optimal lining of the bottom of the channel. Unattached cells were removed after 30 min and ECs cultured overnight statically in supplemented ECGM spiked with 10% FCS (SH3006603, ThermoFisher) to enhance EC attachment and proliferation. Fibroblasts were seeded on the following days as outlined in Table 1, including the addition of FluoSpheres®.

6.3. Cell & Tissue Characterization

6.3.1. Histology

Samples were washed with PBS, followed by fixation with Bouin's fixative (6482.3 Carl ROTH) or HistoFix (P087.5, Carl ROTH) for 20-60 min for tissue engineered samples, and overnight for cervical tissues. Samples were thoroughly washed in PBS and then subjected to a multistep process established for generating sections from on-chip tissues (**Figure 21**):

1. The bottom PC layer was removed to prevent sample destruction by the rigid PC layer during sectioning with the microtome. The platform was flipped, and a square carved into the bottom layer with a scalpel (**Figure 19**). After incubating in 70% ethanol for 10-20 min at RT, the PC layer was peeled off with tweezers.
2. Platforms were warmed in PBS in the incubator or water bath for approx. 15 min to prevent HistoGel (HG-4000-012, Thermo Fisher Scientific) from clogging the channel during introduction. A small volume of warm, liquified HistoGel was added into a P1000 tip and quickly placed in one port. To fill the channel, HistoGel was aspirated with an empty tip from the opposite port. HistoGel was solidified for 10 min at 4 °C.
3. A 4 mm biopsy punch (49401, pfm medical) was placed close to one side of the reservoir well and pushed through the SEBS material of the media and bottom layer. By extracting the tissue asymmetrically, tissue orientation was maintained throughout the process.
4. 3D-printed molds were sealed with parafilm and filled with very warm HistoGel (risk of introducing bubbles if HistoGel has cooled down). Up to four samples were quickly placed vertically in the HistoGel, starting with the first sample at the pointed end of the mold. After solidification of HistoGel at RT or at 4 °C, samples were stored in PBS at 4 °C.
5. The HistoGel block was removed from the mold and subjected to automated paraffin embedding according to standard protocols. Removing corners of the paraffin block after blocking helps to maintain the orientation of the samples. 6) Samples were cut into 3-10 μm thick sections, mounted on superfrost slides, and dried at 37 °C for 2 h to overnight. 7) Sections were stained with HE or antibody-solutions as described before.

Alternatively, frozen sections were prepared. An EtOH-resistant pen was used to mark the PC layer with a small line next to the channel to aid orientation. The samples were retrieved with a biopsy punch, as described before, and placed in a 96 well plate containing 30% sucrose and subsequently OCT Embedding Matrix each for 7 h to overnight. A mold, slightly shorter than a microscope slide, was prepared with aluminum foil, marked at the top to maintain the orientation of the samples, and filled with OCT (**Figure 20**). Samples were placed upside down onto the OCT surface and rapidly frozen by placing the mold on a metal plate in -80 °C EtOH. The samples were transferred to -80 °C overnight. The mold was placed on a cold metal plate to prevent thawing and the bottom-PC and media-SEBS layer were removed with tweezers. Empty spaces and the mold itself were filled with OCT; an OCT-filled syringe with a G23 cannula may be helpful to avoid introduction of bubbles. The samples were then frozen and stored at -80 °C. Sections were prepared at a thickness of 20-30 μm .

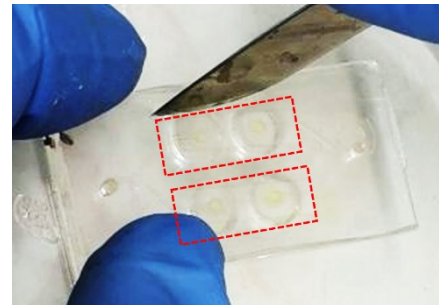


Figure 19: Removal of the Bottom PC-layer.

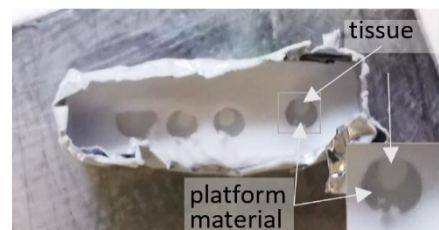


Figure 20: OCT-Embedding.

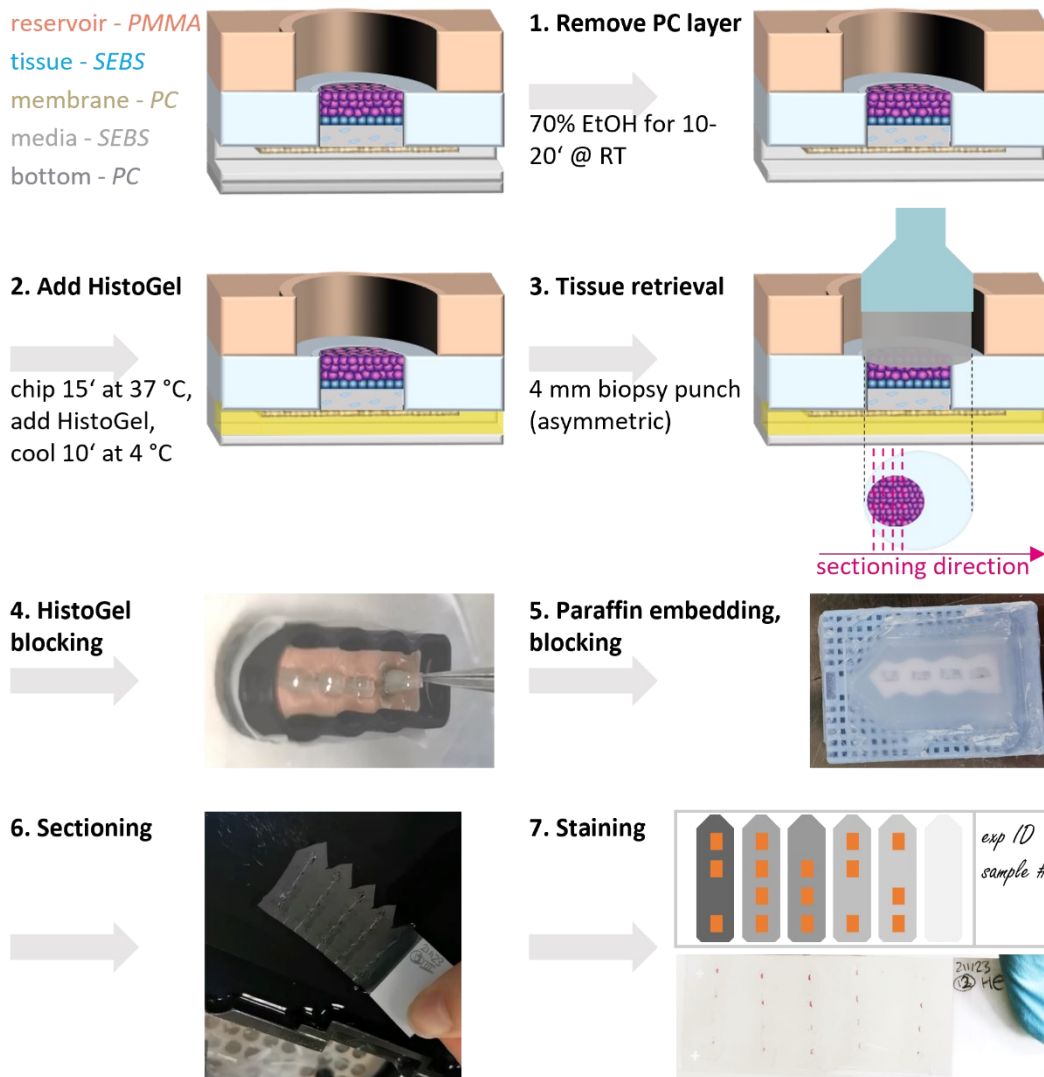


Figure 21: Schematic of the Process for Tissue Retrieval and Generation of FFPE Tissue Sections.

1. First, the bottom PC layer was removed; 2. The channel was filled with HistoGel; 3. The tissue was retrieved from the platform with a biopsy punch; 4. Samples were placed in HistoGel; 5. Samples were embedded and blocked in paraffin; 6. Samples were sectioned; 7. Samples were stained for further analysis.

6.3.2. Staining

Live Cell Staining (CC7)

Cells were stained with CellMask™ Plasma Membrane Stains (C10046, Invitrogen) according to manufacturer instructions for 5-10 min at a dilution of 1:2000.

Viability Staining

Cells or tissues were washed with PBS and stained with FDA (27 µg/mL, F1303 Thermo Fisher Scientific) and PI (135 µg/mL, P4170, Sigma Aldrich) in PBS for 5 min at 37 °C. Subsequently, they were washed with PBS before being imaged with a fluorescence microscope. Alternatively, Calcein AM (1:500, C3099, Thermo Fisher Scientific) and Hoechst 33342 (2 µg/mL, 62249, Thermo Scientific) in PBS were added for 20 min, followed by a 5 min incubation with PI (50 µg/mL). Samples were washed and optionally fixed with HistoFix (P087.5, Carl ROTH) before being imaged with a fluorescence microscope.

Hematoxylin and Eosin Staining

If required, standard protocols for deparaffination were employed and sections stained in eosin (3137.2, Carl Roth) and Hemalum solution acid. Acc. To Mayer (T865.2, Carl Roth).

Antibody Stainings

For immunohistochemistry (IHC) staining, tissue sections were deparaffinized using standard protocols and subjected to antigen retrieval at pH 9 in 10 mM Tris (1115KG001, Bioroxx)/ 1 mM EDTA (A5097, PanReac AppliChem) for 10 min at 90-95 °C. For ICC, samples were fixed with Histofix (P087.5, Carl ROTH) for 10 min at RT and washed with PBS. IHC or ICC samples were permeabilized and blocked for 30 min with triton X-100 (0.1%, X100, Sigma Aldrich)/ BSA (3%, A9647, Sigma Aldrich)/PBS at RT, followed by overnight incubation at 4 °C in antibody diluent (S3022, Dako) at the following dilutions: CK13-AF647 (IHC: 1:100, ICC: 1:200, ab198585, abcam), CK14-PE (IHC: 1:200-1:500, ICC: 1:100, 130-119-729, Miltenyi Biotec), CK19-FITC (IHC: 1:50-1:200, ICC: 1:50 MA5-28576, Invitrogen), CK10-APC (1:100, 130-115-405, Miltenyi Biotec), panCK Basic Cytokeratin Antibody (AE3, 1:100, sc-57004, Santa Cruz), Ki67 (IHC: 1:50-1:500, ICC: 1:200, ab16667, abcam), E-Cad (IHC: 1:500, ICC: 1:50, 610181, BD Transduction Laboratories), FN, (1:200-800, A0245, Agilent), vim (1:1000, MAB2105, R&D Systems), vim in **Figure 12** and **Figure 15** vim-AF405 (1:50, IC2105V, R&D Systems), VWF (1:100, M0616, Agilent), VE Cad (1:100, 610252, BD Transduction Laboratories), CD31 (M082329-2, Agilent), coll IV (1:100, M0785, Agilent). Samples were washed 3 x in IHC Wash Buffer 20x (WL583C0500, DCS Innovative Diagnostik-Systeme), followed by the addition of Goat anti-Rabbit IgG Alexa Fluor 555 (1:500, A21430, Invitrogen), Goat anti-Mouse IgG Alexa Fluor 546 (1:500, A11003, Invitrogen) or Goat anti-Rat Alexa Fluor 488 (1:500, A48263, Invitrogen) secondary antibodies and Hoechst 33342 (2 µg/mL, 62249, Thermo Scientific) for 45-60 min at RT. Samples were washed 3x in IHC Wash Buffer and imaged using a fluorescence microscope.

When animal-free antibodies were evaluated, cervical keratinocytes in 96 well plates were stained as described before with Ki67 (1:200, ab16667, abcam) and Goat anti-Rabbit IgG Alexa Fluor 555 (1:500, A21430, Invitrogen) or with Ki67 (1:20, HCA053, Bio-Rad) with Goat anti-Mouse IgG Alexa Fluor 546 (1:500, A11003, Invitrogen). CKs were stained with Broad Spectrum Cytokeratin (1:100, MSK019, Zytomed) with Human anti Mouse IgG1:DyLight®488 (1:500, HCA309D488, Bio-Rad) or with Goat anti-Mouse IgG Alexa Fluor 546 (1:500, A11003, Invitrogen).

For on-chip immunofluorescent staining, samples were washed with PBS, fixed with Histofix (P087.5, Carl ROTH) for 20-40 min, washed with PBS, permeabilized and blocked for 30-60 min in triton X-100 (0.1%, X100, Sigma Aldrich)/ BSA (3%, A9647, Sigma Aldrich)/PBS at RT. For the staining of ECs in the channel of **Figure 16**, permeabilization/blocking solution was additionally supplemented with donkey serum (3%, D9663 Sigma Aldrich). Primary antibodies were diluted in Antibody Diluent (S3022, Dako) and incubated at 4 °C overnight or for 3 days for **Figure 13** at the following concentrations: CK13-AF647 (1:100, ab198585, abcam), CK14-PE (1:100, 130-119-729, Miltenyi Biotec), CK19-FITC (1:50 MA5-28576, Invitrogen), VE Cad (1:50, 36-1900, Invitrogen), CD31 (1:50, M082329-2, Agilent). Following 3 washes in IHC Wash Buffer 20x (WL583C0500, DCS Innovative Diagnostik-Systeme), samples were incubated with a secondary antibody and Hoechst 33342 (2 µg/mL, 62249, Thermo Scientific) at 4 °C overnight for **Figure 13** or at RT for 45 min for **Figure 16**. Samples were washed 3x in IHC Wash Buffer and imaged with a fluorescence microscope.

7. References

1. Nawroth, J., Rogal, J., Weiss, M., Brucker, S. Y., & Loskill, P. (2018). Organ-on-a-Chip Systems for Women's Health Applications. *Advanced Healthcare Materials*, 7(2). <https://doi.org/10.1002/adhm.201700550>
2. Stolnicu, S., & Goldfrank, D. (2021). Anatomy, Histology, Cytology, and Colposcopy of the Cervix. In R. A. Soslow, K. J. Park, & S. Stolnicu (Eds.), *Atlas of Diagnostic Pathology of the Cervix: A Case-Based Approach* (pp. 1–23). Springer International Publishing. https://doi.org/10.1007/978-3-030-49954-9_1
3. McBride, A. A. (2017). Mechanisms and strategies of papillomavirus replication. *Biological Chemistry*, 398(8), 919–927. <https://doi.org/10.1515/hsz-2017-0113>
4. Champer, M., Wong, A., Champer, J., Brito, I., Messer, P., Hou, J., & Wright, J. (2018). The role of the vaginal microbiome in gynaecological cancer. *BJOG: An International Journal of Obstetrics & Gynaecology*, 125(3), 309–315. <https://doi.org/10.1111/1471-0528.14631>
5. Alzamil, L., Nikolakopoulou, K., & Turco, M. Y. (2021). Organoid systems to study the human female reproductive tract and pregnancy. *Cell Death & Differentiation*, 28(1), Article 1. <https://doi.org/10.1038/s41418-020-0565-5>
6. Chesson, H. W., Dunne, E. F., Hariri, S., & Markowitz, L. E. (2014). The Estimated Lifetime Probability of Acquiring Human Papillomavirus in the United States. *Sexually Transmitted Diseases*, 41(11), 660–664. <https://doi.org/10.1097/OLQ.0000000000000193>
7. Evander, M., Edlund, K., Gustafsson, Å., Jonsson, M., Karlsson, R., Rylander, E., & Wadell, G. (1995). Human Papillomavirus Infection Is Transient in Young Women: A PopulationBased Cohort Study. *The Journal of Infectious Diseases*, 171(4), 1026–1030. <https://doi.org/10.1093/infdis/171.4.1026>
8. Alhamlan, F. S., Alfageeh, M. B., Al Mushait, M. A., Al-Badawi, I. A., & Al-Ahdal, M. N. (2021). Human Papillomavirus-Associated Cancers. In U. Kishore (Ed.), *Microbial Pathogenesis: Infection and Immunity* (pp. 1–14). Springer International Publishing. https://doi.org/10.1007/978-3-030-67452-6_1
9. Kutle, I., Polten, R., Hachenberg, J., Klapdor, R., Morgan, M., & Schambach, A. (2023). Tumor Organoid and Spheroid Models for Cervical Cancer. *Cancers*, 15(9), Article 9. <https://doi.org/10.3390/cancers15092518>
10. Ferrall, L., Lin, K. Y., Roden, R. B. S., Hung, C.-F., & Wu, T.-C. (2021). Cervical Cancer Immunotherapy: Facts and Hopes. *Clinical Cancer Research : An Official Journal of the American Association for Cancer Research*, 27(18), 4953–4973. <https://doi.org/10.1158/1078-0432.CCR-20-2833>
11. Moody, C. A. (2017). Mechanisms by which HPV Induces a Replication Competent Environment in Differentiating Keratinocytes. *Viruses*, 9(9), 261. <https://doi.org/10.3390/v9090261>
12. Graham, S. (2010). Human papillomavirus: Gene expression, regulation and prospects for novel diagnostic methods and antiviral therapies. *Future Microbiology*, 5(10), 1493–1506. <https://doi.org/10.2217/fmb.10.107>
13. Basu, P., Taghavi, K., Hu, S.-Y., Mogri, S., & Joshi, S. (2018). Management of cervical premalignant lesions. *Current Problems in Cancer*, 42(2), 129–136. <https://doi.org/10.1016/j.currproblcancer.2018.01.010>
14. Stanley, M. (2010). Pathology and epidemiology of HPV infection in females. *Gynecologic Oncology*, 117(2, Supplement), S5–S10. <https://doi.org/10.1016/j.ygyno.2010.01.024>
15. Singer, A., & Jordan, J. A. (2006). The Functional Anatomy of the Cervix, the Cervical Epithelium and the Stroma. In *The Cervix* (pp. 13–37). John Wiley & Sons, Ltd. <https://doi.org/10.1002/9781444312744.ch2>
16. Stanley, M. A. (2006). Immunochemistry and Immunology of the Cervix. In *The Cervix* (pp. 49–61). John Wiley & Sons, Ltd. <https://doi.org/10.1002/9781444312744.ch4>
17. Muntean, M., Simionescu, C., Taslîcă, R., Gruia, C., Comanescu, A., Pătrână, N., & Fota, G. (2010). Cytological And Histopathological Aspects Concerning Preinvasive Squamous Cervical Lesions.

18. Park, K. J. (2021). Precursor Lesions of the Cervix: Squamous Precursor Lesions. In R. A. Soslow, K. J. Park, & S. Stolnicu (Eds.), *Atlas of Diagnostic Pathology of the Cervix: A Case-Based Approach* (pp. 105–124). Springer International Publishing. https://doi.org/10.1007/978-3-030-49954-9_5
19. Bruno, M. T., Cassaro, N., Mazza, G., Guaita, A., & Boemi, S. (2022). Spontaneous regression of cervical intraepithelial neoplasia 3 in women with a biopsy—Cone interval of greater than 11 weeks. *BMC Cancer*, 22, 1072. <https://doi.org/10.1186/s12885-022-10179-1>
20. Moscicki, A.-B., Shiboski, S., Hills, N. K., Powell, K. J., Jay, N., Hanson, E. N., Miller, S., Canjura-Clayton, L. K., Farhat, S., Broering, J. M., & Darragh, T. M. (2004). Regression of low-grade squamous intra-epithelial lesions in young women. *The Lancet*, 364(9446), 1678–1683. [https://doi.org/10.1016/S0140-6736\(04\)17354-6](https://doi.org/10.1016/S0140-6736(04)17354-6)
21. Ye, J., Zheng, L., He, Y., & Qi, X. (2023). Human papillomavirus associated cervical lesion: Pathogenesis and therapeutic interventions. *MedComm*, 4(5), e368. <https://doi.org/10.1002/mco2.368>
22. Tainio, K., Athanasiou, A., Tikkinen, K. A. O., Aaltonen, R., Cárdenas, J., Hernández, null, Glazer-Livson, S., Jakobsson, M., Joronen, K., Kiviharju, M., Louvanto, K., Oksjoki, S., Tähtinen, R., Virtanen, S., Nieminen, P., Kyrgiou, M., & Kalliala, I. (2018). Clinical course of untreated cervical intraepithelial neoplasia grade 2 under active surveillance: Systematic review and meta-analysis. *BMJ (Clinical Research Ed.)*, 360, k499. <https://doi.org/10.1136/bmj.k499>
23. Ostör, A. G. (1993). Natural history of cervical intraepithelial neoplasia: A critical review. *International Journal of Gynecological Pathology: Official Journal of the International Society of Gynecological Pathologists*, 12(2), 186–192.
24. Mello, V., & Sundstrom, R. K. (2023). Cervical Intraepithelial Neoplasia. In *StatPearls*. StatPearls Publishing. <http://www.ncbi.nlm.nih.gov/books/NBK544371/>
25. Long, S., & Leeman, L. (2013). Treatment Options for High-Grade Squamous Intraepithelial Lesions. *Obstetrics and Gynecology Clinics of North America*, 40(2), 291–316. <https://doi.org/10.1016/j.ogc.2013.03.004>
26. Sand, F. L., Frederiksen, K., Munk, C., Jensen, S. M., & Kjær, S. K. (2018). Long-term risk of cervical cancer following conization of cervical intraepithelial neoplasia grade 3—A Danish nationwide cohort study. *International Journal of Cancer*, 142(9), 1759–1766. <https://doi.org/10.1002/ijc.31202>
27. Schiffman, M., Doorbar, J., Wentzensen, N., de Sanjosé, S., Fakhry, C., Monk, B. J., Stanley, M. A., & Franceschi, S. (2016). Carcinogenic human papillomavirus infection. *Nature Reviews Disease Primers*, 2(1), Article 1. <https://doi.org/10.1038/nrdp.2016.86>
28. Xiong, Y., Cui, L., Bian, C., Zhao, X., & Wang, X. (2020). Clearance of human papillomavirus infection in patients with cervical intraepithelial neoplasia. *Medicine*, 99(46), e23155. <https://doi.org/10.1097/MD.00000000000023155>
29. Marzi, J., Stope, M. B., Henes, M., Koch, A., Wenzel, T., Holl, M., Layland, S. L., Neis, F., Bösmüller, H., Ruoff, F., Templin, M., Krämer, B., Staebler, A., Barz, J., Carvajal Berrio, D. A., Enderle, M., Loskill, P. M., Brucker, S. Y., Schenke-Layland, K., & Weiss, M. (2022). Noninvasive Physical Plasma as Innovative and Tissue-Preserving Therapy for Women Positive for Cervical Intraepithelial Neoplasia. *Cancers*, 14(8), 1933. <https://doi.org/10.3390/cancers14081933>
30. Weiss, M., Arnholdt, M., Hißnauer, A., Fischer, I., Schönfish, B., Andress, J., Gerstner, S., Dannehl, D., Bösmüller, H., Staebler, A., Brucker, S. Y., & Henes, M. (2023). Tissue-preserving treatment with non-invasive physical plasma of cervical intraepithelial neoplasia—A prospective controlled clinical trial. *Frontiers in Medicine*, 10, 1242732. <https://doi.org/10.3389/fmed.2023.1242732>
31. Barra, F., Della Corte, L., Noberasco, G., Foreste, V., Riemma, G., Di Filippo, C., Bifulco, G., Orsi, A., Icardi, G., & Ferrero, S. (2020). Advances in therapeutic vaccines for treating human

- papillomavirus-related cervical intraepithelial neoplasia. *Journal of Obstetrics and Gynaecology Research*, 46(7), 989–1006. <https://doi.org/10.1111/jog.14276>
32. Sung, H., Ferlay, J., Siegel, R. L., Laversanne, M., Soerjomataram, I., Jemal, A., & Bray, F. (2021). Global Cancer Statistics 2020: GLOBOCAN Estimates of Incidence and Mortality Worldwide for 36 Cancers in 185 Countries. *CA: A Cancer Journal for Clinicians*, 71(3), 209–249. <https://doi.org/10.3322/caac.21660>
 33. Aggarwal, S., Agarwal, P., & Singh, A. K. (2023). Human papilloma virus vaccines: A comprehensive narrative review. *Cancer Treatment and Research Communications*, 37, 100780. <https://doi.org/10.1016/j.ctarc.2023.100780>
 34. Wähner, C., Hübner, J., Meisel, D., Schelling, J., Zingel, R., Mihm, S., Wölle, R., & Reuschenbach, M. (2023). Uptake of HPV vaccination among boys after the introduction of gender-neutral HPV vaccination in Germany before and during the COVID-19 pandemic. *Infection*, 51(5), 1293–1304. <https://doi.org/10.1007/s15010-023-01978-0>
 35. Watson, M., Saraiya, M., Benard, V., Coughlin, S. S., Flowers, L., Cokkinides, V., Schwenn, M., Huang, Y., & Giuliano, A. (2008). Burden of cervical cancer in the United States, 1998–2003. *Cancer*, 113(S10), 2855–2864. <https://doi.org/10.1002/cncr.23756>
 36. Spurgeon, M. E., & Lambert, P. F. (2017). Human Papillomavirus and the Stroma: Bidirectional Crosstalk during the Virus Life Cycle and Carcinogenesis. *Viruses*, 9(8), Article 8. <https://doi.org/10.3390/v9080219>
 37. Walboomers, J. M., Jacobs, M. V., Manos, M. M., Bosch, F. X., Kummer, J. A., Shah, K. V., Snijders, P. J., Peto, J., Meijer, C. J., & Muñoz, N. (1999). Human papillomavirus is a necessary cause of invasive cervical cancer worldwide. *The Journal of Pathology*, 189(1), 12–19. [https://doi.org/10.1002/\(SICI\)1096-9896\(199909\)189:1<12::AID-PATH431>3.0.CO;2-F](https://doi.org/10.1002/(SICI)1096-9896(199909)189:1<12::AID-PATH431>3.0.CO;2-F)
 38. de Sanjose, S., Quint, W. G., Alemany, L., Geraets, D. T., Klaustermeier, J. E., Lloveras, B., Tous, S., Felix, A., Bravo, L. E., Shin, H.-R., Vallejos, C. S., de Ruiz, P. A., Lima, M. A., Guimera, N., Clavero, O., Alejo, M., Llombart-Bosch, A., Cheng-Yang, C., Tatti, S. A., ... Retrospective International Survey and HPV Time Trends Study Group. (2010). Human papillomavirus genotype attribution in invasive cervical cancer: A retrospective cross-sectional worldwide study. *The Lancet. Oncology*, 11(11), 1048–1056. [https://doi.org/10.1016/S1470-2045\(10\)70230-8](https://doi.org/10.1016/S1470-2045(10)70230-8)
 39. Malevolti, M. C., Maci, C., Lugo, A., Possenti, I., Gallus, S., Gorini, G., & Carreras, G. (2023). Second-hand smoke exposure and cervical cancer: A systematic review and meta-analysis. *Journal of Cancer Research and Clinical Oncology*, 149(15), 14353–14363. <https://doi.org/10.1007/s00432-023-04841-9>
 40. Chen, T., Jansen, L., Gondos, A., Emrich, K., Holleczeck, B., Luttmann, S., Waldmann, A., Brenner, H., & Gekid Cancer Survival Working Group. (2012). Survival of cervical cancer patients in Germany in the early 21st century: A period analysis by age, histology, and stage. *Acta Oncologica (Stockholm, Sweden)*, 51(7), 915–921. <https://doi.org/10.3109/0284186X.2012.708105>
 41. Song, Z., Zou, K., & Zou, L. (2022). Immune checkpoint blockade for locally advanced or recurrent/metastatic cervical cancer: An update on clinical data. *Frontiers in Oncology*, 12, 1045481. <https://doi.org/doi.org/10.3389/fonc.2022.1045481>
 42. Sun, C., Brown, A. J., Jhingran, A., Frumovitz, M., Ramondetta, L., & Bodurka, D. C. (2014). Patient Preferences for Side Effects Associated With Cervical Cancer Treatment. *International Journal of Gynecologic Cancer*, 24(6). <https://doi.org/10.1097/IGC.000000000000149>
 43. Moreira, A. S. L., Cunha, T. M., & Esteves, S. (2020). Cervical cancer recurrence – can we predict the type of recurrence? *Diagnostic and Interventional Radiology*, 26(5), 403–410. <https://doi.org/10.5152/dir.2020.19437>
 44. Obermair, A., Asher, R., Pareja, R., Frumovitz, M., Lopez, A., Moretti-Marques, R., Rendon, G., Ribeiro, R., Tsunoda, A., Behan, V., Buda, A., Bernadini, M. Q., Zhao, H., Vieira, M., Walker, J., Spirtos, N. M., Yao, S., Chetty, N., Zhu, T., ... Ramirez, P. T. (2020). Incidence of adverse events in minimally invasive vs open radical hysterectomy in early cervical cancer: Results of a

- randomized controlled trial. *American Journal of Obstetrics & Gynecology*, 222(3), 249.e1-249.e10. <https://doi.org/10.1016/j.ajog.2019.09.036>
45. Federico, C., Sun, J., Muz, B., Alhallak, K., Cosper, P. F., Muhammad, N., Jeske, A., Hinger, A., Markovina, S., Grigsby, P., Schwarz, J. K., & Azab, A. K. (2021). Localized Delivery of Cisplatin to Cervical Cancer Improves Its Therapeutic Efficacy and Minimizes Its Side Effect Profile. *International Journal of Radiation Oncology, Biology, Physics*, 109(5), 1483–1494. <https://doi.org/10.1016/j.ijrobp.2020.11.052>
 46. Jha, A. K., Mithun, S., Sherkhane, U. B., Jaiswar, V., Osong, B., Purandare, N., Kannan, S., Prabhaskar, K., Gupta, S., Vanneste, B., Rangarajan, V., Dekker, A., & Wee, L. (2023). Systematic review and meta-analysis of prediction models used in cervical cancer. *Artificial Intelligence in Medicine*, 139, 102549. <https://doi.org/10.1016/j.artmed.2023.102549>
 47. Jiang, P., Li, X., Shen, H., Chen, Y., Wang, L., Chen, H., Feng, J., & Liu, J. (2023). A systematic review of deep learning-based cervical cytology screening: From cell identification to whole slide image analysis. *Artificial Intelligence Review*, 56(2), 2687–2758. <https://doi.org/10.1007/s10462-023-10588-z>
 48. Rosado-Mendez, I. M., Palmeri, M. L., Drehfal, L. C., Guerrero, Q. W., Simmons, H., Feltoich, H., & Hall, T. J. (2017). Assessment of Structural Heterogeneity and Viscosity in the Cervix Using Shear Wave Elasticity Imaging: Initial Results from a Rhesus Macaque Model. *Ultrasound in Medicine & Biology*, 43(4), 790–803. <https://doi.org/10.1016/j.ultrasmedbio.2016.12.006>
 49. Vargas-Cardona, H. D., Rodriguez-Lopez, M., Arrivillaga, M., Vergara-Sanchez, C., García-Cifuentes, J. P., Bermúdez, P. C., & Jaramillo-Botero, A. (2023). Artificial intelligence for cervical cancer screening: Scoping review, 2009-2022. *International Journal of Gynaecology and Obstetrics: The Official Organ of the International Federation of Gynaecology and Obstetrics*. <https://doi.org/10.1002/ijgo.15179>
 50. Larmour, L. I., Jobling, T. W., & Gargett, C. E. (2015). A Review of Current Animal Models for the Study of Cervical Dysplasia and Cervical Carcinoma. *International Journal of Gynecologic Cancer*, 25(8). <https://doi.org/10.1097/IGC.0000000000000525>
 51. Tanaka, T., Nishie, R., Ueda, S., Miyamoto, S., Hashida, S., Konishi, H., Terada, S., Kogata, Y., Sasaki, H., Tsunetoh, S., Taniguchi, K., Komura, K., & Ohmichi, M. (2021). Patient-Derived Xenograft Models in Cervical Cancer: A Systematic Review. *International Journal of Molecular Sciences*, 22(17), 9369. <https://doi.org/10.3390/ijms22179369>
 52. Cadena, I., Chen, A., Arvidson, A., & Fogg, K. C. (2021). Biomaterial strategies to replicate gynecological tissue. *Biomaterials Science*, 9(4), 1117–1134. <https://doi.org/10.1039/D0BM01240H>
 53. De Gregorio, V., Urciuolo, F., Netti, P. A., & Imparato, G. (2020). In Vitro Organotypic Systems to Model Tumor Microenvironment in Human Papillomavirus (HPV)-Related Cancers. *Cancers*, 12(5), Article 5. <https://doi.org/10.3390/cancers12051150>
 54. Francés-Herrero, E., Lopez, R., Hellström, M., de Miguel-Gómez, L., Herraiz, S., Brännström, M., Pellicer, A., & Cervelló, I. (2022). Bioengineering trends in female reproduction: A systematic review. *Human Reproduction Update*, 28(6), 798–837. <https://doi.org/10.1093/humupd/dmac025>
 55. Löhmußaar, K., Boretto, M., & Clevers, H. (2020). Human-Derived Model Systems in Gynecological Cancer Research. *Trends in Cancer*, 6(12), 1031–1043. <https://doi.org/10.1016/j.trecan.2020.07.007>
 56. Chumduri, C., & Turco, M. Y. (2021). Organoids of the female reproductive tract. *Journal of Molecular Medicine (Berlin, Germany)*, 99(4), 531–553. <https://doi.org/10.1007/s00109-020-02028-0>
 57. Haider, S., & Beristain, A. G. (2023). Human organoid systems in modeling reproductive tissue development, function, and disease. *Human Reproduction*, 38(8), 1449–1463. <https://doi.org/10.1093/humrep/dead085>

58. Mitchell, M. F., Hamada, K., Sastry, K. J., Sarkar, A., Tortolero-Luna, G., Wharton, J. T., & Roth, J. A. (1996). Transgene expression in the rhesus cervix mediated by an adenovirus expressing β -galactosidase. *American Journal of Obstetrics and Gynecology*, 174(4), 1094–1101. [https://doi.org/10.1016/S0002-9378\(96\)70650-6](https://doi.org/10.1016/S0002-9378(96)70650-6)
59. Zhao, L., Liu, B., Ren, J., Feng, J., Pang, Z., Gao, J., Zhang, H., Tan, W., Tian, H., & Ruan, L. (2011). Immunogenicity in mice and rhesus monkeys vaccinated with recombinant vaccinia virus expressing bivalent E7E6 fusion proteins from human papillomavirus types 16 and 18. *Virology Journal*, 8, 302. <https://doi.org/10.1186/1743-422X-8-302>
60. Slayden, O. D., Friason, F. K. E., Bond, K. R., & Mishler, E. C. (2018). Hormonal regulation of oviductal glycoprotein 1 (OVGP1; MUC9) in the rhesus macaque cervix. *Journal of Medical Primatology*, 47(6), 362–370. <https://doi.org/10.1111/jmp.12357>
61. He, C., Lv, X., Huang, C., Angeletti, P. C., Hua, G., Dong, J., Zhou, J., Wang, Z., Ma, B., Chen, X., Lambert, P. F., Rueda, B. R., Davis, J. S., & Wang, C. (2019). A Human Papillomavirus-Independent Cervical Cancer Animal Model Reveals Unconventional Mechanisms of Cervical Carcinogenesis. *Cell Reports*, 26(10), 2636–2650.e5. <https://doi.org/10.1016/j.celrep.2019.02.004>
62. Munguía-Moreno, J. A., Díaz-Chavéz, J., García-Villa, E., Albino-Sanchez, M. E., Mendoza-Villanueva, D., Ocadiz-Delgado, R., Bonilla-Delgado, J., Marín-Flores, A., Cortés-Malagón, E. M., Alvarez-Rios, E., Hidalgo-Miranda, A., Üren, A., Çelik, H., Lambert, P. F., & Gariglio, P. (2018). Early synergistic interactions between the HPV16-E7 oncoprotein and 17 β -oestradiol for repressing the expression of Granzyme B in a cervical cancer model. *International Journal of Oncology*, 53(2), 579–591. <https://doi.org/10.3892/ijo.2018.4432>
63. Cheon, D.-J., & Orsulic, S. (2011). Mouse Models of Cancer. *Annual Review of Pathology: Mechanisms of Disease*, 6(1), 95–119. <https://doi.org/10.1146/annurev.pathol.3.121806.154244>
64. Rangarajan, A., & Weinberg, R. A. (2003). Comparative biology of mouse versus human cells: Modelling human cancer in mice. *Nature Reviews Cancer*, 3(12), Article 12. <https://doi.org/10.1038/nrc1235>
65. Fan, T., Li, X., Li, Y., Zhi, Y., Rong, S., Cheng, G., & Zhang, X. (2018). An improved method for primary culture of normal cervical epithelial cells and establishment of cell model in vitro with HPV-16 E6 gene by lentivirus. *Journal of Cellular Physiology*, 233(4), 2773–2780. <https://doi.org/10.1002/jcp.25978>
66. Herbst-Kralovetz, M. M., Quayle, A. J., Ficarra, M., Greene, S., Rose II, W. A., Chesson, R., Spagnuolo, R. A., & Pyles, R. B. (2008). Quantification and Comparison of Toll-Like Receptor Expression and Responsiveness in Primary and Immortalized Human Female Lower Genital Tract Epithelia. *American Journal of Reproductive Immunology*, 59(3), 212–224. <https://doi.org/10.1111/j.1600-0897.2007.00566.x>
67. Liu, Y.-Z., Wang, T.-T., & Zhang, Y.-Z. (2016). A modified method for the culture of naturally HPV-infected high-grade cervical intraepithelial neoplasia keratinocytes from human neoplastic cervical biopsies. *Oncology Letters*, 11(2), 1457–1462. <https://doi.org/10.3892/ol.2016.4096>
68. Zuñiga Martínez, M. de L., López Mendoza, C. M., Tenorio Salazar, J., García Carrancá, A. M., Cerbón Cervantes, M. A., & Alcántara-Quintana, L. E. (2022). Establishment, authenticity, and characterization of cervical cancer cell lines. *Molecular & Cellular Oncology*, 9(1), 2078628. <https://doi.org/10.1080/23723556.2022.2078628>
69. De Gregorio, V., La Rocca, A., Urciuolo, F., Annunziata, C., Tornesello, M. L., Buonaguro, F. M., Netti, P. A., & Imparato, G. (2020). Modeling the epithelial-mesenchymal transition process in a 3D organotypic cervical neoplasia. *Acta Biomaterialia*, 116, 209–222. <https://doi.org/10.1016/j.actbio.2020.09.006>
70. Ayehunie, S., Cannon, C., Lamore, S., Kubilus, J., Anderson, D. J., Pudney, J., & Klausner, M. (2006). Organotypic human vaginal-ectocervical tissue model for irritation studies of spermicides,

- microbicides, and feminine-care products. *Toxicology in Vitro*, 20(5), 689–698. <https://doi.org/10.1016/j.tiv.2005.10.002>
71. Delvenne, P., Hubert, P., Jacobs, N., Giannini, S. L., Havard, L., Renard, I., Saboulard, D., & Boniver, J. (2001). The organotypic culture of HPV-transformed keratinocytes: An effective in vitro model for the development of new immunotherapeutic approaches for mucosal (pre)neoplastic lesions. *Vaccine*, 19(17), 2557–2564. [https://doi.org/10.1016/S0264-410X\(00\)00489-8](https://doi.org/10.1016/S0264-410X(00)00489-8)
 72. Deng, H., Mondal, S., Sur, S., & Woodworth, C. D. (2019). Establishment and Optimization of Epithelial Cell Cultures from Human Ectocervix, Transformation Zone and Endocervix. *Journal of Cellular Physiology*, 234(6), 7683–7694. <https://doi.org/10.1002/jcp.28049>
 73. Jacobs, N., Moutschen, M. P., Franzen-Detrooz, E., Boniver, V., Boniver, J., & Delvenne, P. (1998). Organotypic culture of HPV-transformed keratinocytes: A model for testing lymphocyte infiltration of (pre)neoplastic lesions of the uterine cervix. *Virchows Archiv*, 432(4), 323–330. <https://doi.org/10.1007/s004280050173>
 74. Lechanteur, A., Furst, T., Evrard, B., Delvenne, P., Piel, G., & Hubert, P. (2017). Promoting Vaginal Distribution of E7 and MCL-1 siRNA-Silencing Nanoparticles for Cervical Cancer Treatment. *Molecular Pharmaceutics*, 14(5), 1706–1717. <https://doi.org/10.1021/acs.molpharmaceut.6b01154>
 75. Martin, S. F., Wood, A. D., McRobbie, M. M., Mazilu, M., McDonald, M. P., Samuel, I. D. W., & Herrington, C. S. (2007). Fluorescence spectroscopy of an in vitro model of human cervical precancer identifies neoplastic phenotype. *International Journal of Cancer*, 120(9), 1964–1970. <https://doi.org/10.1002/ijc.22517>
 76. Villa, P. L., Jackson, R., Eade, S., Escott, N., & Zehbe, I. (2018). Isolation of Biopsy-Derived, Human Cervical Keratinocytes Propagated as Monolayer and Organoid Cultures. *Scientific Reports*, 8, 17869. <https://doi.org/10.1038/s41598-018-36150-4>
 77. Zadora, P. K., Chumduri, C., Imami, K., Berger, H., Mi, Y., Selbach, M., Meyer, T. F., & Gurumurthy, R. K. (2019). Integrated Phosphoproteome and Transcriptome Analysis Reveals Chlamydia-Induced Epithelial-to-Mesenchymal Transition in Host Cells. *Cell Reports*, 26(5), 1286-1302.e8. <https://doi.org/10.1016/j.celrep.2019.01.006>
 78. Chumduri, C., Gurumurthy, R. K., Berger, H., Dietrich, O., Kumar, N., Koster, S., Brinkmann, V., Hoffmann, K., Drabkina, M., Arampatzi, P., Son, D., Klemm, U., Mollenkopf, H.-J., Herbst, H., Mangler, M., Vogel, J., Saliba, A.-E., & Meyer, T. F. (2021). Opposing Wnt signals regulate cervical squamocolumnar homeostasis and emergence of metaplasia. *Nature Cell Biology*, 23(2), 184–197. <https://doi.org/10.1038/s41556-020-00619-0>
 79. Löhmußaar, K., Oka, R., Espejo Valle-Inclan, J., Smits, M. H. H., Wardak, H., Korving, J., Begthel, H., Proost, N., van de Ven, M., Kranenburg, O. W., Jonges, T. G. N., Zweemer, R. P., Veersema, S., van Boxtel, R., & Clevers, H. (2021). Patient-derived organoids model cervical tissue dynamics and viral oncogenesis in cervical cancer. *Cell Stem Cell*, 28(8), 1380-1396.e6. <https://doi.org/10.1016/j.stem.2021.03.012>
 80. Seol, H. S., Oh, J. H., Choi, E., Kim, S., Kim, H., & Nam, E. J. (2022). Preclinical investigation of patient-derived cervical cancer organoids for precision medicine. *Journal of Gynecologic Oncology*, 34(3). <https://doi.org/10.3802/jgo.2023.34.e35>
 81. Marshall, L. J., Bailey, J., Cassotta, M., Herrmann, K., & Pistollato, F. (2023). Poor Translatability of Biomedical Research Using Animals—A Narrative Review. *Alternatives to Laboratory Animals*, 51(2), 102–135. <https://doi.org/10.1177/02611929231157756>
 82. Ingber, D. E. (2022). Human organs-on-chips for disease modelling, drug development and personalized medicine. *Nature Reviews Genetics*, 23(8), Article 8. <https://doi.org/10.1038/s41576-022-00466-9>
 83. Mastrangeli, M., Millet, S., Partners, T. O., & Raaij, J. van den E. (2019). Organ-on-chip in development: Towards a roadmap for organs-on-chip. *ALTEX - Alternatives to Animal Experimentation*, 36(4), Article 4. <https://doi.org/10.14573/altex.1908271>

84. Rogal, J., Schlünder, K., & Loskill, P. (2022). Developer's Guide to an Organ-on-Chip Model. *ACS Biomaterials Science & Engineering*, 8(11), 4643–4647. <https://doi.org/10.1021/acsbiomaterials.1c01536>
85. Huh, D., Matthews, B. D., Mammoto, A., Montoya-Zavala, M., Yuan Hsin, H., & Ingber, D. E. (2010). Reconstituting Organ-Level Lung Functions on a Chip. *Science (New York, N.Y.)*, 328(5986), 1662–1668. <https://doi.org/10.1126/science.1188302>
86. Lin, L., Lin, X., Lin, L., Feng, Q., Kitamori, T., Lin, J.-M., & Sun, J. (2017). Integrated Microfluidic Platform with Multiple Functions To Probe Tumor–Endothelial Cell Interaction. *Analytical Chemistry*, 89(18), 10037–10044. <https://doi.org/10.1021/acs.analchem.7b02593>
87. Tantengco, O. A. G., Richardson, L. S., Medina, P. M. B., Han, A., & Menon, R. (2021). Organ-on-chip of the cervical epithelial layer: A platform to study normal and pathological cellular remodeling of the cervix. *FASEB Journal : Official Publication of the Federation of American Societies for Experimental Biology*, 35(4), e21463. <https://doi.org/10.1096/fj.202002590RRR>
88. Izadifar, Z., Cotton, J., Chen, S., Bustos, N. A., Horvath, V., Stejskalova, A., Wu, C., Gulati, A., LoGrande, N. T., Budnik, B., Shahriar, S., Doherty, E. R., Xie, Y., To, T., Gilpin, S. E., Sesay, A. M., Goyal, G., Ribbeck, K., Lebrilla, C., & Ingber, D. E. (2023). *Mucus production, host-microbiome interactions, hormone sensitivity, and innate immune responses modeled in human cervix chips* (p. 2023.02.22.529436). bioRxiv. <https://doi.org/10.1101/2023.02.22.529436>
89. Toepke, M. W., & Beebe, D. J. (2006). PDMS absorption of small molecules and consequences in microfluidic applications. *Lab on a Chip*, 6(12), 1484–1486. <https://doi.org/10.1039/b612140c>
90. Greenhead, P., Hayes, P., Watts, P. S., Laing, K. G., Griffin, G. E., & Shattock, R. J. (2000). Parameters of Human Immunodeficiency Virus Infection of Human Cervical Tissue and Inhibition by Vaginal Virucides. *Journal of Virology*, 74(12), 5577–5586. <https://www.ncbi.nlm.nih.gov/pmc/articles/PMC112045/>
91. Michelini, M., Rosellini, A., Papini, S., Revoltella, R. P., Michelini, M., Rosellini, A., Papini, S., & Simoncini, T. (2004). A three-dimensional organotypic culture of the human uterine exocervix for studying mucosal epithelial differentiation and migrating leukocytes. *Differentiation*, 72(4), 138–149. <https://doi.org/10.1111/j.1432-0436.2004.07204001.x>
92. Shan, Y., Ding, Z., Cui, Z., & Chen, A. (2023). Incidence, prognostic factors and a nomogram of cervical cancer with distant organ metastasis: A SEER-based study. *Journal of Obstetrics and Gynaecology*, 43(1), 2181690. <https://doi.org/10.1080/01443615.2023.2181690>
93. Schneider, S., Brás, E. J. S., Schneider, O., Schlünder, K., & Loskill, P. (2021). Facile Patterning of Thermoplastic Elastomers and Robust Bonding to Glass and Thermoplastics for Microfluidic Cell Culture and Organ-on-Chip. *Micromachines*, 12(5), 575. <https://doi.org/10.3390/mi12050575>
94. Boudko, S. P., Danylevych, N., Hudson, B. G., & Pedchenko, V. K. (2018). Basement membrane collagen IV: Isolation of functional domains. *Methods in Cell Biology*, 143, 171–185. <https://doi.org/10.1016/bs.mcb.2017.08.010>
95. Jiang, J., Li, X., Yin, X., Zhang, J., & Shi, B. (2019). Association of low expression of E-cadherin and β -catenin with the progression of early stage human squamous cervical cancer. *Oncology Letters*, 17(6), 5729–5739. <https://doi.org/10.3892/ol.2019.10266>
96. Goncharov, N. V., Popova, P. I., Avdonin, P. P., Kudryavtsev, I. V., Serebryakova, M. K., Korf, E. A., & Avdonin, P. V. (2020). Markers of Endothelial Cells in Normal and Pathological Conditions. *Biochemistry (Moscow) Supplement. Series A, Membrane and Cell Biology*, 14(3), 167–183. <https://doi.org/10.1134/S1990747819030140>
97. Ridky, T. W., Chow, J. M., Wong, D. J., & Khavari, P. A. (2010). Invasive three-dimensional organotypic neoplasia from multiple normal human epithelia. *Nature Medicine*, 16(12), Article 12. <https://doi.org/10.1038/nm.2265>
98. Kisiel, M. A., & Klar, A. S. (2019). Isolation and Culture of Human Dermal Fibroblasts. In S. Böttcher-Haberzeth & T. Biedermann (Eds.), *Skin Tissue Engineering: Methods and Protocols* (pp. 71–78). Springer. https://doi.org/10.1007/978-1-4939-9473-1_6

99. Rogal, J., Roosz, J., Teufel, C., Cipriano, M., Xu, R., Eisler, W., Weiss, M., Schenke-Layland, K., & Loskill, P. (2022). Autologous Human Immunocompetent White Adipose Tissue-on-Chip. *Advanced Science*, *9*(18), 2104451. <https://doi.org/10.1002/advs.202104451>
100. Li, C., & Hua, K. (2022). Dissecting the Single-Cell Transcriptome Network of Immune Environment Underlying Cervical Premalignant Lesion, Cervical Cancer and Metastatic Lymph Nodes. *Frontiers in Immunology*, *13*, 897366. <https://doi.org/10.3389/fimmu.2022.897366>
101. Ledsgaard, L., Kilstrup, M., Karatt-Vellatt, A., McCafferty, J., & Laustsen, A. H. (2018). Basics of Antibody Phage Display Technology. *Toxins*, *10*(6), 236. <https://doi.org/10.3390/toxins10060236>
102. CELLnTEC. (n.d.). *Full Thickness Skin Models*. https://cellntec.com/wp-content/uploads/pdf/16.FT_Skin_Model_Protocol_2022.pdf
103. Nishiguchi, A., Yoshida, H., Matsusaki, M., & Akashi, M. (2011). Rapid Construction of Three-Dimensional Multilayered Tissues with Endothelial Tube Networks by the Cell-Accumulation Technique. *Advanced Materials*, *23*(31), 3506–3510. <https://doi.org/10.1002/adma.201101787>
104. House, M., Kaplan, D. L., & Socrate, S. (2009). Relationships between Mechanical Properties and Extracellular Matrix Constituents of the Cervical Stroma during Pregnancy. *Seminars in Perinatology*, *33*(5), 300–307. <https://doi.org/10.1053/j.semperi.2009.06.002>
105. Lotz, C., Schmid, F. F., Oechsle, E., Monaghan, M. G., Walles, H., & Groeber-Becker, F. (2017). Cross-linked Collagen Hydrogel Matrix Resisting Contraction To Facilitate Full-Thickness Skin Equivalents. *ACS Applied Materials & Interfaces*, *9*(24), 20417–20425. <https://doi.org/10.1021/acsami.7b04017>
106. Park, S. E., Georgescu, A., Oh, J. M., Kwon, K. W., & Huh, D. (2019). Polydopamine-Based Interfacial Engineering of Extracellular Matrix Hydrogels for the Construction and Long-Term Maintenance of Living Three-Dimensional Tissues. *ACS Applied Materials & Interfaces*, *11*(27), 23919–23925. <https://doi.org/10.1021/acsami.9b07912>
107. Schimek, K., Hsu, H.-H., Boehme, M., Kornet, J. J., Marx, U., Lauster, R., Pörtner, R., & Lindner, G. (2018). Bioengineering of a Full-Thickness Skin Equivalent in a 96-Well Insert Format for Substance Permeation Studies and Organ-On-A-Chip Applications. *Bioengineering*, *5*(2), Article 2. <https://doi.org/10.3390/bioengineering5020043>
108. Stadelmann, K., Weghofer, A., Urbanczyk, M., Maulana, T. I., Loskill, P., Jones, P. D., & Schenke-Layland, K. (2022). Development of a bi-layered cryogenic electrospun polylactic acid scaffold to study calcific aortic valve disease in a 3D co-culture model. *Acta Biomaterialia*, *140*, 364–378. <https://doi.org/10.1016/j.actbio.2021.11.030>
109. Kamal, M. (2022). Cervical Pre-cancers: Biopsy and Immunohistochemistry. *CytoJournal*, *19*, 38. https://doi.org/10.25259/CMAS_03_13_2021
110. Friedl, F., Kimura, I., Osato, T., & Ito, Y. (1970). Studies on a new human cell line (SiHa) derived from carcinoma of uterus. I. Its establishment and morphology. *Proceedings of the Society for Experimental Biology and Medicine. Society for Experimental Biology and Medicine (New York, N.Y.)*, *135*(2), 543–545. <https://doi.org/10.3181/00379727-135-35091a>
111. Krüger-Genge, A., Blocki, A., Franke, R.-P., & Jung, F. (2019). Vascular Endothelial Cell Biology: An Update. *International Journal of Molecular Sciences*, *20*(18), Article 18. <https://doi.org/10.3390/ijms20184411>
112. Trimm, E., & Red-Horse, K. (2023). Vascular endothelial cell development and diversity. *Nature Reviews Cardiology*, *20*(3), Article 3. <https://doi.org/10.1038/s41569-022-00770-1>
113. Dobbs, S. P., Brown, L. J. R., Ireland, D., Abrams, K. R., Murray, J. C., Gatter, K., Harris, A., Steward, W. P., & O'Byrne, K. J. (2000). Platelet-derived endothelial cell growth factor expression and angiogenesis in cervical intraepithelial neoplasia and squamous cell carcinoma of the cervix. *Annals of Diagnostic Pathology*, *4*(5), 286–292. <https://doi.org/10.1053/adpa.2000.17872>
114. Mondal, S. K., Dasgupta, S., Mandal, P. K., Chatterjee, S., & Chakraborty, D. (2014). Is there any role of mast cell density and microvessel density in cervical squamous cell carcinoma? A

- histologic study with special reference to CD-34 immunomarker staining. *Indian Journal of Medical and Paediatric Oncology: Official Journal of Indian Society of Medical & Paediatric Oncology*, 35(2), 165–169. <https://doi.org/10.4103/0971-5851.138994>
115. Toussaint-Smith, E., Donner, D. B., & Roman, A. (2004). Expression of human papillomavirus type 16 E6 and E7 oncoproteins in primary foreskin keratinocytes is sufficient to alter the expression of angiogenic factors. *Oncogene*, 23(17), 2988–2995. <https://doi.org/10.1038/sj.onc.1207442>
 116. Chen, W., Li, F., Mead, L., White, H., Walker, J., Ingram, D. A., & Roman, A. (2007). Human papillomavirus causes an angiogenic switch in keratinocytes which is sufficient to alter endothelial cell behavior. *Virology*, 367(1), 168–174. <https://doi.org/10.1016/j.virol.2007.05.030>
 117. Lehman, H. M. L., & Thomas, G. M. (2006). Management of Cervical Cancer by Radiotherapy and Chemotherapy. In *The Cervix* (pp. 601–608). John Wiley & Sons, Ltd. <https://doi.org/10.1002/9781444312744.ch43>
 118. Michnov, O., Solomayer, E., Fehm, T., Stubenrauch, F., & Iftner, T. (2012). Knock down of p53 or its ubiquitin ligase E6AP does not affect the sensitivity of human papillomavirus-positive cervical cancer cells to cisplatin. *American Journal of Cancer Research*, 2(3), 309–321. <https://www.ncbi.nlm.nih.gov/pmc/articles/PMC3365809/>
 119. Chuchuy, J., Rogal, J., Ngo, T., Stadelmann, K., Antkowiak, L., Achberger, K., Liebau, S., Schenke-Layland, K., & Loskill, P. (2021). Integration of Electrospun Membranes into Low-Absorption Thermoplastic Organ-on-Chip. *ACS Biomaterials Science & Engineering*, 7(7), 3006–3017. <https://doi.org/10.1021/acsbomaterials.0c01062>
 120. Cai, L., Yang, S., Ding, H., Cai, J., & Wang, Z. (2013). Tumor-associated lymphatic endothelial cell promotes invasion of cervical cancer cells. *APMIS*, 121(12), 1162–1168. <https://doi.org/10.1111/apm.12068>
 121. Lanbeck, P., & Paulsen, O. (2001). Short-Term Effects of Four Antibiotics on DNA Synthesis in Endothelial Cells. *Pharmacology & Toxicology*, 88(4), 204–208. <https://doi.org/10.1111/j.1600-0773.2001.880408.x>
 122. gibco. (2013). *Human Endothelial-SFM*. 1(Publication Number MAN0007352). https://assets.fishersci.com/TFS-Assets/LSG/manuals/HumanEndothelialSFM_man.pdf
 123. Maas-Szabowski, N., Shimotoyodome, A., & Fusenig, N. E. (1999). Keratinocyte growth regulation in fibroblast cocultures via a double paracrine mechanism. *Journal of Cell Science*, 112 (Pt 12), 1843–1853. <https://doi.org/10.1242/jcs.112.12.1843>
 124. Schumacher, M., Schuster, C., Rogon, Z. M., Bauer, T., Caushaj, N., Baars, S., Szabowski, S., Bauer, C., Schorpp-Kistner, M., Hess, J., Holland-Cunz, S., Wagner, E. F., Eils, R., Angel, P., & Hartenstein, B. (2014). Efficient keratinocyte differentiation strictly depends on JNK-induced soluble factors in fibroblasts. *The Journal of Investigative Dermatology*, 134(5), 1332–1341. <https://doi.org/10.1038/jid.2013.535>
 125. Lee, H., Lee, H., & Cho, Y. K. (2017). Cytokeratin7 and cytokeratin19 expression in high grade cervical intraepithelial neoplasm and squamous cell carcinoma and their possible association in cervical carcinogenesis. *Diagnostic Pathology*, 12, 18. <https://doi.org/10.1186/s13000-017-0609-4>
 126. Menz, A., Bauer, R., Kluth, M., Marie von Bargen, C., Gorbokon, N., Viehweger, F., Lennartz, M., Völkl, C., Fraune, C., Uhlig, R., Hube-Magg, C., De Wispelaere, N., Minner, S., Sauter, G., Kind, S., Simon, R., Burandt, E., Clauditz, T., Lebok, P., ... Bernreuther, C. (2021). Diagnostic and prognostic impact of cytokeratin 19 expression analysis in human tumors: A tissue microarray study of 13,172 tumors. *Human Pathology*, 115, 19–36. <https://doi.org/10.1016/j.humpath.2021.05.012>
 127. Ganesan, R., & Rollason, T. P. (2006). Pathology of neoplastic squamous lesions. In *The Cervix* (pp. 301–316). John Wiley & Sons, Ltd. <https://doi.org/10.1002/9781444312744.ch9>

128. Buckley, C. E., & St Johnston, D. (2022). Apical–basal polarity and the control of epithelial form and function. *Nature Reviews Molecular Cell Biology*, 23(8), Article 8. <https://doi.org/10.1038/s41580-022-00465-y>
129. Matlin, K. S., Myllymäki, S.-M., & Manninen, A. (2017). Laminins in Epithelial Cell Polarization: Old Questions in Search of New Answers. *Cold Spring Harbor Perspectives in Biology*, 9(10), a027920. <https://doi.org/10.1101/cshperspect.a027920>
130. Gnecco, J. S., Brown, A., Buttrey, K., Ives, C., Goods, B. A., Baugh, L., Hernandez-Gordillo, V., Loring, M., Isaacson, K. B., & Griffith, L. G. (2023). Organoid co-culture model of the human endometrium in a fully synthetic extracellular matrix enables the study of epithelial-stromal crosstalk. *Med*, 4(8), 554-579.e9. <https://doi.org/10.1016/j.medj.2023.07.004>
131. Mincheva, A., Gissmann, L., & zur Hausen, H. (1987). Chromosomal integration sites of human papillomavirus DNA in three cervical cancer cell lines mapped by in situ hybridization. *Medical Microbiology and Immunology*, 176(5), 245–256. <https://doi.org/10.1007/BF00190531>
132. Rataj, O., Haedicke-Jarboui, J., Stubenrauch, F., & Iftner, T. (2019). Brd4 inhibition suppresses HPV16 E6 expression and enhances chemoresponse: A potential new target in cervical cancer therapy. *International Journal of Cancer*, 144(9), 2330–2338. <https://doi.org/10.1002/ijc.31986>
133. Xu, F., Cao, M., Shi, Q., Chen, H., Wang, Y., & Li, X. (2015). Integration of the full-length HPV16 genome in cervical cancer and Caski and Siha cell lines and the possible ways of HPV integration. *Virus Genes*, 50(2), 210–220. <https://doi.org/10.1007/s11262-014-1164-7>
134. Bekeschus, S., Winterbourn, C. C., Kolata, J., Masur, K., Hasse, S., Bröker, B. M., & Parker, H. A. (2016). Neutrophil extracellular trap formation is elicited in response to cold physical plasma. *Journal of Leukocyte Biology*, 100(4), 791–799. <https://doi.org/10.1189/jlb.3A0415-165RR>
135. Aird, W. C. (2003). Endothelial cell heterogeneity. *Critical Care Medicine*, 31(4), S221. <https://doi.org/10.1097/01.CCM.0000057847.32590.C1>
136. Paik, D. T., Tian, L., Williams, I. M., Rhee, S., Zhang, H., Liu, C., Mishra, R., Wu, S. M., Red-Horse, K., & Wu, J. C. (2020). Single-Cell RNA Sequencing Unveils Unique Transcriptomic Signatures of Organ-Specific Endothelial Cells. *Circulation*. <https://doi.org/10.1161/CIRCULATIONAHA.119.041433>
137. Amersfoort, J., Eelen, G., & Carmeliet, P. (2022). Immunomodulation by endothelial cells—Partnering up with the immune system? *Nature Reviews Immunology*, 22(9), Article 9. <https://doi.org/10.1038/s41577-022-00694-4>
138. Robert, J. (2023). Sex differences in vascular endothelial cells. *Atherosclerosis*, 384, 117278. <https://doi.org/10.1016/j.atherosclerosis.2023.117278>
139. Cipriano, M., Schlünder, K., Probst, C., Linke, K., Weiss, M., Fischer, M. J., Mesch, L., Achberger, K., Liebau, S., Mesquida, M., Nicolini, V., Schneider, A., Giusti, A. M., Kustermann, S., & Loskill, P. (2022). Human immunocompetent choroid-on-chip: A novel tool for studying ocular effects of biological drugs. *Communications Biology*, 5(1), Article 1. <https://doi.org/10.1038/s42003-021-02977-3>
140. Cimpan, A. M., Mazuru, V., Cernii, A., Ceausu, R., Saptefrati, L., Cebanu, A., Fit, A. M., & Raica, M. (2011). Detection of early lymphangiogenesis by lymphatic microvascular density and endothelial proliferation status in preneoplastic and neoplastic lesions of the uterine cervix. *Pathology International*, 61(7), 395–400. <https://doi.org/10.1111/j.1440-1827.2011.02673.x>
141. Loncaster, J. A., Cooper, R. A., Logue, J. P., Davidson, S. E., Hunter, R. D., & West, C. M. L. (2000). Vascular endothelial growth factor (VEGF) expression is a prognostic factor for radiotherapy outcome in advanced carcinoma of the cervix. *British Journal of Cancer*, 83(5), Article 5. <https://doi.org/10.1054/bjoc.2000.1319>
142. Chopra, V., Dinh, T. V., & Hannigan, E. V. (1997). Three-dimensional endothelial-tumor epithelial cell interactions in human cervical cancers. *In Vitro Cellular & Developmental Biology - Animal*, 33(6), 432–442. <https://doi.org/10.1007/s11626-997-0061-y>

143. Zhang, B., Xie, F., Dong, C.-L., Gu, C.-J., Cheng, J., Wang, Y., Xu, X.-Z., Pu, H., Wu, Y.-B., Qi, X.-W., Li, D.-J., Yu, J.-J., & Li, M.-Q. (2017). The cross talk between cervical carcinoma cells and vascular endothelial cells mediated by IL-27 restrains angiogenesis. *American Journal of Reproductive Immunology*, *78*(4), e12706. <https://doi.org/10.1111/aji.12706>
144. Zhuang, Y., Huang, Y., He, Z., Liu, T., Yu, X., & Xin, S. X. (2022). Effect of substrate stiffness on the mechanical properties of cervical cancer cells. *Archives of Biochemistry and Biophysics*, *725*, 109281. <https://doi.org/10.1016/j.abb.2022.109281>
145. Cui, Y., Zhang, X., You, K., Guo, Y., Liu, C., Fang, X., & Geng, L. (2017). Nanomechanical Characteristics of Cervical Cancer and Cervical Intraepithelial Neoplasia Revealed by Atomic Force Microscopy. *Medical Science Monitor : International Medical Journal of Experimental and Clinical Research*, *23*, 4205–4213. <https://doi.org/10.12659/MSM.903484>
146. Villegas-Pineda, J. C., Ramírez-de-Arellano, A., Bueno-Urquiza, L. J., Lizarazo-Taborda, M. del R., & Pereira-Suárez, A. L. (2023). Cancer-associated fibroblasts in gynecological malignancies: Are they really allies of the enemy? *Frontiers in Oncology*, *13*, 1106757. <https://doi.org/10.3389/fonc.2023.1106757>
147. Festen, R. (2007). Understanding Animal Sera: Considerations for Use in the Production of Biological Therapeutics. In *Medicines from Animal Cell Culture* (pp. 45–58). John Wiley & Sons, Ltd. <https://doi.org/10.1002/9780470723791.ch4>
148. van der Valk, J., Bieback, K., Buta, C., Cochrane, B., Dirks, W., Fu, J., Hickman, J., Hohensee, C., Kolar, R., Liebsch, M., Pistollato, F., Schulz, M., Thieme, D., Weber, T., Wiest, J., Winkler, S., & Gstraunthaler, G. (2018). *Fetal Bovine Serum (FBS): Past – Present – Future* [/Dk/atira/pure/researchoutput/researchoutputtypes/contributiontojournal/article]. <https://doi.org/10.14573/altex.1705101>
149. Pilgrim, C. R., McCahill, K. A., Rops, J. G., Dufour, J. M., Russell, K. A., & Koch, T. G. (2022). A Review of Fetal Bovine Serum in the Culture of Mesenchymal Stromal Cells and Potential Alternatives for Veterinary Medicine. *Frontiers in Veterinary Science*, *9*. <https://www.frontiersin.org/articles/10.3389/fvets.2022.859025>
150. Karnieli, O., Friedner, O. M., Allickson, J. G., Zhang, N., Jung, S., Fiorentini, D., Abraham, E., Eaker, S. S., Yong, tan K., Chan, A., Griffiths, S., Wehn, A. K., Oh, S., & Karnieli, O. (2017). A consensus introduction to serum replacements and serum-free media for cellular therapies. *Cytotherapy*, *19*(2), 155–169. <https://doi.org/10.1016/j.jcyt.2016.11.011>
151. Caliarì, S. R., & Burdick, J. A. (2016). A practical guide to hydrogels for cell culture. *Nature Methods*, *13*(5), Article 5. <https://doi.org/10.1038/nmeth.3839>

8. Acknowledgements

I would like to express my sincere gratitude to Prof. Dr. **Peter Loskill**, who has guided my scientific journey with his extraordinary interdisciplinary knowledge, his myriad number of ideas and engaging discussions. I am thankful for the opportunities to participate at numerous international conferences and for the freedom to explore, fail, learn, grow, and eventually succeed. I extend my thanks to Prof. Dr. **Ulrich Rothbauer**, my second advisor, for his genuine interest in the project and his kind, honest and valuable feedback that helped me to advance the project. I appreciate his supervision and examination of this thesis.

Mentoring **Corinna Zimmermann**, **Friederike Floegel**, **Alina Kohler**, and **Alicia Geier** has been a transformative experience. I am grateful for their support, ideas, and contributions to the project. Each team member played a crucial role, from Corinna's early work on cell isolations to Friederike's testing of the cell accumulation technique, Alina's 3D engineering, and Alicia's vast knowledge on neutrophils. Furthermore, I would like to acknowledge Jana Reiser for consistently providing well-constructed chips, distinguished by her steady hand, thoroughness, and flexibility.

After setting up the new laboratories in Tuebingen and working there on my own for a year, I found myself appreciating the exchange and engaging discussions even more when Dr. **Claudia Teufel**, Dr. **Hui-Yu Liu**, and **Adrian Weghofer** joined. Their involvement in connected projects with the same platforms allowed an exchange of ideas on everyday challenges, which contributed to an improved workflow and alleviated the sense of self-doubt. I would like to thank Dr. **Ning Zhang** for his aid in exploring hydrogels. Being part of the international μ Organo team has been an honor, and I am thankful for the ambitious work environment created by highly motivated individuals with interdisciplinary expertise.

I extend my thanks to Jun. Prof. Dr. med. **Martin Weiss** and the **Pathology** department at the Eberhard Karls University Tübingen, along with numerous **donors** who consented to the use of their cervical tissue or blood samples in science. Without their contributions, the project would not have been possible.

I express my heartfelt thanks to my **family** for their unwavering support throughout my academic journey over many years, with continuous encouragement, relentless and genuine concerns, and an everlasting willingness to listen. Last but certainly not least, special acknowledgment goes to **Jan Hodapp**. He not only lent a patient ear during moments of frustration and challenges in the laboratory, but also provided a tidy apartment, clean clothes, and a consistent food supply in the final weeks of experimentation, ensuring I could focus on my work. I miraculously managed to write the paper and this thesis in challenging times, and I owe much of that accomplishment to his unparalleled support.

9. Declaration

Ich erkläre hiermit, dass ich die zur Promotion eingereichte Arbeit mit dem Titel: "Human Cervix In Vitro Models of Healthy, Neoplastic and Cancerous Tissues Based on Organ-on-Chip Technology" selbständig verfasst, nur die angegebenen Quellen und Hilfsmittel benutzt und wörtlich oder inhaltlich übernommene Zitate als solche gekennzeichnet habe. Ich erkläre, dass die Richtlinien zur Sicherung guter wissenschaftlicher Praxis der Universität Tübingen (Beschluss des Senats vom 25.5.2000) beachtet wurden. Ich versichere an Eides statt, dass diese Angaben wahr sind und dass ich nichts verschwiegen habe. Mir ist bekannt, dass die falsche Abgabe einer Versicherung an Eides statt mit Freiheitsstrafe bis zu drei Jahren oder mit Geldstrafe bestraft wird.

Herrenberg, 5. Februar 2024

Elena Kromidas

10. Enclosed Publications

Publication [1]

www.nature.com/scientificreports

**SCIENTIFIC
REPORTS**
nature research

OPEN **WAT-on-a-chip integrating human mature white adipocytes for mechanistic research and pharmaceutical applications**

Julia Rogal^{1,2}, Carina Binder¹, Elena Kromidas^{1,2}, Julia Roosz¹, Christopher Probst¹, Stefan Schneider¹, Katja Schenke-Layland^{2,3,4} & Peter Loskill^{1,2*}

Obesity and its numerous adverse health consequences have taken on global, pandemic proportions. White adipose tissue (WAT) – a key contributor in many metabolic diseases – contributes about one fourth of a healthy human's body mass. Despite its significance, many WAT-related pathophysiological mechanisms in humans are still not understood, largely due to the reliance on non-human animal models. In recent years, Organ-on-a-chip (OoC) platforms have developed into promising alternatives for animal models; these systems integrate engineered human tissues into physiological microenvironment supplied by a vasculature-like microfluidic perfusion. Here, we report the development of a novel OoC that integrates functional mature human white adipocytes. The WAT-on-a-chip is a multilayer device that features tissue chambers tailored specifically for the maintenance of 3D tissues based on human primary adipocytes, with supporting nourishment provided through perfused media channels. The platform's capability to maintain long-term viability and functionality of white adipocytes was confirmed by real-time monitoring of fatty acid uptake, by quantification of metabolite release into the effluent media as well as by an intact responsiveness to a therapeutic compound. The novel system provides a promising tool for wide-ranging applications in mechanistic research of WAT-related biology, in studying of pathophysiological mechanisms in obesity and diabetes, and in R&D of pharmaceutical industry.

The global obesity pandemic poses one of today's biggest challenges to public health. Each year, 2.8 million people die from causes related to overweight or obesity¹. Since the 1970s, the worldwide prevalence of obesity has nearly tripled, also leading to an upsurge in associated comorbidities such as type 2 diabetes (Fig. 1a)². Future projections reveal the gravity of this public health crisis: the prevalence rates of childhood obesity are increasing at an alarming pace³, and by 2030, more than 50% of U.S. adults are predicted to be obese⁴. White adipose tissue (WAT) is the principal organ in obesity. In healthy human adults, WAT comprises approximately 20–25% of the total body mass, thus constituting the second largest organ, after the skin. In obese individuals, WAT's contribution to the total body mass may become as high as 50% (Fig. 1b)⁵.

WAT is tightly involved in the two most important functions of an organism – energy homeostasis and reproduction⁶. In energy homeostasis, not only does WAT act as the main storage site of excess dietary energy (Fig. 1c), it also performs crucial endocrine and metabolic functions (Fig. 1d)^{7,8}. WAT can sense the body's energy status, and respond appropriately, either by storing fuel, in the form of triacylglycerides, or by releasing it as glycerol and fatty acids, for ultimate delivery to organs in need. While this classically described role of WAT already entailed extensive crosstalk between WAT and other organs, its inter-organ communications extend beyond simple feedback loops activated by fed- or fasted states. Endocrine functions of white adipocytes, and other WAT-resident cells in the stromal vascular fraction, are performed by the release of a variety of adipokines (adipose-associated

¹Fraunhofer Institute for Interfacial Engineering and Biotechnology IGB, Nobelstrasse 12, 70569, Stuttgart, Germany. ²Department of Women's Health, Research Institute for Women's Health, Eberhard Karls University, Calwerstrasse 7, 72076, Tübingen, Germany. ³NMI Natural and Medical Sciences Institute at the University of Tübingen, Markwiesenstr. 55, 72770, Reutlingen, Germany. ⁴Department of Medicine/Cardiology, Cardiovascular Research Laboratories, David Geffen School of Medicine at UCLA, 675 Charles E. Young Drive South, MRL 3645, Los Angeles, CA, USA. *email: peter.loskill@igb.fraunhofer.de

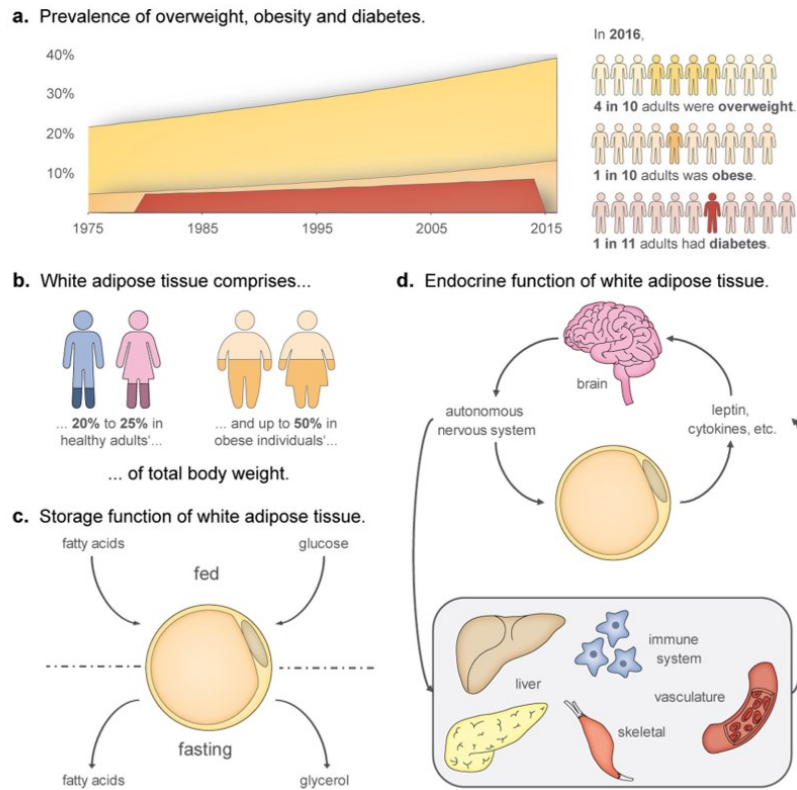


Figure 1. Relevance of research on WAT. (a) The worldwide prevalence of obesity has nearly tripled since 1975; in 2016, almost 40% of adults aged 18 and over could be classified as overweight, 13% of them were even obese. This developments has coincided with a rising prevalence of diabetes, which in 2016 affected approximately 9% of adults worldwide. T2DM – the most prevalent form of diabetes – often develops during chronic positive energy balance, e.g., by a combination of excessive energy intake and physical inactivity^{1,2}. (b) WAT’s contribution to body mass is 20–25% in healthy individuals, and up to 50% in the obese³. (c) Traditional view of WAT as an organ primarily for energy storage. (d) Additional, modern-day concepts of WAT functionality, including extensive endocrine functions.

cytokines) which affect the functioning of the brain, liver, pancreas and immune system⁹. Besides managing nutritional homeostasis, WAT contributes to the regulation of the hypothalamic-pituitary-gonadal axis by secreting and metabolizing sex steroids⁷. Especially adipose tissue intracrinology, i.e., the modulation of sex steroid levels by significant numbers of locally expressed enzymes that activate, convert, or inactivate circulating steroid hormones, plays important roles in human reproductive function^{7,10,11}. Given its prominent endocrine functions and extensive cross-talk with other organs, it comes as little surprise that abnormal amounts, or altered functioning of WAT may result in wide-ranging disorders, including hepatic and cardiovascular diseases^{12,13}, diabetes and cancer^{14–16}.

In line with its important roles in metabolism, inflammation and cancer, WAT has emerged as a drug target with major therapeutic potential for a variety of diseases^{17–19}. Additionally, storage metabolism by WAT can have a major impact on the efficacy of drug therapies, such as those for cardiovascular diseases and cancer^{20,21}. For instance, adipocytes may metabolize and inactivate the chemotherapeutic Daunorubicin²¹, which strongly affects the efficacy of this anticancer therapeutic. Furthermore, the capacity of WAT to sequester hydrophobic compounds, gives the tissue a prominent role in absorption, distribution, metabolism, and excretion (ADME) processes.

Even though WAT plays such a significant role in many diseases, surprisingly little is known about pathophysiological processes of WAT, especially when considering the ever-increasing prevalence of obesity and its co-morbidities. An important reason for this lacking insight is that mechanistic studies in humans often involve

unacceptable health risks. Hence, most research depends on clinical observation, genome-wide association studies (GWAS) as well as animal studies²². Although animal models have led to many insights in obesity and diabetes, they often are lacking in predictive validity for human body functioning, first because of important species differences in nutrition and metabolism, and second because the distinct, unique physiological and pathophysiological roles of WAT in humans²³. Alternatively, conventional, cell culture-based *in vitro* models have been widely utilized and are significantly less controversial ethically. Typically, researchers have used a variety of cell sources, ranging from (immortalized) murine, to primary human (pre-)adipocytes, each featuring distinct advantages and limitations²⁴. *In vitro* differentiation of adipogenic progenitor cells, i.e., either pre-adipocytes or multipotent stem cell lines, or (induced) pluripotent stem cells, is often the method of choice due to the availability of donor-specific information, and the capacity of these cells to undergo expansion and cryopreservation while retaining their characteristic fat depot. Yet, the *in vitro* use of differentiated adipocytes has two major drawbacks: unlike their *in situ* matured congeners, (i) their lipid contents never reach a state of unilocularity, but remain distributed among multiple small lipid vacuoles, and (ii) their gene expression and secretome differs significantly in the relative proportions of adipose-associated hormones^{25–27}. Both phenomena reflect a pre-mature state of the *in vitro* differentiated adipocytes, which strongly suggests that mature human adipocytes provide the best recapitulation of a mature human adipocyte physiology. Yet, the *ex vivo* culture of primary human adipocytes is extremely challenging, due to issues with the cells' buoyancy, fragility and de-differentiation, which so far have hindered development of robust protocols for long-term culturing. Similarly, studies using whole WAT explants are restricted to short culture durations. Additionally, inter-individual variability complicates the interpretation of study results based on samples from different donors²⁸.

Overall, it is of utmost importance to develop microscale platforms that provide microphysiological environments for the long-term culture of white adipocytes in structures that may recapitulate *in vivo* physiology, and functionality based on a minimal amount of cells. By combining modern techniques in microfabrication, biomaterials and tissue engineering, organ-on-a-chip technology has enabled the construction of promising platforms for mechanistic and pharmaceutical studies, that have great potential for disease modeling as well as the optimization of personalized medical treatments of obesity and diabetes^{29–32}. The integration of tissues with *in vivo*-like structure and functionality in perfused microenvironments is of particular interest when studying endocrine tissues and multi-factorial diseases, due to the possibility to combine individual chips into multi-organ systems^{33,34}. However, although organ-on-a-chip research has burgeoned in recent years, and numerous platforms have been developed for many organs and tissues, WAT appears to have been largely overlooked, and only a few relevant efforts have been undertaken²⁵. Several research groups injected pre-adipocytes from murine^{35,36} or human^{37–39} sources into microfluidic chambers, and were able to subsequently induce adipogenesis. Others directly introduced primary adipocytes from mice into mesoscopic, perfused reservoirs⁴⁰. In a recently introduced elegant approach, Harms *et al.* cultured mature human white adipocytes in multiwell plates underneath membranes in a transwell format⁴¹. All of these innovative approaches, however, did not enable the generation of human white adipose tissue-like structures with *in vivo*-like physiology.

Here, we present the first OoC platform that integrates human primary mature adipocytes into a perfused microfluidic chip. The human WAT-on-a-chip consists of multiple, tissue-specific chambers that are fluidically connected to a vasculature-like microchannel, while being shielded from the shear forces of the perfusion fluid. Using specifically tailored isolation and injection protocols, 3D microtissues based on freshly isolated adipocytes are generated inside a series of individual chambers. Thus, a large number of independent replicate cell cultures from individual donors can be produced and kept viable – as well as functional – for over one month. By analyzing media effluents and taking advantage of the optical accessibility of the tissue chambers, the patency of cells as well as key cell-physiological aspects, e.g., fatty acid metabolism and drug responsiveness, could be monitored successfully.

Materials and Methods

Fabrication and characterization of microfluidic platforms. *Chip fabrication by soft lithography and replica molding.* The microfluidic platform is a custom-designed three-layered hybrid device featuring two micro-patterned polydimethylsiloxane (PDMS; Sylgard 184, Dow Corning, USA) layers, which are separated by an isoporous semipermeable membrane. The media channel and tissue chamber microstructures in the PDMS slabs were generated using two differently patterned master wafers that served as positive molding templates. The intricately structured masters were fabricated by commonly used photolithographic processes described previously³⁶. The chips' PDMS structures were created using two different molding techniques: standard molding to obtain thicker slabs with closed structures, and exclusion molding to obtain thin layers with open structures (cf. "Replica molding of PDMS parts" in the supplements section). To prepare the semipermeable membranes, commercially available polyethylene terephthalate (PET) membranes ($r_p = 3 \mu\text{m}$; $\rho_p = 8 \times 10^5$ pores per cm^2 ; TRAKETCH® PET 3.0 p S210 \times 300, SABEU GmbH & Co. KG, Northeim, Germany) were functionalized by a plasma-enhanced, chemical vapor deposition (PECVD) process (cf. "Membrane functionalization" in the supplements section). In a final step, chips were assembled in three subsequent O_2 -plasma activation (15 s, 50 W; Diener Zepto, Diener electronic GmbH + Co. KG, Ebhausen, Germany) and bonding steps, followed by an overnight exposure to 60 °C for bonding enhancement (cf. "Chip assembly" in the supplements section).

Chip preparation for experiments. On the day before cell injection, chips were O_2 -plasma sterilized (60 s, 50 W) and subsequently filled with Dulbecco's phosphate-buffered saline without MgCl_2 and CaCl_2 (PBS^- ; Sigma-Aldrich Chemie GmbH, Steinheim, Germany), under sterile conditions. Then, the PBS^- filled chips were kept overnight at 4 °C in PBS^- to allow evacuation of residual air from the channel systems.

Numerical modeling. To model fluid flow and transport of a diluted species, COMSOL Multiphysics (COMSOL, Stockholm, Sweden) software was used. The process was based on a numerical model which was previously published for our previous murine WAT-on-a-chip³⁰. Briefly, the incompressible stationary free fluid flow was modeled by the Navier-Stokes equation with the properties of water (dynamic viscosity $\mu = 1 \times 10^{-3} \text{ m}^2/\text{s}$, density $\rho = 1000 \text{ kg/m}^3$) at a flow of 20 $\mu\text{l/h}$. Fluid flow from the media channel through the isoporous membrane into the tissue channel was modeled using Darcy's law (porosity = 0.056, hydraulic permeability $\kappa = 1.45 \times 10^{-14} \text{ m}^2$). The transport of diluted species was described by the time-dependent convection-diffusion with a diffusion coefficient $1 \times 10^{-9} \text{ m}^2/\text{s}$ and an initial concentration of 1 mol/m³.

Diffusive transport. To visualize diffusion of compounds from the media microchannels over the isoporous membrane into the tissue chamber inside the microfluidic platform, we monitored the perfusion of a 0.5 mg/ml fluorescein isothiocyanate-dextran (FITC-dextran; 150 kDa, 46946, Sigma-Aldrich Chemie GmbH) solution in PBS⁻ in the system. Prior to the diffusion experiment, the tissue chambers were filled with the collagen hydrogel matrix commonly used to encapsulate the adipocytes (cf. "Injection of human mature adipocytes into the microfluidic platform"). The flow rate was set to 40 $\mu\text{l/h}$ and the fluorescence intensity was measured every 6.2 s for three positions in the chip – the media channel, the top of the underlying tissue chamber, as well as the bottom of the same tissue chamber.

Isolation and culture of primary human adipocytes. *Human tissue samples.* Human adiposetissue biopsies were obtained from plastic surgeries performed by Dr. Ulrich E. Ziegler (Klinik Charlottenhaus, Stuttgart, Germany), approved by the local medical ethics committee: Patients gave an informed consent according to the permission of the "Landesärztekammer Baden-Württemberg" (IRB#: F-2012-078; for normal skin from elective surgeries). All procedures were carried out in accordance with the rules for medical research of human subjects, as defined in the Declaration of Helsinki. All primary mature adipocytes were isolated from biopsies that were taken from female, pre-obese donors (BMI 25.0 - 29.9, as per the WHO classification), aged 45 to 55.

Isolation of primary human adipocytes. Primary mature adipocytes were isolated from subcutaneous adipose tissue samples. The isolation protocol was performed as previously described^{42,43}, with slight modifications. In brief, the subcutaneous adipose tissue was rinsed twice with Dulbecco's phosphate buffered saline with MgCl₂ and CaCl₂ (PBS⁺; Sigma-Aldrich Chemie GmbH), and visible blood vessels, as well as connective-tissue structures, were thoroughly removed. The remaining adipose tissue was cut into fine pieces of approximately 1 cm³, and digested with a collagenase solution [(0.13 U/ml collagenase type NB4 (Serva Electrophoresis GmbH, Heidelberg, Germany) in Dulbecco's Modified Eagle Medium (DMEM/Ham's-F12; Thermo Fisher Scientific, Waltham, USA), with 1% bovine serum albumin (BSA; Sigma-Aldrich Chemie GmbH)] for 60 min at 37 °C on a rocking shaker (50 cycles/min; Polymax 1040, Heidolph Instruments GmbH & Co. KG, Schwabach, Germany). Next, the digested tissue was passed through cell strainers (mesh size: 500 μm), and subsequently washed three times with DMEM/Ham's-F12. For each washing step, adipocytes and medium were mixed, and left to rest for 10 min to allow separation of the buoyant adipocytes and the medium; this was followed by aspiration of the liquid media from underneath the packed layer of adipocytes.

Injection of human mature adipocytes into the microfluidic platform. Immediately after the isolation of white adipocytes from tissue samples, the adipocytes were prepared for injection into the microfluidic platforms. Sixty μl of densely packed adipocytes were mixed with 24 μl of a dispersion of 10 mg/ml collagen type 1 (from rat, provided by Fraunhofer IGB), 6 μl neutralization buffer [DMEM/Ham's-F-12 (10 \times); Biochrom GmbH, Berlin, Germany], and 50 mM NaOH in Aqua dest (1:1) with 0.2 M NaHCO₃ and 0.225 M HEPES (Carl Roth GmbH + Co. KG, Karlsruhe, Germany)] and immediately injected into the chip's tissue-chamber system by manual pressure. Each system of connected tissue chambers was loaded individually at a steady pace, to ensure that the collagen hydrogel reached the tissue chambers before the onset of gelation.

On-chip culture of adipose tissue. During on-chip culturing, the WAT-chips were maintained in a humidified incubator at 37 °C and a 5% CO₂ atmosphere. The adipocytes were supplied with a 20–40 $\mu\text{l/h}$ flow of Subcutaneous Adipocyte Maintenance Medium (AM-1; BioCat GmbH, Heidelberg, Germany) maintained by positive pressure from an automated syringe pump (LA-190, Landgraf Laborsysteme HLL GmbH, Langenhagen, Germany). Under sterile conditions, media reservoirs were re-filled with fresh media every other day, and the media effluents were collected from the media-systems' outlets once every 1–2 days (depending on the experiment), and stored at –80 °C for subsequent analysis of metabolites.

Structural and functional characterization of on-chip adipose tissues. *Fluorescent double staining of intracellular lipid vacuoles and nuclei.* To visualize the structure of on-chip adipose tissues, intracellular lipid vacuoles and nuclei were stained using the neutral lipid stain BODIPYTM 493/503 (4,4-Difluoro-1,3,5,7,8-Pentamethyl-4-Bora-3a,4a-Diaza-s-Indacene; D3922, Thermo Fisher Scientific) and 4',6-Diamidin-2-phenylindol (DAPI; D8417, Sigma-Aldrich Chemie GmbH). All fixation- and staining solutions were flushed through the chip at a rate of 80 $\mu\text{l/h}$ by a syringe pump. The in-chip adipocytes were fixed overnight with 4% phosphate-buffered formaldehyde solution (Roti[®]-Histofix 4%, P087, Carl Roth GmbH + Co. KG). Next, permeabilization was achieved by flushing the chip for 3 h with PBST [PBS⁺ with 0.1% Tween-20 (P7949, Sigma-Aldrich Chemie GmbH)]. Then, the fluorescence staining solution – PBST with 1 $\mu\text{g/ml}$ BODIPYTM 493/503 and 1 $\mu\text{g/ml}$ DAPI – was pumped through the system for 2 h, and finally washed out with PBS⁺ for at least 30 min to remove residual staining solution. To stain explants, chunks of approximately 100 mm³ were cut off from the biopsy, washed with PBS⁺ twice and fixed for 1 h with 4% phosphate-buffered formaldehyde solution.

Afterwards, the fixed explants were washed with PBS⁺, permeabilized and stained as described above (1 h of incubation time for each step). Finally, the explants were washed three times in PBS⁺ to remove residual staining solution and stored in PBS⁺ until imaging.

Imaging of the stained adipocytes was performed and processed by a laser scanning microscope (Zeiss LSM 710, Carl Zeiss, Oberkochen, Germany) with specialized software (ZEN 2012 SP1 (black edition), Release Version 8.1)).

Live/dead staining of integrated white adipose tissue. To assess the viability of the adipocytes on-chip, a live/dead-assay based on fluorescein diacetate (FDA; F1303, Thermo Fisher Scientific) and propidium iodide (PI; P3566, Thermo Fisher Scientific) was performed. Prior to staining, the culture medium was removed from the chip by flushing the media channels with PBS, using gravitational flow. The staining solution containing FDA (final concentration 27 µg/ml) and PI (final concentration 135 µg/ml) diluted in PBS, was flushed into the media channel by gravitational flow, and incubated for 25 min in a humidified incubator at 37 °C and 5% CO₂. The staining solution was then removed by flushing PBS through the media channels using gravitational flow. Right after that, imaging was performed by an inverted fluorescence microscope (Leica DMi8, LEICA Microsystems GmbH, Wetzlar, Germany).

Monitoring and analysis of fatty acid uptake and release. For online monitoring of fatty acid uptake by the adipocytes, 4 µM of the fluorescently-labeled fatty acid analog, BODIPY[™] 500/510 C1, C12 (4,4-Difluoro-5-Methyl-4-Bora-3a,4a-Diaza-s-Indacene-3-Dodecanoic Acid; D3823, Thermo Fisher Scientific), was added to the culture medium for a duration of 60 min and pumped through the media systems at 80 µl/h via positive pressure provided by a syringe pump. Next, the culture medium was switched to AM-1 only, to visualize the release of the fluorescent fatty acid analog. During the experiment, the chips were placed under complete darkness in an incubator chamber that was fitted to the microscope stage, and set to 37 °C. Imaging was performed using the inverted Leica DMi8 fluorescence microscope. During the 120 min running time of the experiment, images of both bright-field (BF) and FITC-channels were captured every two minutes from each tissue chamber on the chip. As a reference, each position was imaged at time point 0 min (t₀).

To quantify the patterns of fluorescence intensity during the uptake and release of the fluorescent fatty acid analog, the mean gray value of the fluorescence of the individual tissue chambers and the fluorescence of the background were measured for each time point using ImageJ 1.50i software (National Institute of Health, Bethesda, USA). After subtracting the background levels from the fluorescence intensities measured in the chambers, the offset was calculated by setting the intensity measured at t₀ to a fluorescence intensity of 0 A.U. Then, the intensities for each chamber were expressed as a percentage of the highest recorded intensity from that chamber during the experiment. Note: Normalization on the chamber-level was considered to be necessary, because the amount of injected adipocytes varied between the chambers with the used WAT-chip design.

Responsiveness to β-adrenoreceptor agonistic drugs. To assess the effect of β-adrenergic agonist drugs on fatty acid metabolism, AM-1 medium was supplemented with 10 µM isoproterenol hydrochloride (16504, Sigma-Aldrich Chemie GmbH). Fluorescence intensity was measured for 60 min with, and then for 60 min without addition of 4 µM BODIPY[™] 500/510 C1, C12 to the conditioned medium at 37 °C with an inverted fluorescence microscope (LEICA DMi8, LEICA Microsystems GmbH) to assess the dynamics of fatty acid uptake and release. Measurement and analysis of fluorescence was performed as described above.

Non-invasive analysis of cytotoxicity from media effluents. The release of lactate dehydrogenase (LDH) was quantified from the media effluents to non-invasively assess the adipocytes' on-chip viability. The medium effluents were collected for a sampling time of 24 h on different days of on-chip culture. For analysis of the medium effluents, we used the CytoTox 96[®] Non-Radioactive Cytotoxicity Assay (G1780; Promega GmbH, Walldorf, Germany) and followed the manufacturer's instructions for performing the assay in a 384-well plate format. This assay allows for colorimetric the detection of necrotic and late-stage apoptotic cells. For a Target Cell Maximum LDH Release Control, adipocytes were injected into two chips as described above. After injection, the adipocytes were perfused with lysis buffer for 2 h until all adipocytes were lysed. The mean of the acquired absorbance was assumed to be the maximum LDH release possible for the given experimental setup including chip design and adipocyte donor. All other acquired LDH data were normalized to this value.

Analysis of adipose-associated metabolites. The non-esterified fatty acid (NEFA) contents of medium effluents were determined by enzymatic analysis, using the ACS-ACOD-MEHA method (NEFA-HR(2) Assay, FUJIFILM Wako Chemicals Europe GmbH, Neuss, Germany). Effluents were thawed and centrifuged at 10,000 × g for 10 min. Then, 25 µl of sample [i.e. the effluents' supernatant, or AM-1 as blank, or oleic acid for a standard curve (270-77000, FUJIFILM Wako Chemicals Europe GmbH)] were supplemented with 100 µl of the R1 solution (434-91795, FUJIFILM Wako Chemicals Europe GmbH) and 50 µl of the R2 solution (436-91995, Wako Chemicals GmbH), incubating 10 min at 37 °C after each addition. NEFA concentrations were determined by measuring absorbance at 550 nm (Infinite[®] 200 PRO, Tecan Trading AG, Switzerland). To assess the influence of albumin on NEFA release, 0.2% human serum albumin (HSA; A1653, Sigma-Aldrich Chemie GmbH) was added to the culture medium for 24 h. To ensure that increases in the measured NEFA concentrations could not be attributed to the presence of HSA during assay performance, we performed NEFA-measurements on the oleic acid standard with and without HSA. No differences were observed in the detected NEFA-concentration between the two conditions (Fig. S4).

As another readout for lipolysis, glycerol concentrations were determined using a colorimetric assay. Media effluents were thawed and centrifuged at 10,000 × g for 10 min. Then, 40 µl of sample [i.e. the effluents' supernatants, or AM-1 as blank, or Glycerol Standard Solution for a standard curve (G7793, Sigma-Aldrich Chemie

GmbH)] were supplemented with 60 μ l of the Free Glycerol Reagent (F6428, Sigma-Aldrich Chemie GmbH). After a 5-min incubation at 37 °C, absorbance at 540 nm was recorded.

Statistical analysis. All graphs show raw data means \pm standard deviation (unless otherwise indicated). We annotated or sample size n as follows:

- For analyses pertaining to data at tissue chamber level (e.g. from fatty acid transport assays), n denotes the number of tested tissue chambers.
- For analyses pertaining on tissue system level only, i.e., the collectivity of eight chambers connected via one media channel, (e.g. metabolite measurements), n denotes the number of tested tissue systems.

For statistical analysis of differences, we performed independent two-sample t -tests using OriginPro 2018 software (OriginLab, Northhampton, MA, USA). Unless otherwise indicated, a p -value threshold for significance of 0.05 was used.

Results and Discussion

Concept and characterization of the microfluidic platform. In order to generate a microphysiological environment capable of generating a human WAT-model, and maintaining tissue viability and functionality during long-term culture, we developed a specifically tailored microfluidic platform featuring a footprint comparable to the size of a stamp (2×2 cm). The essential features of the platform, depicted in Fig. 2a, are 3D-tissue chambers and perfusable microchannels that are separated by an isoporous membrane. Each chip platform houses two identical, independent systems each featuring eight individual tissue chambers. All tissue chambers are located at the end of individual branches of a main channel, which can be accessed via a common inlet for cell injection. The tissue chambers are specifically designed to accommodate adipose tissue, particularly its large-sized, fragile and buoyant adipocytes: they are cylindrical structures with a diameter of 720 μ m and a height of 200 μ m. The tissue-chamber microstructures are encased by transparent glass (cover slip or microscope slide) at the bottom, enabling easy visual inspection of the tissues with most current types of microscope, and by an isoporous membrane on the top side. The membrane was specifically functionalized (Supplement S2) to ensure a tight sealing of chip components, and to provide a porous barrier to the adjacent media microchannels. The channels can be connected to external devices (e.g. syringe- or peristaltic pumps), to achieve a vasculature-like perfusion with media. This allows for a precisely controllable convective transport of nutrients, metabolites, and other dissolved molecules towards, as well as away from, the tissue chambers, mimicking the *in vivo* circulation of blood. It also opens up the possibility to administer compounds with high temporal resolution. The membrane further ensures that convective transport is restricted to the media channels, thereby shielding the tissue chambers from non-physiological shear forces (Fig. 2b). Through the micropores, dissolved molecules may diffuse quickly in and out of the tissue chambers, as confirmed by computational modeling and by dynamic tracking of a fluorescent dye in different channel- and chamber locations (Fig. 2b). In sum, the membrane constitutes an endothelial-like barrier that separates perfused media from the chip-embedded tissues. Although this artificial barrier admittedly does not recapitulate active transport processes occurring *in vivo*, it does provide a potential scaffold for the inclusion of endothelial cells in future generations of the platform.

Generation and functional validation of human white adipose tissue on-chip. Two major difficulties of mature adipocytes – their buoyancy and fragility – have traditionally hampered the *in vitro* culture of WAT. We developed specifically optimized cell-isolation and -injection protocols to enable the integration of freshly isolated, mature primary adipocytes from humans into the tissue chambers of our microphysiological platform. By suspending the isolated cells into a collagen hydrogel before injection, their viability and integrity could be preserved. The use of the hydrogel ensures both the protection and the 3D arrangement of the fragile cells during the formation of the microtissue. Moreover, the hydrogel and the location of the cell-injection inlets on the bottom of the tissue chambers (Figs. 2a and 3) help to overcome the issue of adipocyte buoyancy. Successful cell loading generates 8 independent, parallel 3D WAT-like microtissues per system (and 16 per platform).

Due to the microscale footprints of chambers and platform, only a small number of cells are required per chamber. This is of particular importance, as the tissues are based on primary, non-proliferating cells, and multiple chips (independent replicates) can be loaded with cells from a single biopsy, enabling testing under multiple experimental and control conditions of microtissues from the same donor. This is of crucial advantage when dealing with inter-donor variability, while it also enables patient-specific experiments.

Structural analysis of adipocytes on-chip. To investigate the structural arrangement of the generated adipose tissue, we established a staining protocol that enabled the on-chip visualization of intracellular lipid vacuoles using a neutral lipid stain. After six days of on-chip culturing, confocal imaging confirmed the formation of dense, 3D tissues composed of large unilocular adipocytes (Fig. 3a). The observable, mature phenotype of adipocytes suggests that the tissue-generation and -culture methods were capable of creating and maintaining physiological microenvironments and conditions. Inappropriate culture conditions have been frequently reported to induce cell dedifferentiation^{43,44} which would lead to highly proliferative dedifferentiated fat cells (DFAT) with multilineage character⁴⁵. One of the first hallmarks of dedifferentiation is the re-organization of lipids into multiple lipid droplets (i.e., a multilocular phenotype) and an increased rate of lipolysis⁴⁴.

Moreover, we analyzed the microfluidic platform for a potential selectivity in terms of adipocyte structure by comparing the size of the lipid vacuoles of adipocytes on-chip to that of the respective donor-specific explants (Fig. 3b). Due to the unilocularity of mature adipocytes, determining lipid droplet size is an indirect measure for the adipocytes' size. The quantitative analysis revealed that both average size as well as the distribution of

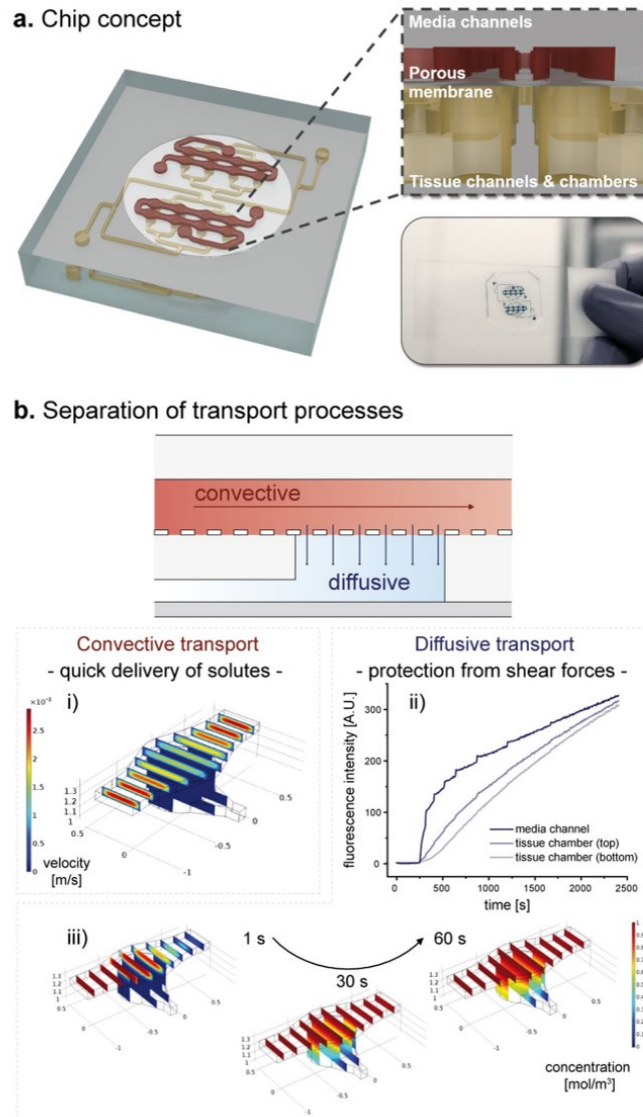


Figure 2. Concept of the microphysiological platform and microfluidic perfusion. **(a)** Schematic of the chip platform featuring two independent systems with eight tissue chambers each. As shown in the cross-sectional zoom-in, tissue chambers, which feature tissue channel inlets at the bottom, are located right below the perfusable media channels, and separated from them by a microporous membrane. **(b)** During flow, the chip's circuitry imposes a separation of the two transport processes, convection and diffusion. Convective flow is confined to the vasculature-like media channels, as confirmed by computational modeling (i). The tissue chambers are supplied by a diffusive transport as confirmed by observable diffusion of a fluorescent dye from the media channel into a hydrogel-filled tissue chamber (ii), as well as by computational modeling (iii).

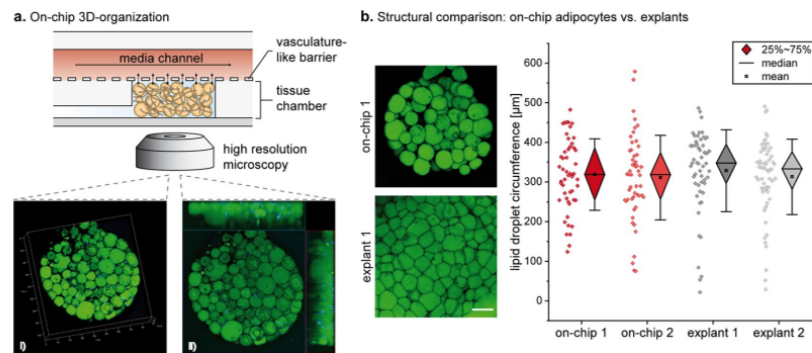


Figure 3. Structural characterization of human WAT-on-a-chip. **(a)** On day 6 of on-chip culture, intracellular lipid vacuoles (green; neutral lipid stain BODIPY[™] 493/503) and nuclei (blue; DAPI) were visualized by confocal imaging. As shown by a 3D-rendered Z-stack of one WAT-chamber (i) (steps on the scale in 100 µm) and the corresponding maximum intensity projection with two sectional planes (ii), the individual adipocytes were unilocular and formed a densely packed 3D microtissue throughout the tissue chamber. **(b)** Comparison of lipid vacuole size of adipocytes on-chip versus explants (two replicates per condition). Scale bar equals 150 µm.

individual cell sizes are very similar between explant and on-chip culture. This indicates that the WAT-on-a-chip does indeed recapitulate the morphological heterogeneity of mature adipocytes in WAT *in vivo*.

Validation of adipocyte functionality on-chip. To assess the capability of the WAT-on-a-chip system to maintain viability and functionality of the integrated tissues, we deployed a comprehensive toolbox of chip-specific, functional readout methods. First, the viability and integrity of the vast majority of cells after eight days of on-chip culture was confirmed using a FDA/PI-based live/dead-staining protocol tailored specifically for the chip's configuration (Fig. 4a). In addition, to verify that the objective of any microphysiological OoC system – the recapitulation of *in vivo* functionality – was indeed attained, we examined multiple functional endpoints. Taking advantage of the optical accessibility and continuous medium perfusion through our system, we performed non-invasive imaging and analysis of media effluents under several conditions.

To monitor fatty acid metabolism in real-time, we added the fluorescently tagged fatty dodecanoic acid (C₁₂H₂₄O₂) analog (BODIPY[™] 500/510 C1, C12) to the perfusion medium, and characterized the dynamics of fatty acid influx into, and efflux from, the WAT-model. This assay represents a powerful tool that allows non-invasive assessment of the cellular uptake of fatty acids, their accumulation in intracellular lipid vacuoles, and their release from adipocytes when the fatty-acid analog is removed from the medium. Utilizing time-resolved fluorescence microscopy, we were able to observe these characteristic uptake and secretion kinetics in the adipocytes cultured on-chip (Fig. 4b).

The continuous, convective transport by the perfusion flow of metabolized and secreted factors away from the tissues, provides opportunities for effluent sampling in a time-resolved manner, allowing the dynamics of e.g. metabolism, secretion, and endocrine functionality to be measured. Using colorimetric assays, we characterized the levels of oleic acid, a representative of non-esterified fatty acids (NEFAs), and of glycerol in the effluent medium, and found that their concentrations remained very stable for several days of culturing (Fig. 4c). The measured NEFA and glycerol levels were comparable to levels from human subcutaneous adipose tissue explants immediately after biopsy⁴⁶. In a similar approach, we examined the impact on fatty acid release of a 0.2 (w/v)% supplementation of the perfusion medium with human serum albumin (HSA). After 24 h of perfusion, we observed a significant increase of NEFA levels in the effluent (Fig. 4d). Thus, in our system, effluent sampling provided a powerful, non-invasively obtained readout of secretome and metabolome dynamics with high temporal resolution (depending on the sensitivity of the employed assay). This constitutes an effective link for the cross-correlation with clinical data and biomarker development. The general applicability of effluent sampling, however, is restricted by the base material PDMS, which is utilized for the majority of microfluidic platforms and also for our WAT-on-a-chip. The major limitation of many polymers and especially PDMS is the absorption of small hydrophobic molecules, which is especially an issue in microfabricated devices due to the large surface-to-volume ratio⁴⁷. Hence, many hormones as well as adipokines can partition into the polymer leading to an uncontrolled reduction of their concentration in the effluent down to undetectable amounts. This is, for instance, the case for the important adipokine adiponectin (Supplement S5). To account for this, future generations of the WAT-chip are envisioned to employ alternative materials or surface coatings.

Long-term functionality of integrated white adipose tissue. One of the main challenges of conventional adipocyte *in vitro* culture is the long-term maintenance of functional stability. As discussed above, issues related to buoyancy, fragility and de-differentiation of adipocytes typically limit the duration of integrity of *in vitro* cultures to a couple of days at most^{46,48}. Our structural and functional characterization of the

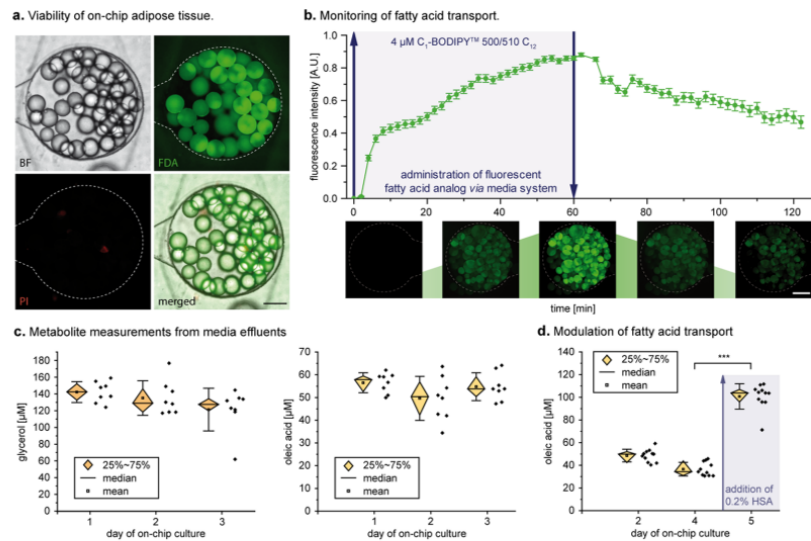


Figure 4. Functional validation of the human WAT-on-a-chip. **(a)** Live/dead-staining of adipocytes on day 8 of on-chip culture. FDA (green) marks live adipocytes by confirming membrane integrity and esterase activity in the vast majority of the integrated adipocytes. PI (red) staining indicates a very low number of apoptotic/necrotic and dead adipocytes. Scale bar equals 150 μm . **(b)** On-line monitoring of fatty acid transport on day 6. Monitoring of fatty acid uptake and accumulation was realized by the addition of a fluorescent fatty acid analog (4 μM BODIPYTM 500/510 C1, C12) to the perfused medium for one hour, followed by measurement of the mean fluorescence intensity. Upon removal of the fatty acid analog from the medium, fatty acid release could be observed (n = 47 individual tissue chambers). Scale bar equals 150 μm . **(c)** Evaluation of fatty acid metabolites in media effluents. Using colorimetric assays, glycerol and oleic acid (representative of non-esterified fatty acids) concentrations were found to be stable for the first three days of on-chip culture (n = 8 systems with 8 tissue chambers each). **(d)** Upon addition of 0.2% w/v human serum albumin (HSA) to the culture medium for 24 h, fatty acid release significantly increased compared to that during previous days (p < 0.005; n = 11 systems with eight tissue chambers each).

WAT-on-a-chip indicated that this microphysiological platform is capable of maintaining stable culture conditions over prolonged time periods. However, to investigate the potential of the platform to support a robust, long-term culture, we non-invasively monitored cell viability for a culture time of 36 days (Fig. 5a) by analyzing the release of lactate dehydrogenase (LDH) to the medium effluents. Throughout the culture, LDH levels were below 5% of LDH levels measured in the target cell maximum LDH release control (positive control) indicating a good overall on-chip viability. These findings were further supported by a live/dead-staining performed as an endpoint analysis of the long-term culture. To additionally investigate the long-term functionality, we performed fatty acid uptake assays on the tissues after 6 days, as well as after 36 days of on-chip culture (Fig. 5b). We observed that even after more than a month of *in vitro* culture, adipocytes still showed functional uptake and accumulation of fatty acids. Interestingly, a difference in initial uptake rates emerged, which might be related to size limitation of the “long-term-fed” cells on day 36. Still, these findings highlight that the WAT-on-a-chip is indeed capable of maintaining the functionality of adipose tissue for much longer periods than are conventional methods. This brings within reach a variety of novel opportunities for *in vitro* studies, e.g. of long-term effects of nutrition, repeated exposure of potential toxicants, or of long-term endocrine dynamics⁴⁹.

Applicability of WAT-on-a-chip for drug testing. Since an important area of application for the organ-on-a-chip technology is drug development, we conducted a proof of concept compound test to assess the applicability of our WAT-on-a-chip for pharmaceutical research. After 6 days of on-chip culture, we exposed the WAT-chip to the β -adrenergic agonist isoproterenol, which is known to induce lipolysis. By additionally supplementing the medium with the fluorescently tagged fatty acid analog (BODIPYTM 500/510 C1, C12) for 60 minutes, we were able to monitor isoproterenol-related effects on fatty acid uptake and release by adipocytes, using standard fluorescence microscopy (Fig. 6). While media with fluorescently tagged fatty acids was perfused, the normalized fluorescent intensity in the isoproterenol-treated systems increased significantly more slowly than in non-treated control systems. After switching to media without the fluorescently tagged fatty acid analog, the fluorescent intensity decreased much quicker in the isoproterenol-treated systems. Taken together, this means that the isoproterenol exposure induced a reduction of the net uptake rate of fatty acids and an increase of their release rate. Both findings are in line with the expected lipolysis-inducing effect of isoproterenol.

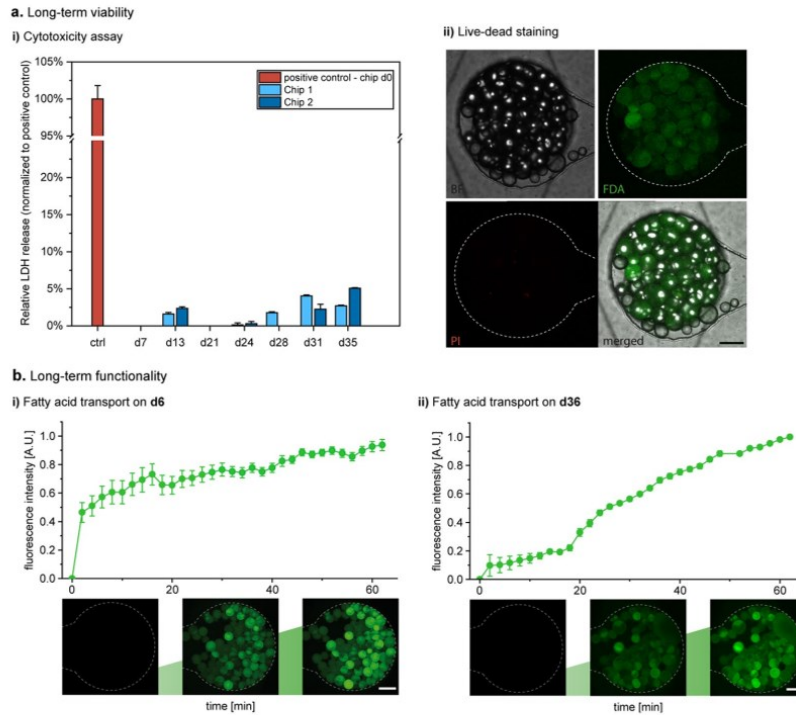


Figure 5. Long-term viability and functionality of the human WAT-on-a-chip. **(a)** Long-term viability determined via **(a.i)** non-invasive measurement of LDH release from medium effluents (absence of bars indicates no detectable difference to 0) as well as **(a.ii)** live/dead staining at day 36. Scale bar equals 150 μm . **(b)** Dynamic measurement of the normalized fluorescence intensity in tissue chambers perfused with medium containing a fluorescent fatty acid analog (4 μM BODIPYTM 500/510 C1, C12) revealed functional fatty acid uptake and accumulation in the WAT-model after **(b.i)** 6 as well as **(b.ii)** 36 days of on-chip culture (n = 6 individual tissue chambers). Scale bars equal 150 μm .

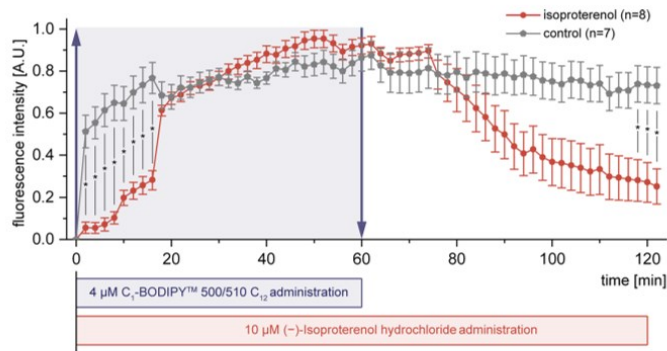


Figure 6. Applicability for drug testing illustrated by the effect of isoproterenol on fatty acid uptake and release. Normalized mean fluorescence intensity obtained by time-lapse fluorescence microscopy of WAT-on-a-chip systems perfused with medium supplemented with the fluorescently tagged fatty acid analog (4 μM BODIPYTM 500/510 C1, C12) during the first 60 minutes. Kinetics in systems exposed to 10 μM Isoproterenol (red circles) show significant differences to non-treated controls (grey polygons) (n = 7 and n = 8 individual tissue chambers; mean fluorescence intensities \pm SEM are presented).

Evidently, the used approach based on standard microscopy provides facile and non-invasive read-outs for drug screening, with a very high time-resolution, which is amenable for massive parallelization and automation. One noteworthy limitation is the requirement for normalization of readings from individual tissue chambers. Absolute quantitative values would provide even more information and potential for cross-correlation; it is, therefore, planned to address this in future generations of chips and readout-infrastructure. Overall, the successful proof of concept highlights the applicability of the WAT-on-a-chip system for screening purposes and the potential the system can have for drug development purposes.

Conclusion

Due to the lack of suitable experimental human model systems, research in adipose tissue biology and obesity has so far relied mostly on animal models, non-physiological *in vitro* systems, GWAS studies and (clinical) epidemiology. The first two approaches have major limitations in terms of their translatability to humans; the latter two require complex statistical analyses of large data sets and do not permit strong conclusions on pathophysiological mechanisms or efficacy of therapeutic interventions in individuals. The human WAT-on-a-chip platform presented here provides a novel tool that enables the maintenance, monitoring and manipulation of human adipocytes in a durably stable, tissue-like microphysiological environment. As an engineered model system, there are naturally still differences compared to complex *in vivo* tissue, which could be further reduced in the future, e.g. by the integration of WAT-resident immune cells and further cells from the stromal vascular fraction. Nevertheless, the vasculature-like perfusion provides opportunities for biomarker evaluation and “liquid biopsies” that can be cross-correlated with clinical endpoints, as well as a potential connection link for integration with other organ-on-a-chip platforms³⁴. Multi-organ-chips integrating WAT-models are likely to be of major interest e.g. for ADMET, diabetes or non-alcoholic steatohepatitis (NASH) studies.

Overall, the introduced WAT-on-a-chip system offers new perspectives and opportunities in mechanistic studies, pharmaceutical development and testing, as well as in personalized medicine.

Received: 17 May 2019; Accepted: 31 March 2020;

Published online: 20 April 2020

References

- World Health Organization (WHO), *Obesity*, <https://www.who.int/news-room/facts-in-pictures/detail/6-facts-on-obesity> (accessed 16 February 2019).
- World Health Organization (WHO), *Global Health Observatory (GHO) data*, <https://www.who.int/gho/en/> (accessed 16 February 2019).
- World Health Organization (WHO), *Facts and figures on childhood obesity*, <https://www.who.int/end-childhood-obesity/facts/en/> (accessed 16 February 2019).
- Wang, Y., Beydoun, M. A., Liang, L., Caballero, B. & Kumanyika, S. K. Will All Americans Become Overweight or Obese? Estimating the Progression and Cost of the US Obesity Epidemic. *Obesity* **16**, 2323–2330 (2008).
- Young, B., O’Dowd, G. & Woodford, P. *Wheater’s Functional Histology*, Churchill Livingstone, 6th Edition, ISBN 9780702047473 (2014).
- Rosen, E. D. & Spiegelman, B. M. What We Talk About When We Talk About Fat. *Cell* **156**, 20–44 (2014).
- Kershaw, E. E. & Flier, J. S. Adipose Tissue as an Endocrine Organ. *J. Clin. Endocrinol. Metab.* **89**, 2548–2556 (2004).
- Scherer, P. E. Adipose Tissue: From Lipid Storage Compartment to Endocrine Organ. *Diabetes* **55**, 1537–1545 (2006).
- Fasshauer, M. & Blüher, M. Adipokines in health and disease. *Trends Pharmacol. Sci.* **36**, 461–470 (2015).
- Bélangier, C., Luu-The, V., Dupont, P. & Tchernof, A. Adipose Tissue Intracrinology: Potential Importance of Local Androgen/Estrogen Metabolism in the Regulation of Adiposity. *Horm. Metab. Res.* **34**, 737–745 (2002).
- Mayes, J. S. & Watson, G. H. Direct effects of sex steroid hormones on adipose tissues and obesity. *Obes. Rev.* **5**, 197–216 (2004).
- Marra, F. & Bertolani, C. Adipokines in liver diseases. *Hepatology* **50**, 957–969 (2009).
- Berg, A. H. & Scherer, P. E. Adipose tissue, inflammation, and cardiovascular disease. *Circ. Res.* **96**, 939–949 (2005).
- Zhang, Z. & Scherer, P. E. Adipose tissue: The dysfunctional adipocyte — a cancer cell’s best friend. *Nat. Rev. Endocrinol.* **14**, 132–134 (2018).
- Hajer, G. R., van Haefen, T. W. & Visseren, F. L. J. Adipose tissue dysfunction in obesity, diabetes, and vascular diseases. *Eur. Heart J.* **29**, 2959–2971 (2008).
- Pérez-Hernández, A. I., Catalán, V., Gómez-Ambrosi, J., Rodríguez, A. & Frühbeck, G. Mechanisms linking excess adiposity and carcinogenesis promotion. *Front. Endocrinol. (Lausanne)*. **5**, 65 (2014).
- Nawrocki, A. R. & Scherer, P. E. Keynote review: the adipocyte as a drug discovery target. *Drug Discov. Today* **10**, 1219–1230 (2005).
- Kusminski, C. M., Bickel, P. E. & Scherer, P. E. Targeting adipose tissue in the treatment of obesity-associated diabetes. *Nat. Rev. Drug Discov.* **15**, 639 (2016).
- Haas, B., Schlinkert, P., Mayer, P. & Eckstein, N. Targeting adipose tissue. *Diabetol. Metab. Syndr.* **4**, 43 (2012).
- Sankaralingam, S., Kim, R. B. & Padwal, R. S. The Impact of Obesity on the Pharmacology of Medications Used for Cardiovascular Risk Factor Control. *Can. J. Cardiol.* **31**, 167–176 (2015).
- Sheng, X. *et al.* Adipocytes Sequester and Metabolize the Chemotherapeutic Daunorubicin. *Mol. Cancer Res.* **15**, 1704–1713 (2017).
- Kleinert, M. *et al.* Animal models of obesity and diabetes mellitus. *Nat. Rev. Endocrinol.* **14**, 140 (2018).
- King, A. & Bowe, J. Animal models for diabetes: Understanding the pathogenesis and finding new treatments. *Biochem. Pharmacol.* **99**, 1–10 (2016).
- Poulos, S. P., Dodson, M. V. & Hausman, G. J. Cell line models for differentiation: preadipocytes and adipocytes. *Exp. Biol. Med.* **235**, 1185–1193 (2010).
- Li, X. & Easley, C. J. Microfluidic systems for studying dynamic function of adipocytes and adipose tissue. *Anal. Bioanal. Chem.* **410**, 791–800 (2018).
- Mandrup, S., Loftus, T. M., MacDougald, O. A., Kuhajda, F. P. & Lane, M. D. Obese gene expression at *in vivo* levels by fat pads derived from sc implanted 3T3-F442A preadipocytes. *Proc. Natl. Acad. Sci. U.S.A.* **94**, 4300–5 (1997).
- Volz, A.-C., Omengo, B., Gehrke, S. & Kluger, P. J. Comparing the use of differentiated adipose-derived stem cells and mature adipocytes to model adipose tissue *in vitro*. *Differentiation* **110**, 19–28 (2019).
- Abbott, R. D. *et al.* Variability in responses observed in human white adipose tissue models. *J. Tissue Eng. Regen. Med.* **12**, 840–847 (2017).
- Rogal, J., Zbinden, A., Schenke-Layland, K. & Loskill, P. Stem-cell based organ-on-a-chip models for diabetes research. *Adv. Drug Deliv. Rev.* **140**, 101–128 (2019).

30. Esch, E. W., Bahinski, A. & Huh, D. Organs-on-chips at the frontiers of drug discovery. *Nat. Rev. Drug Discov.* **14**, 248–260 (2015).
31. Ahadian, S. *et al.* Organ-On-A-Chip Platforms: A Convergence of Advanced Materials. *Cells, and Microscale Technologies. Adv. Healthc. Mater.* **7**, 1700506 (2018).
32. Berg, A. V. D., Mummery, C. L., Passier, R. & Van Der Meer, A. D. Personalised organs-on-chips: functional testing for precision medicine. *Lab Chip* **19**, 198–205 (2019).
33. Esch, M. B. *et al.* Multi-Organ toxicity demonstration in a functional human *in vitro* system composed of four organs. *Adv. Drug Deliv. Rev.* **69–70**, 158–169 (2014).
34. Rogal, J., Probst, C. & Loskill, P. Integration concepts for multi-organ chips: how to maintain flexibility?! *Futur. Sci. OA FSO* **180** (2017).
35. Dugan, C. E. & Kennedy, R. T. *Measurement of lipolysis products secreted by 3T3-L1 adipocytes using microfluidics*, Elsevier Inc., 1st edn., vol. 538 (2014).
36. Loskill, P. *et al.* WAT-on-a-chip: a physiologically relevant microfluidic system incorporating white adipose tissue. *Lab Chip* **17**, 1645–1654 (2017).
37. Abbott, R. D. *et al.* Long term perfusion system supporting adipogenesis. *Methods* **84**, 84–89 (2015).
38. Liu, Y. *et al.* Adipose-on-a-chip: a dynamic microphysiological *in vitro* model of the human adipose for immune-metabolic analysis in type II diabetes. *Lab Chip* **19**, 241–253 (2019).
39. Kongsuphol, P. *et al.* *In vitro* micro-physiological model of the inflamed human adipose tissue for immune-metabolic analysis in type II diabetes. *Sci. Rep.* **9**, 4887 (2019).
40. Godwin, L. A. *et al.* A microfluidic interface for the culture and sampling of adiponectin from primary adipocytes. *Analyst* **140**, 1019–1025 (2015).
41. Harms, M. J. *et al.* Mature Human White Adipocytes Cultured under Membranes Maintain Identity, Function, and Can Transdifferentiate into Brown-like Adipocytes. *Cell Rep.* **27**, 213–225.e5 (2019).
42. Zhang, H. H., Kumar, S., Barnett, A. H. & Eggo, M. C. Surface Proteins of Gram-Positive Bacteria and How They Get There. *J. Endocrinol.* **164**, 119–128 (2000).
43. Huber, B. *et al.* Integration of Mature Adipocytes to Build-Up a Functional Three-Layered Full-Skin Equivalent. *Tissue Eng. Part C Methods* **22**, 756–764 (2016).
44. Sugihara, H., Yonemitsu, N., Miyabara, S. & Yun, K. Primary cultures of unilocular fat cells: characteristics of growth *in vitro* and changes in differentiation properties. *Differentiation* **31**, 42–49 (1986).
45. Matsumoto, T. *et al.* Mature adipocyte-derived dedifferentiated fat cells exhibit multilineage potential. *J. Cell. Physiol.* **215**, 210–222 (2008).
46. Decaunes, P., Bouloumié, A., Ryden, M. & Galitzky, J. *Ex vivo* Analysis of Lipolysis in Human Subcutaneous Adipose Tissue Explants. *Bio-protocol* **8**, 1–12 (2018).
47. Toepke, M. W. & Beebe, D. J. PDMS absorption of small molecules and consequences in microfluidic applications. *Lab Chip* **6**, 1484–1486 (2006).
48. Maurizi, G. *et al.* Human white adipocytes convert into “rainbow” adipocytes *in vitro*. *J. Cell. Physiol.* **232**, 2887–2899 (2017).
49. Nawroth, J., Rogal, J., Weiss, M., Brucker, S. Y. & Loskill, P. Organ-on-a-Chip Systems for Women's Health Applications. *Adv. Healthc. Mater.* **1700550** (2017).

Acknowledgements

The authors thank Dr. Ziegler (Klinik Charlotenhaus, Stuttgart) for the kind provision of human adipose tissue from plastic surgery, Dr. Jakob Barz for help with the PECVD coating process, and Silvia Kolbus-Hernandez, Elena Rubiu as well as Luisa Merz for their assistance with cell culture and chip fabrication. We further thank Prof. Andreas Stahl and Pete Zushin for helpful discussions and Joost Overduin for language-editing. The research was supported in part by the Fraunhofer-Gesellschaft internal programs Talenta Start (to J.R.) and Attract (601543), the DAAD funded by the Bundesministerium für Bildung und Forschung (BMBF) (PPP USA 2018, 57387214) (all to P.L.), as well as the Ministry of Science, Research and the Arts of Baden-Württemberg (Az: 7542.2-501-1/13/6 to P.L. and Az: 33-729.55-3/214-8 to K.S.-L.).

Author contributions

J.R. and P.L. designed the device. J.R. and C.B. fabricated the device. J.R., C.B., E.K. and J.Rz. performed and analyzed the experiments. S.S. performed membrane characterization. C.P. performed simulations. K.S.-L. gave biological advice. J.R., K.S.-L. and P.L. wrote the manuscript. J.R. and P.L. designed the study.

Competing interests

The authors declare no competing interests.


Additional information

Supplementary information is available for this paper at <https://doi.org/10.1038/s41598-020-63710-4>.

Correspondence and requests for materials should be addressed to P.L.

Reprints and permissions information is available at www.nature.com/reprints.

Publisher's note Springer Nature remains neutral with regard to jurisdictional claims in published maps and institutional affiliations.

 **Open Access** This article is licensed under a Creative Commons Attribution 4.0 International License, which permits use, sharing, adaptation, distribution and reproduction in any medium or format, as long as you give appropriate credit to the original author(s) and the source, provide a link to the Creative Commons license, and indicate if changes were made. The images or other third party material in this article are included in the article's Creative Commons license, unless indicated otherwise in a credit line to the material. If material is not included in the article's Creative Commons license and your intended use is not permitted by statutory regulation or exceeds the permitted use, you will need to obtain permission directly from the copyright holder. To view a copy of this license, visit <http://creativecommons.org/licenses/by/4.0/>.

© The Author(s) 2020



Contents lists available at ScienceDirect

Advanced Drug Delivery Reviews

journal homepage: www.elsevier.com/locate/adr



Immunocompetent cancer-on-chip models to assess immuno-oncology therapy [☆]



Tengku Ibrahim Maulana ^{a,b,1}, Elena Kromidas ^{a,b,1}, Lars Wallstabe ^c, Madalena Cipriano ^b, Miriam Alb ^c, Cécile Zaupa ^d, Michael Hudecek ^c, Birgit Fogal ^e, Peter Loskill ^{a,b,*}

^a Department of Biomedical Science, Faculty of Medicine, Eberhard Karls University Tübingen, Österbergstraße 3, 72074 Tübingen, Germany

^b Fraunhofer Institute for Interfacial Engineering and Biotechnology IGB, Nobelstrasse 12, 70569 Stuttgart, Germany

^c Universitätsklinikum Würzburg, Medizinische Klinik und Poliklinik II, Oberdürrbacherstrasse 6, 97080 Würzburg, Germany

^d Transgene S.A, 400 Boulevard Gonther d'Andernach, 67405 Illkirch-Graffenstaden, France

^e Non-clinical Drug Safety, Boehringer Ingelheim Pharmaceuticals Inc., Ridgefield, CT, USA

ARTICLE INFO

Article history:
 Received 8 November 2020
 Revised 8 March 2021
 Accepted 17 March 2021
 Available online 30 March 2021

Keywords:
 Tumor-on-chip
 Microphysiological systems
 Immunotherapy
In vitro models
 Adoptive cell therapy
 Immune checkpoint inhibitor
 Cytokine therapy
 Oncolytic viruses
 Cancer vaccine

ABSTRACT

The advances in cancer immunotherapy come with several obstacles, limiting its widespread use and benefits so far only to a small subset of patients. One of the underlying challenges remains to be the lack of representative nonclinical models that translate to human immunity and are able to predict clinical efficacy and safety outcomes. In recent years, immunocompetent Cancer-on-Chip models emerge as an alternative human-based platform that enables the integration and manipulation of complex tumor microenvironment. In this review, we discuss novel opportunities offered by Cancer-on-Chip models to advance (mechanistic) immuno-oncology research, ranging from design flexibility to multimodal analysis approaches. We then exemplify their (potential) applications for the research and development of adoptive cell therapy, immune checkpoint therapy, cytokine therapy, oncolytic virus, and cancer vaccines.

© 2021 The Author(s). Published by Elsevier B.V. This is an open access article under the CC BY-NC-ND license (<http://creativecommons.org/licenses/by-nc-nd/4.0/>).

Contents

1. Introduction	282
2. New opportunities provided by immunocompetent Cancer-on-Chip models	283
2.1. Fit-for-purpose tailoring of models for specific questions	283
2.2. Modeling and manipulating the tumor microenvironment	285
2.2.1. Cellular components	286
2.2.2. Local oxygen content	286

Abbreviations: ACT, adoptive cell therapy; ADCC, antibody-dependent cellular cytotoxicity; APC, antigen-presenting cells; BiTEs, bispecific T cell engagers; CAF, cancer-associated fibroblast; CAR, chimeric antigen receptor; CRS, cytokine release syndrome; CTLA-4, cytotoxic T-lymphocyte-associated Protein 4; ECM, extracellular matrix; DC, dendritic cell; iPSC, induced pluripotent stem cell; irAE, immune related adverse events; HER2, human epidermal growth factor receptor 2; ICI, immune checkpoint inhibitor; iCoC, immunocompetent Cancer-on-Chip; NK cells, natural killer cells; OoC, Organ-on-Chip; OV, oncolytic virus; PD-1, programmed cell death protein-1; PD-L1, programmed death-ligand 1; PMN, polymorphonuclear neutrophil; TAM, tumor associated macrophage; TIL, tumor-infiltrating lymphocyte; TME, tumor microenvironment; TCR, T cell receptor; Treg, regulatory T cell.

[☆] This review is part of the Advanced Drug Delivery Reviews theme issue on “Disease Models”.

* Corresponding author at: Department of Biomedical Science, Faculty of Medicine, Eberhard Karls University Tübingen, Österbergstr 3, 72074 Tübingen, Germany.

E-mail address: peter.loskill@uni-tuebingen.de (P. Loskill).

¹ Contributed equally.

<https://doi.org/10.1016/j.addr.2021.03.015>

0169-409X/© 2021 The Author(s). Published by Elsevier B.V.

This is an open access article under the CC BY-NC-ND license (<http://creativecommons.org/licenses/by-nc-nd/4.0/>).

2.2.3.	Chemokine gradient	286
2.2.4.	Cell scaffolds and other biophysical forces	287
2.2.5.	Vasculature and perfusion	287
2.3.	Optical accessibility and high-content analysis	288
2.4.	Short platform development time	289
3.	Applications of iCoCs to test immunotherapy approaches	289
3.1.	Adoptive cell therapy	289
3.1.1.	iCoC approaches to study TME effects on ACTs	290
3.1.2.	Modeling ACT-mediated toxicities	291
3.2.	Immune checkpoint inhibitors	291
3.2.1.	Identification of responders in patient-specific iCoCs	291
3.2.2.	iCoCs as high(er)-throughput screening tools	292
3.2.3.	Overcoming resistance by defining synergistic drug combinations in iCoCs	292
3.2.4.	Dissecting effects of the immunosuppressive TME on ICI therapies	293
3.2.5.	An unmet need: Researching immune-related adverse events of ICIs	296
3.3.	Cytokine therapy	296
3.4.	Oncolytic viruses	298
3.5.	Cancer vaccines	298
4.	Outlook	298
	Funding	299
	Declaration of Competing Interest	299
	Acknowledgments	299
	Appendix A. Supplementary material	299
	References	299

1. Introduction

Cancer is one of the most frequent causes of death worldwide. Conventionally, therapeutic strategies based on radiation, chemotherapy, and surgical removal are applied. In the last decades, immunotherapy has established itself as an additional treatment option. Cancer immunotherapy aims to eliminate cancer cells by unleashing the immune system, in particular T cells. It encompasses a broad range of modalities, such as adoptive cell therapy, immune checkpoint inhibition, cytokine therapy, oncolytic viruses, and cancer vaccines [1–4]. The first immune system-related cancer treatment dates back to the end of the 19th century [5]. Since then, numerous discoveries have elucidated the central role of the immune system in the control of malignantly transformed cells. Nowadays, immunotherapeutic approaches have led to a breakthrough in cancer treatment by prolonging the survival of patients suffering from rapidly progressing malignancies.

Despite the explosion of interest in cancer immunotherapy in the past years, the failure rate in oncology drug development is still 2-fold higher than for non-oncology drugs; spanning throughout the entire process from phase I studies to approval. In fact, the likelihood of approval is currently only 5% [6]. A major issue is that the translation from preclinical animal models often fails due to poor recapitulation of the human carcinogenesis and human response to cancer therapy [7], including tumor resistance and immune escape through defects in (neo)antigen presentation, upregulation of additional inhibitory checkpoints and immunosuppressive features of the tumor microenvironment [8–12]. The induction of artificial carcinogenic processes in animals does not parallel the multifactorial and life-style related tumor etiology in humans. Furthermore, in humans, cancer is often associated with aging which is not reflected in most mouse models, thereby additionally hampering the translatability of preclinical studies to the situation in patients [13]. As most tumor mouse models are still relying on inoculation of *in vitro* grown tumor cell lines, these models also fail to recapitulate e.g. the interplay of the malignant cells with immune cells and other cells within the tumor microenvironment such as fibroblasts [14]. Similarly, the development of immune cells in response to tumor growth are not always recapitulated in these models, such as e.g. tissue-resident memory T cells, which have been shown to play an important role in controlling tumor

growth and express many of the immune checkpoint receptors targeted by immunotherapy [15]. The key immunological processes that are essential to allow cancer progression or to effectively mimic the therapeutic responses to immuno-oncology therapies differ significantly between species [16]. Many immune cell subsets important to control tumor growth differ in development, regulation, and signaling pathways, and some important cell types, such as certain subsets of $\gamma\delta$ T cells are not represented in mice at all [17]. The differences in the composition of immune cell subsets and expression of receptors between mice and humans can, however, be of utmost importance for the prediction of possible toxicities, e.g. differences in CD28 expression caused serious side effects in the first-in-human trial of TGN1412 which were not foreseen during preclinical development [17–19]. Last, the safety of many immune therapies is assessed in healthy animals lacking tumors, and as such, tumor-induced changes to the targeted immune cells are not represented. Despite this, more than 10% (more than 1 million) of all animals used in research and testing in the EU were used for human cancer studies in 2017. In the case of applied/translational science, cancer research accounted for the most used animals overall; In basic science, cancer research holds on to the 3rd “place” [20]. The limited predictive ability of the current preclinical models is depicted in the clinical results, where various issues related to safety and efficacy are becoming more apparent [21–29]. Hence, alternative model systems that are able to recapitulate the human disease and feature both patient cancer cells and human immune cells are of utmost importance to increase the success rates in immunotherapy discovery and development.

To this end, advanced human-based *in vitro* models have been developed to allow targeted mechanistic research, gain early information about on-target off-tumor and off-target toxicities, and increase confidence in the mechanisms of action. Ideally, an *in vitro* cancer model should comprise three-dimensional (3D) cancer tissue integrated within a tumor microenvironment (TME) featuring vascularization and immune components [30]. The latter is an essential aspect of both carcinogenesis and cancer therapy: Tumor growth often depends on the silencing of the immune response [31]. The vasculature is also crucial as it provides nutrient and oxygen supply. It can dynamically adapt to stimuli from the tumor and is a key element of immune cell interaction [32].

In the last decade, Organ-on-Chip(OoC)-technology has emerged as a promising platform for the generation of microphysiological tissue models that mimic the key functional units of organs. By integrating 3D co-cultures of relevant cell types with vasculature-like perfusion, OoCs allow to study the communication between individual cells, tissue components, or entire tissues [33–35]. By combining microfabrication and biomaterials with tissue engineering and cell biology, the research community now has complex human-relevant model systems at its disposal that are able to provide answers to questions that animal models were not [36,37]. Cancer research has been a major application area for microfluidic cell culture systems; for instance, to generate defined gradients and investigate tumor cell migration, to study the behavior of circulating tumor cells, or for cancer cell detection [38–40]. More recently, Cancer-on-Chip systems with higher degrees of complexity have been introduced to model tumor heterogeneity and tumor microenvironments, comprehensively covered by several recent overview articles [41–43]. In this review, we first take a closer look at the state of the art of Cancer-on-Chip models that integrate immune components and discuss the advances they bring to (mechanistic) immuno-oncology research. Afterwards, we highlight examples of how these human-based immunocompetent Cancer-on-Chip (iCoC) models can be applied to assess the efficacy and safety of various immunotherapy modalities.

2. New opportunities provided by immunocompetent Cancer-on-Chip models

Traditionally, microfluidics technology has been utilized broadly for (immuno-)oncology research, for instance, to isolate circulating tumor cells, immobilize single cells, and pair individual immune-cancer cells to study direct cell-cell interactions [44–47]. The convergence of microfluidics, microfabrication, biomaterials, and tissue engineering research has provided the opportunity to create complex vascularized and perfused structures in a tightly controlled microenvironment accessible by a wide range of analysis methods. Immunocompetence is added to Cancer-on-Chip models by integrating human immune cells capable of generating an immune response into models that feature human cancer cells presenting target antigen and carefully tailored TME relevant to a specific human tumor type. First-generation iCoC models focused mostly on recapitulating and studying 2D cell migration in response to cytokine/chemokine gradients. More recent models aim at mimicking the complex 3D cancer microenvironment including the extracellular matrix (ECM), dynamic vasculature-like perfusion, for instance with self-assembled microvessels. Moreover, novel iCoCs shift from cancer cell lines to tumor biopsies, spheroids, or organoids and are combined with high-content imaging to gain intricate insights in immune-cancer interaction dynamics. In the following sections, we give an overview of the concepts and potentials of iCoC models specifically for immuno-oncology research. We highlight how they can provide useful mechanistic insights about immune-cancer interaction by leveraging aspects, such as their adjustable degree of complexity through a fit-for-purpose approach, the opportunity to tune tumor microenvironmental parameters, the applicability of high-content imaging and analysis, as well as the accelerated platform development time relative to e.g. animal models.

2.1. Fit-for-purpose tailoring of models for specific questions

OoC technology provides a platform of engineered compartments, channels, and barriers for the co-culture of different cell types and tissues in a fit-for-purpose manner [48,49]. The ability

to design customized cellular microenvironments enables researchers to determine flexibly the desired cellular organization and relative position between different cell populations according to the experimental requirements and research questions. In the human body, immune cells are highly mobile and actively migrate from one tissue to another. They move under flow conditions inside the vasculature, extravasate, infiltrate the TME, and interact with cancer cells, all of which can be readily recapitulated inside iCoCs through guided spatial compartmentalization. This compartmentalization also serves further purposes, such as the generation of concentration gradients, temporal control of cell-cell interaction, creation of multilayered 3D-structures, immobilization of tissue fragments, as well as monitoring the behavior (viability, morphology, motility, etc.) of cancer and immune cells.

In simple microfluidic systems, monocultures of cancer or immune cells were exposed to gradients of chemoattractants or conditioned media to study migratory behavior. Gradients were thereby generated by mixing continuous laminar flows based on the pressure difference between in- and outlets [50–52] or by adding soluble factors directly into the micro-chamber with a microinjector for short-term gradients [53]. Via real-time imaging, cell migration without directional constraints [50,51,53] or with directional movement guided through channels [52] was observed. Cultivation of more than one cell type was implemented in various ways: Most simply, two different cell types were mixed and cultivated in the same culture chamber for stromal support [54] or to observe direct interactions of tumor cells with immune cells [55]. Businaro et al. designed a microfluidic device with two main culture chambers connected with a central compartment via microchannels [56]. This platform allows chemical and physical contact between tumor cells and immune cells and was used for migration studies (Fig. 1A). A slightly modified version of this chip was used to characterize migration of immune cells in competition conditions: Dendritic cells (DC) in the central compartment were exposed to the secretome of treated cancer cells (RI) and either matrix or untreated (NT) cancer cells that were embedded in the right and left chamber, respectively (Fig. 1B, supplementary video) [57]. To mimic varying physical confinement and complex pathways that cells encounter *in vivo*, Um et al. oriented channels of 5 μm or 50 μm width in a maze [58]. Bait cells (normal or cancerous cells) were placed at the outlets of the maze and the path pattern of dendritic cells was monitored (Fig. 1C). This platform sheds light on the physical and chemical microenvironment and their impact on the trajectories of immune cells.

Fluidic manipulation in iCoC models allows both temporal and directional control over the media flow, which has been used to temporally control paracrine signaling between different cell types. For example, Hsu et al. used pneumatic microvalves to control the interaction between cancer cells, immune cells, and fibroblasts that are cultured in separate chambers [59]. The media was directed into the different compartments to pretreat/activate cells in a temporally controlled manner. In another platform, developed by Wu et al., microvalves were leveraged to pattern a well-defined antibody barcode in a channel between two adjacent cell culture chambers [60]; thereby, intercellular communication could be assessed via surface-enhanced Raman scattering on-chip. Guo et al. employed precise fluidic flow control to assess the invasive behavior of tumor cells [61]. In one chamber, tumor cells and macrophages were cultivated in close proximity on both sides of a membrane, which induced epithelial-to-mesenchymal transition (EMT) in tumor cells and tumor-associated macrophage (TAM)-like phenotype in macrophages. Conditioned media of the co-culture was directed to a distant tumor cell culture chamber to activate cancer cells. Subsequent redirection of the medium via microvalves lead to a gradient in a hydrogel-loaded migration chamber and promoted cancer cell invasion. Rather than manipulating the

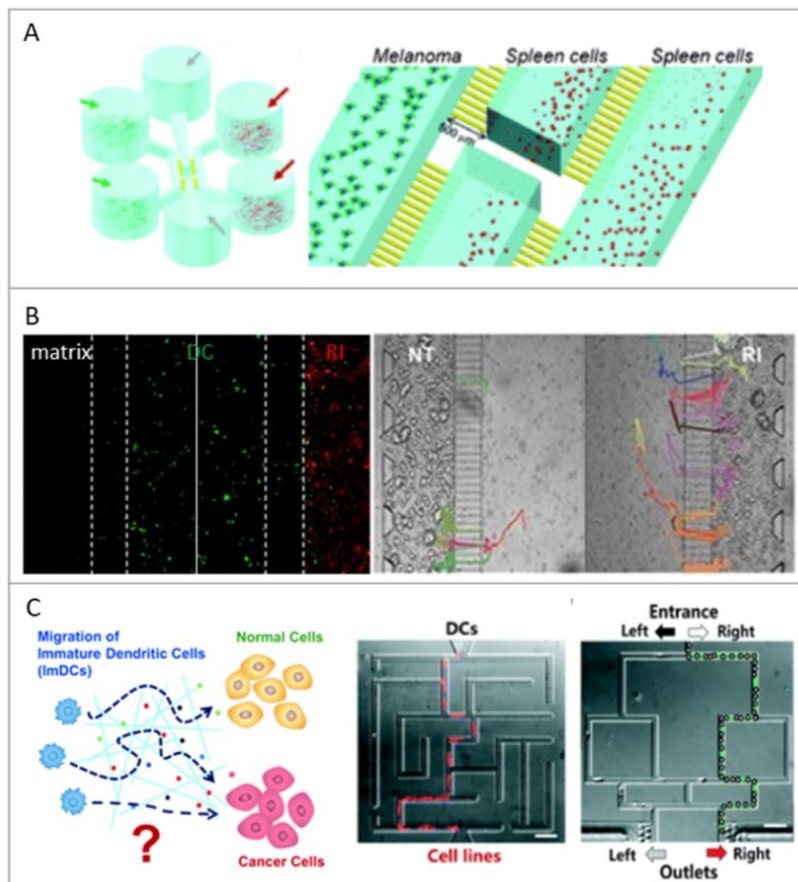


Fig. 1. Different examples of fit-for-purpose iCoC Designs: A) In a co-culture iCoC model, two main culture chambers and a central compartment are connected via micro-channels and allow chemical and physical contact between tumor cells and immune cells. The secretion of chemokines by melanoma cells induces migration of spleen cells through micro-channels that mimic body venules (Republished with permission of Royal Society of Chemistry, from Ref. [56]). B) In a similar iCoC as in A), dendritic cells (DC) in the central channel were cultivated in no competition conditions in between treated cancer cells (RI) and a channel filled with matrix as shown in the fluorescent image (DC = green, RI = red). In competition conditions, the matrix was replaced by untreated cancer cells (NT) and the migratory pattern of DCs was analyzed as depicted in the bright field image by colored lines. DC preferentially migrated towards treated cancer cells rather than an empty matrix or untreated cancer cells. Reproduced from [57], CC BY 4.0. C) Channels with varying sizes oriented in a maze allow the investigation of directional choices of immune cells towards bait cells in a physically confined environment (Republished with permission of Royal Society of Chemistry, from Ref. [58]). (For interpretation of the references to colour in this figure legend, the reader is referred to the web version of this article.)

fluidics, Yu et al. temporally controlled the paracrine signaling between immune and cancer cells using a system with reconfigurable stacks of cultured tissues. With this system, each tissue compartment can be cultured separately and interfaced with the other compartments at arbitrary time points. This enabled the generation of organotypic differentiated tumor-associated macrophages in a tumor-specific and patient-specific manner [62].

More recent iCoC models integrate ECM scaffolds to provide a 3D environment for different cell populations (Fig. 2A). These scaffolds enable the creation of a more physiologically relevant biophysical/chemical landscape within the TME. The integration of the TME components is crucial as it is known to heavily attenuate tumor immunosurveillance, influence treatment responses, and mediate resistance, hence have been aimed as potential targets

in immuno-oncology [63–66]. A number of studies demonstrated that 3D microfluidic cancer model incorporating multiple cell populations exhibited a substantially different response to immunotherapeutic drugs compared to 2D models [67–71]. In fact, drug effects are often overestimated in 2D models [72–74]. However, an underestimation of the effects of immunomodulatory agents targeting immune checkpoints in 2D immune-cancer models was observed when compared with an iCoC model that integrates multiple aspects of the TME. This was caused by the upregulation of immune exhaustion markers in the iCoC model, but not in the 2D plate control [71]. This suggests that understanding the contribution of the tumor microenvironment is crucial, and using a relevant model for drug testing forms the basis of designing effective cancer immunotherapy [66].

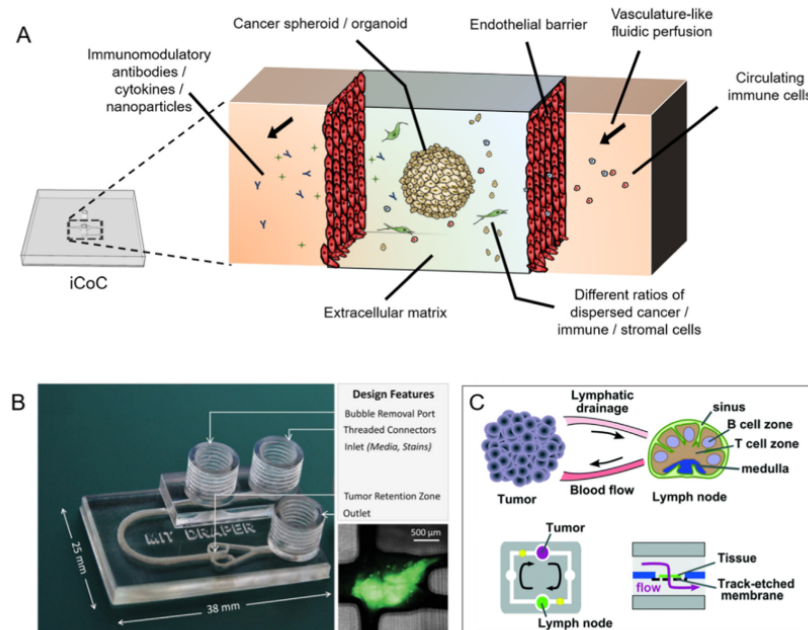


Fig. 2. Compartmentalization of 3D tissues in iCoC models. A) Various components can be integrated into the iCoC model to create a complex 3D tumor microenvironment, shown here in an exemplary iCoC with vertical tissue-tissue interfaces. B) Trapping patient-derived tumor fragments and applying perfusion through the construct have enabled multiple-days culture of the tumor and personalized immune checkpoint therapy assessment (Reproduced from Ref. [83]. Copyright © 2019 by John Wiley Sons, Inc. Reprinted by permission of John Wiley & Sons, Inc.). C) Applying continuous circulating flow between *ex vivo* tissues in iCoC platform has emulated distant bidirectional communication between tumor and lymph node tissue that are placed in different chambers (Reproduced with permission of the Royal Society of Chemistry from Ref. [84]).

One of the most common architectures of 3D iCoC models includes a vertical tissue-tissue interface (Fig. 2A). One advantage of such an interface is the easy visualization of the dynamic cellular interaction and migration in the lateral dimension, as the resolution and optical accessibility in *x-y*-direction is generally higher than in *z*-direction. Several techniques have been developed to create this interface, including sequential hydrogel photopatterning [68,75], micro-molding [76], as well as capillary pinning e.g. by using a series of regularly spaced pillars [69,70,77–80]. These approaches have been used to analyze the migration dynamics of natural killer (NK) cells, genetically engineered T cells, dendritic cells, neutrophils, and monocytes into the tumor mass [57,68,69,76,80]. Moreover, such interfaces also allow lateral fluid diffusion and have been utilized to assess the diffusion of immunomodulatory nanoparticles across the endothelial barrier into the tumor mass [81,82].

Besides establishing tissue barriers for dispersed cell populations and cellular monolayer, spatial confinement also enables the integration of spheroids, organoids, and tumor fragments. Patient-derived tumor fragments have been used for *ex vivo* profiling of immune checkpoint blockade in a microfluidic system, showing early promise in its use for evaluating combination therapies (Fig. 2B) [83,85,86]. Additional to short-distance cell-cell or tissue-tissue interactions, compartmentalization also allows the modeling of distant inter-tissue crosstalk between *ex vivo* tumor and lymphoid tissue slices; enabling e.g. the study of tumor-mediated lymph node immunosuppression (Fig. 2C) [84].

Design features of microfluidic iCoC can readily be modified according to the application or to answer specific immuno-

oncological research questions. Simpler iCoC models can be used, for example, for studies that require higher throughput. On the other hand, more comprehensive systems that integrate tumor spheroids/organoids, mobile immune cells, vasculature, and stromal components with multiple microenvironmental factors can be utilized to investigate the mechanisms of action of immunotherapies and immune-cancer interaction in a more complex biological setting.

2.2. Modeling and manipulating the tumor microenvironment

Understanding the TME is crucial, as it currently presents major barriers to effective cellular immunotherapy, especially in solid tumors [87]. For engineered T and NK cells, for example, they first need to infiltrate the dense stromal elements of solid tumors and overcome hostile microenvironment characterized by i) altered metabolic conditions such as hypoxia, oxidative stress, and acidic pH, ii) the presence of immunosuppressive cytokines, as well as iii) the recruitment of immunosuppressive myeloid cells, regulatory T cells (Tregs), and TAMs [88–92]. Immunosuppressive innate immune cells play a major role in shaping the tumor microenvironment as they release immunosuppressive cytokines (IL-10, TGF- β) and express receptors (PD-L1) that negatively affect the adaptive immune response/cellular immunotherapy [14,93]. Additionally, the dense cancer cell-cell junctions in a tumor can limit therapeutic antibodies penetration [76]. Therefore, modeling these factors to better assess the efficacy of immunotherapy is of great interest to drug developers [94,95].

The use of animal models to study the TME is particularly challenging because the various immunosuppressive aspects are interdependent and not readily controllable, thereby making it difficult to interpret their individual contribution [14,25]. One additional drawback is the partial HLA mismatch in mouse models using tumor cell lines of human origin and e.g. CAR-T cells from a third-party donor [96]. Mouse models using patient-derived tumors (PDX models) as well as patient-derived stem cells for engraftment of a functional immune system may overcome such drawbacks but are highly dependent on the appropriate cells for engraftment of the immune system and the TME might only reflect partially the TME in patients [93,96]. Additionally, special considerations need to be taken in all models to avoid xeno-graft-versus-host-disease against mouse tissues [97]. iCoC models present the potential to make experimental modifications of cellular and biochemical composition. This allows to dissect individual roles of immunosuppressive factors and increase physiological relevance at the same time. In these systems, a defined 3D spatial organization also enables tight control of cytokine gradients [98], oxygen level [68,70,75], as well as other biophysical forces [99], which allows the investigation of how these factors might alter immune/cancer cell behavior and interaction. Testing and validating tumor microenvironmental factors in iCoC models can be done via computational approaches, modeling e.g. oxygen and chemokine transport, interstitial fluid flow, or shear stress [68,75,99,100].

2.2.1. Cellular components

Along with their relative positions, the ratio of the different cell types can be easily modified to mimic physiological conditions. By adjusting the population density of immune and cancer cells, it is possible to analyze different states of early cancer-immune interaction, such as early infiltration (immune cells are more excluded at the tumor periphery and in relatively small number compared to cancer cells) and post-infiltration phase (higher immune cell/cancer cell ratio) [101]. This could serve as a powerful solid tumor model to evaluate the efficacy of engineered immune cells and other immunomodulatory drugs in a temporally specific fashion. In addition, it allows the investigation of cancer treatment's mode of actions when multiple cell types are incorporated. For instance, by increasing the proportion of immune cells in co-culture with cancer cells and cancer-associated fibroblasts (CAFs) in their iCoC model, Nguyen et al. recapitulated one of trastuzumab's mode of actions: it increases the antibody-dependent cellular cytotoxicity (ADCC) against the cancer cells. Increasing the ratio of immune cells (PBMCs) to cancer cells (human epidermal growth factor receptor 2 (HER2)+ BT474 cell line) from 5:1 to 25:1 allowed them to reveal that trastuzumab-induced ADCC may require high immune cell density that infiltrates the TME from the vasculature, as the number of apoptotic cancer cells was ~10-fold higher in 25:1 immune cell/cancer cell ratio compared to 5:1 [79]. Moreover, increasing effector to target (E:T) ratio of chimeric antigen receptor (CAR)-T cells and ovarian cancer cells (SKOV3) from 1:1 to above 10:1 allowed Ando et al. to reveal a significant increase of CAR-T cell-mediated cytotoxicity using 2D multiwell plate, but not in their 3D iCoC model [68]. Differences in cytotoxic activity between 2D system and 3D microfluidic model were also observed when comparing the killing ratio of HeLa cells by NK-92 cells and HepG2 target cells by T cell receptor (TCR)-T cells [69,70,78]. This exemplifies how different factors within the 3D TME might reduce engineered T cells cytotoxic ability even in a higher E:T ratio [68]. For another T cell-based immunotherapy, such as bi-specific T cell engagers (BiTEs), the ratio of Tregs within the peripheral blood can determine the outcome of the therapy [102]. Potentially, varying different E:T ratios in iCoC models can be used for BiTEs dose prediction and safety evaluation.

Besides bottom-up approaches based on single cells, the integration of organoids and spheroids provides a great synergistic potential [103–105]. For iCoC platforms, in particular, cancer organoids can add *in vivo*-like cancer cell heterogeneity. This heterogeneity and the loss of antigenicity and immunogenicity by a subset of cancer cell population is a crucial aspect of immune escape mechanisms [106,107]. In fact, heterogeneity of cancer antigen expression remains a challenge in designing an effective CAR-T/NK cell construct [108]. The advantage of integrated iCoC systems over conventional cancer organoid models is the surrounding TME [109].

One consideration for cellular components in immunocompetent iCoC platforms is the potential for HLA-mismatch between immune cells and co-cultured tissue cells, which might complicate interpretation of results both for safety and for efficacy investigations. Similar limitations apply to other preclinical models, as discussed above, and could be overcome through the utilization of HLA-matched or induced pluripotent stem cells (iPSCs) derived tissues as well as careful testing to understand where these limitations apply.

2.2.2. Local oxygen content

A widely-studied characteristic of the TME is the oxygen level. Hypoxic conditions often occur in solid tumors where oxygen delivery is no longer sufficient to sustain ATP production by the cancer cells via oxidative phosphorylation. This is regarded as one of the main obstacles in immunotherapy due to its negative effect on anti-tumor immune response [110–113]. Using microfluidics, oxygen gradients/levels in solid tumors can be modeled in various ways: by physical barriers that selectively block oxygen diffusion (Fig. 3A) [68], by using tumor spheroid to naturally establish a hypoxic core within its own structure (Fig. 3B) [75,76], or by placing the entire system inside a hypoxic chamber (Fig. 3C) [70]. Other Cancer-on-Chip models utilize flanking channels filled with oxygen supplying and scavenging medium (e.g. sodium sulfite) respectively to create a precise gradient across the tissue compartment [114], e.g. to reproduce the HIF-1 α -mediated tumor growth and migratory behavior in lower ($\leq 5\%$) oxygen level [115].

The microscale characteristic of iCoCs offers a more accurate regulation of local oxygen levels than traditional *in vitro* models in hypoxia cancer research. Hypoxia chambers, for instance, do not allow control of pericellular oxygen conditions [116]. Using microfluidics, a defined oxygen level in a certain location of the tumor mass can be tailored to investigate immune and cancer response. Understanding the molecular mechanisms of hypoxia-regulated tumor immunity could provide a therapeutic value of targeting hypoxia-induced immunosuppressive cells and other molecular mechanisms. This could potentially serve as a combination therapy along with other cellular immunotherapies; thereby improve the overall efficacy of current treatment approaches.

2.2.3. Chemokine gradient

In vivo, various soluble factors from tumor cells, intratumor stromal cells, and intratumor leukocytes can stimulate the recruitment of tumor-infiltrating T cells, natural killer cells, and dendritic cells into the tumor site [117,118]. This process, however, is extremely complex and can be both tumor-promoting and -suppressive [119]. Precisely controlled levels and gradients of chemokines can be generated similarly to oxygen gradients by leveraging microfluidic approaches [120], for instance, using source/sink approaches [121].

To this end, microfluidic chips have been used in several immune-cancer interaction studies to perform chemokine-guided migration assays; looking at, for example, how macrophages induce cancer cells' migration [52,61,122] and how pre-activated NK cells migrate towards cancer cells [55]. Gradient control in

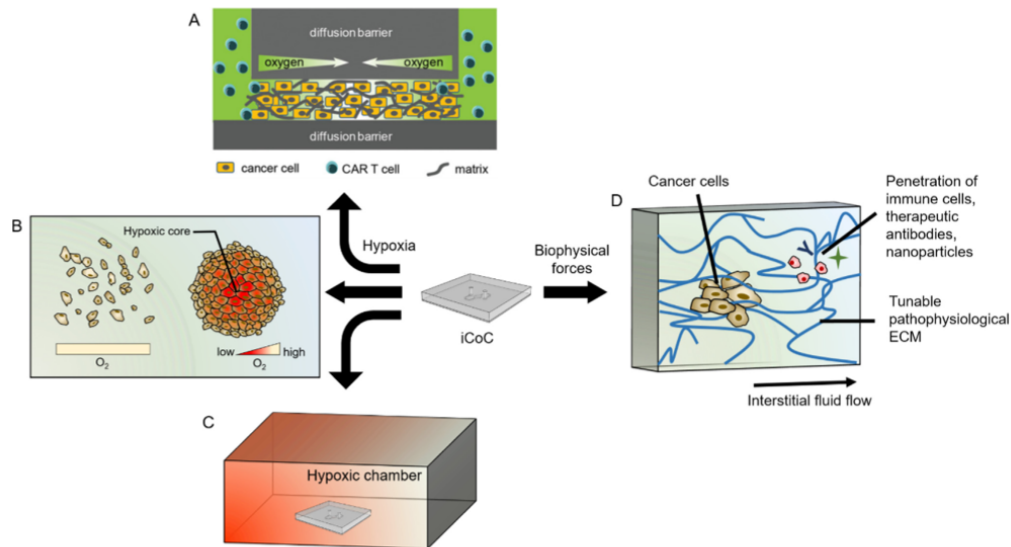


Fig. 3. Different approaches to modulate oxygen and biophysical forces in iCoC models. A) Selectively blocking oxygen diffusion by applying gas-impermeable chip material and varying cancer cell density within the solid tumor mass allowed Ando et al. to create a oxygen gradient and investigated its effect on CAR-T cell cytotoxicity (Reproduced from Ref [68]. Copyright © 2019 by John Wiley Sons, Inc. Reprinted by permission of John Wiley & Sons, Inc.). B) By creating cancer spheroids, hypoxic cores that are naturally generated can be recapitulated. C) Another approach is to place the whole iCoC platform into a hypoxic chamber, which allowed the adjustment of oxygen concentrations. D) Tuning biophysical microenvironments allow the investigation of how ECM stiffness, porosity, as well as interstitial fluid flow affect immune cell infiltration and therapeutic antibodies and nanoparticles penetration towards the cancer cells.

3D scaffold has often been employed for studying endothelial sprouting in response to VEGF gradient [115,123,124], directed migration/sprouting of cancer cells/spheroids [125], chemotherapeutic screening of different anticancer drugs [126], as well as investigating chemokine-guided immune cell migration into 3D TME [99,121,127].

2.2.4. Cell scaffolds and other biophysical forces

In iCoC systems, scaffold modulation allows researchers to investigate how stiffness, porosity, and composition of the ECM affect the migratory behavior of immune cells into the tumor site, viability of cancer cells, as well as cancer cell growth [68,75]. *In vivo*, the ECM presents a physical barrier that hinders therapeutic antibody penetration as well as engineered immune cell migration into the TME [88,128–131]. In the case of adoptive cell therapy, this challenge has already led to the development of CAR-T cells that target cancer-associated fibroblasts [132] and the ECM itself [133]. iCoCs featuring pathophysiological ECM conditions provide a platform to test these approaches and to optimize the transport efficiency of therapeutic antibodies and other immunomodulatory drugs (Fig. 3D) [76,81].

ECM of varying stiffness can be patterned *in situ* to mimic different types and stages of solid tumors. Ando et al., for instance, utilized a UV-crosslinkable gelatin methacryloyl (GelMA) hydrogel to generate a tailored ECM with stiffness (~6 kPa) and porosity resembling multiple cancer matrices. This model was used to evaluate CAR-T cell cytotoxicity against the cancer cells embedded in the hydrogel (Fig. 3A) [68]. A further correlation between ECM and immune cell's cytotoxicity was revealed by Park et al.: Using a microfluidic hydrogel patterning array, collagen-I concentration (2–4 mg/mL) was varied to investigate its impact on NK cells (NK-92) migration and cytotoxicity towards cancer cells (HeLa).

Their preliminary 3D cytotoxicity assay revealed that although denser ECM indeed impedes the migration of NK cells, it enhances the effectiveness of contact-mediated killing [78].

In addition to tumor-secreted cytokines, Lee et al. mimicked interstitial fluid pressure; a further important aspect within the TME [99]. This aspect is a critical tumor-associated biophysical factor that promotes tumor growth and can be integrated into the iCoC model by adding fluidic perfusion through the TME (Fig. 3D) [134]. In this work, the authors investigated the individual role of interstitial fluid pressure and tumor-secreted factors in promoting macrophage migration into the tumor site (macrophage density in the TME correlates with increased metastasis [135]). They demonstrated that interstitial pressure and tumor-secreted cytokines can act independently in increasing migration directedness and speed. Interestingly, however, no additive effect was observed under the simultaneous presence of both factors. They revealed that antibody blockade against IL-8 and/or CCL2 inhibited macrophage migration, but could be restored by interstitial flow, indicating the presence of a cytokine-independent pathway.

2.2.5. Vasculature and perfusion

The vasculature is a crucial component of the TME: it affects immune-cancer interaction in various ways, such as the active suppression of the recruitment, adhesion, and activity of T cells, the support of immunoevasion, as well as the build-up of cancer cells' resistance to immunotherapies [32]. Despite its significance, the vasculature is inherently lacking in traditional *in vitro* models in immuno-oncology research. In this regard, microfluidic cancer models provide a direct advantage by integrating vasculature-like perfusion and channels. Various groups have integrated endothelial cells into their iCoC models to specifically study immune-cancer-endothelial cells crosstalk investigating angiogenesis

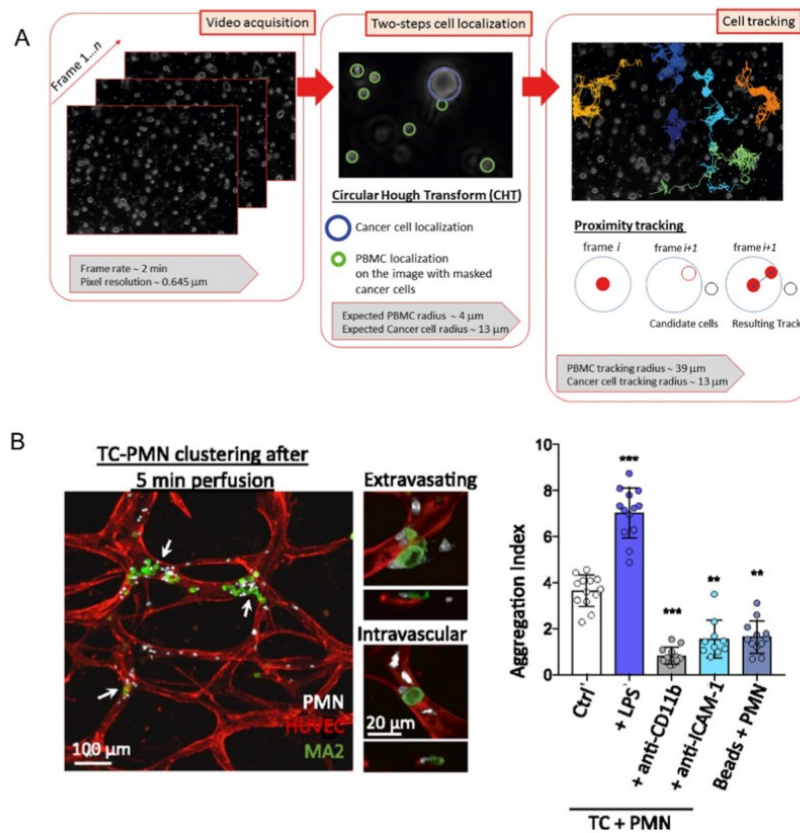


Fig. 4. Examples of high-content imaging performed on iCoC models. A) In an iCoC platform that includes multiple cell types (PBMCs, BT474 cancer cells, and Hs578T cancer-associated fibroblasts), advanced live imaging and automated image analysis was utilized to enable high-throughput tracking at the single-cell level and massive quantifications of cell-cell interaction. This allowed the assessment of real-time drug response and dissect the roles of each individual cell type [79]. B) High-content time-lapse imaging was used to monitor and quantify aggregate formation and motility of neutrophils (PMNs) and A375-MA2 tumor cells (TCs) inside self-assembled microvasculature after different pretreatment conditions. This revealed the role of neutrophils in supporting cancer cells' extravasation (Republished with permission from the National Academy of Sciences from Ref. [77]).

[136], cancer cells intravasation [137], and immune/cancer cells extravasation [75,77,80,82,138]. Others have established endothelial barriers to mimic *in vivo*-like nutrient/immunomodulatory drug delivery to the surrounding tissue [76,81]. Such endothelial barriers can be formed in microfluidic channel via different approaches, such as the creation of planar monolayers, vascular lumen, or self-assembled microvessels [139]. As human endothelial cells can express both MHC class I and II [140], and have the ability to present antigens [141], it is important to consider the interpretation of results that HLA mismatched endothelial cells might result in T cell activation independent of tested immunotherapies. However, endothelial cells can be derived from the same donors, e.g. from blood outgrowth endothelial cells [142].

In addition to the cellular component of the vasculature, the biophysical aspect of perfusion further increases physiological relevance and accessible endpoints: It enables i) constant nutrient delivery and removal of metabolic waste products from the TME [143], ii) the study of immune cells dynamics under vascular intraluminal flow (e.g. adhesion and extravasation) as well as the

migratory behavior inside the TME under interstitial flow [77,99], and iii) the integration into multi-organ-chips to study off-target toxicity and pharmacokinetics of immunotherapeutic drugs [144]. Furthermore, perfusion enables convective transport of nutrients through thick tissue and has therefore enabled multiple-days culture of thick tumor fragments for analyzing its response to circulating tumor-infiltrating lymphocytes (TILs) and immune checkpoint inhibitors for personalized testing [83,145].

2.3. Optical accessibility and high-content analysis

Due to their transparency and microscale, iCoC platforms provide superior optical accessibility allowing high-resolution real-time imaging to study spatiotemporal dynamics. Compared to *in vivo* intravital imaging, imaging of microfluidic devices requires less specialized equipment and expertise [146]. Compared to traditional 3D *in vitro* models, the height of the tissues and their distance to the microscope objective are typically significantly smaller. Primary cancer organoids, for instance, are grown in a

millimeters-thick 3D matrix, where they are located at different focal planes. Co-culturing cancer organoids with immune cells and monitoring key parameters for cell-mediated cytotoxicity such as effector cell recruitment, motility, and interaction with cancer cells and therefore extracting quantitative data from such live imaging experiments are challenging.

Live-cell imaging in iCoC platforms has been used for quantifying immune/cancer cell migration speed and directedness in many studies [57,99,138] as well as to uncover specific interaction behaviors between heterotypic cell-cell populations [77,79]. Nguyen et al., for example, conducted parallelized single-cell tracking and quantification of cell-cell interactions on chip to assess the immunosuppressive effect of CAFs [79]. They quantified the growth, motility, mitosis, and apoptosis of individual cancer cells (HER2+ BT474 cell line) when co-cultured with immune cells (PBMC), CAFs (Hs578T), with or without trastuzumab treatment (Fig. 4A). Employing high-resolution live-cell imaging in self-assembled microvessels, Chen et al. revealed the dynamic roles of inflamed neutrophils in exerting proextravasation effects of cancer cells (A375-MA2 melanoma) through the formation of intraluminal clusters of neutrophils and cancer cells. By quantifying aggregate formation and the motility of cluster-associated/free neutrophils over time, they revealed that the cluster formation is dependent on physical trapping and adhesive interactions between neutrophils and endothelial cells (HUVECs) (Fig. 4B) [77]. These visualizations can provide useful insights not only for studying immune-cancer interaction, but also for assessing cellular therapies and other immunomodulatory drugs in real-time, which would be more challenging to perform *in vivo*.

Additional to endpoint analysis via live-cell imaging, immune-cancer interactions in iCoCs can be monitored using a variety of *in situ* as well as terminal assays: Besides conventional cell/tissue culture assays such as qRT-PCR, RNA-Seq, or immunohistochemistry, the perfusion provides the opportunity to dynamically sample the effluent (perfused media) and analyze, for instance, the kinetics of secreted factors such as released cytokines and the state of circulating tumor/immune cells with a high temporal resolution [77,84,147].

2.4. Short platform development time

For personalized screening applications, the establishment of iCoC platforms can be much faster than patient-derived xenograft (PDX) murine models, which can take up to 6 months or longer [148]. Once established, iCoC models also have a much better potential for parallelized, quantitative clinical analysis than animal studies [96,146]. Early development phase can be completely independent of the final cell source, for example by using cell lines in proof of concept studies before integrating patient-derived cancer, immune, and stromal cells. The platform can be developed via iterative design optimization assisted by a computational modeling approach and exploiting different microfabrication methods.

3. Applications of iCoCs to test immunotherapy approaches

As elaborated on in the previous chapter, iCoC models provide the opportunity to model immune-cancer interactions in entirely new ways and can be utilized to unravel mechanisms of cell-mediated cytotoxicity. In this chapter, we now discuss how these novel iCoCs can be translated and applied to advance the development of novel immunotherapies. We address challenges the different immunotherapy modalities are currently facing and exemplify how iCoC models can provide nonclinical insights to address those challenges.

The advances in cancer immunotherapy come with several roadblocks limiting their widespread use and their benefits to so far only a small subset of patients. The lack of representative pre-clinical models that translate to human immunity, thereby, remains one of the greatest challenges [13,26]. Current nonclinical model systems are mostly unable to provide predictive information on the efficacy and safety of immunotherapy. The efficacy is clinically hampered by the immunosuppressive TME [26,149,150], which conventional model systems do not recapitulate. This is due to the dense nature of tumor extracellular matrix, high interstitial fluid pressure, abundant immunosuppressive cytokines, presence of suppressive regulatory myeloid cells, upregulated immune checkpoints, hypoxia, and nutrient starvation. Additionally, the inherent heterogeneity in antigen expression within solid tumors poses challenges to identify an optimal target [21,23]. In terms of safety evaluation, a growing body of literature has pointed out the inadequateness of most animal models to capture immune-mediated toxicities [22–25,27–29,151–153]. It is currently difficult to model on-target, off-tumor toxicities, and systemic inflammatory response syndrome using animal models. This is partly due to a lacking homology of tumor-associated antigen proteins in humans and animals [23]. Advances in humanized murine models enabled the reproduction of cytokine release syndrome (CRS) and neurotoxicity after CAR-T treatment [154–156]. The underlying mechanisms, however, could not be completely identified due to complicated interdependencies of many factors [25]. In general, many of the mechanisms of immune-mediated toxicities in humans are still unknown and human-based alternative models are much-needed.

In this chapter, we review application examples and discuss how iCoC models can help to elucidate the underlying mode of actions in adoptive cell therapy, immune checkpoint therapy, cytokine therapy, oncolytic virus therapy, and cancer vaccines. We believe that innovative models are needed to assist in the nonclinical-assessment of immunomodulatory therapy safety and efficacy. Such models could not only improve the development of safer and more efficacious therapies, but also help identify responders and better predict therapeutic window and combinations.

3.1. Adoptive cell therapy

Through progress in genetic engineering and *ex vivo* T cell manufacturing processes, adoptive cell therapy (ACT) has risen to be one of the fastest-growing immuno-oncology fields in the past decades [22,157]. This therapy encompasses broad approaches to isolate cancer-reactive immune cells from the body, enhance and expand them *ex vivo*, and reinfuse them back into the patient. ACT utilizes endogenous tumor-infiltrating lymphocytes or genetically engineered T cells that express either highly specific TCRs or CARs. Genetic modification to generate CAR expression has been successfully implemented not only on T cells, but also on NK cells and macrophages [158,159]. In contrast to TCR-T cells, CAR-modified cells can detect epitopes of tumor-associated antigens independent of the presence of the major histocompatibility complex (MHC) molecules on the cancer cell's surface, which they often lose to evade the immune system [22,160]. Growing interest in ACT is marked by remarkable results from clinical trials using anti-CD19 CAR-T cells against B cell malignancies. These results led to the FDA approval of the first cell therapy for cancer treatment, and subsequently its integration into standard cancer care [21,161]. In fact, compared with other immuno-oncology therapies, ACT represents the largest growth of development in 2017–2019, with nearly 1200 new cell therapy products that are currently in preclinical and clinical evaluation [162,163].

One of the major question marks for ACT, specifically CAR-T cell therapy, is whether it will expand beyond B cell malignancies to

other cancer types, including solid tumors [161]. So far, the success of CAR-T cell therapy against solid tumors remains limited due to various challenges associated with the TME [88]. Moreover, ACT can be accompanied by severe side effects such as CRS, which is an overreaction of the immune system that can be lethal if not treated [164]. Besides CRS, there are a number of further complications associated with ACT, such as neurotoxicity (cerebral edema, seizures, delirium, aphasia) and hemodynamic instability (capillary leak syndrome, hypotension, tachycardia), which can lead to widespread organ dysfunction [22,165]. Below, we discuss how iCoC platforms have been utilized to elucidate the underlying complex mechanisms of both the immunosuppressive TME and ACT-mediated adverse events.

3.1.1. iCoC approaches to study TME effects on ACTs

Various aspects of the TME are suggested to be the major obstacle to CAR-T therapy: The TME presents both physical and biochemical barriers to the infiltrating T cells and might consequently induce their exhaustion [21,88]. Attempts to gain further insights into these mechanisms in 3D microenvironment have been done using 3D *in vitro* models such as spheroids, organoids, and scaffold-based constructs [166–170]. Wallstabe et al., for instance, tried to assess the efficacy of CAR-T cells against human lung and mamma carcinoma by measuring their infiltration, proliferation, cytolytic activity, and cytokine secretion in a dynamic flow setting using decellularized porcine jejunum matrix [170].

As next-generation *in vitro* models, microfabrication and microfluidics-based iCoCs now enable to precisely manipulate the spatial location of the cells, vascular barriers, oxygen/chemokine transport, and biophysical forces on physiological length scales. Ando et al., for instance, investigated the effect of hypoxia on CAR-T cell infiltration into a solid tumor utilizing a microphysiological tumor model featuring defined oxygen gradients and comprising HER2+ ovarian cancer cells (SKOV3) embedded in a GelMA hydrogel [68]. By combining computational modeling of oxygen transport with fluorescent oxygen sensor-based characterization of the gradient, they were able to precisely tune oxygen levels in the tumor mass in the microfluidic channel. Their findings showed that lower oxygen levels (6–17%) actually enhance the cytotoxic activity of HER2-targeting CAR-T cells in a spatially-modulated manner. Despite the evidence of increased therapeutic resistance, heterogeneity, and progression of tumor under a hypoxic microenvironment, certain hypoxic levels may actually support higher cytotoxic effector function of T cells [112], which was revealed in the iCoC model. This result also suggests that clinical observations of T cell suppression in lower oxygenated TME might not be a direct effect of oxygen level, but rather due to metabolic alterations driven by hypoxia [113,171]. Their iCoC model also recapitulated further clinical observation, namely that effector T cells enter the periphery of the hypoxic tumor mass but are excluded from the hypoxic core [172,173]. Despite this shallow penetration, the treatment still increases cancer cell death in the hypoxic core in the iCoC. Interestingly, this hypoxic core is absent of Granzyme B, a serine protease secreted by cytotoxic T cells during cellular immune response that induces cancer cell death. Granzyme B has been proposed as a potential early biomarker of efficacious cellular immunotherapy to identify responders, as it indicates the presence of actively engaged cytotoxic T cells [174,175]. The absence of Granzyme B in the core region might suggest that the noncontact mediated CAR-T cell cytotoxicity may not be dependent on Granzyme B but rather due to metabolic competition between cancer and CAR-T cells.

Another approach to model oxygen gradients was demonstrated by Aung et al., who recapitulated the hypoxic core of solid tumors by using spheroids of breast cancer cell lines (MCF-7 and

MDA-MB-231) in their iCoC model [75]. By co-culturing the hypoxic-core cancer spheroids with monocytes (THP-1) encapsulated within a GelMA hydrogel, they showed that monocytes promoted T cell (TALL-104) infiltration through the endothelial barrier (HUVECs) into the tumor site by secreting CCL4, CCL5, CCL11, CCL20, and CXCL8. Their platform also provided mechanistic insights about the regulation of T cell infiltration by monocytes: their findings showed that the chemokine release might be associated with hypoxia as their concentrations were not as high as when dispersed cancer cells (no oxygen gradient within the tumor mass) were employed.

Modeling the immunosuppressive TME is not only beneficial to compare cytotoxic ability of genetically engineered versus untreated T cells, but also of the same engineered T cells that underwent different preparation methods. By exposure to different microenvironmental conditions, for instance, the efficacy of TCR-T cells prepared via retroviral transduction and via mRNA electroporation was compared [70]. Thereto, TCR-T cells were injected into a microfluidic channel where they encountered and penetrated a three-dimensional solid tumor mass in the adjacent channel (human HepG2 liver carcinoma cells embedded in collagen type I hydrogel). Interestingly, they demonstrated that mRNA-TCR-T cells were overall less cytotoxic than retroviral-transduced TCR-T cells, which is not in agreement with the results from conventional 2D assays. This suggests that the cytotoxic ability of specific TCR-T cell variants might be influenced by T cell motility, which is not fully recapitulated in a 2D environment. The exact mechanisms are, however, still under investigation. Moreover, this microfluidic model was able to recapitulate a reduced cell killing of dispersed cancer cells by TCR-T cells by exposing the entire microfluidic chip to a low oxygen level (2%). The authors also showed that the addition of pro-inflammatory cytokines (IFN γ and TNF α) into the culture condition increases TCR-T cell cytotoxic ability against cancer cell aggregates, particularly in higher oxygen level (20%).

Using a similar model, Lee et al. investigated the immunosuppressive role of monocytes towards hepatitis B virus (HBV)-specific TCR-T cells with regards to programmed cell death protein-1 (PD-1)/programmed death-ligand 1 (PD-L1) signaling contribution [69]. Here, they showed that the proportion of PD-L1+ monocytes is significantly higher compared to those observed on cancer cells. This shows that the monocytes (not the cancer cells) might have a fundamental impact on impeding the TCR-T cells cytotoxic activity. Indeed, multiple myeloid cells express inhibitory molecules and therefore have been proposed to serve as therapeutic targets [176,177]. The iCoC model also confirmed this potential of TCR-T cells inhibition by monocytes through PD1/PD-L1 signaling; no difference of TCR-T cell cytotoxicity was observed in standard 2D cytotoxicity assays. Remarkably, however, such inhibition by monocytes was only seen on retrovirally transduced TCR-T cells, while mRNA electroporated TCR-T cells remained unaffected. Similar to the study described above, this implies that differences in engineering methods, culture, and expansion processes of TCR-T cells might render them more sensitive toward PD-1 inhibition, and that oversimplified models might not capture the implication of such differences. Potentially, such screening can be implemented in early drug development phases to evaluate ACT preparation methodologies, as well as in clinical setting to identify the most efficacious TCR-T cell types for personalized therapy.

Taken together, iCoC models were able to provide new insights about the roles of different immunosuppressive factors in the TME on ACT by precisely adjusting the relevant proportion of specific cell population, ECM, and oxygen level. The platforms can potentially be used to investigate further biophysical and biochemical cues listed in chapter 2. Moreover, such models have also been employed to evaluate drug candidates and recreate scenarios that

are often encountered in clinical setting, such as pretreatment with immunosuppressive agents and co-treatment with immune checkpoint inhibitor [68,70].

3.1.2. Modeling ACT-mediated toxicities

The Organ-on-Chip technology presents a great potential to address ACT-mediated toxicities, as it is able to recapitulate immune responses in different organs [178–181]. In addition, linking multiple organ chips allows the recreation of systemic interaction between multiple tissues and organs to predict unexpected adverse drug and inflammatory effects (Fig. 5) [182]. For example, the significant increase of inflammatory cytokine release (such as IFN γ and IL-2) by CAR-T cells upon their activation has been modeled *in vitro* [170]. This can potentially be recreated using OoC technology and coupled to other OoC platforms, such as the vasculature, to assess the effect of inflammatory cytokines to the endothelial activation, capillary leakage, and its subsequent effects (e.g. neurotoxicity) in a distant organ, similar to previous studies on neurovascular units [183,184]. A recent study reported the use of OoCs to study on-target off-tumor toxicities of BiTEs in the lung and the intestine [185]. The same concept can be applied to study on-target off-tumor toxicities of ACTs as these have been reported to occur in the liver, colon, and lung [186–188].

Additionally, the use of iCoCs is not limited to the assessment of endothelial cells activation and permeability, but also for investigating the crosstalk between engineered T cells and innate immune cells (e.g. macrophages, dendritic cells) and how they might contribute to adverse events leading to CRS. Owing to their ability to model immune response and simultaneously combine multiple organ systems, iCoC models present enormous potential to provide new insights into the pathogenesis of CRS and other ACT-mediated toxicities in a controllable and fully human setting.

3.2. Immune checkpoint inhibitors

Numerous immune cells, e. g. T cells, bear distinct “recognizing” receptors for receiving a primary, antigen-specific signal for initiation of a response to extracellular stimuli [189]. However, the direction and magnitude of the response are decided by the interplay of co-stimulating and co-inhibitory signals that are mediated by immune checkpoints: For initiation of the immune response, co-stimulating signals are required. Co-inhibitory signals serve as a negative feedback loop and play an important role in discontinua-

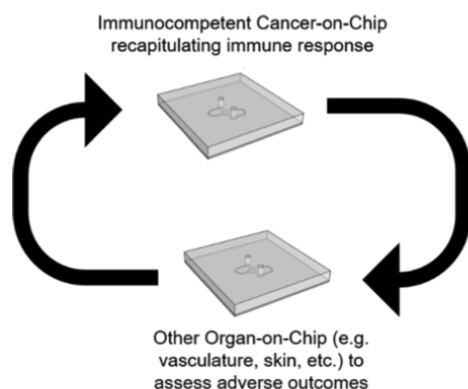


Fig. 5. Multi-organ-Chip approach to recapitulate systemic toxicities. Linking iCoC models with other OoC models may enable the recapitulation of immune-related adverse events in distant organs.

tion of immune response and prevention of autoimmune reactions. The expression of immune checkpoints is differentially and tightly regulated through every stage and location of immune cell activation. For instance, co-stimulating CD28 is constitutively expressed on T cells, while one of the major negative regulators cytotoxic T-lymphocyte-associated Protein 4 (CTLA-4) is rapidly transported to the cell surface upon T cell activation, downregulating the immune response through competitive inhibition. Hence, inhibition of the checkpoint CTLA-4 leads to an enhanced activation and priming of antigen-specific T cells, acting primarily at the level of T cell activation and proliferation in the draining lymph nodes [189]. To the contrary, PD-1 is highly expressed on T cells with exhausted phenotypes as a result of constant exposure to antigen stimuli, as present in the TME. PD-1 interacts with its ligand PD-L1, which is expressed on many cancer cells and tumor-infiltrating immune cells and may contribute to immune escape. Inhibition of the PD-1/PD-L1 axis can remove suppression and restore preexisting T cell effector function, primarily at the site of the tumor [190]. While ICIs targeting these two axes are now standard treatments in oncology, several additional checkpoints expressed on exhausted T cells and associated with tumor-mediated immune modulation are currently of interest and might benefit from iCoC systems to improve understanding of efficacy, appropriate patient population, and most suitable combination therapies. This next generation of checkpoint inhibitors includes both receptors modulating T cells, such as e.g. LAG-3, TIM-3, VISTA (PD-H1), GITR, OX-40, IDO, ICOS, and TIGIT, but also Killer inhibitory receptors expressed by NK cells [191–193], and receptors modulating tumor-associated macrophage activity [194], with about 800 targets currently being investigated in clinical trials [162].

The treatment modality of immune checkpoint inhibitors (ICI) aims at restoring immune function in a dysregulated cancer immune environment by blocking key inhibitory regulators of the immune system. Since the approval of the CTLA-4 inhibitor ipilumab by the FDA for the treatment of metastatic melanoma in 2011 [195,196], the interest in ICI has grown enormously due to its substantial clinical benefit and durable response in multiple tumor types. The number of preclinical and clinical trials evaluating T cell-targeted modulators has increased to more than 4000 in 2020 [162]. To date, seven ICIs were approved by the FDA, including the aforementioned CTLA-4 inhibitor and three inhibitors each targeting PD-1 and PD-L1 [197]. Despite the promising long-term response with approved therapies in multiple carcinomas, some tumor types are completely refractory, and a significant number of patients who initially respond to the treatment eventually acquire resistance. Several resistance mechanisms have been identified, such as defects in antigen presentation, upregulation of additional inhibitory checkpoints, neoantigen depletion, and the immunosuppressive features of TME (reviewed by [8–11]). Thus, the lack of detailed understanding of the immunosuppressive TME and the numerous additional resistance mechanisms that are still unknown pose critical challenges in ICI therapy [198]. In addition, recent failures of ICI therapies in combination trials [199] despite promising pre-clinical data highlight the need for better pre-clinical models. Together with challenges in fully understanding the patient-specific risk for immune-related adverse events in patients treated with ICIs, the need for more physiologically relevant *in vitro* models is clearly highlighted.

3.2.1. Identification of responders in patient-specific iCoCs

The dynamic variation of immunogenicity in patients and cancer types makes it difficult to identify prognostic and predictive indicators for treatment success, contributing to a low response rate to ICI [11,200]. Many cancer patients with the targeted tumor type that fit all defined inclusion criteria for the use of an ICI emerge as non-responders [201]. The discovery by Chowell et al.

that a greater diversity of HLA molecules results in a larger repertoire of presented neoantigens and influences survival to ICIs underlines the importance of including the patient's genotype [202]. To capture the genetical phenotype, primary cells or iPSCs can be integrated in *in vitro* models. While stem cell derived sources are considered a solution when primary tissues from donors cannot be accessed, the immature phenotype, as well as the time and resources needed, represent drawbacks [203]. iCoCs reflecting the patient-specific genetic background pose a promising (screening) tool to identify responders to specific ICIs and are able to provide a balanced and personalized safety and efficacy profile before treatment. Moreover, they can be applied to establish biomarkers that guide the use of ICIs in the most appropriate patients.

Beckwith et al. and Moore et al. developed iCoC models that integrate tumor with native features of the TME such as the heterogeneity of the tumor and its microenvironment, containing resident and potentially exhausted TILs [83,145]. Beckwith et al. captured fragments of human non-small-cell lung carcinoma (NSCLC) biopsies in a retention zone in a microfluidic device (Fig. 2B). Constant perfusion not only delivered nutrients and removed metabolic waste via convective transport into the thick tissue fragments, but also mimicked high intratumoral hydrostatic pressure and enabled dynamic PD-1 inhibitor exposure. In tumor fragments of one of the two NSCLC patients, PD-1 inhibitors decreased tumor cell viability over the time course of 72 h. Whether these results correlate with the clinical benefits of PD-1 inhibitor treatment for (exclusively) one of the patients is unknown, but cross-correlation of *ex vivo* and *in vivo* results are aimed for and can be anticipated in the future. Decreased cancer cell viability was co-localized with tumor resident lymphocytes, supporting a hypothesized involvement of tissue-resident lymphocytes in viability decline. In a proof-of-concept study, Moore et al. captured 12 fragments from murine MC38 colorectal carcinoma biopsies in parallel in a platform termed EVIDENT (*ex vivo* immuno-oncology dynamic environment for tumor biopsies). In order to assess the killing efficiency of TILs, TILs were isolated from the same tumor biopsies, perfused through the system, and allowed to infiltrate into the tumor fragments. The authors claim that pre-treatment of TILs with PD-1 inhibitor resulted in increased tumor cell death in proximity to infiltrated TILs in the murine model. Similar effects were observed in human NSCLC patients' specimen with autologous TILs. In addition to these proof-of-concept experiments, images of tumor viability and TIL infiltration were analyzed and quantified automatically based on machine learning, laying the foundation for a scalable platform to evaluate a patient's response to ICI.

While those two biopsy fragment-based *ex vivo* models are rather quick to set-up, *ex vivo* platforms do not allow the control of individual parameters similar to bottom-up approaches as described in Section 2.2. Al-Samadi et al. chose a bottom-up approach for their iCoC by embedding HSC-3 cancer cells in myogel, a human tumor-derived ECM [204]. Thereby, they could show that the migratory behavior of PBMCs from healthy donors was dependent on cancer cell density in the hydrogel, potentially reflecting gradients of chemokines. Using an advanced version of the model integrating patient-derived cancer cells and autologous serum, interpatient variability in migratory behavior of PBMCs upon PD-L1 inhibitor treatment was observed. To the contrary, migration of immune cells towards cancer cells in both patients was increased upon inhibition of IDO 1, an immune checkpoint protein that evokes T cell apoptosis and promotion of Treg differentiation and is known to be upregulated in HNSC patients. By using the patients derived cancer and immune cells with autologous serum in a human tumor-derived matrix, they provide a fully human TME to the cancer cells; this is an important step towards

precision medicine. Investigating new immune checkpoints as targets for ICI poses an important opportunity in the fight against resistance. Since inflamed "hot" tumors are associated with favorable response to ICI therapy [205], induction of immune infiltration with IDO 1 inhibitor opens the door to sensitize tumors to PD-L1 treatment, and testing synergistic effects of IDO 1 and PD-L1 inhibitors in a follow-up study would be intriguing.

3.2.2. iCoCs as high(er)-throughput screening tools

Compared to 2017, the number of T cell-targeted as well as other immunomodulators in the development pipeline increased by more than 220% in 2020 [162], underlining the high demand for high-throughput screening tools. Sarkar et al. applied a droplet-based screening platform as a high throughput microfluidic cytotoxicity assay, in which a multiple myeloma cell line and donor-derived NK cells or an NK cell line were encapsulated [206]. They observed a significantly increased target cell death upon treatment with α PD-L1 as well as lenalidomide, an immunomodulator that has demonstrated activation of T and NK cells and anti-cancer effects. However, basic interactive characteristics such as contact or death times were not affected by the treatments. With the gained information, a computational drug screening approach was implemented to determine the efficiency of NK-mediated immunotherapies against multiple myeloma. The droplet-based platform paves the way for patient-specific cytotoxicity assays in immunotherapy screenings, but has its limitations with regards to the microenvironment and long-term cultivation. In an advanced droplet-based screening platform, immunogenic diffuse large B cell lymphoma (DLBCL) spheroids were generated, cultivated, and assessed in a single device [207]. Tumor-stromal-immune spheroids comprised a mixture of cells similar to the TME in Non-Hodgkin lymphoma and were embedded in a composite hydrogel. Subsequently, these spheroids were trapped in a docking array and continuously perfused with a flow rate similar to the velocity of blood in the tumor. In these co-culture spheroids, lenalidomide exhibited direct anti-proliferative effects on both DLBCL and stromal cells while enhancing the proliferation of activated immune cells. Via secretome profiling, dynamic changes of several pro- and anti-inflammatory cytokines upon lenalidomide treatment were detected. Compared to the perfused 3D spheroids, stromal and tumor cell proliferation and death were notably higher when cultivated in monolayers in microplates. In this study, the immunomodulatory compound lenalidomide was applied. However other immunotherapies such as ICIs may also be tested using this platform. This platform succeeded in recapitulating many parameters of the TME while keeping higher-throughput modalities. In the future, the system could be advanced to a patient-specific screening tool to validate immunotherapies.

3.2.3. Overcoming resistance by defining synergistic drug combinations in iCoCs

A pressing challenge in immunotherapy is to increase the population that would benefit from immunomodulating agents [201]. Underlying resistance mechanisms can be rooted in every step of the immune-cancer interaction and enable therapeutic interventions at distinct targets and stages of the immune response. Different immunotherapeutic strategies can be combined with each other and with chemotherapy, targeted therapy, and radiotherapy to achieve therapeutic effects that are superior to the additive effect of each of the components [208]. Hence, there is a great need to further elucidate mechanisms of resistance and determine effective and tolerable combination therapies, including dosing and scheduling thereof [9]. iCoCs can recapitulate several steps of the cancer-immune interaction, facilitating the simultaneous testing of therapeutic strategies that intervene at different stages of the immune response in the same model.

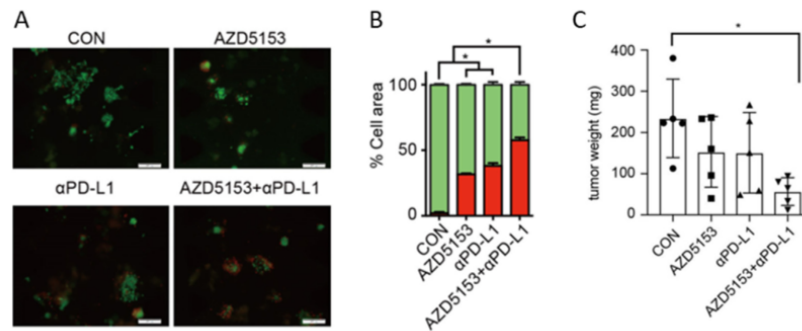


Fig. 6. Comparing *in vitro* response of PDOTS in iCoCs to combinational therapy with *in vivo* data of a mouse model. A) PDOTS from ascites of an untreated ovarian cancer patient were treated with a single exposure to AZD5153 or α PD-L1, and combinational strategy demonstrates synergistic effects of both agents. B) Corresponding live/dead quantification of A). C) Mice were treated with the same conditions as in (A) and cytotoxic and synergistic effects of AZD5153 and α PD-L1 with PDOTS in iCoCs were confirmed in mouse models (Reproduced from [211], CC BY).

A common combination tested in immunotherapy is the combination of a CTLA-4 inhibitor, leading to enhanced priming and activation, and inhibition of the PD-/PD-L1 axis, acting on the effector phase in the TME [209]. This combination was studied by Jenkins et al. and Aref et al. [85,86] on murine- and patient-derived organotypic tumor spheroids (MDOTS/PDOTS). MDOTS of several cell sources with contrasting sensitivities were created and *in vitro* efficacy of PD-1 inhibition in terms of cell death was compared to *in vivo* data in terms of mouse survival. Furthermore, PDOTS from patients with the shortest progression-free survival elaborated immunosuppressive cytokines/chemokines in the microfluidic device, of which several are components of the recently reported innate PD-1 resistance gene expression signature. The concept of dual therapy was applied to PDOTS derived from melanoma, thyroid, and pancreatic adenocarcinoma, determining the upregulation of the cytokines CCL19/CXCL13 as a readout. Upregulation of CCL19/CXCL13 is a measure of early immune activation and an important feature of the immune response to PD-1 blockade, as shown in biopsy samples. Dual treated PDOTS did not show an increased upregulation of the cytokines compared to PD-1 alone, and was minimal upon CTLA-4 treatment. In a follow-up study, Aref et al. [86] used the same platform and confirmed that α CTLA-4 is not contributing to immune-mediated killing with PD-1 inhibition by measuring direct cytotoxic effects. However, cellular changes were mapped via RNA-sequencing, revealing an expansion of CD8+ T cells and M0 macrophages in PDOTS treated with PD-1 + CTLA-4 inhibitor. Neither upregulation of cytokines nor cytotoxicity upon ICI treatment could be replicated in multi-well plates, where cells were grown in 2D. Furthermore, Jenkins et al. combined inhibition of PD-L1 and TBK1/IKK ϵ , two immune signaling kinases that have been shown to restrain T cell activation. In an attempt to render the immunosuppressive TME more permissive for T cell function, TBK1/IKK ϵ were inhibited with Cmpd1 in MDOTS and mice. In combination with PD-L1 inhibitor, *ex vivo* killing of MDOTS was enhanced upon TBK1/IKK ϵ inhibition with Cmpd1, and survival of syngeneic mice was prolonged compared with either treatment alone.

Li et al. exposed PDOTS of high-grade serious ovarian cancer as well as mice to a combination of a PD-L1 inhibitor and the BRD4 inhibitor AZD5153, known to reprogram tumor-associated macrophages from M2 to M1-like macrophages *in vitro* [210]. Tumor weight of mice receiving the combination therapy was more reduced compared to a single administration of the molecules and synergistic effects were replicated in the microfluidic system,

showing extended cell death with the combination compared to the single agents (Fig. 6).

Combinations of immune checkpoint inhibitors and ACTs are also promising and have already been tested in iCoCs: Ando et al. modeled the heterogeneous oxygen landscape within a tunable ECM for the evaluation of CAR-T cell cytotoxicity and infiltration in solid tumors [68] (Section 3.1). The authors claim an overall upregulation of PD-L1 under hypoxic conditions (oxygen levels of 0–17%) and an increased surface expression, making PD-L1 a promising target to render the hostile microenvironment more responsive to CAR-T cell therapy. Hence, in an attempt to rescue low CAR-T induced cytotoxicity, combination treatment of PD-L1 inhibition and CAR-T cells was tested but did not yield any significant therapeutic benefits. Lee et al. increased the architectural complexity of the TME by adding cellular components [69]. Monocytes were reported to impede natural T cell functions via PD-L1/PD-1 pathway in hepatitis B virus (HBV)-related hepatocellular carcinoma (HCC). Therefore, the authors investigated the immunosuppressive potential of monocytes towards HBV-specific TCR-T cells. Suppression of HBV-specific TCR-T cell cytotoxicity by monocytes depended on the production method of TCR-T cells and could be rescued by blocking the PD-L1/PD-1 signaling pathway. These mechanistic insights provide the potential to optimize the currently described therapeutic strategies.

3.2.4. Dissecting effects of the immunosuppressive TME on ICI therapies

Immune cell extravasation, migration, and effector functions are tightly regulated and potentially hindered by immunosuppressive factors present in some solid tumors, making the TME one of the major causes of failure of ICI therapies. In the TME, there are many factors that influence each other, and dissecting the role of each parameter provides valuable mechanistic insight in this interplay. In the following studies, the immunosuppressive TME was modeled to dissect the roles of immunosuppressive components.

In the study of Cui et al., a glioblastoma model with TAMs as stromal cells and T cells as immune components was utilized to dissect the heterogeneity of the immunosuppressive TME and optimize PD-1 therapy [212]. Glioblastoma (GBM) is a genetically heterogeneous disease with a highly immunosuppressive TME, marked by a high abundance of TAMs and a low number of CD8+ T cells. The microfluidic model contains human brain microvascular endothelial cells in an outer ring, and TAM as well as patient-derived GBM cells of three distinct GBM subtypes in an adjacent

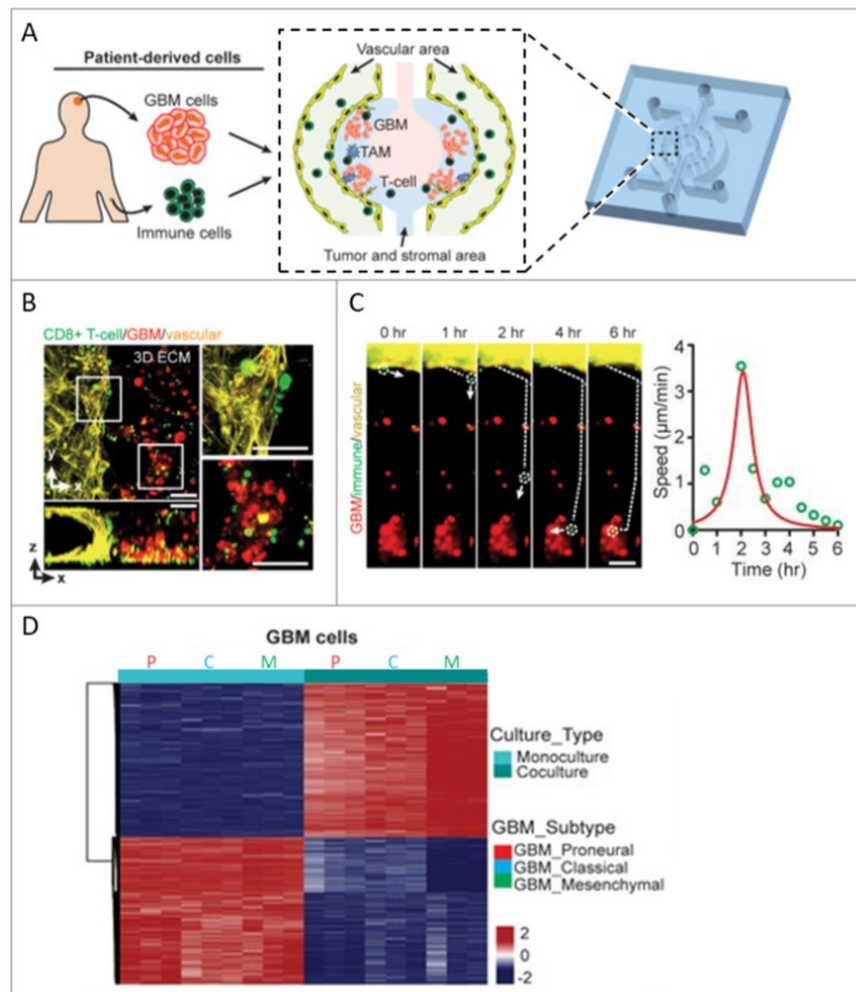


Fig. 7. Glioblastoma-on-Chip for dissecting the effects of TAMs. A) Schematic illustrating the iCoC with patient-resected glioblastoma (GBM) cells and human primary immune cells. The peripheral vascular region (yellow) is perfused and delivers T-cells. The middle area contains tumor cells and TAMs in a hydrogel mimicking ECM (blue) and surrounds a central region for medium supply (pink). B) Confocal immunofluorescence image showing endothelial lining of the microvessel (yellow) and GBM cells (red) with T cells (green) in close proximity to both. Scale bar is 50 μm . C) Time-lapsed images showing extravasation, infiltration, and interaction of a single T cell with GBM tumor (colors as in B). Scale bar is 50 μm . Quantification of migration speed indicates maximum speed after extravasation and before contacting GBM cells. D) GBM cells from patients of the proneural (P), classical (C), and mesenchymal (M) subtype were cultivated in the iCoC for 3 days. Up to 10,000 probes were differentially methylated when cultivated in coculture with macrophages. (This section is an excerpt of the original, since the annotation was modified. Reproduced from [212], CC BY). (For interpretation of the references to colour in this figure legend, the reader is referred to the web version of this article.)

compartment (Fig. 7A). Allogeneic IL-2 activated CD8+ T cells were perfused through the endothelial lined microvessels to investigate dynamic extravasation, migration, interaction with TAMs and GBM, and cytotoxic activity (Fig. 7B and C). In their model, the therapeutically least responsive subtype of GBM showed the highest number of immunosuppressive features, consistent with clinical data. Specifically, compared to the classical and proneural subtypes, the mesenchymal subtype (MES) showed the lowest number of extravasated T cells and the highest number of M2-

like TAMs. The presence of TAMs not only reduced T cell extravasation which suggests inhibitory effects of TAMs, but changed the methylation of GBM cells of all subtypes (Fig. 7D). Migration trajectories and speed showed reduced motility of T cells in MES models. Accordingly, expression of T cell markers for activation and cytotoxicity was lowest and PD-1 expression highest in MES models compared to the other subtypes. These immunosuppressive features could be attributed to the presence of MES GBM cancer cells, which also exhibited the highest PD-L1 levels, as their

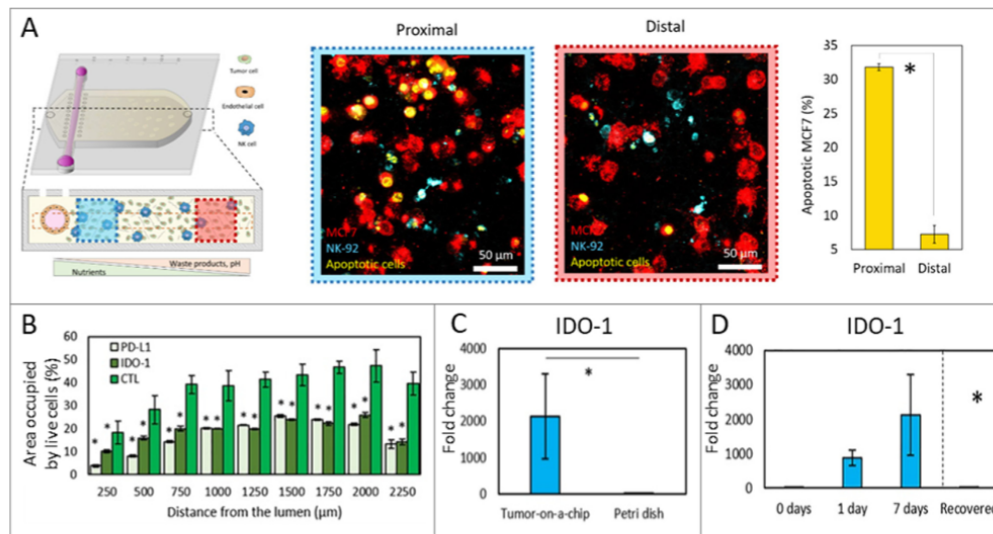


Fig. 8. MCF-7 induced suppressive environment induces exhausted phenotype in NK cells. A) Schematic of the iCoC and confocal images showing NK-92 cells (cyan) and MCF-7 cells (red) proximal to the lumen (blue box) or in greater distance (red box). NK cell cytotoxicity was reduced in the distal region as reflected by the number of apoptotic cells (yellow), quantifications are shown in the bar graph. B) Cytotoxic capacity of NK-92 was restored with the α PD-L1 antibody or IDO-1 inhibitor. C) Bar graphs depicting the change in gene expression of IDO-1 in an iCoC versus a petri dish. D) Bar graphs showing IDO-1 upregulation in NK-92 during 7 days of co-culture with MCF-7 in the iCoC. Upon 1 week of recovery in a monoculture in a traditional flask, IDO-1 returned to the basal expression. (This section is an excerpt of the original, since the annotation was modified. Reproduced from [71], CC BY-NC). (For interpretation of the references to colour in this figure legend, the reader is referred to the web version of this article.)

absence reversed these effects. MES GBM highly secreted M2-promoting CSF-1 and further cytokine profiling revealed a milieu that favors TAM polarization towards M2, which is reflected in the profound number of M2-like TAMs in the MES models. The presence of TAMs not only impacted CD8⁺ T cell infiltration, but also changed the epigenetic signature in GBM cells in co-culture and vice versa.

Other than dissecting the influence of the cellular components of the GBM model, Cui et al. also optimized PD-1 therapy by simultaneously applying the CSF-1R inhibitor BLZ945. BLZ945 suppressed M2 phenotype without affecting PD-L1 expression on TAM or GBM, suggesting an insufficient reversion of immunosuppression in monotherapy. However, CSF-1R inhibition significantly enhanced CD8⁺ T cell extravasation. Inhibition of PD-1 enhanced CD8⁺ activation, and dual blockade combined both effects, resulting in reversed TNF α and TGF β profiles and augmented cytotoxicity, in particular in the MES subtype.

This study demonstrates how a complex model of the immunosuppressive TME can profoundly increase our understanding of immune-cancer interaction by dissecting the influence of its single components. Correlation with clinical data confirms the relevance and indicates translatability to patients. Testing of adjuvant therapy that simultaneously targets M2-polarization via CSF-1 signaling and PD-1 proves to be a promising strategy, in particular in the MES subtype that is associated with a highly immunosuppressive TME and poor prognosis.

Nguyen et al. investigated the effects of CAFs and the targeted therapeutic trastuzumab on the immune response [79]. While the mechanism of action of trastuzumab differs from ICIs, both therapies apply a monoclonal antibody and the investigation of cellular components of the TME is just as relevant for ICI therapy as for all immunotherapies. Trastuzumab targets HER2 on breast

cancer cells, but does not only act via direct inhibition of proliferation and induction of apoptosis, but also indirectly by inducing immune response mediated through ADCC. The central compartment of the microfluidic platform was lined by a monolayer of endothelial cells and flanked by two chambers that contained HER2⁺ breast cancer cells with PBMCs in collagen hydrogels. Exclusively one of the chambers also comprised CAFs in order to be able to compare conditions within the same chip. The platform mirrored the *in vivo* microarchitecture and proportion of cell types and enabled modulation of the experimental setup to dissect the effects of specific cellular components or a therapeutic antibody. Cytostatic and cytotoxic effects of trastuzumab as well as increased frequency of interactions of immune cells with cancer cells was observed via live-cell imaging and quantified with automated image analysis (Section 2.3). Trastuzumab promoted long-term cancer-immune interactions (>50 min) with correlated stimulation of cancer apoptosis, but failed with cancer cells that were not HER⁺. These results suggest a recapitulation of anti-tumoral ADCC as a consequence of trastuzumab binding the HER2 receptor on-chip. In terms of stromal effects, this study revealed that trastuzumab-induced ADCC is dependent on the local density of infiltrating immune cells. Furthermore, immune-suppressive CAFs antagonized increased frequency of contacts between cancer and immune cells and slightly inhibited trastuzumab-induced ADCC. In the absence of trastuzumab, augmentation of the velocity of cancer cell migration was detected, suggesting pro-invasive effects of CAFs. This iCoC could be further used for basic studies focusing on the TME and the investigation of tumor response to treatments such as ICI.

A further iCoC from Ayuso et al. created a suppressive environment that compromised NK cell cytotoxic capacity [71]. In the microfluidic device, a HUVEC-lined lumen was surrounded by

MCF-7 tumor cell-containing collagen with NK-92 either dispersed within the hydrogel or added via perfusion through the lumen (Fig. 8A). A gradient of nutrients, pH, waste, etc. was generated by the metabolic activity of MCF-7 and led to environmental stress on NK-92 cells. As a result, the cytotoxic activity of NK-92 in greater distance from the lumen was reduced (Fig. 8A). Furthermore, exhaustion genes such as IDO-1, PD-1, and CTLA4 were upregulated and activation/prosurvival markers such as GZMB and BCL1 downregulated. The exhausted phenotype could not be replicated in a 3D culture in a traditional dish, suggesting that chronic activation through co-culture plays a minor role in immune exhaustion compared to the environmental stress generated by MCF-7 in the iCoC (Fig. 8C). α PD-L1 antibody atezolizumab and IDO-1 inhibitor epacadostat restored cytotoxic activity in the tumor-chip particularly in close proximity to the lumen (Fig. 8B), with little efficacy in traditional well plates. Recovery of NK-92 from the microfluidic platform and cultivating exposed NK-92 in a traditional flask for a week showed that multiple genes returned to basal level (IDO-1, Fig. 8D), while others showed only partial (GZMB) or no (IL-1) recovery compared to naïve NK-92 cells. This platform provides a tool to investigate epigenetic and molecular alterations that lead to long-lasting immunosuppressive effects of environmental stress on NK cell biology.

3.2.5. An unmet need: Researching immune-related adverse events of ICIs

Although ICIs are well tolerated, undesired immune responses appear as a result of unleashing the immune system by inhibiting the physiological brake of immune activation and disrupting the balance between tolerance and immunity. The mechanism of immune-related adverse events (irAE) differs between ICIs: PD-1/PD-L1 inhibition, for instance, occurs in peripheral tissue on T cells that are already engaged in an ongoing effector T cell response. Hence, irAE seem less likely than for CTLA-4 inhibition, which regulates early T cell activation and might take place in all lymph nodes where an immune response is initiated [213]. Effects on non-tumor-specific T cells that target self-antigens on healthy tissue result in immune-mediated inflammation of almost any organ or tissue with varying incidences and severities [214–216]. Up to 70% of patients treated with a PD-1/PD-L1 antibody experience severe irAEs, frequently affecting the skin, the digestive tract, and the liver [217–221]. More rare, but significant due to associated mortality, are reported events of ICI-associated myocarditis [222,223]. Toxicities of ICI combination therapy are associated with a markedly greater risk of severe adverse events such as diarrhea/colitis, transaminitis, and fatigue [218]. In severe cases, additional immunosuppressive therapy or discontinuation of immunotherapy may be required [224]. However, currently no robust testing, diagnostic and management approaches for ICI toxicity are established and represent an unmet need [225]. To our knowledge, no iCoCs were yet applied for toxicity studies despite the relevance of irAE in ICI therapy. As in the previously discussed efficacy studies, predictive biomarkers for irAE are absent and patient-specific *in vitro* models may provide the opportunity to take irAE into consideration for treatment-related decisions [226]. For instance, to identify the population of certain cancer types where the benefit of combination therapy outweighs risk [227]. Furthermore, combining iCoCs with organs such as skin, intestine, liver, or heart might provide a valuable tool to investigate off-target effects (Fig. 5).

3.3. Cytokine therapy

Cytokines can act during every phase of cancer-immune interactions by, for instance, improving antigen priming, enhancing the recruitment of effector immune cells into the TME, or increas-

ing their cytotoxicity [190]. Cytokines impact tumor growth directly via anti-proliferative or pro-apoptotic activity or indirectly by stimulating cytotoxicity of the effector cells [4]. Since the potent anti-tumor activities of pro-inflammatory cytokines were discovered, interferon-alpha (IFN- α) and interleukin-2 (ILN-2) were approved by the FDA for several malignant diseases. Moreover, inhibition of immunosuppressive cytokines as well as novel targets are currently explored. In general, however, cytokine therapy is limited by the short half-life of most cytokines, a narrow therapeutic window with only modest anti-tumor efficacy, and a less favorable safety profile compared to ICI. As with the previously discussed modalities, synergistic combinations (e. g. with ICI or CAR-T) to increase efficacy are a potential option. Furthermore, several strategies are being tested to enhance local concentration, such as intratumoral gene therapy vectors that encode cytokines. In this section, we review studies of cytokines in iCoCs, which encompass target discovery, combinational therapy, and targeted chemokine delivery.

To identify and validate cytokines as potential therapeutic targets, Xie et al. [51] and Wu et al. [60] exposed iCoCs integrating monolayers of cancer cells and adhering immune cells to immunosuppressive cytokines. Xie et al. studied the inhibitory effect on cell migration by monitoring the migratory responses of metastatic breast cancer cells and neutrophils in the microfluidic platform [51]. Cancer or immune cells were aligned at docking structures before exposure to a stable gradient of activin A, a cytokine of the transforming growth factor beta 1 (TGFB-1) superfamily that is overexpressed in breast cancer cells. Cell migration analysis at the single-cell level provided information on migration distance and chemotaxis, including transendothelial migration. Using this rather simple iCoC, the authors successfully characterized the effect of activin A on neutrophil-cancer migratory interactions and identified activin A as a potential therapeutic target.

Wu et al. employed a more complex optofluidic drug-screening platform that enables simultaneous cancer secretion profiling, analysis of cancer-immune system communication and drug screening on a single device [60]. The immunosuppressive secretome of HeLa cells was quantified on-chip by a surface-enhanced Raman scattering (SERS)-assisted multiplex immunoassay with high sensitivity. Conditioned culture medium was perfused from the culture chamber into the antibody barcode, which was patterned with TGFB-1, prostaglandin E2 (PGE2) and interleukin 10 (IL-10) antibodies and captured corresponding secreted proteins. After profiling of the cancer secretion, the medium was redirected into the extracellular environment of T cells and their proliferation monitored. Thereby an inhibitory effect on immune cell proliferation was observed which could be partially recovered by addition of neutralizing antibodies or artemunate, a drug that inhibits the secretion of these cytokines. This confirmed anti-proliferative effects of TGFB-1, PGE2 and IL-10 induced by HeLa secretions. This integrated SERS-microfluidic platform nicely highlighted how target identification as well as discovery and validation of novel drugs could be accelerated in preclinical studies.

The first two steps in the immune-cancer response are the release of cancer cell antigens and the subsequent antigen uptake and presentation by DC initiating an antigen-specific response. These two steps are targeted in the iCoC of Parlato et al., who enhanced immunogenic cell death of cancer cells with a histone deacetylase inhibitor (HDACi) and activated DCs with IFN- α [57]. Their iCoC consists of a central chamber containing IFN- α activated DCs and two flanking compartments with colorectal cancer cells embedded in a hydrogel. The central chamber and flanking compartments are connected via micro-channels featuring dimensions and geometry similar to the blood vessel and tissue interstitial areas. The microarchitecture, porosity, and stiffness of the hydrogel were adapted to recapitulate physical and biochemical cues *in vivo*.

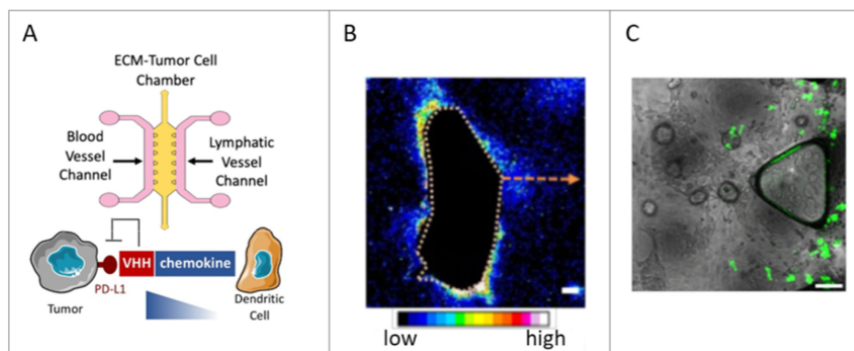


Fig. 9. Applying iCoC to evaluate the dynamics of chemokine-conjugated antibodies and their impact on immune cells. A) The microfluidic device contains an ECM-tumor cell chamber positioned between two microfluidic channels containing media, each lined with HUVECs or human lymphatic dermal microvascular endothelial cells. B) CCL21(T)-B3 effectively targets the tumor cells and creates a steep concentration gradient in close proximity of the tumor spheroid (outlined with dashed line). Scale bar is 10 μm . C) CCL21(T)-B3 increases infiltration BMDC (green) and directs the movement towards tumor cells. Scale bar is 50 μm . Reprinted with permission from [229]. Copyright 2019 American Chemical Society. (For interpretation of the references to colour in this figure legend, the reader is referred to the web version of this article.)

Monitoring of the infiltration of IFN- α treated DCs through the micro-channels into the cancer compartment revealed an enhanced migration towards HDACi treated cancer cells. This was largely guided by an upregulation of the chemokine CCL12 and the respective receptor CXCR4 on DCs. Migration velocity reversely correlated with longer interaction times, suggesting pausing of DCs for endocytosis. Subsequent to antigen uptake, there is evidence that antigen-loaded DC may make a direction choice and choose to leave the tumor environment, indicating trafficking towards lymph nodes. This model shows how two different anti-tumor agents can have complimentary anti-cancer effects and enable mechanistic analysis of immune-cancer interaction.

The type, density, and location of tumor-infiltrating immune cells are critical determinants of patient outcome [228]. Enhancing the homing of effector cells with chemokines may improve immune response and efficacy of immunotherapies such as CAR-T therapy or ICI. In the following iCoC studies, the immunosuppressive TME was modeled to investigate dynamics, specificity, and effects of targeted chemokines and immune cells on cancer.

Fang et al. conjugated the chemokine CCL21 to a PD-L1 blocking single-domain antibody fragment to exploit its therapeutic effects as well as its specific targeting properties; thereby the bispecific molecule should be localized in close proximity to the tumor (Fig. 9A and B) [229]. In the iCoC model, B16 melanoma cells were embedded in a collagen hydrogel, flanked by two channels lined with human umbilical vein endothelial cells (HUVECs) and human lymphatic microvascular endothelial cells (Lym-HMVEC) that mimic blood and lymph vessels respectively (Fig. 9A). Utilizing this system, the specific binding of the fusion protein to PD-L1 expressing melanoma cells could be verified, eliciting a concentration gradient in the tumor spheroids vicinity (Fig. 9B). Indeed, in the presence of the bispecific molecule, bone-marrow-derived dendritic cells (BMDCs) extravasated through the lymphatic channel and migrated through the hydrogel towards the tumor spheroid with increased speed and persistence (Fig. 9C). In this study, a therapeutic molecule that could enhance immune cell infiltration as well as a model that elucidates drug distribution and its influence on cell migration within the TME was developed.

Ayuso et al. applied an iCoC to elucidate the dynamics of NK cells and a chemokine-conjugated antibody, as well as subsequent cytotoxic effects and NK-mediated ADCC [76]. The microfluidic platform incorporated an MCF-7 breast cancer spheroid with a

hypoxic core in a collagen hydrogel, mimicking a solid tumor model that may obstruct drug penetration and cell migration. Two lumens lined with endothelial cells crossed the hydrogel and could be perfused with media, NK cells, macromolecules, or combinations thereof. Perfusion with an α -EPCAM antibody revealed its ability to cross the endothelial barrier and passively diffuse through the collagen hydrogel. However, cell-cell junctions of the cancer spheroid posed an impermeable barrier and hindered antibody penetration into the spheroid. Antibodies on the tumor cells' surface were endocytosed into intracellular lipids, which was not observed in spheroids of healthy breast cell lines MCF-10A and suggests an immune escape mechanism by the MCF-7 tumor cells. In contrary to the antibody, NK cells exhibited intense chemotactic migration towards the spheroid with increased directionality in proximity to the tumor. In a cell density-dependent manner, NK cells penetrated the spheroid by squeezing through the cell-cell junctions and killed tumor cells in the center of the spheroid, despite hypoxia. In the presence of an IL-2 conjugated α -EPCAM antibody, NK cell-mediated cytotoxicity was significantly increased and located mainly at the spheroid periphery, presumably due to the limited penetration of the targeted cytokine into the tumor. This study sheds light on endothelial permeability, tumor penetration, and antibody clearance by tumor cells and identifies several potential targets for immunotherapy. In this model, compounds targeting the tumor shedding mechanism could be tested. Further research with this model may elucidate how NK cells move through the tumor cell-cell junctions to generate NK cells with higher penetration capabilities as well as identification of new therapeutic targets that prevent NK cell exhaustion in long-term studies.

In cytokine therapy, iCoCs were applied for target discovery, showing the potential of an integrated platform and the testing of a synergistic combination, gaining insights in migration characteristics and antigen uptake by DCs. In more complex models, dynamics and effects of a targeted cytokine and immune cells were investigated and evidence of replicating a tumor evasion mechanism was demonstrated. Such a complex iCoC represents a valuable tool that could further contribute to examine other immunotherapeutics, including but not limited to the investigation of antibody dynamics within a TME for ICI therapy or T cell engagers. Moreover, many additional synergistic combinations could be tested as well as alternative delivering strategies, e.g. intratumoral

gene therapy, which would greatly benefit from the 3D TME context.

3.4. Oncolytic viruses

Oncolytic viruses (OV) encompass immunotherapy and cytotoxic drug properties. They preferentially target tumor cells inside which they replicate to lead to their destruction along with the release of progeny virions. The new viral particles can then attack additional tumor cells while sparing healthy cells. Such virus-driven attack awakes the immune response against the infected cells including innate and adaptive immunity leading to a specific antitumor immune response [230]. Over the years, numerous clinical trials have proven the good safety record of OV derived from different virus families. In 2015, Tamoligene Laherparepvec (T-vec), an HSV-1 derived virus expressing GM-SCF, was approved by the USA, European Union, and Australia for advanced recurrent melanoma [231]. Nevertheless, clinical efficacy of OV as a single agent is extremely limited compared to what has been anticipated by preclinical assessments. Several obstacles encountered by the OV are underestimated and not fully understood. Among them are 1) their tumor delivery in a perfused environment, comprising immune components that can sequester and clear the virus 2) their spreading inside a tumor mass with high interstitial pressure, rich in ECM and stromal cells 3) the interplay with the antiviral immune response [232]. As the virus tropism varies greatly between species, human iCoC models appear as privileged tools to address these questions. For example, evaluation of oncolytic Vesicular Stomatitis Virus (VSV) properties in an OoC comprised of vessel-like channels and 3D multicellular tumor spheroids, showed a more restricted tropism and replication than previously established in 2D culture [233]. Combined with real-time monitoring, this system successfully demonstrated the propagation of oncolytic VSV from a primary-infected tumor spheroid to a secondary one mimicking *in vivo* targeting of metastasis site by OV [234]. The model, however, was lacking immune cells, which are crucial to fully capture OV mode of action. Indeed, interplays between OV, immune system, and tumor are numerous and complex with the immune response being an essential part of OV activity while limiting OV spread [235]. iCoCs will be valuable assets to decipher such dynamics. By mimicking an immunocompetent tumor microenvironment with the ability to control its key components (Section 2.2), iCoCs should enable to break down the impact of different immune and stromal cells either on antitumor immunity or antiviral immunity and ultimately on the tumor destruction. Such mechanistic insights will allow the identification of cells that need to be boosted or impeded to optimize OV efficiency. These functions may then be implemented with the expression of therapeutic genes by OV [236]. Furthermore, OV offer a privileged approach to inflame tumor and potentialize the effect of other immunotherapies like ICI or ACT [237]. Due to iCoC's ability to emulate human TME with its physical barriers, intercellular crosstalk, and realistic cell motion in and out of the tumor, assessment of combination therapies with multiple variables (doses, timing of injection) holds the promise to more accurately predict clinical outcome. Moreover, it will avoid the need of surrogate viruses or agents with the suitable species-specificity for *in vivo* model. Lastly, iCoCs open the door for personalized medicine with the addition of immune and tumor components from each patient to assess their own susceptibility to different OV families and payloads.

3.5. Cancer vaccines

Cancer vaccines aim to induce *de novo* or boost antitumor immunity in “cold” tumors and in “hot” tumors, respectively. Different types of cancer vaccines have been developed including

molecular vaccines (DNA-, RNA-, or peptide-based)-, virus vector vaccines, and cellular vaccines [238]. Molecular- and viral-based vaccine components can be delivered to the patient via direct intranodal injection, passively through the lymphatic route, as well as active targeting of antigen-presenting cells (APCs) specific receptors [239]. Upon activation by the vaccine, the APCs can then mature, present tumor antigen, undergo trafficking to the tumor-draining lymph nodes, and ultimately prime effector T cells. Consequently, this should promote the proliferation of activated T cells and their migration to the tumor site to eventually kill cancer cells that display the associated target-antigen [239]. Cellular vaccines, on the other hand, rely on the *ex vivo* modification of patient-derived APCs to express tumor antigens, which are then reinfused back to the patient. In fact, the only cancer vaccine approved by the FDA so far, Provenge (Sipuleucel-T), uses this approach by activating autologous dendritic cells *ex vivo* and reinfusing them to prime the endogenous T cells and elicit an antitumor response [240]. Despite the enthusiasm that it brought to the field since its FDA approval a decade ago, broad adoption of cancer vaccines remains limited so far due to different sets of challenges. Clinical translation of therapeutic efficacy has often been poor [241,242], which mostly stem from the low immunogenicity of the vaccine and the negative regulatory mechanisms orchestrated by the tumor that induce immune tolerance [243]. Here, the use of nonclinical models that can translate to human immunity will be important to better predict clinical response upon vaccination and thereby optimize immunization strategy. A number of different approaches to model lymphoid tissues including microfluidic-based models have been introduced in recent years [244–247]. Linking iCoC models to these platforms is of high interest and can be used, for example, to evaluate effector T cells cytotoxicity after cancer vaccine treatment and assess the overall efficacy of combination therapy (e.g with ICI or targeted adjuvants).

To improve the therapeutic efficacy and the delivery of cancer vaccines, other approaches have been explored such as the use of multiple immunogenic antigens, and the integration of nanoparticles to facilitate vaccine transport to the lymph node [248,249]. The nanocarrier design, such as the particle size, composition, shape, chemistry, stiffness, etc., is influenced by the choice of antigen to be delivered [239]. As previously reported, OoC models can be used to evaluate the transport mechanism of nanoparticles through 3D tissue and barriers [250]. Connecting lymph-node chip to iCoC models could therefore also allow the assessment of nanoparticles' delivery and efficacy, thereby potentially accelerate nanocarrier design development. Taken together, iCoC models have the potential to boost cancer vaccine development by providing a human platform for nonclinical basic research and personalized screening in the complex TME.

4. Outlook

In 2016, Boussommier-Calleja et al. proposed the need to employ microfluidic systems to model the complex tumor microenvironment for studies on immune-cancer interactions due to their tremendous potential [146]. Now, iCoC models have been increasingly utilized to characterize mechanisms of actions of different types of immunotherapies and will potentially become a valuable asset in immuno-oncology research. The iCoC platforms highlighted here show that leveraging recent advances in microfabrication, microfluidics, biomaterials, and tissue engineering, complex immunocompetent cancer models that are human-relevant can be generated. The potential application areas of these systems are manifold, ranging from i) basic research of immune-cancer interaction, ii) efficacy and safety studies of different immunotherapies, to iii) personalized immunotherapy screening.

To reach the ambitious goal of broad application among biomedical research communities and drug developers, however, several challenges remain to be solved; many of which are related to the challenges OoC technology in general is facing [203,251]. For instance, iCoC models need to increase their throughput, manufacturability, and scalability in order to incorporate them in different stages of the immunotherapy development pipeline such as biomarker identification, target validation, lead selection, and lead optimization [203]. Owing to the bottom-up approach of the technology, it could in principle be possible to use the simpler iCoC models for higher throughput screenings for target identification, whereas the more complex iCoC models could be used for non-clinical efficacy and toxicity studies.

In the future, further research should target at incorporating multiple immune cell types, such as other myeloid-derived suppressor cells and Tregs, due to their critical immunosuppressive role within the TME [252,253]. Additionally, tissue/organ-specific resident cell types could be included to elucidate their possible role in modulating immune-cancer interaction within that specific organ. For example, in fat-rich tissues such as breast and prostate, cancer cells grow either nearby or in direct contact with adipocytes, which, in obese condition, can promote cancer progression by triggering chronic inflammatory responses. This is characterized by an increase of macrophages infiltration, chronic dendritic cell activation, and eventually T cell exhaustion [254,255]. This aspect could be addressed by direct integration of cancer tissue in immunocompetent "host" organ-on-chip models such as lung, liver, or adipose [256–258]. Linking iCoCs with other OoC-models has the potential to recapitulate systemic toxicities or other adverse effects of immunotherapy, such as CRS.

In terms of clinical translation, close interaction with biomarker development could be mutually beneficial: iCoCs could be used to discover novel biomarkers; established biomarkers could be utilized to correlate iCoC data to clinical data. Future works should also capitalize on the high-content characteristic of iCoC models by applying AI-based data analysis, e.g. for image interpretation. Other computational modeling approaches, such as modeling transport phenomenon in microfluidic devices [68,75] and molecular biocomputation for modeling signaling pathways [99], could be more widely integrated to support experimental data. Lastly, we believe that the utilization of iCoC models can provide entirely new and human-relevant insights for immunotherapy research, add an additional immune-competent nonclinical model for safety and efficacy testing of immune-based therapeutics, promote patient-specific medicine, and ultimately improve patient outcomes.

Funding

This project has received funding from the German Federal Institute for Risk Assessment under grant agreement No 60-0102-01.P581, the European Union's Horizon 2020 research and innovation programme under the Marie Skłodowska-Curie grant agreement No 845147, and the Innovative Medicines Initiative 2 Joint Undertaking (JU) under grant agreement No 853988. The JU receives support from the European Union's Horizon 2020 research and innovation programme and EFPIA and JDRF INTERNATIONAL.

Declaration of Competing Interest

The authors declare the following financial interests/personal relationships which may be considered as potential competing interests: Cecile Zaupé is employee of Transgene S. A. Michael Hudecek is an inventor on granted patents and patent applications

relating to CAR-T cell therapy. Birgit Fogal is an employee of Boehringer Ingelheim Pharmaceuticals, Inc.

Acknowledgments

We thank Claudia Teufel (University of Tübingen) for comments that greatly improved the manuscript.

Appendix A. Supplementary material

Supplementary data to this article can be found online at <https://doi.org/10.1016/j.addr.2021.03.015>.

References

- [1] A.D. Waldman, J.M. Fritz, M.J. Lenardo, A guide to cancer immunotherapy: from T cell basic science to clinical practice, *Nat. Rev. Immunol.* (2020) 1–18, <https://doi.org/10.1038/s41577-020-0306-5>.
- [2] J. Raja, J.M. Ludwig, S.N. Gettinger, K.A. Schalper, H.S. Kim, Oncolytic virus immunotherapy: Future prospects for oncology, *J. Immunother. Cancer.* 6 (2018) 140, <https://doi.org/10.1186/s40425-018-0458-z>.
- [3] A.M. Huehls, T.A. Coupet, C.L. Sentman, Bispecific T-cell engagers for cancer immunotherapy, *Immunol. Cell Biol.* 93 (2015) 290–296, <https://doi.org/10.1038/icb.2014.93>.
- [4] P. Berraondo, M.F. Sanmamed, M.C. Ochoa, I. Etxeberria, M.A. Aznar, J.L. Pérez-Gracia, M.E. Rodríguez-Ruiz, M. Ponz-Sarvise, E. Castañón, I. Melero, Cytokines in clinical cancer immunotherapy, *Br. J. Cancer.* 120 (2019) 6–15, <https://doi.org/10.1038/s41416-018-0328-y>.
- [5] S.J. Oiseth, M.S. Aziz, Cancer immunotherapy: a brief review of the history, possibilities, and challenges ahead, *J. Cancer Metastasis Treat.* 3 (2017) 261.
- [6] Bio, Biomedtracker, Amplion, Clinical Development Success Rates 2006–2015, 2016.
- [7] I.W.Y. Mak, N. Evaniev, M. Ghert, Lost in translation: Animal models and clinical trials in cancer treatment, *Am. J. Transl. Res.* 6 (2014) 114–118.
- [8] C.M. Fares, E.M. Van Allen, C.G. Drake, J.P. Allison, S. Hu-Lieskovan, Mechanisms of Resistance to Immune Checkpoint Blockade: Why Does Checkpoint Inhibitor Immunotherapy Not Work for All Patients?, *Am. Soc. Clin. Oncol. Educ. B.* 39 (2019) 147–164, https://doi.org/10.1200/edbk_240837.
- [9] L. Tran, D. Theodorescu, Determinants of resistance to checkpoint inhibitors, MDPI AG (2020), <https://doi.org/10.3390/ijms21051594>.
- [10] T.S. Nowicki, S. Hu-Lieskovan, A. Ribas, Mechanisms of Resistance to PD-1 and PD-L1 Blockade, *Cancer J. (United States)* 24 (2018) 47–53, <https://doi.org/10.1097/PP0.0000000000000303>.
- [11] E. Koustas, P. Sarantis, A.G. Papavassiliou, M.V. Karamouzis, The resistance mechanisms of checkpoint inhibitors in solid tumors, *Biomolecules.* 10 (2020) 666, <https://doi.org/10.3390/biom10050666>.
- [12] J. Bubienik, Tumour MHC class I downregulation and immunotherapy, *Oncol. Rep.* 10 (2003) 2005–2008, <https://doi.org/10.3892/or.10.6.2005>.
- [13] L.E. Klevorn, R.M. Teague, Adapting Cancer Immunotherapy Models for the Real World, *Trends Immunol.* (2016), <https://doi.org/10.1016/j.it.2016.03.010>.
- [14] M. De Palma, D. Hanahan, The biology of personalized cancer medicine: Facing individual complexities underlying hallmark capabilities, *Mol. Oncol.* (2012), <https://doi.org/10.1016/j.molonc.2012.01.011>.
- [15] F. Mami-Chouaib, C. Blanc, S. Corgnac, S. Hans, I. Malenica, C. Granier, I. Tihy, E. Tartour, Resident memory T cells, critical components in tumor immunology, *J. Immunother. Cancer.* 6 (2018) 1–10, <https://doi.org/10.1186/s40425-018-0399-6>.
- [16] Z. Bjornson-Hooper, G. Fragiadakis, M. Spitzer, D. Madhiredy, D. McLlwin, G. Nolan, A comprehensive atlas of immunological differences between humans, mice and non-human primates, *BioRxiv.* (2019), <https://doi.org/10.1101/574160>.
- [17] J. Mestas, C.C.W. Hughes, Of Mice and Not Men: Differences between Mouse and Human Immunology, *J. Immunol.* (2004), <https://doi.org/10.4049/jimmunol.172.5.2731>.
- [18] D. Eastwood, L. Findlay, S. Poole, C. Bird, M. Wadhwa, M. Moore, C. Burns, R. Thorpe, R. Stebbings, Monoclonal antibody TGN1412 trial failure explained by species differences in CD28 expression on CD4+ effector memory T-cells, *Br. J. Pharmacol.* (2010), <https://doi.org/10.1111/j.1476-5381.2010.00922.x>.
- [19] N. Porciello, P. Grazioli, A.F. Campese, M. Kunkl, S. Caristi, M. Mastrogianni, M. Muscolini, F. Spadaro, C. Favre, J.A. Nuñez, A. Borroto, B. Alarcon, I. Screpanti, L. Tuosto, A non-conserved amino acid variant regulates differential signalling between human and mouse CD28, *Nat. Commun.* (2018), <https://doi.org/10.1038/s41467-018-03385-8>.
- [20] European Commission, REPORT FROM THE COMMISSION TO THE EUROPEAN PARLIAMENT AND THE COUNCIL 2019 report on the statistics on the use of animals for scientific purposes in the Member States of the European Union in 2015–2017, 2020.
- [21] N.N. Shah, T.J. Fry, Mechanisms of resistance to CAR T cell therapy, *Nat. Rev. Clin. Oncol.* 16 (2019) 372–385, <https://doi.org/10.1038/s41571-019-0184-6>.

- [22] C.H. June, R.S. O'Connor, O.U. Kawalekar, S. Ghassemi, M.C. Milone, CAR T cell immunotherapy for human cancer, *Science* (80-.). 359 (2018) 1361–1365. <https://doi.org/10.1126/science.aar6711>.
- [23] D. Migliorini, N.J. Mason, A.D. Posey, Keeping the engine running: the relevance and predictive value of preclinical models for CAR-T cell development, *ILARJ*, 59 (2018) 276–285. <https://doi.org/10.1093/ilarj/ilz009>.
- [24] M. Kalatsidou, G. Kueberuwa, A. Schütt, D.E. Gilham, CAR T-cell therapy: toxicity and the relevance of preclinical models, *Immunotherapy* 7 (2015) 487–497. <https://doi.org/10.2217/imt.14.123>.
- [25] M. Ruela, C.H. June, Predicting dangerous off-targets: bridging the gap between mice and humans, *Mol. Ther.* 26 (2018) 1401–1403. <https://doi.org/10.1016/j.jymthe.2018.05.005>.
- [26] P.S. Hegde, D.S. Chen, Top 10 challenges in cancer immunotherapy, *Immunity* 52 (2020) 17–35. <https://doi.org/10.1016/j.immuni.2019.12.011>.
- [27] C. Kamperschroer, J. Shenton, H. Lebrech, J.K. Leighton, P.A. Moore, O. Thomas, Summary of a workshop on preclinical and translational safety assessment of CD3 bispecifics, *J. Immunotoxicol.* (2020). <https://doi.org/10.1080/1547691X.2020.1729902>.
- [28] H. Saber, P. Del Valle, T.K. Ricks, J.K. Leighton, An FDA oncology analysis of CD3 bispecific constructs and first-in-human dose selection, *Regul. Toxicol. Pharmacol.* (2017). <https://doi.org/10.1016/j.yrtph.2017.09.001>.
- [29] M.E. Goebeler, R.C. Bargou, T cell-engaging therapies – BiTEs and beyond, *Nat. Rev. Clin. Oncol.* (2020). <https://doi.org/10.1038/s41571-020-0347-5>.
- [30] A. Boussomnier-Calleja, *In vitro* models of cancer, Elsevier Ltd., 2020. <https://doi.org/10.1016/b978-0-12-813886-1.00013-9>.
- [31] M.F. Sanmamed, L. Chen, A paradigm shift in cancer immunotherapy: from enhancement to normalization, *Cell*, 175 (2018) 313–326. <https://doi.org/10.1016/j.cell.2018.09.035>.
- [32] M.B. Schaaf, A.D. Garg, P. Agostinis, Defining the role of the tumor vasculature in antitumor immunity and immunotherapy article, *Cell Death Dis.* (2018). <https://doi.org/10.1038/s41419-017-0061-0>.
- [33] S.N. Bhatia, D.E. Ingber, Microfluidic organs-on-chips, *Nat. Biotechnol.* 32 (2014) 760–772. <https://doi.org/10.1038/nbt.2989>.
- [34] S. Ahadian, R. Civitarese, D. Bannerman, M.H. Mohammadi, R. Lu, E. Wang, L. Davenport-Huy, B. Lai, B. Zhang, Y. Zhao, S. Mandla, A. Korolj, M. Radisic, Organ-on-a-chip platforms: a convergence of advanced materials, cells, and microscale technologies, *Adv. Healthc. Mater.* 7 (2018). <https://doi.org/10.1002/adhm.201700506>.
- [35] J.P. Wikswio, The relevance and potential roles of microphysiological systems in biology and medicine, *Exp. Biol. Med.* 239 (2014) 1061–1072. <https://doi.org/10.1177/1535370214542068>.
- [36] R.W. Peck, C.D. Hinojosa, G.A. Hamilton, Organs-on-chips in clinical pharmacology: putting the patient into the center of treatment selection and drug development, *Clin. Pharmacol. Ther.* 107 (2020) 181–185. <https://doi.org/10.1002/cpt.1688>.
- [37] U. Marx, T. Akabane, T.B. Andersson, E. Baker, M. Beilmann, S. Beken, S. Brendler-Schwaab, M. Cirit, R. David, E.M. Dehne, I. Durieux, L. Ewart, S.C. Fitzpatrick, O. Frey, F. Fuchs, L.G. Griffith, G.A. Hamilton, T. Hartung, J. Hoeng, H. Hogberg, D.J. Hughes, D.E. Ingber, A. Iskandar, T. Kanamori, H. Kojima, J. Kuehni, M. Leist, B. Li, P. Loskill, D.L. Mendrick, T. Neumann, G. Pallocca, I. Rusyn, L. Smirnova, T. Steger-Hartmann, D.A. Tagle, A. Tonevitsky, S. Tsyb, M. Trapecar, B. Van de Water, J. Van den Eijnden-van Raaij, P. Vulto, K. Watanabe, A. Wolf, X. Zhou, A. Roth, Biology-inspired microphysiological systems to advance patient benefit and animal welfare in drug development, *ALTEX* 37 (2020) 364–394. <https://doi.org/10.14573/altex.2001241>.
- [38] M. Håkansson, E. Cukierman, M. Charnley, Miniaturized pre-clinical cancer models as research and diagnostic tools, *Adv. Drug Deliv. Rev.* 69–70 (2014) 52–66. <https://doi.org/10.1016/j.addr.2013.11.010>.
- [39] Z. Zhang, S. Nagrath, Microfluidics and cancer: are we there yet?, *Biomed. Microdevices*, (2013). <https://doi.org/10.1007/s10544-012-9734-8>.
- [40] J. Chen, J. Li, Y. Sun, Microfluidic approaches for cancer cell detection, characterization, and separation, *Lab Chip* (2012). <https://doi.org/10.1039/c2lc21273k>.
- [41] S.J. Hachey, C.C.W. Hughes, Applications of tumor chip technology, *Lab Chip* 18 (2018) 2893–2912. <https://doi.org/10.1039/c8lc00330k>.
- [42] H.-F. Tsai, A. Trubelja, A.Q. Shen, G. Bao, Tumour-on-a-chip: microfluidic models of tumour morphology, growth and microenvironment, *J. R. Soc. Interface*, 14 (2017). <https://doi.org/10.1098/rsif.2017.0137>.
- [43] K.E. Sung, D.J. Beebe, Microfluidic 3D models of cancer, *Adv. Drug Deliv. Rev.* 79 (2014) 68–78. <https://doi.org/10.1016/j.addr.2014.07.002>.
- [44] N.M. Karabacak, P.S. Spuhler, F. Fachin, E.J. Lim, V. Pai, E. Ozkumur, J.M. Martel, N. Kojic, K. Smith, P.L. Chen, J. Yang, H. Hwang, B. Morgan, J. Trautwein, T.A. Barber, S.L. Stott, S. Maheswaran, R. Kapur, D.A. Haber, M. Toner, Microfluidic, marker-free isolation of circulating tumor cells from blood samples, *Nat. Protoc.* (2014). <https://doi.org/10.1038/nprot.2014.044>.
- [45] D. Ravi, S. Sarkar, S. Purvey, F. Passero, A. Beheshti, Y. Chen, M. Mokhtar, K. David, T. Konry, A.M. Evens, Interaction kinetics with transcriptomic and secretory responses of CD19-CAR natural killer cell therapy in CD20 resistant non-hodgkin lymphoma, *Leukemia* 34 (2020) 1291–1304. <https://doi.org/10.1038/s41375-019-0663-x>.
- [46] A.I. Segaliny, G. Li, L. Kong, C. Ren, X. Chen, J.K. Wang, D. Baltimore, G. Wu, W. Zhao, Functional TCR T cell screening using single-cell droplet microfluidics, *Lab Chip* (2018). <https://doi.org/10.1039/c8lc00818c>.
- [47] F.C. Jammes, S.J. Maerkl, How single-cell immunology is benefiting from microfluidic technologies, *Microsystems Nanoeng.* (2020). <https://doi.org/10.1038/s41378-020-0140-8>.
- [48] M. Mastrangeli, S. Millet, ORCHID partners, J. van den Eijnden-Van Raaij, Organ-on-chip in development: Towards a roadmap for organs-on-chip, *ALTEX* 36 (4) (2019) 650–668. <https://doi.org/10.14573/altex.1908271>.
- [49] B. Zhang, A. Korolj, B.F.L. Lai, M. Radisic, Advances in organ-on-a-chip engineering, *Nat. Rev. Mater.* 3 (2018) 257–278. <https://doi.org/10.1038/s41578-018-0034-7>.
- [50] K. Yang, J. Wu, H. Peretz-Soroka, L. Zhu, Z. Li, Y. Sang, J. Hipolito, M. Zhang, S. Santos, C. Hillier, R.L. de Faria, Y. Liu, F. Lin, M.Kit: A cell migration assay based on microfluidic device and smartphone, *Biosens. Bioelectron.* 99 (2018) 259–267. <https://doi.org/10.1016/j.bios.2017.07.064>.
- [51] D. Xie, Z. Liu, J. Wu, W. Feng, K. Yang, J. Deng, G. Tian, S. Santos, X. Cui, F. Lin, The effects of activin A on the migration of human breast cancer cells and neutrophils and their migratory interaction, *Exp. Cell Res.* 357 (2017) 107–115. <https://doi.org/10.1016/j.yexcr.2017.05.003>.
- [52] S.G. Allen, Y.C. Chen, J.M. Madden, C.L. Fournier, M.A. Altamem, A.B. Hizirolu, Y.H. Cheng, Z.F. Wu, L. Bao, J.A. Yates, E. Yoon, S.D. Merajver, Macrophages enhance migration in inflammatory breast cancer cells via RhoC GTPase signaling, *Sci. Rep.* (2016). <https://doi.org/10.1038/step39190>.
- [53] E. Ashihara, T. Munaka, S. Kimura, S. Nakagawa, Y. Nakagawa, M. Kanai, H. Hirai, H. Abe, T. Miida, S. Yamato, S. Shoji, T. Maekawa, Isopentenyl pyrophosphate secreted from Zoledronate-stimulated myeloma cells, activates the chemotaxis of $\gamma\delta$ T cells, *Biochem. Biophys. Res. Commun.* 463 (2015) 650–655. <https://doi.org/10.1016/j.bbrc.2015.05.118>.
- [54] F. Apoorva, A.M. Loiben, S.B. Shah, A. Purwada, L. Fontan, R. Goldstein, B.J. Kirby, A.M. Melnick, B.D. Cosgrove, A. Singh, How biophysical forces regulate human B cell lymphomas, *Cell Rep.* 23 (2018) 499–511. <https://doi.org/10.1016/j.celrep.2018.03.069>.
- [55] X. Ren, A. Alami, J. Hipolito, F. Lin, S.K.P. Kung, *Applications of Microfluidic Devices In Advancing NK-cell Migration Studies*, 1st ed., Elsevier Inc., 2020.
- [56] L. Businaro, A. De Ninno, G. Schiavoni, V. Lucarini, G. Ciasca, A. Gerardino, F. Belardelli, L. Gabriele, F. Mattei, Cross talk between cancer and immune cells: exploring complex dynamics in a microfluidic environment, *Lab Chip* 13 (2013) 229–239. <https://doi.org/10.1039/c2lc40887b>.
- [57] S. Parlato, A. De Ninno, R. Molfetta, E. Toschi, D. Salerno, A. Mencattini, G. Romagnoli, A. Fragale, L. Roccazzello, M. Buoncervello, I. Canini, E. Bentivegna, M. Falchi, F.R. Bertani, A. Gerardino, E. Martinielli, C. Natale, R. Paolini, L. Businaro, L. Gabriele, 3D Microfluidic model for evaluating immunotherapy efficacy by tracking dendritic cell behaviour toward tumor cells, *Sci. Rep.* 7 (2017) 1093. <https://doi.org/10.1038/s41598-017-01013-x>.
- [58] E. Um, J.M. Oh, J. Park, T. Song, T.E. Kim, Y. Choi, C. Shin, D. Kolygina, J.H. Jeon, B.A. Grzybowski, Y.K. Cho, Immature dendritic cells navigate microscopic mazes to find tumor cells, *Lab Chip* 19 (2019) 1665–1675. <https://doi.org/10.1039/c9lc00150f>.
- [59] T.H. Hsu, Y.L. Kao, W.L. Lin, J.L. Xiao, P.L. Kuo, C.W. Wu, W.Y. Liao, C.H. Lee, The migration speed of cancer cells influenced by macrophages and myofibroblasts co-cultured in a microfluidic chip, *Integr. Biol.* 4 (2012) 177–182. <https://doi.org/10.1039/c2ib00112h>.
- [60] L. Wu, Z. Wang, Y. Zhang, J. Fei, H. Chen, S. Zong, Y. Cui, In situ probing of cell-cell communications with surface-enhanced Raman scattering (SERS) nanoprobes and microfluidic networks for screening of immunotherapeutic drugs, *Nano Res.* 10 (2017) 584–594. <https://doi.org/10.1007/s12274-016-1316-2>.
- [61] Z. Guo, J. Song, J. Hao, H. Zhao, X. Du, E. Li, Y. Kuang, F. Yang, W. Wang, J. Deng, Q. Wang, M2 macrophages promote NSCLC metastasis by upregulating CRYAB, *Cell Death Dis.* (2019). <https://doi.org/10.1038/s41419-019-1618-x>.
- [62] J. Yu, E. Berthier, A. Craig, T.E. de Groot, S. Sparks, P.N. Ingram, D.F. Jarrard, W. Huang, D.J. Beebe, A.B. Theberge, Reconfigurable open microfluidics for studying the spatiotemporal dynamics of paracrine signalling, *Nat. Biomed. Eng.* 3 (2019) 830–841. <https://doi.org/10.1038/s41551-019-0421-4>.
- [63] M.R. Junttila, F.J. De Sauvage, Influence of tumour micro-environment heterogeneity on therapeutic response, *Nature*, (2013). <https://doi.org/10.1038/nature12626>.
- [64] F. Klemm, J.A. Joyce, Microenvironmental regulation of therapeutic response in cancer, *Trends Cell Biol.* (2015). <https://doi.org/10.1016/j.tcb.2014.11.006>.
- [65] A.K. Palucka, L.M. Coussens, The Basis of Oncoimmunology, *Cell.* (2016). <https://doi.org/10.1016/j.cell.2016.01.049>.
- [66] J.M. Pitt, A. Marabelle, A. Eggermont, J.C. Soria, G. Kroemer, L. Zitvogel, Targeting the tumor microenvironment: Removing obstruction to anticancer immune responses and immunotherapy, *Ann. Oncol.* (2016). <https://doi.org/10.1093/annonc/mdw168>.
- [67] A.R. Aref, R.Y.J. Huang, W. Yu, K.N. Chua, W. Sun, T.Y. Tu, J. Bai, W.J. Sim, I.K. Zervantonakis, J.P. Thiery, R.D. Kamm, Screening therapeutic EMT blocking agents in a three-dimensional microenvironment, *Integr. Biol. (United Kingdom)*, (2013). <https://doi.org/10.1039/c2ib20209c>.
- [68] Y. Ando, E.L. Siegler, H.P. Ta, G.E. Cinay, H. Zhou, K.A. Gorrell, H. Au, B.M. Jarvis, P. Wang, K. Shen, Evaluating CAR-T cell therapy in a hypoxic 3D tumor model, *Adv. Healthc. Mater.* 8 (2019) 1900001. <https://doi.org/10.1002/adhm.201900001>.
- [69] S.W.L. Lee, G. Adriani, E. Ceccarello, A. Pavesi, A.T. Tan, A. Bertoletti, R.D. Kamm, S.C. Wong, Characterizing the role of monocytes in T cell cancer immunotherapy using a 3d microfluidic model, *Front. Immunol.* 9 (2018). <https://doi.org/10.3389/fimmu.2018.00416>.
- [70] A. Pavesi, A.T. Tan, S. Koh, A. Chia, M. Colombo, E. Antonecchia, C. Miccolis, E. Ceccarello, G. Adriani, M.T. Raimondi, R.D. Kamm, A. Bertoletti, A 3D microfluidic model for preclinical evaluation of TCR-engineered T cells

- against solid tumors, *JCI Insight* 2 (2017), <https://doi.org/10.1172/jci.insight.89762>.
- [71] J.M. Ayuso, S. Rehman, M. Virumbrales-Munoz, P.H. McMin, P. Geiger, C. Fitzgerald, T. Heaster, M.C. Skala, D.J. Beebe, Microfluidic tumor-on-a-chip model to evaluate the role of tumor environmental stress on NK cell exhaustion, *Sci. Adv.* 7 (2021) eabc2331, <https://doi.org/10.1126/sciadv.abc2331>.
- [72] C. Fischbach, R. Chen, T. Matsumoto, T. Schmelzle, J.S. Brugge, P.J. Polverini, D.J. Mooney, Engineering tumors with 3D scaffolds, *Nat. Methods* (2007), <https://doi.org/10.1038/nmeth1085>.
- [73] L.A. Kunz-Schughart, J.P. Freyer, F. Hofstaedter, R. Ebner, The use of 3-D cultures for high-throughput screening: the multicellular spheroid model, *J. Biomol. Screen.* (2004), <https://doi.org/10.1177/1087057104265040>.
- [74] R. Edmondson, J.J. Broglie, A.F. Adcock, L. Yang, Three-dimensional cell culture systems and their applications in drug discovery and cell-based biosensors, *Assay Drug Dev. Technol.* (2014), <https://doi.org/10.1089/adt.2014.573>.
- [75] A. Aung, V. Kumar, J. Theprungsirikul, S.K. Davey, S. Varghese, An engineered tumor-on-a-chip device with breast cancer-immune cell interactions for assessing T-cell recruitment, *Cancer Res.* 80 (2020) 263–275, <https://doi.org/10.1158/0008-5472.CCR-19-0342>.
- [76] J.M. Ayuso, R. Truttschel, M.M. Gong, M. Humayun, M. Virumbrales-Munoz, R. Vitek, M. Felder, S.D. Gillies, P. Sondel, K.B. Wisinski, M. Patankar, D.J. Beebe, M.C. Skala, Evaluating natural killer cell cytotoxicity against solid tumors using a microfluidic model, *Oncoimmunology* 8 (2019), <https://doi.org/10.1080/2162402X.2018.1553477>.
- [77] M.B. Chen, C. Hajal, D.C. Benjamin, C. Yu, H. Azizgolshani, R.O. Hynes, R.D. Kamm, Inflamed neutrophils sequestered at entrapped tumor cells via chemotactic confinement promote tumor cell extravasation, *Proc. Natl. Acad. Sci. USA* 115 (2018) 7022–7027, <https://doi.org/10.1073/pnas.1715932115>.
- [78] D. Park, K. Son, Y. Hwang, J. Ko, Y. Lee, J. Doh, N.L. Jeon, High-throughput microfluidic 3D cytotoxicity assay for cancer immunotherapy (CACI-Impact platform), *Front. Immunol.* 10 (2019) 1–9, <https://doi.org/10.3389/fimmu.2019.01133>.
- [79] M. Nguyen, A. De Ninno, A. Mencattini, F. Mermet-Meillon, G. Fornabai, S.S. Evans, M. Cossutta, Y. Khira, W. Han, P. Sirven, F. Pelon, D. Di Giuseppe, F.R. Bertani, A. Gerardino, A. Yamada, S. Descroix, V. Soumelis, F. Mechta-Grigoriou, G. Zalzman, J. Camonis, E. Martinelli, L. Businaro, M.C. Parrini, Dissecting effects of anti-cancer drugs and cancer-associated fibroblasts by on-chip reconstitution of immunocompetent tumor microenvironments, *Cell Rep.* 25 (2018) 3884–3893.e3, <https://doi.org/10.1016/j.celrep.2018.12.015>.
- [80] H. Kim, H. Chung, J. Kim, D.H. Choi, Y. Shin, Y.G. Kang, B.M. Kim, S.U. Seo, S. Chung, S.H. Seok, Macrophages-triggered sequential remodeling of endothelium-interstitial matrix to form pre-metastatic niche in microfluidic tumor microenvironment, *Adv. Sci.* 6 (2019), <https://doi.org/10.1002/advs.201900195>.
- [81] D.C. Wimalachandra, Y. Li, J. Liu, S. Shikha, J. Zhang, Y.C. Lim, Y. Zhang, Microfluidic-based immunomodulation of immune cells using upconversion nanoparticles in simulated blood vessel-tumor system, *ACS Appl. Mater. Interfaces* 11 (2019) 37513–37523, <https://doi.org/10.1021/acsami.9b15178>.
- [82] D. Di Mascolo, S. Varesano, R. Benelli, H. Mollica, A. Salis, M.R. Zocchi, P. Decuzzi, A. Poggi, Nanofabricated zoledronic acid boosts the V62T cell immunotherapeutic potential in colorectal cancer, *Cancers (Basel)* 12 (2020), <https://doi.org/10.3390/cancers12010104>.
- [83] A.L. Beckwith, L.F. Velásquez-García, J.T. Borenstein, Microfluidic model for evaluation of immune checkpoint inhibitors in human tumors, *Adv. Healthc. Mater.* 8 (2019) 1900289, <https://doi.org/10.1002/adhm.201900289>.
- [84] S. Shim, M.C. Belanger, A.R. Harris, J.M. Munson, R.R. Pompano, Two-way communication between ex vivo tissues on a microfluidic chip: application to tumor-lymph node interaction, *Lab Chip* 19 (2019) 1013–1026, <https://doi.org/10.1039/C8LC00957K>.
- [85] R.W. Jenkins, A.R. Aref, P.H. Lizotte, E. Ivanova, S. Stinson, C.W. Zhou, M. Bowden, J. Deng, H. Liu, D. Miao, M.X. He, W. Walker, G. Zhang, T. Tian, C. Cheng, Z. Wei, S. Palakurthi, M. Bittinger, H. Vitzthum, J.W. Kim, A. Merlino, M. Quinn, C. Venkataramani, J.A. Kaplan, A. Portell, P.C. Gokhale, B. Phillips, A. Smart, A. Rotem, R.E. Jones, L. Keogh, M. Anguiano, L. Stapleton, Z. Jia, M. Barzily-Rokni, I. Cañadas, T.C. Thai, M.R. Hammond, R. Vlahos, E.S. Wang, H. Zhang, S. Li, G.J. Hanna, W. Huang, M.P. Hoang, A. Piris, J.P. Eliane, A.O. Stemmer-Rachamimov, L. Cameron, M.J. Su, P. Shah, B. Izar, M. Thakuria, N.R. LeBoeuf, G. Rabinowitz, V. Gunda, S. Parangi, J.M. Cleary, B.C. Miller, S. Kitajima, R. Thummalapalli, B. Miao, T.U. Barbie, V. Sivathanu, J. Wong, W.G. Richards, R. Bueno, C.H. Yoon, J. Miret, M. Herlyn, L.A. Garraway, E.M. Van Allen, G.J. Freeman, P.T. Kirschmeier, J.H. Lorch, P.A. Ott, F. Stephen Hodi, K.T. Flaherty, R.D. Kamm, G.M. Boland, K.K. Wong, D. Dornan, C.P. Paweletz, D.A. Barbie, Ex vivo profiling of PD-1 blockade using organotypic tumor spheroids, *Cancer Discov.* 8 (2018) 196–215, <https://doi.org/10.1158/2159-8290.CD-17-0833>.
- [86] A.R. Aref, M. Campisi, E. Ivanova, A. Portell, D. Larios, B.P. Piel, N. Mathur, C. Zhou, R.V. Coakley, A. Bartels, M. Bowden, Z. Herbert, S. Hill, S. Gilhooly, J. Carter, I. Cañadas, T.C. Thai, S. Kitajima, V. Chiono, C.P. Paweletz, D.A. Barbie, R.D. Kamm, R.W. Jenkins, 3D microfluidic: Ex vivo culture of organotypic tumor spheroids to model immune checkpoint blockade, *Lab Chip* 18 (2018) 3129–3143, <https://doi.org/10.1039/C8LC00322J>.
- [87] M. Yamauchi, T.H. Barker, D.L. Gibbons, J.M. Kurie, The fibrotic tumor stroma, *J. Clin. Invest.* (2018), <https://doi.org/10.1172/JCI93554>.
- [88] K. Newick, S. O'Brien, E. Moon, S.M. Albelda, CAR T cell therapy for solid tumors, *Annu. Rev. Med.* 68 (2017) 139–152, <https://doi.org/10.1146/annurev-med-062315-120245>.
- [89] E. Donnadieu, L. Dupré, L.G. Pinho, V. Cotta-de-Almeida, Surmounting the obstacles that impede effective CAR T cell trafficking to solid tumors, *J. Leukoc. Biol.* (2020), <https://doi.org/10.1002/jlb.1MR0520-746R>.
- [90] A. Rodriguez-Garcia, A. Palazon, E. Noguera-Ortega, D.J. Powell, S. Guedan, CAR-T cells hit the tumor microenvironment: strategies to overcome tumor escape, *Front. Immunol.* (2020), <https://doi.org/10.3389/fimmu.2020.01109>.
- [91] S. Tahmasebi, R. Elahi, A. Esmaeilzadeh, Solid tumors challenges and new insights of CAR T cell engineering, *Stem Cell Rev. Reports* (2019), <https://doi.org/10.1007/s12015-019-09901-7>.
- [92] M. Martinez, E.K. Moon, CAR T cells for solid tumors: new strategies for finding, infiltrating, and surviving in the tumor microenvironment, *Front. Immunol.* (2019), <https://doi.org/10.3389/fimmu.2019.00128>.
- [93] P. Ginefra, G. Lorusso, N. Vannini, Innate immune cells and their contribution to t-cell-based immunotherapy, *Int. J. Mol. Sci.* (2020), <https://doi.org/10.3390/ijms21124441>.
- [94] S. Gasser, L.H.K. Lim, F.S.G. Cheung, The role of the tumour microenvironment in immunotherapy, *Endocr. Relat. Cancer* (2017), <https://doi.org/10.1530/ERC-17-0146>.
- [95] J.L. da Silva, A.L.S. Dos Santos, N.C.C. Nunes, F. de Moraes Lino, C.G.M. da Silva, A.C. de Ferreira, Melo, Cancer immunotherapy: the art of targeting the tumor immune microenvironment, *Cancer Chemother. Pharmacol.* (2019), <https://doi.org/10.1007/s00280-019-03894-3>.
- [96] D.S. Chulpanova, K.V. Kitaeva, C.S. Rutland, A.A. Rizvanov, V.V. Solovyeva, Mouse tumor models for advanced cancer immunotherapy, *Int. J. Mol. Sci.* (2020), <https://doi.org/10.3390/ijms21114118>.
- [97] P. De La Rochere, S. Guil-Luna, D. Decaudin, G. Azar, S.S. Sidhu, E. Piaggio, Humanized mice for the study of immuno-oncology, *Trends Immunol.* 39 (2018) 748–763, <https://doi.org/10.1016/j.it.2018.07.001>.
- [98] K. Aizel, A.C. Clark, A. Simon, S. Geraldo, A. Funtak, P. Vargas, J. Bibette, D.M. Vignjevic, N. Bremond, A tuneable microfluidic system for long duration chemotaxis experiments in a 3D collagen matrix, *Lab Chip* 17 (2017) 3851–3861, <https://doi.org/10.1039/c7lc00649g>.
- [99] S.W.L. Lee, R.J. Seager, F. Litvak, F. Spill, J.L. Sieow, P.H. Leong, D. Kumar, A.S.M. Tan, S.C. Wong, G. Adriani, M.H. Zaman, A.R.D. Kamm, Integrated in silico and 3D in vitro model of macrophage migration in response to physical and chemical factors in the tumor microenvironment, *Integr. Biol.* (Camb) 12 (2020) 90–108, <https://doi.org/10.1093/intbio/zyaa007>.
- [100] Q. Huang, X. Hu, W. He, Y. Zhao, S. Hao, Q. Wu, S. Li, S. Zhang, M. Shi, Fluid shear stress and tumor metastasis, *Am. J. Cancer Res.* (2018).
- [101] M. Binnewies, E.W. Roberts, K. Kersten, V. Chan, D.F. Fearon, M. Merad, L.M. Coussens, D.I. Gabrilovich, S. Ostrand-Rosenberg, C.C. Hedrick, R.H. Vonderheide, M.J. Pittet, R.K. Jain, W. Zou, T.K. Howcroft, E.C. Woodhouse, R.A. Weinberg, M.F. Krummel, Understanding the tumor immune microenvironment (TIME) for effective therapy, *Nat. Med.* (2018), <https://doi.org/10.1038/s41591-018-0014-x>.
- [102] J. Duell, M. Ditttrich, T. Bedke, T. Mueller, F. Eisele, A. Rosenwald, L. Rasche, E. Hartmann, T. Dandekar, H. Einsele, M.S. Topp, Frequency of regulatory T cells determines the outcome of the T-cell-engaging antibody blinatumomab in patients with B-precursor ALL, *Leukemia* (2017), <https://doi.org/10.1038/leu.2017.41>.
- [103] T. Takebe, B. Zhang, M. Radisic, Synergistic engineering: organoids meet organs-on-a-chip, *Cell Stem Cell* 21 (2017) 297–300, <https://doi.org/10.1016/j.stem.2017.08.016>.
- [104] S.E. Park, A. Georgescu, D. Huh, Organoids-on-a-chip, *Science* 80 (2019), <https://doi.org/10.1126/science.aaw7894>.
- [105] K. Achberger, C. Probst, J.C. Haderspeck, S. Bolz, J. Rogal, J. Chuchuy, M. Nikolova, V. Cora, L. Antkowiak, W. Haq, N. Shen, K. Schenke-Layland, M. Ueffing, S. Liebau, P. Loskill, Merging organoid and organ-on-a-chip technology to generate complex multi-layer tissue models in a human retina-on-a-chip platform, *Elife* 8 (2019) e46188, <https://doi.org/10.7554/eLife.46188>.
- [106] F. Weeber, S.N. Ooft, K.K. Dijkstra, E.E. Voest, Tumor organoids as a pre-clinical cancer model for drug discovery, *Cell Chem. Biol.* (2017), <https://doi.org/10.1016/j.cchembiol.2017.06.012>.
- [107] G.L. Beatty, W.L. Gladney, Immune escape mechanisms as a guide for cancer immunotherapy, *Clin. Cancer Res.* (2015), <https://doi.org/10.1158/1078-0432.CCR-14-1860>.
- [108] S. Kailayangiri, B. Altvater, M. Wiebel, S. Jamitzky, C. Rossig, Overcoming heterogeneity of antigen expression for effective car t cell targeting of cancers, *Cancers (Basel)* (2020), <https://doi.org/10.3390/cancers12051075>.
- [109] D. Tuveson, H. Clevers, Cancer modeling meets human organoid technology, *Science* (80-) (2019), <https://doi.org/10.1126/science.aaw6985>.
- [110] A. Francis, G.H. Venkatesh, R.F. Zaarour, N.A. Zeinelabdin, H.H. Nawafleh, P. Prasad, S. Buart, S. Terry, S. Chouaib, Tumor hypoxia: A key determinant of microenvironment hostility and a major checkpoint during the antitumor response, *Crit. Rev. Immunol.* (2018), <https://doi.org/10.1615/CritRevImmunol.2019030168>.
- [111] M.Z. Noman, M. Hasmim, A. Lequeux, M. Xiao, C. Duhem, S. Chouaib, G. Berchem, B. Janji, Improving cancer immunotherapy by targeting the hypoxic tumor microenvironment: new opportunities and challenges, *Cells* (2019), <https://doi.org/10.3390/cells8091083>.
- [112] S. Chouaib, M.Z. Noman, K. Kosmatopoulos, M.A. Curran, Hypoxic stress: obstacles and opportunities for innovative immunotherapy of cancer, *Oncogene* (2017), <https://doi.org/10.1038/onc.2016.225>.

- [113] A. Schurich, I. Magalhaes, J. Mattsson, Metabolic regulation of CAR T cell function by the hypoxic microenvironment in solid tumors, *Immunotherapy* (2019), <https://doi.org/10.2217/imt-2018-0141>.
- [114] J.F. Sleebloom, J.M.J. Den Toonder, C.M. Sahlgren, Mda-mb-231 breast cancer cells and their csc population migrate towards low oxygen in a microfluidic gradient device, *Int. J. Mol. Sci.* (2018), <https://doi.org/10.3390/ijms19103047>.
- [115] V.S. Shirure, S.F. Lam, B. Shergill, Y.E. Chu, N.R. Ng, S.C. George, Quantitative design strategies for fine control of oxygen in microfluidic systems, *Lab Chip* (2020), <https://doi.org/10.1039/d0lc00350f>.
- [116] T.L. Place, F.E. Domann, A.J. Case, Limitations of oxygen delivery to cells in culture: An underappreciated problem in basic and translational research, *Free Radic. Biol. Med.* (2017), <https://doi.org/10.1016/j.freeradbiomed.2017.10.003>.
- [117] N. Nagarsheth, M.S. Wicha, W. Zou, Chemokines in the cancer microenvironment and their relevance in cancer immunotherapy, *Nat. Rev. Immunol.* (2017), <https://doi.org/10.1038/nri.2017.49>.
- [118] A.E. Vilgelm, A. Richmond, Chemokines modulate immune surveillance in tumorigenesis, metastasis, and response to immunotherapy, *Front. Immunol.* (2019), <https://doi.org/10.3389/fimmu.2019.00333>.
- [119] M.T. Chow, A.D. Luster, Chemokines in cancer, *Cancer Immunol. Res.* 2 (2014) 1125–1131, <https://doi.org/10.1158/2326-6066.CCR-14-0160>.
- [120] X. Wang, Z. Liu, Y. Pang, Concentration gradient generation methods based on microfluidic systems, *RSC Adv.* (2017), <https://doi.org/10.1039/c7ra04494a>.
- [121] U. Haessler, Y. Kalinin, M.A. Swartz, M. Wu, An agarose-based microfluidic platform with a gradient buffer for 3D chemotaxis studies, *Biomed. Microdevices.* (2009), <https://doi.org/10.1007/s10544-009-9299-3>.
- [122] Y. Zhao, D. Wang, T. Xu, P. Liu, Y. Cao, Y. Wang, X. Yang, X. Xu, X. Wang, H. Niu, Bladder cancer cells re-educate TAMs through lactate shuttling in the microfluidic cancer microenvironment, *Oncotarget*. 6 (2015) 39196–39210, <https://doi.org/10.18632/oncotarget.5538>.
- [123] D.H.T. Nguyen, S.C. Stapleton, M.T. Yang, S.S. Cha, C.K. Choi, P.A. Galie, C.S. Chen, Biomimetic model to reconstitute angiogenic sprouting morphogenesis in vitro, *Proc. Natl. Acad. Sci. USA* 110 (2013) 6712–6717, <https://doi.org/10.1073/pnas.1221526110>.
- [124] A. Tourouvskaia, M. Fauver, G. Kramer, S. Simonson, T. Neumann, Tissue-engineered microenvironment systems for modeling human vasculature, *Exp. Biol. Med.* 239 (2014) 1264–1271, <https://doi.org/10.1177/1535370214539228>.
- [125] J. Sai, M. Rogers, K. Hockemeyer, J.P. Wikswo, A. Richmond, Study of chemotaxis and cell-cell interactions in cancer with microfluidic devices, *Methods Enzymol.* (2016), <https://doi.org/10.1016/bs.mie.2015.09.023>.
- [126] K. Kwapiszewska, A. Michalczuk, M. Rybka, R. Kwapiszewski, Z. Brzózka, A microfluidic-based platform for tumour spheroid culture, monitoring and drug screening, *Lab Chip* (2014), <https://doi.org/10.1039/c4lc00291a>.
- [127] H. Hwang, C. Shin, J. Park, E. Kang, B. Choi, J.A. Han, Y. Do, S. Ryu, Y.K. Cho, Human breast cancer-derived soluble factors facilitate CCL19-induced chemotaxis of human dendritic cells, *Sci. Rep.* (2016), <https://doi.org/10.1038/srep30207>.
- [128] I.J. Cohen, B. Blasberg, Impact of the tumor microenvironment on tumor-infiltrating lymphocytes: focus on breast cancer, *Breast Cancer Basic Clin. Res.* (2017), <https://doi.org/10.1177/1178223417731565>.
- [129] J.A. Joyce, D.T. Fearon, T cell exclusion, immune privilege, and the tumor microenvironment, *Science* (80-) (2015), <https://doi.org/10.1126/science.aaa6204>.
- [130] H. Jiang, S. Hegde, D.G. DeNardo, Tumor-associated fibrosis as a regulator of tumor immunity and response to immunotherapy, *Cancer Immunol. Immunother.* (2017), <https://doi.org/10.1007/s00262-017-2003-1>.
- [131] I.K. Choi, R. Strauss, M. Richter, C.O. Yun, A. Lieber, Strategies to increase drug penetration in solid tumors, *Front. Oncol.* (2013), <https://doi.org/10.3389/fonc.2013.00193>.
- [132] L.C.S. Wang, A. Lo, J. Scholler, J. Sun, R.S. Majumdar, V. Kapoor, M. Antziz, C.E. Cotner, L.A. Johnson, A.C. Durham, C.C. Solomides, C.H. June, E. Puré, S.M. Albelda, Targeting fibroblast activation protein in tumor stroma with chimeric antigen receptor T cells can inhibit tumor growth and augment host immunity without severe toxicity, *Cancer Immunol. Res.* (2014), <https://doi.org/10.1158/2326-6066.CCR-13-0027>.
- [133] I. Caruana, B. Savoldo, V. Hoyos, G. Weber, H. Liu, E.S. Kim, M.M. Ittmann, D. Marchetti, G. Dotti, Heparanase promotes tumor infiltration and antitumor activity of CAR-redirection T lymphocytes, *Nat. Med.* (2015), <https://doi.org/10.1038/nm.3833>.
- [134] D. Wirtz, K. Konstantopoulos, P.C. Searson, The physics of cancer: The role of physical interactions and mechanical forces in metastasis, *Nat. Rev. Cancer.* (2011), <https://doi.org/10.1038/nrc3080>.
- [135] B.Z. Qian, J.W. Pollard, Macrophage diversity enhances tumor progression and metastasis, *Cell* (2010), <https://doi.org/10.1016/j.cell.2010.03.014>.
- [136] X. Cui, R.T.T. Morales, W. Qian, H. Wang, J.P. Gagner, I. Dolgalev, D. Placantonakis, D. Zagzag, L. Cimmino, M. Snuderl, R.H.W. Lam, W. Chen, Hacking macrophage-associated immunosuppression for regulating glioblastoma angiogenesis, *Biomaterials* (2018), <https://doi.org/10.1016/j.biomaterials.2018.01.053>.
- [137] I.K. Zervantonakis, S.K. Hughes-Alford, J.L. Charest, J.S. Condeelis, F.B. Gertler, R.D. Kamm, Three-dimensional microfluidic model for tumor cell intravasation and endothelial barrier function, *Proc. Natl. Acad. Sci. USA* (2012), <https://doi.org/10.1073/pnas.1210182109>.
- [138] A. Boussommier-Calleja, Y. Atiyas, K. Haase, M. Headley, C. Lewis, R.D. Kamm, The effects of monocytes on tumor cell extravasation in a 3D vascularized microfluidic model, *Biomaterials* (2019), <https://doi.org/10.1016/j.biomaterials.2018.03.005>.
- [139] K. Haase, R.D. Kamm, Advances in on-chip vascularization, *Regen. Med.* (2017), <https://doi.org/10.2217/rme-2016-0152>.
- [140] J.K. Choo, J.D. Seebach, V. Nickenleit, A. Shimizu, H. Lei, D.H. Sachs, J.C. Madsen, Species differences in the expression of major histocompatibility complex class II antigens on coronary artery endothelium: Implications for cell-mediated xenoreactivity, *Transplantation* 64 (1997) 1315–1322, <https://doi.org/10.1097/00007890-199711150-00014>.
- [141] J. Mestas, C.C.W. Hughes, Endothelial cell costimulation of T cell activation through CD58-CD2 interactions involves lipid raft aggregation, *J. Immunol.* 167 (2001) 4378–4385, <https://doi.org/10.4049/jimmunol.167.8.4378>.
- [142] M.L. Ormiston, M.R. Toshner, F.N. Kiskin, C.J.Z. Huang, E. Groves, N.W. Morrell, A.A. Rana, Generation and culture of blood outgrowth endothelial cells from human peripheral blood, *J. Vis. Exp.* 2015 (2015) 53384, <https://doi.org/10.3791/53384>.
- [143] L.L. Sohn, P. Schwillie, A. Hierlemann, S. Tay, J. Samitier, J. Fu, P. Loskill, How can microfluidic and microfabrication approaches make experiments more physiologically relevant?, *Cell Syst.* 11 (3) (2020) 209–211, <https://doi.org/10.1016/j.cels.2020.07.003>.
- [144] M.A. Luque-González, R.L. Reis, S.C. Kundu, D. Caballero, Human microcirculation-on-chip models in cancer research: key integration of lymphatic and blood vasculatures, *Adv. Biosyst.* 4 (2020) 1–21, <https://doi.org/10.1002/adbi.202000045>.
- [145] N. Moore, D. Doty, M. Zielstorff, I. Kariv, L.Y. Moy, A. Gimbel, J.R. Chevillet, N. Lowry, J. Santos, V. Mott, L. Kratchman, T. Lau, G. Addona, H. Chen, J.T. Borenstein, A multiplexed microfluidic system for evaluation of dynamics of immune-tumor interactions, *Lab Chip* 18 (2018) 1844–1858, <https://doi.org/10.1039/c8lc00256h>.
- [146] A. Boussommier-Calleja, R. Li, M.B. Chen, S.C. Wong, R.D. Kamm, Microfluidics: a new tool for modeling cancer-immune interactions, *Trends in Cancer* 2 (2016) 6–19, <https://doi.org/10.1016/j.trecan.2015.12.003>.
- [147] C. Goyal, B. Bausk, P. Prabhala, L. Xie, D. Curran, J. Long, L. Cohen, O. Levy, R. Prantl-Baun, D. Walt, D. Ingber, Lymph node follicle formation and vaccination responses reconstituted in vitro in a Human Organ Chip (2019), <https://doi.org/10.1101/806505>.
- [148] Y. Choi, S. Lee, K. Kim, S.H. Kim, Y.J. Chung, C. Lee, Studying cancer immunotherapy using patient-derived xenografts (PDXs) in humanized mice, *Exp. Mol. Med.* (2018), <https://doi.org/10.1038/s12276-018-0115-0>.
- [149] K. Newick, E. Moon, S.M. Albelda, Chimeric antigen receptor T-cell therapy for solid tumors, *Mol. Ther. - Oncolytics* 3 (2016) 16006, <https://doi.org/10.1038/mt.2016.6>.
- [150] G.W. Tormoen, M.R. Crittenden, M.J. Gough, Role of the immunosuppressive microenvironment in immunotherapy, *Adv. Radiat. Oncol.* 3 (2018) 520–526, <https://doi.org/10.1016/j.adro.2018.08.018>.
- [151] S. Srivastava, S.R. Riddell, Chimeric antigen receptor T cell therapy: challenges to bench-to-bedside efficacy, *J. Immunol.* 200 (2018) 459–468, <https://doi.org/10.4049/jimmunol.1701155>.
- [152] N.H. Overgaard, T.M. Fan, K.M. Schachtschneider, D.R. Principe, L.B. Schook, G. Jungersen, Of mice, dogs, pigs, and men: choosing the appropriate model for immuno-oncology research, *ILAR J.* (2018), <https://doi.org/10.1093/ilar/ily014>.
- [153] D. Masopust, C.P. Sivula, S.C. Jameson, Of mice, dirty mice, and men: using mice to understand human immunology, *J. Immunol.* (2017), <https://doi.org/10.4049/jimmunol.1700453>.
- [154] M. Norelli, B. Camisa, G. Barbiera, L. Falcone, A. Purevdorj, M. Genua, F. Sanvito, M. Ponzoni, C. Dogliani, P. Cristofori, C. Traversari, C. Bordignon, F. Ciceri, R. Ostuni, C. Bonini, M. Casucci, A. Bondanza, Monocyte-derived IL-1 and IL-6 are differentially required for cytokine-release syndrome and neurotoxicity due to CAR T cells, *Nat. Med.* (2018), <https://doi.org/10.1038/s41591-018-0036-4>.
- [155] C.A. Pennell, J.L. Barnum, C.S. McDonald-Hyman, A. Panoskaltsis-Mortari, M.J. Riddle, Z. Xiong, M. Loschi, G. Thangavelu, H.M. Campbell, M.D. Storie, Y. Refaelli, S.N. Furlan, M.C. Jensen, L.S. Kean, J.S. Miller, J. Tolar, M.J. Osborn, B.R. Blazar, Human CD19-targeted mouse T cells induce B cell aplasia and toxicity in human CD19 transgenic mice, *Mol. Ther.* (2018), <https://doi.org/10.1016/j.ymthe.2018.04.006>.
- [156] T. Giavridis, S.J.C. Van Der Stegen, J. Eyquem, M. Hamieh, A. Piersigilli, M. Sadelain, CAR T cell-induced cytokine release syndrome is mediated by macrophages and abated by IL-1 blockade, *Nat. Med.* (2018), <https://doi.org/10.1038/s41591-018-0041-7>.
- [157] J. Tang, A. Shalabi, V.M. Hubbard-Lucey, Comprehensive analysis of the clinical immuno-oncology landscape, *Ann. Oncol.* (2018), <https://doi.org/10.1093/annonc/mdx755>.
- [158] K. Rezvani, R. Rouse, E. Liu, E. Shpall, Engineering natural killer cells for cancer immunotherapy, *Mol. Ther.* (2017), <https://doi.org/10.1016/j.ymthe.2017.06.012>.
- [159] M. Klichinsky, M. Ruella, O. Shestova, X.M. Lu, A. Best, M. Zeeman, M. Schmierer, K. Gabrusiewicz, N.R. Anderson, N.E. Petty, K.D. Cummins, F. Shen, X. Shan, K. Veliz, K. Blouch, Y. Yashiro-Ohtani, S.S. Kenderian, M.Y. Kim, R.S. O'Connor, S.R. Wallace, M.S. Kozlowski, D.M. Marchione, M. Shestov, B.A. Garcia, C.H. June, S. Gill, Human chimeric antigen receptor macrophages for cancer immunotherapy, *Nat. Biotechnol.* (2020), <https://doi.org/10.1038/s41587-020-0462-y>.

- [160] M. Sadelain, CAR therapy: the CD19 paradigm, *J. Clin. Invest.* (2015), <https://doi.org/10.1172/JCI80010>.
- [161] C.E. Brown, C.L. Mackall, Year in Review response and resistance, *Nat. Rev. Immunol.* 19 (2019) 73–74.
- [162] S. Upadhyay, V.M. Hubbard-Lucey, J.X. Yu, Immuno-oncology drug development forges on despite COVID-19, *Nat. Rev. Drug Discov.* (2020), <https://doi.org/10.1038/d41573-020-00166-1>.
- [163] J. Xin Yu, V.M. Hubbard-Lucey, J. Tang, Immuno-oncology drug development goes global, *Nat. Rev. Drug Discov.* 18 (2019) 899–900, <https://doi.org/10.1038/d41573-019-00167-9>.
- [164] M.S. Thakar, T.J. Kearn, S. Malarkannan, Controlling cytokine release syndrome to harness the full potential of CAR-based cellular therapy, *Front. Oncol.* (2020), <https://doi.org/10.3389/fonc.2019.01529>.
- [165] J. Garcia Borrega, P. Gödel, M.A. Rüger, Ö.A. Onur, A. Shimabukuro-Vornhagen, M. Kochanek, B. Böll, In the eye of the storm: immune-mediated toxicities associated with car-t cell therapy, *HemaSphere* (2019), <https://doi.org/10.1097/H9S.00000000000000191>.
- [166] T. Courrau, J. Bonnerau, J. Chicoteau, H. Bottaïs, R. Remark, L. Assante Miranda, A. Toubert, M. Blery, T. Aparicio, M. Allez, L. Le Bourhis, Cocultures of human colorectal tumor spheroids with immune cells reveal the therapeutic potential of MICA/B and NKG2A targeting for cancer treatment, *J. Immunother Cancer* 7 (2019) 1–14, <https://doi.org/10.1186/s40425-019-0553-9>.
- [167] Z. Zhang, D. Jiang, H. Yang, Z. He, X. Liu, W. Qin, L. Li, C. Wang, Y. Li, H. Li, H. Xu, H. Jin, Q. Qian, Modified CAR T cells targeting membrane-proximal epitope of mesothelin enhances the antitumor function against large solid tumor, *Cell Death Dis.* 10 (2019) 1–12, <https://doi.org/10.1038/s41419-019-1711-1>.
- [168] T.E. Schnalzer, M.H. Groot, C. Zhang, M.H. Mosa, B.E. Michels, J. Röder, T. Darvishi, W.S. Wels, H.F. Farin, 3D model for CAR-mediated cytotoxicity using patient-derived colorectal cancer organoids, *EMBO J.* 38 (2019) 1–15, <https://doi.org/10.15252/embj.2018100928>.
- [169] F. Jacob, R.D. Salinas, D.Y. Zhang, P.T.T. Nguyen, J.G. Schnell, S.Z.H. Wong, R. Thokala, S. Sheikh, D. Saxena, S. Prokop, D. Ao Liu, X. Qian, D. Petrov, T. Lucas, H.I. Chen, J.F. Dorsey, K.M. Christian, Z.A. Binder, M. Nasrallah, S. Brem, D.M. O'Rourke, G. Li Ming, H. Song, A Patient-derived glioblastoma organoid model and biobank recapitulates inter- and intra-tumoral heterogeneity, *Cell.* 180 (2020) 188–204.e22, <https://doi.org/10.1016/j.cell.2019.11.036>.
- [170] L. Wallstabe, C. Göttlich, L.C. Nelke, J. Kühnemundt, T. Schwarz, T. Nerretter, H. Einsele, H. Walles, G. Danekar, S.L. Nietzer, M. Hudecek, ROR1-CAR T cells are effective against lung and breast cancer in advanced microphysiologic 3D tumor models, *JCI Insight* 4 (2019), <https://doi.org/10.1172/jci.insight.126345>.
- [171] A.L. Mellor, D.H. Munn, Creating immune privilege: active local suppression that benefits friends, but protects foes, *Nat. Rev. Immunol.* (2008), <https://doi.org/10.1038/nri2233>.
- [172] A. Palazón, I. Martínez-Forero, A. Teixeira, A. Morales-Kastresana, C. Alfaro, M. F. Sanmamed, J.L. Perez-Gracia, I. Peñuelas, S. Hervás-Stubbs, A. Rouzaut, M.O. de Landázuri, M. Jure-Kunkel, J. Aragonés, I. Melero, The HIF-1 α hypoxia response in tumor-infiltrating T lymphocytes induces functional CD137 (4-1BB) for immunotherapy, *Cancer Discov.* (2012), <https://doi.org/10.1158/2159-8290.CD-11-0314>.
- [173] S.M. Hatfield, J. Kjaergaard, D. Lukashew, T.H. Schreiber, B. Belikoff, R. Abbott, S. Sethumadhavan, P. Philbrook, K. Ko, R. Cannici, M. Thayer, S. Rodig, J.L. Kutok, E.K. Jackson, B. Karger, E.R. Podack, A. Ohta, M.V. Sitkovsky, Immunological mechanisms of the antitumor effects of supplemental oxygenation, *Sci. Transl. Med.* (2015), <https://doi.org/10.1126/scitranslmed.aaa1260>.
- [174] J.C. Briones, W.V. Espulgar, S. Koyama, H. Yoshikawa, J.H. Park, Y. Naito, A. Kumanooh, E. Tamiya, H. Takamatsu, M. Saito, A microfluidic platform for single cell fluorometric granzyme B profiling, *Theranostics* (2020), <https://doi.org/10.7150/thno.37728>.
- [175] B.M. Larimer, E. Wehrenberg-Klee, F. Dubois, A. Mehta, T. Kalomeris, K. Flaherty, G. Boland, U. Mahmood, Granzyme B PET imaging as a predictive biomarker of immunotherapy response, *Cancer Res.* (2017), <https://doi.org/10.1158/0008-5472.CAN-16-3346>.
- [176] H.R. Kim, S.J. Ha, M.H. Hong, S.J. Heo, Y.W. Koh, E.C. Choi, E.K. Kim, K.H. Pyo, I. Jung, D. Seo, J. Choi, B.C. Cho, S.O. Yoon, PD-L1 expression on immune cells, but not on tumor cells, is a favorable prognostic factor for head and neck cancer patients, *Sci. Rep.* (2016), <https://doi.org/10.1038/srep36956>.
- [177] V. Prima, L.N. Kaliberova, S. Kaliberov, D.T. Curiel, S. Kusmartsev, COX2/mPGES1/PGI2 pathway regulates PD-L1 expression in tumor-associated macrophages and myeloid-derived suppressor cells, *Proc. Natl. Acad. Sci. USA* (2017), <https://doi.org/10.1073/pnas.1612920114>.
- [178] C.P. Miller, W. Shin, E.H. Ahn, H.J. Kim, D.H. Kim, Engineering microphysiological immune system responses on chips, *Trends Biotechnol.* 38 (2020) 857–872, <https://doi.org/10.1016/j.tibtech.2020.01.003>.
- [179] A. Polini, L.L. del Mercato, A. Barra, Y.S. Zhang, F. Calabi, G. Gigli, Towards the development of human immune-system-on-a-chip platforms, *Drug Discov. Today* (2019), <https://doi.org/10.1016/j.drudis.2018.10.003>.
- [180] S. Maharjan, B. Cecen, Y.S. Zhang, 3D immunocompetent organ-on-a-chip models, *Small Methods* 4 (2020) 1–21, <https://doi.org/10.1002/smt.202000235>.
- [181] W. Sun, Z. Luo, J. Lee, H.J. Kim, K.J. Lee, P. Tebon, Y. Feng, M.R. Dokmeci, S. Sengupta, A. Khademhosseini, Organ-on-a-chip for cancer and immune organs modeling, *Adv. Healthc. Mater.* (2019), <https://doi.org/10.1002/adhm.201801363>.
- [182] E.W. Esch, A. Bahinski, D. Huh, Organs-on-chips at the frontiers of drug discovery, *Nat. Rev. Drug Discov.* (2015), <https://doi.org/10.1038/nrd4539>.
- [183] J.A. Brown, S.G. Codreanu, M. Shi, S.D. Sherrod, D.A. Markov, M.D. Neely, C.M. Britt, O.S. Hoilett, R.S. Reiserer, P.C. Samson, L.J. McCawley, D.J. Webb, A.B. Bowman, J.A. McLean, J.P. Wikswa, Metabolic consequences of inflammatory disruption of the blood-brain barrier in an organ-on-chip model of the human neurovascular unit, *J. Neuroinflammation* (2016), <https://doi.org/10.1186/s12974-016-0760-y>.
- [184] G.D. Vatine, R. Barrile, M.J. Workman, S. Sances, B.K. Barriga, M. Rahnama, S. Barthakur, M. Kasendra, C. Lucchesi, J. Kerns, N. Wen, W.R. Spivia, Z. Chen, J. Van Eyk, C.N. Svendsen, Human iPSC-derived blood-brain barrier chips enable disease modeling and personalized medicine applications, *Cell Stem Cell.* (2019), <https://doi.org/10.1016/j.stem.2019.05.011>.
- [185] S.J. Kerns, C. Belgur, D.B. Petropolis, R. Barrile, M. Kanelias, J. Sam, T. Weinzierl, T. Fauti, A. Freimoser-Grundschober, J. Eckmann, C. Hage, M. Geiger, P. Ng, W. Tien-Street, D.V. Manatakis, V. Micallef, R. Gerard, M. Bscheider, E. Breous-Nystrom, A. Schneider, A.-M. Giusti, C. Bertinetti-Lapacki, H.S. Grant, A.B. Roth, G.A. Hamilton, T. Singer, K. Karalis, A. Moisan, P. Bruenker, C. Klein, M. Bacac, N. Gjorevski, L. Cabon, Human immunocompetent Organ-on-Chip platforms allow safety profiling of tumor-targeted T-cell bispecific antibodies, *BioRxiv*. 2021 (02) (2021), <https://doi.org/10.1101/2021.02.22.432308>.
- [186] M.R. Parkhurst, J.C. Yang, R.C. Langan, M.E. Dudley, D.A.N. Nathan, S.A. Feldman, J.L. Davis, R.A. Morgan, M.J. Merino, R.M. Sherry, M.S. Hughes, U.S. Kammula, G.Q. Phan, R.M. Lim, S.A. Wank, N.P. Restifo, P.F. Robbins, C.M. Laurencot, S.A. Rosenberg, T cells targeting carcinoembryonic antigen can mediate regression of metastatic colorectal cancer but induce severe transient colitis, *Mol. Ther.* (2011), <https://doi.org/10.1038/mt.2010.272>.
- [187] R.A. Morgan, J.C. Yang, M. Kitano, M.E. Dudley, C.M. Laurencot, S.A. Rosenberg, Case report of a serious adverse event following the administration of T cells transduced with a chimeric antigen receptor recognizing ERBB2, *Mol. Ther.* (2010), <https://doi.org/10.1038/mt.2010.24>.
- [188] C.H.J. Lamers, S. Sleijfer, S. Van Steenberghe, P. Van Elzakker, B. Van Krimpen, C. Groot, A. Vulto, M. Den Bakker, E. Oosterwijk, R. Debets, J.W. Gratama, Treatment of metastatic renal cell carcinoma with CAIX CAR-engineered T cells: clinical evaluation and management of on-target toxicity, *Mol. Ther.* (2013), <https://doi.org/10.1038/mt.2013.17>.
- [189] Y. Zhu, S. Yao, L. Chen, Cell surface signaling molecules in the control of immune responses: a tide model, *Immunology* 34 (2011) 466–478, <https://doi.org/10.1016/j.immuni.2011.04.008>.
- [190] D.S. Chen, I. Mellman, Oncology meets immunology: the cancer-immunity cycle, *Immunity* 39 (2013) 1–10, <https://doi.org/10.1016/j.immuni.2013.07.012>.
- [191] S.L. Topalian, C.G. Drake, D.M. Pardoll, Immune checkpoint blockade: a common denominator approach to cancer therapy, *Cancer Cell.* 27 (2015) 450–461, <https://doi.org/10.1016/j.ccr.2015.03.001>.
- [192] P. Sharma, J.P. Allison, The future of immune checkpoint therapy, *Science* (80-) 348 (2015) 56–61, <https://doi.org/10.1126/science.1257652>.
- [193] R. Grosser, L. Cherkassky, N. Chintala, P.S. Adusumilli, Combination immunotherapy with CAR T cells and checkpoint blockade for the treatment of solid tumors, *Cancer Cell.* 36 (2019) 471–482, <https://doi.org/10.1016/j.ccr.2019.09.006>.
- [194] Y. Liu, R. Wang, Immunotherapy targeting tumor-associated macrophages, *Front. Med.* 7 (2020), <https://doi.org/10.3389/fmed.2020.583708>.
- [195] F.S. Hodi, S.J. O'Day, D.F. McDermott, R.W. Weber, J.A. Sosman, J.B. Haanen, R. Gonzalez, C. Robert, D. Schadendorf, J.C. Hassel, W. Akerley, A.J.M. van den Eertwegh, J. Lutzky, P. Lorigan, J.M. Vaubel, G.P. Linette, D. Hogg, C.H. Ottensmeier, C. Lebbé, C. Peschel, I. Quirt, J.I. Clark, J.D. Wolchok, J.S. Weber, J. Tian, M.J. Yellin, G.M. Nichol, A. Hoos, W.J. Urba, Improved survival with Ipilimumab in Patients with Metastatic Melanoma, *N. Engl. J. Med.* 363 (2010) 711–723, <https://doi.org/10.1056/NEJMoa1003466>.
- [196] C. Robert, G.V. Long, B. Brady, C. Dutriaux, M. Maio, L. Mortier, J.C. Hassel, P. Rutkowski, C. McNeil, E. Kalinka-Warzocho, K.J. Savage, M.M. Hernberg, C. Lebbé, J. Charles, C. Mihalciou, V. Chiarion-Sileni, C. Mauch, F. Cognetti, A. Arance, H. Schmidt, D. Schadendorf, H. Gogas, L. Lundgren-Eriksson, C. Horak, B. Sharkey, I.M. Waxman, V. Atkinson, P.A. Ascierto, Nivolumab in previously untreated melanoma without BRAF mutation, *N. Engl. J. Med.* 372 (2015) 320–330, <https://doi.org/10.1056/NEJMoa1412082>.
- [197] R.K. Vaddepally, P. Kharel, R. Pandey, R. Garje, A.B. Chandra, Review of indications of FDA-approved immune checkpoint inhibitors per NCCN guidelines with the level of evidence, *Cancers (Basel)* 12 (2020), <https://doi.org/10.3390/cancers12030738>.
- [198] A.J. Schoenfeld, M.D. Hellmann, Acquired resistance to immune checkpoint inhibitors, *Cancer Cell.* 37 (2020) 443–455, <https://doi.org/10.1016/j.ccr.2020.03.017>.
- [199] G.V. Long, R. Dummer, O. Hamid, T.F. Gajewski, C. Caglevic, S. Dalle, A. Arance, M.S. Carlino, J.J. Grob, T.M. Kim, L. Demidov, C. Robert, J. Larkin, J.R. Anderson, J. Maleski, M. Jones, S.J. Dieder, T.C. Mitchell, Epacodostat plus pembrolizumab versus placebo plus pembrolizumab in patients with unresectable or metastatic melanoma (ECHO-301/KEYNOTE-252): a phase 3, randomised, double-blind study, *Lancet Oncol.* 20 (2019) 1083–1097, [https://doi.org/10.1016/S1470-2045\(19\)30274-8](https://doi.org/10.1016/S1470-2045(19)30274-8).
- [200] L. Sun, L. Zhang, J. Yu, Y. Zhang, X. Pang, C. Ma, M. Shen, S. Ruan, H.S. Wasan, S. Qiu, Clinical efficacy and safety of anti-PD-1/PD-L1 inhibitors for the

- treatment of advanced or metastatic cancer: a systematic review and meta-analysis. *Sci. Rep.* 10 (2020) 1–13. <https://doi.org/10.1038/s41598-020-58674-4>.
- [201] A. Haslam, V. Prasad, Estimation of the percentage of US patients with cancer who are eligible for and respond to checkpoint inhibitor immunotherapy drugs. *JAMA Netw. Open.* 2 (2019). <https://doi.org/10.1001/jamanetworkopen.2019.2535>.
- [202] D. Chowell, L.G.T. Morris, C.M. Grigg, J.K. Weber, R.M. Samstein, V. Makarov, F. Kuo, S.M. Kendall, D. Requena, N. Riaz, B. Greenbaum, J. Carroll, E. Garon, D.M. Hyman, A. Zehir, D. Solit, M. Berger, R. Zhou, N.A. Rizvi, T.A. Chan, Patient HLA class I genotype influences cancer response to checkpoint blockade immunotherapy. *Science* (80-) 359 (2018) 582–587. <https://doi.org/10.1126/science.aao4572>.
- [203] L.A. Low, C. Mummery, B.R. Berridge, C.P. Austin, D.A. Tagle, Organs-on-chips: into the next decade. *Nat. Rev. Drug Discov.* (2020). <https://doi.org/10.1038/s41573-020-0079-3>.
- [204] A. Al-Samadi, B. Poor, K. Tuomainen, V. Liu, A. Hyytiäinen, I. Suleymanova, K. Mesimäki, T. Wilkman, A. Mäkitie, P. Saavalainen, T. Salo, In vitro humanized 3D microfluidic chip for testing personalized immunotherapeutics for head and neck cancer patients. *Exp. Cell Res.* 383 (2019). <https://doi.org/10.1016/j.yexcr.2019.111508>.
- [205] R.S. Herbst, J.C. Soria, M. Kowanzet, G.D. Fine, O. Hamid, M.S. Gordon, J.A. Sosman, D.F. McDermott, J.D. Powderly, S.N. Gettinger, H.E.K. Kohrt, L. Horn, D.P. Lawrence, S. Rost, M. Leabman, Y. Xiao, A. Moktrin, H. Koeppen, P.S. Hegde, I. Mellman, D.S. Chen, F.S. Hodi, Predictive correlates of response to the anti-PD-L1 antibody MPDL3280A in cancer patients. *Nature*. 515 (2014) 563–567. <https://doi.org/10.1038/nature14011>.
- [206] S. Sarkar, S. McKenney, P. Sabhachandani, J. Adler, R. Hu, D. Stroopinsky, J. Rosenblatt, D. Avigan, T. Konry, Anti-myeloma activity and molecular logic operation by Natural Killer cells in microfluidic droplets. *Sensors Actuators B Chem.* (2019). <https://doi.org/10.1016/j.snb.2018.11.068>.
- [207] P. Sabhachandani, S. Sarkar, S. McKenney, D. Ravi, A.M. Evens, T. Konry, Microfluidic assembly of hydrogel-based immunogenic tumor spheroids for evaluation of anticancer therapies and biomarker release. *J. Control. Release*. 295 (2019) 21–30. <https://doi.org/10.1016/j.jconrel.2018.12.010>.
- [208] L.A. Emens, G. Middleton, The interplay of immunotherapy and chemotherapy: Harnessing potential synergies. *Cancer Immunol. Res.* 3 (2015) 436–443. <https://doi.org/10.1158/2326-6066.CCR-15-0064>.
- [209] L.A. Emens, P.A. Ascierto, P.K. Darcy, S. Demaria, A.M.M. Eggermont, W.L. Redmond, B. Seliger, F.M. Marincola, Cancer immunotherapy: opportunities and challenges in the rapidly evolving clinical landscape. *Eur. J. Cancer* 81 (2017) 116–129. <https://doi.org/10.1016/j.ejca.2017.01.035>.
- [210] X. Li, Y. Fu, B. Yang, E. Guo, Y. Wu, J. Huang, X. Zhang, R. Xiao, K. Li, B. Wang, J. Hu, C. Sun, G. Chen, BRD4 inhibition by AZD5153 promotes antitumor immunity via depolarizing M2 macrophages. *Front. Immunol.* 11 (2020) 1–12. <https://doi.org/10.3389/fimmu.2020.00089>.
- [211] X. Li, Y. Fu, B. Yang, E. Guo, Y. Wu, J. Huang, X. Zhang, R. Xiao, K. Li, B. Wang, J. Hu, C. Sun, G. Chen, BRD4 inhibition by AZD5153 promotes antitumor immunity via depolarizing M2 macrophages. *Front. Immunol.* 11 (2020). <https://doi.org/10.3389/fimmu.2020.00089>.
- [212] X. Cui, C. Ma, V. Vasudevaraja, J. Serrano, J. Tong, Y. Peng, M. Delorenzo, G. Shen, J. Frenster, R.-T.T. Morales, W. Qian, A. Tsigirgos, A.S. Chi, R. Jain, S.C. Kurz, E.P. Sulman, D.G. Placantonakis, M. Snuderl, W. Chen, Dissecting the immunosuppressive tumor microenvironments in Glioblastoma-on-a-Chip for optimized PD-1 immunotherapy. *Elife* (2020). <https://doi.org/10.7554/eLife.52253>.
- [213] P.A. Ott, F.S. Hodi, C. Robert, CTLA-4 and PD-1/PD-L1 blockade: New immunotherapeutic modalities with durable clinical benefit in melanoma patients. *Clin. Cancer Res.* 19 (2013) 5300–5309. <https://doi.org/10.1158/1078-0432.CCR-13-0143>.
- [214] K.M. Hargadon, C. Johnson, C.J. Williams, Immune checkpoint blockade therapy for cancer: an overview of FDA-approved immune checkpoint inhibitors. *Int. Immunopharmacol.* 62 (2018) 29–39. <https://doi.org/10.1016/j.intimp.2018.06.001>.
- [215] C. Robert, A decade of immune-checkpoint inhibitors in cancer therapy. *Nat. Commun.* 11 (2020) 3801. <https://doi.org/10.1038/s41467-020-17670-y>.
- [216] J. Choi, S.Y. Lee, Clinical characteristics and treatment of immune-related adverse events of immune checkpoint inhibitors. *Immune Netw.* 20 (1) (2020). <https://doi.org/10.4110/in.2020.20.e9>.
- [217] J.M. Michot, C. Bigenwald, S. Champiat, M. Collins, F. Carbone, S. Postel-Vinay, A. Berdelou, A. Varga, R. Bahleda, A. Hollebecque, C. Massard, A. Fuerea, V. Ribrag, A. Gazzah, J.P. Armand, N. Amellal, E. Angevin, N. Noel, C. Boutros, C. Mateus, C. Robert, J.C. Soria, A. Marabelle, O. Lambotte, Immune-related adverse events with immune checkpoint blockade: a comprehensive review. *Eur. J. Cancer*. 54 (2016) 139–148. <https://doi.org/10.1016/j.ejca.2015.11.016>.
- [218] R. Park, L. Lopes, C.R. Cristancho, I.M. Riano, A. Saeed, Treatment-related adverse events of combination immune checkpoint inhibitors: systematic review and meta-analysis. *Front. Oncol.* 10 (2020) 258. <https://doi.org/10.3389/fonc.2020.00258>.
- [219] I. Parthimos, G. Liamis, E. Dounousi, G. Pentheroudakis, D. Mauri, G. Zarkavelis, M. Florentin, Metabolic consequences of immune checkpoint inhibitors: a new challenge in clinical practice. *Crit. Rev. Oncol. Hematol.* 151 (2020). <https://doi.org/10.1016/j.critrevonc.2020.102979>.
- [220] D.L. Suzman, L. Pelosof, A. Rosenberg, M.I. Avigan, Hepatotoxicity of immune checkpoint inhibitors: an evolving picture of risk associated with a vital class of immunotherapy agents. *Liver Int.* (2018). <https://doi.org/10.1111/liv.13746>.
- [221] T. Peeraphatdit, J. Wang, M.A. Odenwald, S. Hu, J. Hart, M.R. Charlton, Hepatotoxicity from immune checkpoint inhibitors: a systematic review and management recommendation. *Hepatology*. (2020). <https://doi.org/10.1002/hep.31227>.
- [222] N. Palaskas, J. Lopez-Mattei, J.B. Durand, C. Iliescu, A. Deswal, Immune checkpoint inhibitor myocarditis: pathophysiological characteristics, diagnosis, and treatment. *J. Am. Heart Assoc.* (2020). <https://doi.org/10.1161/JAHA.119.013757>.
- [223] S. Ganatra, T.G. Neilan, Immune checkpoint inhibitor-associated myocarditis. *Oncologist* (2018). <https://doi.org/10.1634/theoncologist.2018-0130>.
- [224] J.A. Marin-Acevedo, R.M. Chirila, R.S. Dronca, Immune checkpoint inhibitor toxicities. *Mayo Clin. Proc.* 94 (2019) 1321–1329. <https://doi.org/10.1016/j.jmayocp.2019.03.012>.
- [225] D.B. Johnson, K.L. Reynolds, R.J. Sullivan, J.M. Balko, J.R. Patrinely, L.C. Cappelli, J. Naidoo, J.J. Moslehi, Immune checkpoint inhibitor toxicities: systems-based approaches to improve patient care and research. *Lancet Oncol.* 21 (2020) e398–e404. [https://doi.org/10.1016/S1470-2045\(20\)30107-8](https://doi.org/10.1016/S1470-2045(20)30107-8).
- [226] K. Esfahani, A. Elkrief, C. Calabrese, R. Lapointe, M. Hudson, B. Routy, W.H. Miller, L. Calabrese, Moving towards personalized treatments of immune-related adverse events. *Nat. Rev. Clin. Oncol.* 17 (2020) 504–515. <https://doi.org/10.1038/s41571-020-0352-8>.
- [227] S. Das, D.B. Johnson, Immune-related adverse events and anti-tumor efficacy of immune checkpoint inhibitors. *J. Immunother. Cancer.* 7 (2019) 306. <https://doi.org/10.1186/s40425-019-0805-8>.
- [228] J. Galon, A. Costes, F. Sanchez-Cabo, A. Kirilovsky, B. Mlecnik, C. Lagorce-Pagès, M. Tosolini, M. Camus, A. Berger, P. Wind, F. Zinzindohoué, P. Bruneval, P.H. Cugnenc, Z. Trajanoski, W.H. Fridman, F. Pagès, Type, density, and location of immune cells within human colorectal tumors predict clinical outcome. *Science* (80-) 313 (2006) 1960–1964. <https://doi.org/10.1126/science.1129139>.
- [229] T. Fang, R. Li, Z. Li, J. Cho, J.S. Guzman, R.D. Kamm, H.L. Ploegh, Remodeling of the tumor microenvironment by a chemokine/anti-PD-L1 nanobody fusion protein. *Mol. Pharm.* 16 (2019) 2838–2844. <https://doi.org/10.1021/acs.molpharmaceut.9b00078>.
- [230] A. Ribas, R. Dummer, I. Puzanov, A. VanderWalde, R.H.I. Andtbacka, O. Michielin, A.J. Olszanski, J. Malvehy, J. Cebron, E. Fernandez, J.M. Kirkwood, T.F. Gajewski, L. Chen, K.S. Gorski, A.A. Anderson, S.J. Dieder, M.E. Lassman, J. Gansert, F.S. Hodi, G.V. Long, Oncolytic virotherapy promotes intratumoral T cell infiltration and improves anti-PD-1 immunotherapy. *Cell* 170 (2017) 1109–1119.e10. <https://doi.org/10.1016/j.cell.2017.08.027>.
- [231] R.H.I. Andtbacka, F. Collichio, K.J. Harrington, M.R. Middleton, G. Downey, K. Ohrling, H.L. Kaufman, Final analyses of OPTIM: a randomized phase III trial of talimogene laherparepvec versus granulocyte-macrophage colony-stimulating factor in unresectable stage III-IV melanoma. *J. Immunother. Cancer* 7 (2019) 145. <https://doi.org/10.1186/s40425-019-0623-z>.
- [232] A. Marchini, E.M. Scott, J. Rommelaere, Overcoming barriers in oncolytic virotherapy with HDAC inhibitors and immune checkpoint blockade. *Viruses* 8 (2016). <https://doi.org/10.3390/v8100099>.
- [233] K.J. Lee, S.W. Lee, H.-N. Woo, H.M. Cho, D.B. Yu, S.Y. Jeong, C.H. Joo, G.S. Jeong, H. Lee, Real-time monitoring of oncolytic VSV properties in a novel in vitro microphysiological system containing 3D multicellular tumor spheroids. *PLoS One* 15 (2020). <https://doi.org/10.1371/journal.pone.0235356>.
- [234] S.W. Lee, K.J. Lee, S.Y. Jeong, C.H. Joo, H. Lee, G.S. Jeong, Evaluation of bystander infection of oncolytic virus using a medium flow integrated 3D in vitro microphysiological system. *Adv. Biosyst.* 4 (2020). <https://doi.org/10.1002/adbi.201900143>.
- [235] A. Lemos de Matos, L.S. Franco, G. McFadden, Oncolytic viruses and the immune system: the dynamic duo. *Mol. Ther. Methods Clin. Dev.* 17 (2020) 349–358. <https://doi.org/10.1016/j.omtm.2020.01.001>.
- [236] P. Kleinpeter, L. Fend, C. Thioudellet, M. Geist, N. Sfrontato, V. Koerper, C. Fahrner, D. Schmitt, M. Gantzer, C. Remy-Ziller, R. Brandely, D. Villeval, K. Rittner, N. Silvestre, P. Erbs, L. Zitvogel, E. Quéméneur, X. Prévieux, J.-B. Marchand, Vectorization in an oncolytic vaccinia virus of an antibody, a Fab and a scFv against programmed cell death-1 (PD-1) allows their intratumoral delivery and an improved tumor-growth inhibition. *Oncoimmunology* 5 (2016). <https://doi.org/10.1080/2162402X.2016.1220467>.
- [237] L. Russell, K.W. Peng, S.J. Russell, R.M. Diaz, Oncolytic viruses: priming time for cancer immunotherapy. *BioDrugs* 33 (2019) 485–501. <https://doi.org/10.1007/s40259-019-00367-0>.
- [238] R.E. Hollingsworth, K. Jansen, Turning the corner on therapeutic cancer vaccines. *Npj Vaccines* 4 (2019) 1–10. <https://doi.org/10.1038/s41541-019-0103-y>.
- [239] A.J. Najibi, D.J. Mooney, Cell and tissue engineering in lymph nodes for cancer immunotherapy. *Adv. Drug Deliv. Rev.* 161–162 (2020) 42–62. <https://doi.org/10.1016/j.addr.2020.07.023>.
- [240] P.W. Kantoff, C.S. Ferraro, N.D. Shore, E.R. Berger, E.J. Small, D.F. Penson, C.H. Redfern, A.C. Ferrari, R. Dreicer, R.B. Sims, Y. Xu, M.W. Frohlich, P.F. Schellhammer, Sipuleucel-T immunotherapy for castration-resistant prostate cancer. *N. Engl. J. Med.* (2010). <https://doi.org/10.1056/NEJMoa1001294>.
- [241] A. Mullard, The cancer vaccine resurgence. *Nat. Rev. Drug Discov.* (2016). <https://doi.org/10.1038/nrd.2016.201>.

- [242] J.J.L. Jacobs, C. Snackey, A.A. Geldof, D. Characiejus, R.J.A. Van Moorselaar, W. Den Otter. Review: inefficacy of therapeutic cancer vaccines and proposed improvements. *casus of prostate cancer*, *Anticancer Res.* (2014).
- [243] H. Maeng, M. Terabe, J.A. Berzofsky. Cancer vaccines: translation from mice to human clinical trials. *Curr. Opin. Immunol.* 51 (2018) 111–122, <https://doi.org/10.1016/j.coi.2018.03.001>.
- [244] S. Kim, S.B. Shah, P.L. Graney, A. Singh. Multiscale engineering of immune cells and lymphoid organs. *Nat. Rev. Mater.* 4 (2019) 355–378, <https://doi.org/10.1038/s41578-019-0100-9>.
- [245] A. Shanti, B. Samara, A. Abdullah, N. Hallfors, D. Accoto, J. Sapudom, A. Alatoon, J. Teo, S. Danti, C. Stefanini. Multi-compartment 3D-cultured organ-on-a-chip: towards a biomimetic lymph node for drug development. *Pharmaceutics* (2020), <https://doi.org/10.3390/pharmaceutics12050464>.
- [246] G. Goyal, J. Long, O. Levy, D.E. Ingber. Biologically inspired, iterative engineering of a human lymphoid follicle chip. *J. Immunol.* (2018).
- [247] P. Moura Rosa, N. Gopalakrishnan, H. Ibrahim, M. Haug, Ø. Halaas. The intercell dynamics of T cells and dendritic cells in a lymph node-on-a-chip flow device. *Lab Chip* (2016), <https://doi.org/10.1039/c6lc00702c>.
- [248] M. An, M. Li, J. Xi, H. Liu. Silica nanoparticle as a lymph node targeting platform for vaccine delivery. *ACS Appl. Mater. Interfaces.* (2017), <https://doi.org/10.1021/acsami.7b06024>.
- [249] S. Kang, S. Ahn, J. Lee, J.Y. Kim, M. Choi, V. Gujrati, H. Kim, J. Kim, E.C. Shin, S. Jon. Effects of gold nanoparticle-based vaccine size on lymph node delivery and cytotoxic T-lymphocyte responses. *J. Control. Release* (2017), <https://doi.org/10.1016/j.jconrel.2017.04.024>.
- [250] N.S. Bhise, J. Ribas, V. Manoharan, Y.S. Zhang, A. Polini, S. Massa, M.R. Dokmeci, A. Khademhosseini. Organ-on-a-chip platforms for studying drug delivery systems. *J. Control. Release* (2014), <https://doi.org/10.1016/j.jconrel.2014.05.004>.
- [251] M.C. Cox, L.M. Reese, L.R. Bickford, S.S. Verbridge. Toward the broad adoption of 3D tumor models in the cancer drug pipeline. *ACS Biomater. Sci. Eng.* (2015), <https://doi.org/10.1021/acsbomaterials.5b00172>.
- [252] D.G. DeNardo, B. Ruffell. Macrophages as regulators of tumour immunity and immunotherapy. *Nat. Rev. Immunol.* (2019), <https://doi.org/10.1038/s41577-019-0127-6>.
- [253] I. Pedroza-Pacheco, A. Madrigal, A. Saudemont. Interaction between natural killer cells and regulatory T cells: perspectives for immunotherapy. *Cell. Mol. Immunol.* (2013), <https://doi.org/10.1038/cmi.2013.2>.
- [254] D.F. Quail, A.J. Dannenberg. The obese adipose tissue microenvironment in cancer development and progression. *Nat. Rev. Endocrinol.* (2019), <https://doi.org/10.1038/s41574-018-0126-x>.
- [255] A.J. Cozzo, A.M. Fuller, L. Makowski. Contribution of adipose tissue to development of cancer. *Compr. Physiol.* 8 (2018) 237–282, <https://doi.org/10.1002/cphy.c170008>.
- [256] J. Rogal, C. Binder, E. Kromidas, J. Roos, C. Probst, S. Schneider, K. Schenke-Layland, P. Loskill. WAT-on-a-chip integrating human mature white adipocytes for mechanistic research and pharmaceutical applications. *Sci. Rep.* 10 (2020) 6666, <https://doi.org/10.1038/s41598-020-63710-4>.
- [257] K. Rennert, S. Steinborn, M. Gröger, B. Ungerböck, A.M. Jank, J. Ehgartner, S. Nietzsche, J. Dinger, M. Kiehnopf, H. Funke, F.T. Peters, A. Lupp, C. Gärtner, T. Mayr, M. Bauer, O. Huber, A.S. Mosig. A microfluidically perfused three dimensional human liver model. *Biomaterials* (2015), <https://doi.org/10.1016/j.biomaterials.2015.08.043>.
- [258] D. Huh, B.D. Matthews, A. Mammoto, M. Montoya-Zavala, H. Yuan Hsin, D.E. Ingber. Reconstituting organ-level lung functions on a chip. *Science* (80-) (2010), <https://doi.org/10.1126/science.1188302>.

RESEARCH ARTICLE

Immunocompetent PDMS-Free Organ-on-Chip Model of Cervical Cancer Integrating Patient-Specific Cervical Fibroblasts and Neutrophils

Elena Kromidas, Alicia Geier, Adrian Weghofer, Hui-Yu Liu, Martin Weiss, and Peter Loskill*

Despite preventive measures and available treatments, cervical cancer still ranks as the fourth most prevalent cancer among women worldwide and remains the leading cause of cancer death in women in many developing countries. To gain further insights into pathogenesis and to develop novel (immuno)therapies, more sophisticated human models recreating patient heterogeneities and including aspects of the tumor microenvironment are urgently required. A novel polydimethylsiloxane-free microfluidic platform, designed specifically for the generation and cultivation of cervical cancerous tissue, is introduced. The microscale open-top tissue chambers of the cervical cancer-on-chip (CCoC) enable facile generation and long-term cultivation of SiHa spheroids in co-culture with donor-derived cervical fibroblasts. The resulting 3D tissue emulates physiological architecture and allows dissection of distinct effects of the stromal tissue on cancer viability and growth. Treatment with cisplatin at clinically-relevant routes of administration and dosing highlights the platform's applicability for drug testing. Moreover, the model is amenable for integration and recruitment of donor-derived neutrophils from the microvasculature-like channel into the tissue, all while retaining their ability to produce neutrophil extracellular traps. In the future, the immunocompetent CCoC featuring donor-specific primary cells and tumor spheroids has the potential to contribute to the development of new (immuno)therapeutic options.

1. Introduction

Cervical cancer is the fourth most frequent cancer in women worldwide with about 600 000 new cases being diagnosed in 2020, representing 6.5% of all female cancers.^[1] Infection with human papillomavirus (HPV) stands as a necessary yet insufficient cause of cervical cancer development.^[2] HPV infections are the most common sexually transmitted infection in the United States, with more than 80% of sexually active individuals being infected with HPV at least once during their lifetime.^[3] More than 90% of HPV infections within the cervix resolve naturally,^[4] however, a persistent infection can lead to cervical cancer. A major breakthrough in the battle against HPV-linked diseases was the introduction of prophylactic vaccines designed to thwart high-risk HPV strains HPV16 and HPV18. The remarkably efficacious primary (vaccine) and secondary (screening) preventive measures have rendered cervical cancer nearly entirely preventable. Unfortunately, insufficient vaccine availability and vaccination coverage persist as challenges, resulting in cervical

cancer still being the leading cause of cancer death in 36 countries, particularly in low- and middle-income countries. Since HPV-associated cancers remain a pressing global health concern,^[1] the Director General of the World Health Organization (WHO) announced a global call for action to eliminate cervical cancer.^[5]

Despite technological advancements, many patients are still diagnosed only in an advanced stage with poor prognosis, particularly in developing countries. For these patients, it is important to receive a timely and effective treatment, such as surgery, radiotherapy, and chemotherapy depending on the disease stage. For early-stage disease (FIGO stage IA1-IIA1) the National Comprehensive Cancer Network recommends either surgery or radiotherapy, whereas the treatment recommended for advanced stages (FIGO IIB-IVA) may be combined therapy including external beam radiation, cisplatin-containing chemotherapy, and brachytherapy. In case of metastasis and most recently in case of locally advanced malignancies, targeted therapy with

E. Kromidas, A. Geier, A. Weghofer, H.-Y. Liu, P. Loskill
Department for Microphysiological Systems, Institute of Biomedical Engineering, Faculty of Medicine
Eberhard Karls University Tübingen
72074 Tübingen, Germany
E-mail: peter.loskill@uni-tuebingen.de

M. Weiss, P. Loskill
Department for Biomedicine and Materials Science
NMI Natural and Medical Sciences Institute at the University of Tübingen
72770 Reutlingen, Germany

M. Weiss
Department for Women's Health, Faculty of Medicine
Eberhard Karls University Tübingen
72076 Tübingen, Germany

P. Loskill
3R Center Tübingen for In Vitro Models and Alternatives to Animal Testing
72074 Tübingen, Germany

 The ORCID identification number(s) for the author(s) of this article can be found under <https://doi.org/10.1002/adhm.202302714>

DOI: 10.1002/adhm.202302714

bevacizumab and immunotherapy with immune checkpoint inhibitors have been applied.^[6] Frequent recurrence after treatment and the accompanying side effects and complications emphasize the necessity for alternative cervical cancer treatments that offer minimized adverse outcomes.^[7–10] Even though patients are treated based on defined guidelines, every individual patient shows a different response because of the heterogeneity of patients and their tumors. While certain prognostic factors (e.g., clinical stage, age, tumor histology, depth of invasion, tumor grade, size of primary tumor, lymph node involvement, parametrium involvement, and lymph-vascular space invasion) have been identified, many unknown factors leading to differential treatment success remain.^[11] Therefore, there is an urgent need for patient-specific *in vitro* models to properly stratify and predict the efficacy of available chemotherapeutic, targeted, and immunologic agents as well as to enable the development of novel therapeutic options. Leveraging microfluidic organ-on-chip technology, tissue engineering, and patient-derived primary cells, this study aims to improve (personalized) treatment strategies and outcomes for cervical cancer patients in the future.

The two major histological subtypes of cervical cancer are squamous-cell carcinoma (SCC) and adenocarcinomas, accounting for over 70% and almost 20% of all cervical carcinomas, respectively.^[12] Structurally, invasive SCC is characterized by cancerous nest of neoplastic epithelium infiltrating the stroma.^[13,14] Within the tumor microenvironment (TME), extensive bi-directional communication occurs between HPV-positive epithelial cells and stromal components such as fibroblasts and immune cells.^[13,15] In healthy tissue, resident, quiescent fibroblasts are responsible for extracellular matrix (ECM) homeostasis and play major roles in communicating with other cell types.^[16] In cancer, the initial fibroblast response can be tumor-suppressive through contact- and soluble factor-mediated mechanisms termed neighbor suppression.^[17] However, fibroblasts can be activated by cancer cells and undergo substantial metabolic changes in response to growth factors and the hypoxic environment. These cancer-associated fibroblasts (CAFs) do not only represent the predominant cell type of the TME, but contribute to the malignant, anabolic phenotype of cancer cells by influencing cancer cell survival, proliferation and invasion, leukocyte infiltration, ECM remodeling, angiogenesis and chemoresistance amongst others.^[17–22]

Neutrophils (polymorphonuclear leukocytes, PMNs) are the most abundant, short-lived immune cell in humans and are considered first responder immune cells, as they are rapidly recruited to sites of infection, where they destroy invading pathogens due to their innate recognition of damage and infection and also clear cellular debris.^[23–25] Increasing evidence emphasizes the contribution of PMNs to tumor initiation, progression, metastasis, and therapeutic success. In the TME, tumor-associated neutrophils (TAN) can acquire anti- (N1) or pro-tumoral (N2) properties with heterogenous effects^[26–32] making TANs a promising target for immunotherapeutic interventions.^[28,33–35] Cervical cancer is a compelling candidate for potential immunotherapeutic interventions targeting PMNs, since patients typically exhibit neutrophilia and reduced migratory capacity of peripheral blood PMNs,^[36] and PMNs are the second most abundant immune cell type in the TME of cervical carcinomas.^[15] In cervical cancer, (intratumoral) PMN density was associated with

shorter progression-free survival (PFS),^[37,38] with stromal neutrophil extracellular traps (NETs) as an independent prognostic factor for cervical cancer.^[39] NETs are large, toxic, web-like structures, that are released extracellularly by PMNs by a mechanism generally leading to cell death and, hence, referred to as NETosis. These structures consist mainly of adhesive, decondensed chromatin, spiked with microbicidal proteins such as citrullinated histones (H3cit) as well as granular myeloperoxidase (MPO) and neutrophil elastase (NE).^[40–42] First described as a mechanism to immobilize and kill bacteria,^[40] NETosis has since then been observed in various diseases, including cancer.^[33,42,43] NETs may possess anticarcinogenic properties by destroying cancer cells and stimulating immune cells, but also exhibit numerous protumoral effects such as promotion of cancer cell proliferation and dissemination, creation of a physical barrier of encapsulated tumor cells preventing cancer cell killing by immune cells, aiding extravasation of circulating tumor cells, wakening dormant cancer cells, and driving cancer therapy resistance. Overall, presence of NETs is associated with poor prognosis in multiple cancers and some cancers have been shown to induce NET formation.^[25,29,44] In cervical cancer, NETs are associated with short recurrence-free survival,^[39] and in peripheral blood PMNs, NET levels were larger in cervical cancer patient plasma compared to healthy controls.^[45] These data suggest NETs as a potential prognostic marker and therapeutic target for the development of new generations of immunotherapies, also in combination with immune checkpoint inhibitors.^[25,29,33,39,46]

Developing more effective therapies faces a significant challenge due to a lack of *in vitro* cancer models that adequately capture the complexity of human tumors, particularly with respect to the TME and immune response. Animal models often fail to reproduce human biology.^[47] Distinct differences in cervical cancer biology between humans and mice are, for example, oncogenes E6 and E7. In mice, the HPV-E6-inhibited p53 signaling pathway plays a crucial role in triggering senescence, while in humans, the HPV-E7-inhibited retinoblastoma signaling pathway dominates. Furthermore, carcinomas that develop in transgenic mice often occur in epithelial sites elsewhere in the mouse.^[48] Patient-derived xenograft (PDX)-models capture heterogeneity, histology, and human genetic background, and generally exhibit the metastatic patterns associated with each disease. However, the most common transplantation sites for cervical cancer PDX-models are subcutaneous tissue and the subrenal capsule;^[4] immune cell deficiency, moreover, renders them unsuitable for immunotherapeutic intervention studies. On the other hand, novel bioengineering approaches toward complex microphysiological 3D cancer models promise to better emulate human tumors and TME.^[49] In this context, the sourcing of cells becomes a pivotal consideration—for instance, HPV-immortalized cervical epithelia in Transwell models demonstrated greater invasive behavior when cultured on human fibroblasts as opposed to mouse fibroblasts, emphasizing the importance of employing species-specific fibroblasts in *in vitro* models. With respect to PMNs, so far, the majority of cancer research relied on animal models. However, mouse and human PMNs differ substantially in their biology and functions,^[50,51] highlighting the need for models integrating human PMNs.

In this study, we engineered a complex, human cervical cancer 3D model based on organ-on-chip technology—tumor spheroids

co-cultured alongside tissue-specific cervical fibroblasts were integrated within an ECM-simulating hydrogel in a tailored, polydimethylsiloxane (PDMS)-free microfluidic platform. To demonstrate the utility of our newly devised model for drug testing, we employed the widely used chemotherapeutic agent cisplatin, successfully demonstrating a response to very low, patient-relevant concentrations. Furthermore, donor-derived, PMNs perfused through the vasculature-like channels were recruited into the tissue and retained their capacity for NETosis, illustrating the model's ability to capture and study intricate immune responses.

2. Results

2.1. Tailored Microphysiological Platform for Cervical Cancer Tissue Models

The novel microphysiological platform was designed specifically for the generation and cultivation of cancerous cervical tissues with the capability of recreating dynamic flow and perfusion of immune cells. The PDMS-free cervical cancer-on-chip (CCoC) platform is based on thermoplastic microfluidic modules incorporating two separate channel systems on a standard microscope slide footprint (Figure 1A). Each individual system comprises a straight channel that is separated by a porous membrane (pore size: 5 μm) from four cylindrical, open-top tissue compartments. The modules consist of a stack of three polymer layers sandwiching a laser-cut polyethylene terephthalate (PET) membrane. The channel layer is patterned in a styrene ethylene butylene styrene (SEBS)/polycarbonate (PC) hybrid material via a combined hot embossing and thermal fusion process (Figure 1B). The microchannels (300 μm wide and 200 μm high) are, thereby, structured in the thermoplastic elastomer SEBS, while the thermoplastic PC bottom layer provides mechanical reinforcement for easier handling and enhances optical properties.^[52] The hybrid channel layer is fused to a SEBS tissue layer and a poly(methyl methacrylate) (PMMA) reservoir layer via a thermal bonding process, whereby the PET membrane is sandwiched between channel and tissue layers (Figure 1C). In both tissue and reservoir layer, cylindrical through-holes (diameter 1.5 and 5 mm, respectively) are patterned via laser structuring to generate an open-top cavity. This cavity consists of a tissue well and a media reservoir that allows submersed culture of the tissue and can be sealed during culture. The ports in the reservoir layer are connected to the channel in the media layer and hold adapters for the connection with tubing to the syringe pump or immune cell reservoirs. An essential aspect of the hybrid-material platform is its capability to utilize a biopsy punch to extract tissues for subsequent analyses, allowing for diverse readouts from a single system (Figure 1D). The biopsy punch is small enough to pass through the larger hole of the thermoplastic reservoir layer while maintaining a protective ring of thermoplastic elastomer around the fragile tissue.

2.2. Isolation of Human Donor-Derived Peripheral Neutrophils and Cervical Fibroblasts

To recreate the *in vivo* TME and enable future studies on patient-specific effects, PMNs, and primary cervical fibroblasts were isolated from human, donor-derived biopsies by adapting existing

protocols.^[53,54] Flow cytometry analysis revealed high purity of PMNs isolated from whole blood, with 84.7% of the CD45+ positive population being positive for CD11b+, 93.4% for CD16+, 92.3% for CD66b+, and 84.6% for all CD11b+CD16+CD66b+ (Figure 2A). Cervical fibroblasts were isolated from the subepithelial stroma of cervical tissue biopsies from otherwise indicated surgical tissue removal (e. g. uterus descensus) using specifically tailored protocols and expressed fibroblast-associated vimentin and fibronectin in subsequent expansion culture (Figure 2B).

2.3. On-Chip Generation of a Human 3D Cervical Cancer Tissue

In cervical cancer, epithelial cells cross the basal lamina and form cancerous nests (Figure S2A, Supporting Information) in the stroma featuring fibroblasts as the most abundant cell type of the TME. On-chip, we emulated cancerous nests by integrating cancer cell aggregates into the 3D stromal tissue. These aggregates recapitulate a pathophysiological architecture of solid tumors with resulting internal gradients reminiscent of tumors, including decreasing levels of nutrients, oxygen, pH, and drugs toward their core, along with an accumulation of metabolites amongst others (Figure 3B).^[55,56] Cancer cell aggregates were generated in agarose μ -wells via forced cell aggregation of SiHa cells, an established cell line from a squamous carcinoma grade II.^[57] While forming looser aggregates than, for instance, fibroblasts (Figure 3A and Figure S3, Supporting Information), SiHa could be seeded as aggregates on-chip, replicating multicellular cancerous nests as present in *in vivo* cervical tumors. To model cervical cancer and aspects of the TME, SiHa aggregates (100 000 per mL) were embedded together with cervical fibroblasts (10e6 per mL, based on preliminary test with collagen hydrogels, Figure S2, Supporting Information) in a dextran hydrogel in the tissue chambers of the microfluidic platform (Figure 3B). The chemically defined dextran hydrogel contains covalently attached RGD peptides to promote cell adhesion and a cell-degradable peptide in the hyaluronic acid-based crosslinker, which can be targeted by the human cervical fibroblasts expressing MMP1 and 3.^[58] To culture the cancerous tissue, chemically defined media FTAL5 containing no components of animal or human origin was employed. A continuous supply of FTAL5 at a rate of 20 $\mu\text{L h}^{-1}$ was maintained through the channel to deliver nutrients to the cancerous tissue and remove metabolites from it. A reservoir well above the tissue contained 50 μL of media, maintaining a moist environment that was preserved in sterile conditions using a sealing membrane. The successful formation of a 3D tissue mimicking the physiological architecture was evaluated after 14 days of on-chip culture via immunofluorescence staining with cell type-specific cytokeratin and vimentin markers (Figure 3C). The dextran hydrogel demonstrated good stability without shrinkage and provided a robust 3D matrix for the cells. SiHa spheroids were distributed in the tissue as cancerous nests, with a more defined and compact spheroid-appearance after 3 days of on-chip cultivation in dextran (Figure S4, Supporting Information), as opposed to their loose appearance at the timepoint of seeding (Figure 3A). Fibroblasts were dispersed in-between the μ -tumors. Life/dead staining revealed a high level of tissue

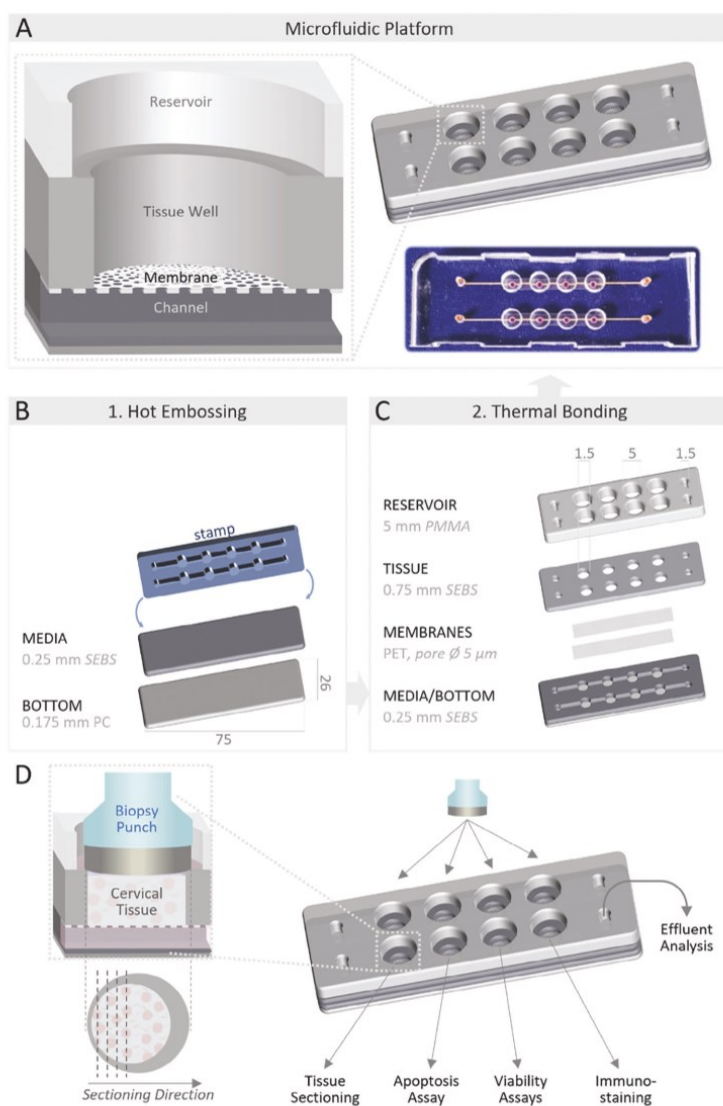


Figure 1. Design and fabrication of the microfluidic platform: A) Schematic and photograph of the microscope-slide sized PDMS-free platform incorporating two independent microfluidic systems, each supplying four open-top tissue compartments consisting of a cylindrical tissue well positioned between a porous membrane and a reservoir. B) The channel layer is patterned in a SEBS/PC hybrid material via a combined hot embossing and thermal fusion process. C) Subsequently, laser-structured PET-membranes, SEBS tissue, and PMMA reservoir layers are fused to the membrane/bottom layer via thermal bonding. D) The hybrid-material platform allows for tissue retrieval with a biopsy punch, providing the opportunity to apply different readout methods on the same system. SEBS: styrene ethylene butylene styrene, PC: polycarbonate, PET: polyethylene terephthalate, PMMA: poly(methyl methacrylate).

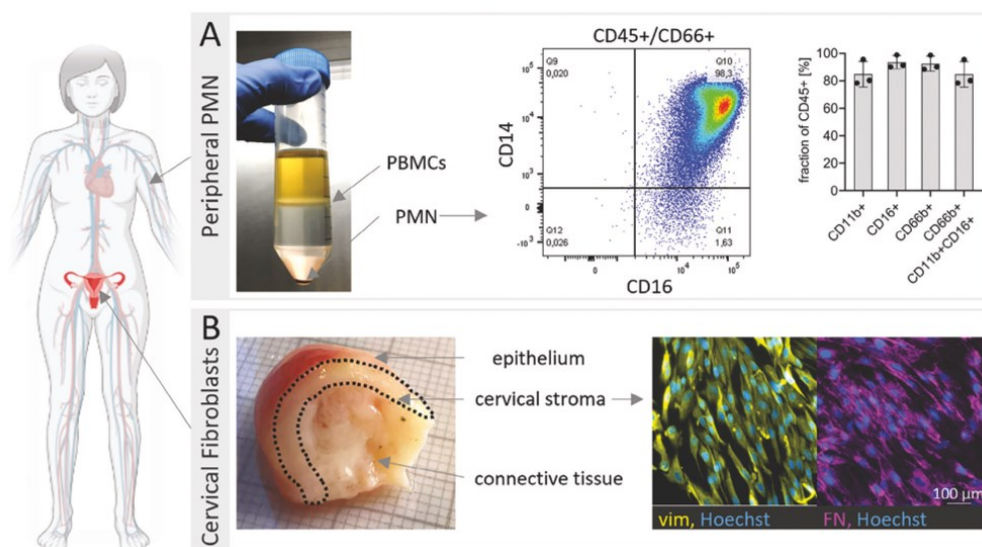


Figure 2. Isolation of human donor-derived peripheral PMNs and cervical fibroblasts: A) Peripheral PMNs were isolated from human whole blood of three donors, separating peripheral blood mononucleated cells (PBMCs) using density gradients, and their purity was assessed via flow cytometry measurements. B) Cervical stromal layers were separated from epithelium and connective tissue and fibroblasts were subsequently isolated and characterized by vimentin (vim) and fibronectin (FN) immunofluorescence staining.

viability, with an increased number of dead cells in the center of large spheroids (Figure 3D).

2.4. Presence of Fibroblasts Impacts Cancer Cell Viability and Proliferation

The inclusion of fibroblasts in tumor models provides a more representative cellular context by considering the influence of fibroblast-mediated signaling in the TME, which can have an impact on overall pathogenesis as well as the efficacy and toxicity of therapeutics. To investigate how fibroblasts affect the viability and proliferation of μ -tumors in the cervix, we generated tissue-chips containing spheroids of either cancer cells or fibroblasts distributed in-between. In comparison to the tissues containing solely cancerous spheroids (SiHa sph), monocultures of primary cervical fibroblasts (F sph + F) exhibited a lower number of dead cells (Figure 4A). However, when fibroblasts were introduced into the TME of SiHa spheroids (SiHa sph + F), the viability of cancer cell spheroids increased significantly as demonstrated via life/dead-stainings and quantification of LDH release in the perfused effluent (Figure 4B). Despite increased cell numbers in the co-culture condition, LDH release was significantly lower compared to the cancer spheroid mono-culture. Additionally, presence of fibroblasts in the tissue supported cancer growth as the spheroids grew larger and featured a higher expression of the proliferation marker Ki67 (Figure 4C).

2.5. Cervical Tissue Responds to Cisplatin Treatment at Patient-Relevant Doses

To demonstrate the applicability of the CCoC model for dynamic testing of cancer therapeutics, we exposed the model to the chemotherapeutic medication cisplatin, and mimicked clinically relevant treatment plans. Cisplatin is one of the most utilized therapeutic agents for addressing various solid cancers. Its anticancer effects rely on multiple mechanisms, with its primary accepted pathway involving the formation of DNA lesions through interactions with purine bases, subsequently triggering various signal transduction pathways leading to apoptosis. Nonetheless, the inherent challenges of cisplatin, encompassing side effects and drug resistance, curtail its applicability and therapeutic efficacy.^[59] For cervical cancer patients, a commonly accepted treatment plan involves weekly administration of 40 mg m^{-2} of cisplatin for 5–6 cycles alongside radiation therapy.^[60] When patients received cisplatin intravenously over 1 h, the cisplatin concentration in the serum reached its peak after 1 h at $c_{max} = 5.37 \mu g mL^{-1}$ (17.9 μM), then decreased rapidly within 4 h to $C_{5h} = 1.73 \mu g mL^{-1}$ (5.8 μM).^[61] To simulate the treatment that a cervical tumor would experience in vivo, we leveraged the perfusion to generate different (dynamic) treatment regimes. In a constant “low” exposure condition, the tissue was treated with 80% of C_{5h} , that is, 1.4 $\mu g mL^{-1}$ (4.6 μM) cisplatin for 24 h, whereby cisplatin delivery to the four wells occurred with small time differences (Figure S5, Supporting Information). Additionally, a “dynamic” treatment regimen was implemented, featuring an initial 1-h

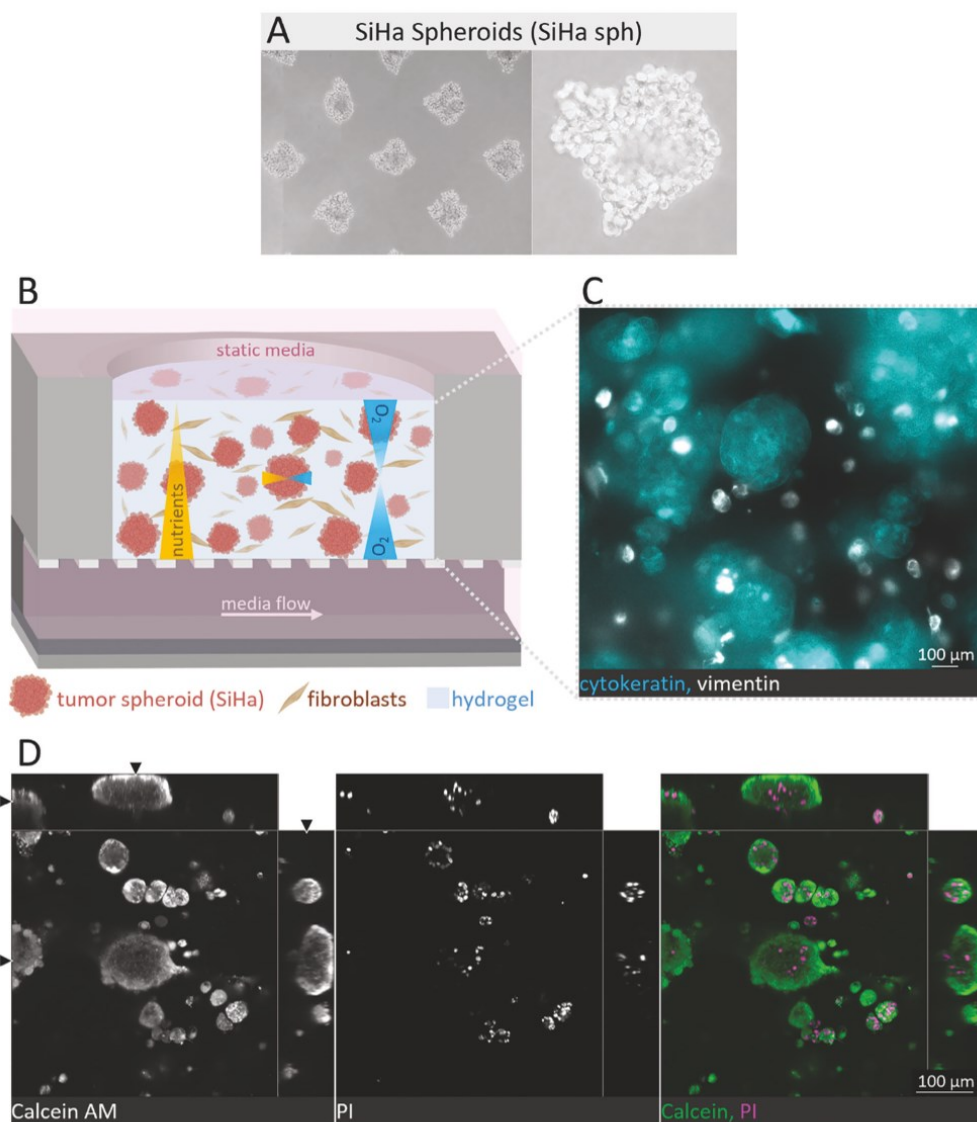


Figure 3. Tissue generation and characterization of the cervical cancer-on-chip: A) SiHa were seeded in μ -agarose wells, where SiHa formed loose aggregates after 24 h. B) Schematic cross-section illustrating the cancer tissue within the tissue well. Media is linearly perfused in the channel at a flow rate of $20 \mu\text{L h}^{-1}$. The local consumption of nutrients and oxygen by the cells and the continuous supply thereof results in the creation of gradients both within the tissue and within the spheroids. C) Fluorescence microscope image of the CCoC after 14 days of on-chip culture, showing single, primary fibroblasts (stained with vimentin-antibody, white) dispersed in between SiHa-spheroids (stained with cytokeratin-antibody, turquoise) in a 3D dextran hydrogel. D) Orthogonal view of confocal microscopy images of a CCoC after 2 weeks of on-chip culture stained with Calcein AM (living cells, green) and PI (dead, magenta), demonstrating high viability.

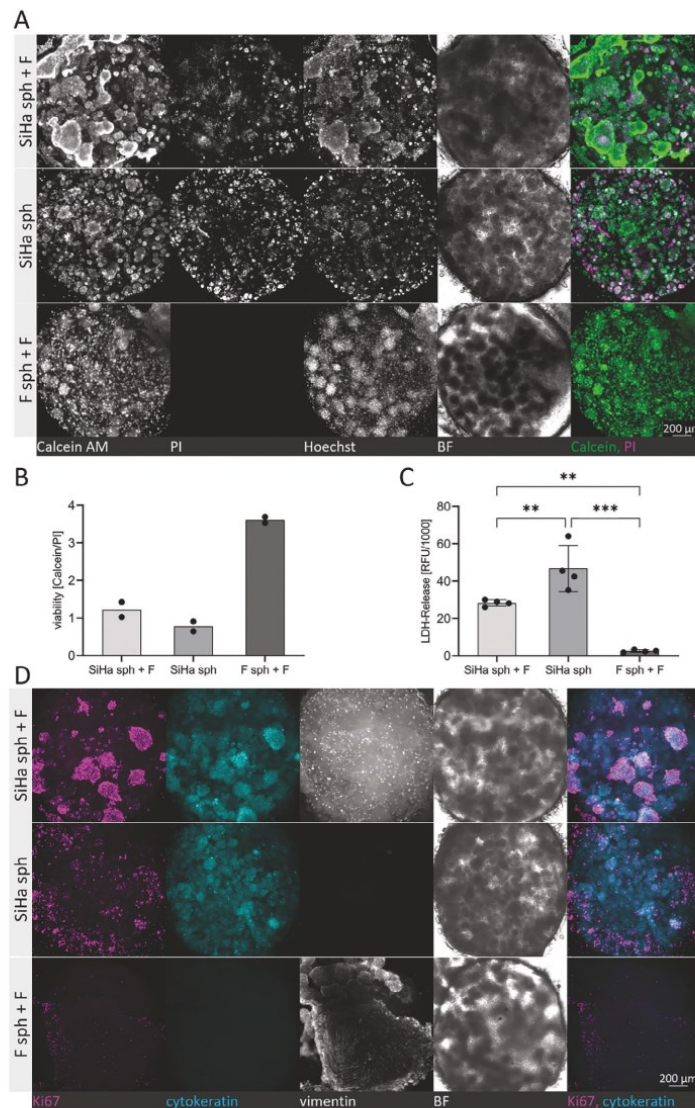


Figure 4. Cervical fibroblasts increase viability and proliferation of the cancerous tissue: A) SiHa and fibroblast spheroids respectively were cultured in the presence (SiHa sph + F or F sph + F) or absence (SiHa sph) of single fibroblasts for 14 days and stained for living (Calcein AM, green) and dead cells (propidium iodide, PI, magenta). Two systems were generated from the same donor and run in parallel to obtain duplicate wells for each condition. The presence of fibroblasts resulted in increased viability and size of SiHa spheroids as shown in the fluorescence images of the tissue on-chip. Brightfield (BF) images show densely packed tissues in all conditions, particularly when SiHa spheroids are present. Viability assessment via B) Calcein/PI staining and C) LDH release into the effluent from the cultures described in (A) demonstrates higher viability when SiHa-spheroids were co-cultured with fibroblasts compared to the mono-culture. Bars represent the mean \pm SD of two wells from two systems (Calcein/PI) and effluent from four systems (LDH) from the same donor run in parallel, each of which was measured in triplicates with the mean of each system shown as single dots. D) The same conditions as described in (A) were stained with the proliferation marker Ki67 (magenta), SiHa marker cytokeratin (turquoise), and fibroblast marker vimentin (white). The fluorescence microscopy images reveal boosted proliferation in the co-culture conditions.

perfusion of cisplatin at 80% of c_{\max} , that is, $4.3 \mu\text{g mL}^{-1}$ ($14.3 \mu\text{M}$), followed by a 23-h perfusion of cisplatin as in the “low” condition. These treatments were initiated 5 days after generating the μ -tissue on-chip and were repeated weekly (Figure 5A). The initial 24-h cisplatin treatment on day 5 and the repetition of the treatment on day 12, demonstrate an impact on cancer cell viability in the dynamic condition, while the constant low condition did not show significant effects (Figure 5B). To assess if the constant low condition will eventually also have an impact, we added a third treatment on day 19. After three cycles of repeated dosing, the constant low condition also exhibited a significant tumor-killing effect as demonstrated by LDH release and TUNEL staining (Figure 5C).

2.6. Neutrophils Are Recruited into the Cancerous Tissue and Are Capable of Producing NETs in the TME

Immune cells in the TME play a crucial role in influencing both pathogenesis and treatment outcomes. Ideally, an in vitro cancer model should integrate cancerous tissue within a 3D TME that includes vascular structures and immune components.^[62] Particularly of interest for cervical cancer are PMNs and their functional structures known as NETs. Hence, we aimed to investigate the amenability of the CCoC for perfusion and recruitment of functional PMNs into the tumor tissue.

To characterize functionality of the donor-derived PMNs, we assessed their capability to undergo NETosis off-chip—thereto, we treated PMNs immediately after isolation for 6 h with 100 nM phorbol 12-myristate 13-acetate (PMA) and subsequently stained for PMN and NETosis markers CD66b, MPO, NE and H3cit as well as nuclear stain Hoechst (Figure S6A, Supporting Information). Upon stimulation, we observed critical hallmarks of NETosis, which include extracellular DNA co-localized with neutrophil-derived proteins as well as H3cit expression.^[41] Without stimulation, intracellular MPO as well as net-like structures were observed, indicating spontaneous NETosis.^[63,64] Collectively, these results show PMA-induced formation of NETs by donor-derived PMNs in vitro. Next, we had to identify a media suitable for cervical (cancer) tissue culture that at the same time supports functionality of PMNs. Several media were screened for PMN viability and their ability to undergo NETosis, including RPMI, as the most commonly used medium for PMN culture,^[63,64] and FTAL5, as the medium previously used for on-chip cancerous tissue culture, as well as further media combinations previously shown to be compatible for the culture of healthy keratinocytes with fibroblasts as well as for the co-culture of microvascular endothelial cells and T cells (Figure S6B, Supporting Information). While PMNs’ ability to undergo NETosis was diminished in the cervical co-culture media “PM + DMEM,” the SYTOX green assay demonstrated functional NETosis for FTAL5. Unstimulated cells featured high viability while PMA stimulation led to an increase in cell death after 2 h with further loss of viability until 6 h.

To mimic PMN circulation through and extravasation from the blood vessels of cancerous tissue, PMNs were added into tailored reservoirs in the inlet ports on day 3 of on-chip culture and perfused through the vasculature-like channels for 5 h (Figure 6A). PMNs, stained with a cell tracker prior to perfusion,

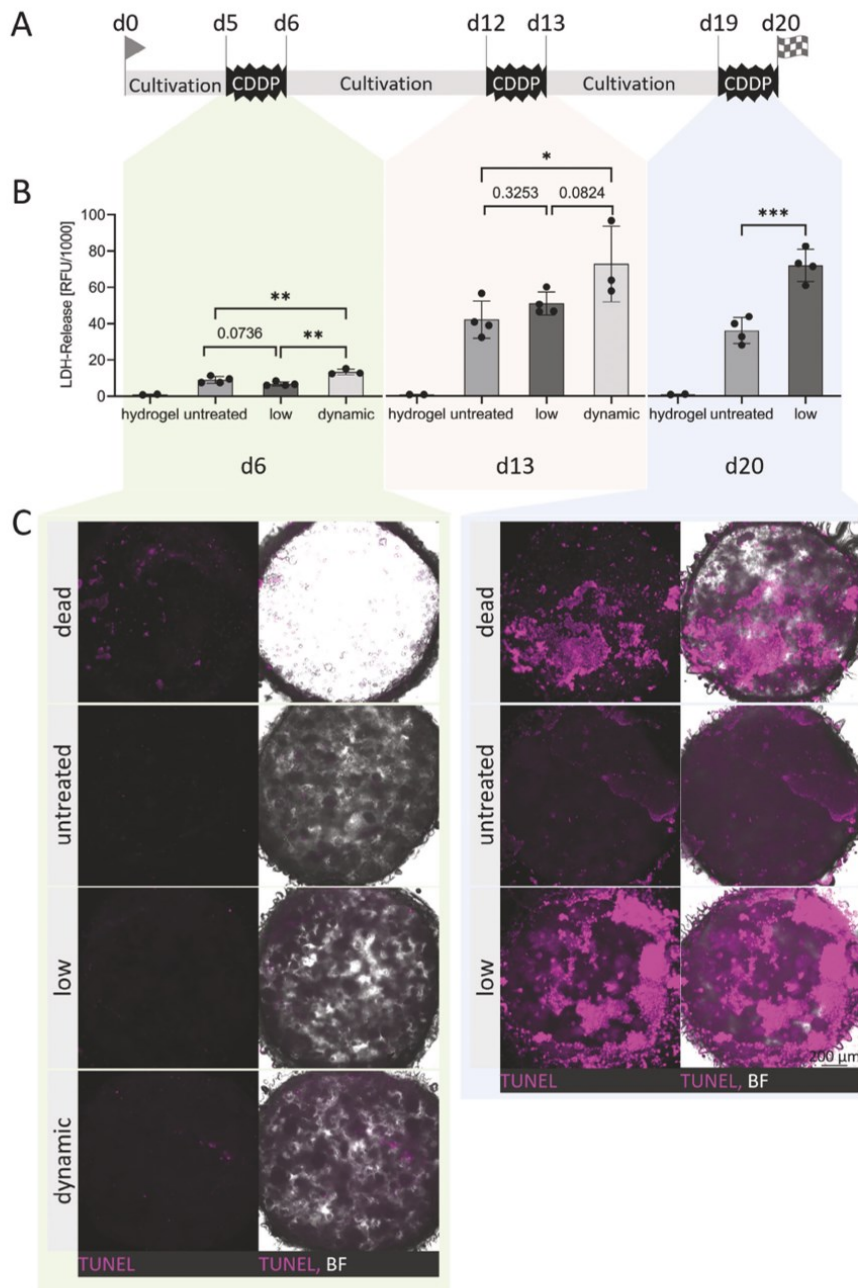
attached to the membrane and could be observed actively migrating through the porous membrane to the μ -tumors and fibroblasts via real-time monitoring. The tissue displayed solely a few single dead cells, indicating high viability across all cell types. Since cell tracking does not provide sufficient information about cell type, CCoCs were stained for PMN markers CD66b and NE as well as T cell marker CD3 after perfusion with unstained PMNs over 5 days (Figure 6B). Contamination with T cells was minimal, and the majority of cells adhering to the membrane at the top of the channel and recruited to the cancerous tissue expressed PMN markers. After PMN-perfusion, the NETosis inducer PMA was introduced for an additional 5 h. While some spontaneous NETosis occurred in both the tissue and in the channel, the addition of PMA strongly increased the formation of NETs in both compartments, as shown with the NETosis markers MPO (Figure 6C; secondary antibody control in Figure S7, Supporting Information).

3. Discussion

To tackle one of the most pressing women’s health-related pathologies, cervical cancer, a leading cause of cancer-related deaths in women, there is an urgent need for physiological model systems with human relevance and predictive value. In this study, we leverage organ-on-chip technology to generate a model that integrates cervical cancer, aspects of the TME as well as vasculature-like perfusion. We introduce a novel open-top microfluidic platform tailored to recreate immunocompetent cervical cancer tissue based on patient-specific primary cells and tumor spheroids and demonstrate its applicability for chemotherapy assessment and immune cell perfusion.

3.1. A Novel PDMS-Free Microfluidic Platform Amenable for Tissue Retrieval

The open-top design of the platform offers direct access to the tissue, facilitating tissue generation and retrieval as well as microscopy. By utilizing thermoplastic materials instead of the commonly used PDMS, we circumvent challenges arising from strong absorption of small hydrophobic molecules; an aspect that is particularly important for women’s health-related cancer models, where a controlled exposure to hormones and drugs that are often strongly hydrophobic could be required in future applications. This is exemplified by metastasis-inducing effects of estradiol (E2), which was demonstrated in the context of PMN in a breast cancer model.^[65] The combination of thermoplastic elastomers and thermoplastics combines the benefits of both materials, that is, stability and optical accessibility as well as amenability for extraction of tissue using a biopsy punch. The latter provides a significant benefit for downstream analysis—retrieval of tissues enables easier and independent analysis of each of the four tissues per chip and improves compatibility with standard cell/tissue culture readout routines, for instance, immunohistochemistry, high-resolution microscopy, and gene expression analysis. The small adapters in the ports allow for flexible connection of tubing and (immune cell) reservoirs. The use of larger media reservoirs proves advantageous for cultivating the tissue, whereas cannulas with short needles as immune cell



reservoirs reduce dead volume and ensure facile incorporation of immune cells into the perfusion. Although we focused on user-friendliness, scalability of fabrication processes, and compatibility with standard equipment,^[66] the general limitation of organ-on-chip experimentation being more complex than conventional cell culture or Transwell assays and requiring specialized training also holds true for the CCoC platform.^[67]

3.2. Microscale Open-Top Tissue Chambers Enable Facile 3D Tissue Generation and Integration of Patient-Derived Cells

The small cultivation area of the CCoC is particularly well-suited for the integration of primary cells, as the cell numbers per biopsy are often limited. Thereby, a large number of individual tissue models can be generated from a single donor, allowing to assess many different conditions for the same patient circumventing donor-to-donor heterogeneity. In this study, we derived primary cervical fibroblasts and PMNs from healthy donors, not only providing human and tissue-specific genetic background, but also allowing, for instance, the study of interindividual differences in NET formation propensity. Cultivating primary cervical cancer cells and patient-derived organoids has proven to be challenging with only a few examples reported to date.^[49] Especially organoids from squamous cervical cancer have been rarely reported and demonstrated very low success rates for organoid generation of 22.2% and 50%.^[68,69] In contrast, a total of at least 52 cervical cancer cell lines have been established, substantially contributing to the advancement of our knowledge and comprehension of cervical cancer pathogenesis and treatment.^[70] To generate cervical carcinoma tissue, we utilized the squamous cervical cancer cell line SiHa, as it represents the most common type of cervical cancer. To recapitulate cell-cell interactions in tumors, the 3D architecture featuring internal gradients of nutrients, oxygen, and signaling factors as well as the drug penetration reminiscent of tumors, 3D spheroids provide a much better approach than single cells or 2D culture and more closely resemble *in vivo* tumor conditions.^[62,71] In the future, the model could be further refined and advanced to fully patient-specific models by integrating cervical cancer organoids instead of SiHa spheroids and by adding further components of the TME such as tissue infiltrating lymphocytes.

3.3. Dynamic Monitoring of Tissue Structure and Function on-Chip

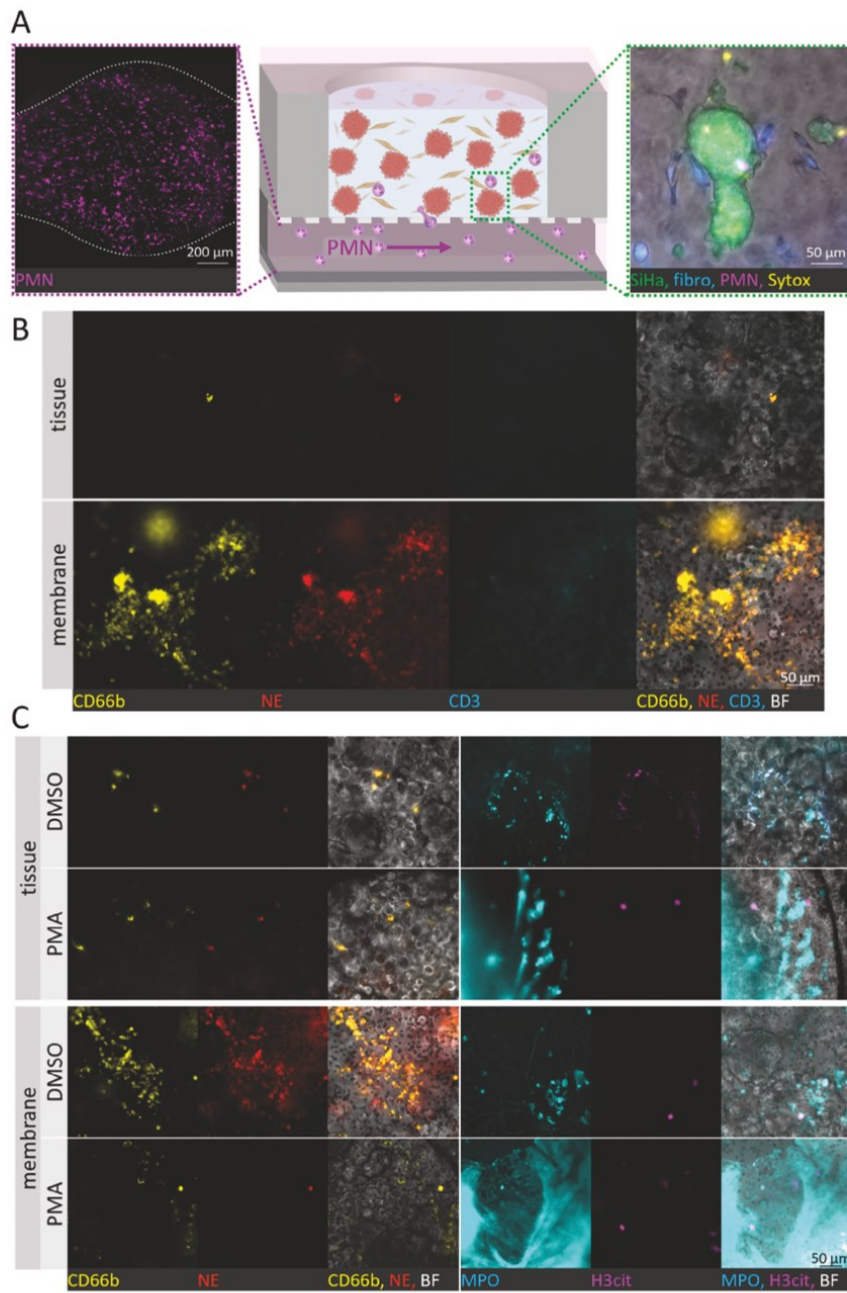
To assess structural and functional hallmarks of the tissues in the CCoC, we focused primarily on immunofluorescence mi-

croscopy as well as effluent analysis, since thereby structural information is maintained, and non-invasive dynamic monitoring enabled. The compatibility of the CCoC with non-invasive live-cell imaging in combination with long-term culture is a powerful tool, in particular when real-time measurements are combined with fluorescent labeling such as cell-trackers, conjugated antibodies, and viability dyes. Confocal microscopy enables imaging up to $\approx 200 \mu\text{m}$ into the tissue ensuring direct structural and functional assessment of a large portion of the 3D model, especially when paired with immunofluorescence staining. In the future, it would be intriguing to employ tissue-clearing techniques to obtain a comprehensive view of the tissue. Constant perfusion of the microfluidic platform allows continuous collection of effluent, providing an additional time-resolved non-invasive method for the dynamic assessment of tissue function and cellular interactions. The analysis of effluents can be performed using many widely available, cost-effective standard readout methods employed in traditional 2D cell cultures, thus expanding the scope of readout options. In this study, we monitored the release of LDH from the tissues into the effluent over a 24-h period; if desired, much higher time resolution could be achieved. Effluent analyses can be further resorted to for a thorough investigation of biochemical factors such as chemokines and cytokines or clinically relevant biomarkers, e. g. the analysis of NET markers, which play an increasingly important role for cancer patients' diagnosis and management.^[45,72]

3.4. Challenges and Opportunities of Long-Term Culture of Complex Multi-Cell-Type Tissues

Long-term culture of cancerous tissue allows for prolonged observation of tumor progression to better understand the underlying mechanisms and factors that contribute to cancer development and metastasis. Through this extended culture time, a deeper understanding of the complex interactions between cancer cells, stromal components, and the surrounding microenvironment can be obtained. After 2 weeks of culture, we evaluated the tissue's viability and observed an overall high viability. In larger spheroids, dead cells were predominantly located in the center, resembling necrotic areas observed *in vivo* within cancerous nests.^[73] The different sizes of spheroids provide a good replication of the size heterogeneity seen in neoplastic clusters in patients. To assess the effects of stromal cell types in the TME, we integrated fibroblasts and observed improved viability and faster growth in the tumor spheroids. These findings suggest paracrine cell-cell communication between cancer cells and fibroblasts. Several studies previously reported two-way communication

Figure 5. Cervical cancer models respond to cisplatin treatment: A) Timeline employed for cisplatin treatment: 5 days post tissue-generation, CCoCs were exposed for 24 h to either a "low" dose of cisplatin at $4.6 \mu\text{M}$, or a "dynamic" treatment with an initial 1 h perfusion of $14.3 \mu\text{M}$ cisplatin (CDDP) followed by 23 h of "low" dose, emulating cisplatin dynamics in patient's blood after intravenous application. Treatment was administered weekly, recapitulating the accepted treatment plan for cervical cancer patients. B) LDH release in perfused effluents from treated as well as untreated CCoCs and hydrogel-only chips were analyzed on days 6, 13, and 20. The initial treatment as well as the second treatment showed significant effects in the dynamic condition. After three treatments, the "low" dose condition also showed a significant effect on viability. Bars represent the mean \pm SD; 4 independent systems for the untreated and low condition, 3 for the dynamic condition, and 2 for the hydrogel-only condition; all replicate systems were generated from the same donor, run in parallel, and measured in triplicates. C) Cell death upon cisplatin treatment was detected using a TUNEL assay (magenta) on d6 and d20 in experiments run sequentially from the same donor. Fluorescence microscopy images reveal minimal cytotoxic effects of the first treatment in all conditions and substantial cell death in the low condition after the third treatment. Brightfield images display tissue growth from day 6 into a densely packed tissue after 20 days of culture, with reduced density upon cell killing with triton (dead) or repeated cisplatin treatment.



between cervical cancer cells and fibroblasts, with numerous pro-tumoral effects summarized and reviewed by Villegas-Pineda et al. and Spurgeon & Lambert.^[13,74] Transforming growth factor-beta (TGF β), for instance, has been shown to play an important role in the interaction of CAFs with CaSki and HeLa, contributing to increased proliferation and decreased apoptosis.^[75,76] In vivo, the growth of cervical cancer cells HeLa and CaSki was enhanced when injected in mice as co-culture with CAFs.^[77] Liang and colleagues, moreover, reported that SiHa cells secrete Wnt2B exosomes, which enhanced CAF markers alpha smooth muscle actin (α -SMA) and fibroblast activation protein (FAP) within 2 days and promoted tumor growth, suggesting a positive feedback loop for SiHa's own growth stimulation.^[78] Hence, our data showing fibroblasts enhancing the viability and proliferation of cervical cancerous tissue aligns with the pro-tumoral effects of CAFs reported in cervical cancer. In future studies, the model could be employed to study fibroblast plasticity and assess CAF-marker expression in the CCoCs, including α -SMA and FAP,^[76,78,79] as well as TGF β in the effluent.

Immune components of the TME tremendously influence disease progression and treatment outcomes. Being able to integrate aspects of the immune system constitutes a powerful opportunity for organ-on-chip technology, particularly for cancer-on-chip models.^[80] PMNs are not only the most abundant circulating leukocyte, but play an important role in tumors, where they can have tumor-antagonizing and -promoting functions. In cervical cancer, TANs are prognostically significant and considered a potential therapeutic target.^[38] As the number of cellular components within the tissue increased, we identified a suitable media that would maintain cellular viability and functionality of all cell types. We investigated the NETotic capacity of PMNs in media used for the culture of cervical tissues as well as microvascular endothelial and immune cells. While some media revealed high spontaneous NETosis or prevented PMA-induced NET-formation, PMNs in FTAL5 displayed high NETotic capacity upon PMA stimulation and high viability with low spontaneous NETosis in the control. When PMNs were perfused through the microvasculature-like channels of the CCoC, adherence to the membrane and recruitment into the tissue could be observed. We confirmed viability as well as cell identity of PMNs on-chip. When NETosis was induced with PMA, critical events of NET formation on-chip could be replicated. In future studies, further investigations could elucidate if NET formation can also be induced by cancer cells directly, as has been shown by several aggressive cancer cells with tumor-derived interleukin 8 (IL-8) and granulocyte colony-stimulating factor (G-CSF) potentially playing critical roles.^[25] NETs have been found in cervical cancer,^[39] however, it is not yet known whether NETs are induced by cervical cancer cells directly. Also, the model could be employed to examine the effects of the co-culture on NETosis, as it has been shown

that CAFs can induce NETs in mice.^[81] Hence, the immunocompetent CCoC can aid further mechanistic investigations into the role of NETosis in cancer and its TME and potentially test (immune)therapeutic options and combinations.

3.5. Monitoring Drug Responses Using Clinically-Relevant Treatment Regimens

In vitro compound testing performed at concentrations much higher than the plasma peak concentrations in humans (up to 20–200 \times), raises the question of whether such high concentrations are relevant in predicting response in human physiology.^[82,83] In previous studies, SiHa spheroids were treated with cisplatin at 20–334 μ M for 3 days, 5.5–88 μ M for 2 days, or 10–100 μ M for 1–2 days.^[84–86] Choice of these concentrations and durations, far above clinical treatment regimes, is often driven by short culture durations and limitations of static well plate culture. We leveraged the capability for long-term culture and perfusion of the CCoC and employed repeated dosing in clinically relevant drug delivery routes, schedules, and concentrations. Specifically, we applied a dynamic condition that mimics in vivo plasma concentrations during 24 h treatment windows in a discretized form by applying a concentration of 80% of c_{max} during the initial hour and 80% of C_{5h} for the remaining 23 h. While we used significantly lower concentrations than previous in vitro studies, the dynamic treatment exhibited significant tumor killing already after the first treatment whereas the constant low condition required three cycles of treatment. This demonstrates on the one hand the potential and the impact provided by the organ-on-chip technology's capability for dynamic concentration profiles but also the necessity to carefully choose clinically relevant dynamic treatment profiles in order to generate predictive and translatable data. For future studies, comparing these outcomes with cisplatin-sensitive cell lines such as CC7 or CC10^[87] or patient-specific cervical cancer organoids^[68,69,88] would be compelling and the approach could potentially be utilized to provide patient-specific dosing recommendations and minimum effective dosing estimations. However, this will require much more comprehensive testing and benchmarking using sets of established and experimental compounds not limited to small molecules and also including immunomodulatory drugs.^[89]

4. Conclusion

We present a novel PDMS-free microfluidic platform tailored for the generation and cultivation of cervical cancerous tissue. The platform is amenable for real-time monitoring and tissue retrieval to employ various readouts from the same chip. The microscale open-top tissue chambers enable facile generation and

Figure 6. PMN Recruitment and NETosis in the CCoC: A) Schematic cross-section of the CCoC perfused with PMNs via the microvasculature-like channel (center). PMNs were labeled with a cell tracker (magenta) and perfusion (left panel) as well as recruitment into the cancerous tissue (right panel) were observed via live-cell imaging with a fluorescent microscope. PMNs (magenta), SiHa (green), and fibroblasts (blue) displayed high viability, evidenced by the minimal number of SYTOX (yellow) positive cells. B) Fluorescence microscopy images of PMN marker CD66b (yellow) and NE (red) as well as T cell marker CD3 (turquoise) confirm the high purity of PMNs. PMN adhered to the membrane and a subset of cells was recruited into the cancerous 3D tissue. C) Following 5 h of PMN-perfusion and exposure to PMA for another 5 h, tissues were stained with CD66b (yellow), NE (red), MPO (turquoise), and H3cit (magenta). Fluorescence microscopy images revealed spotty spontaneous NETosis in the CCoC without stimulation, while PMA-stimulated NETosis was evident as large MPO-positive structures (turquoise) in both tissue and channel.

long-term culture of SiHa spheroids embedded in a stroma containing donor-derived cervical fibroblasts. The 3D tissue recapitulates physiological architecture and cell–cell interactions within the TME, resulting in enhanced tumor viability and growth in the presence of cervical fibroblasts. The tissue structure and function were monitored via (live-cell) immunofluorescence microscopy and effluent analysis. As a proof-of-concept for the applicability of the CCoC for drug testing, response of the CCoC to cisplatin treatments at clinically-relevant treatment regimes, schedules, and routes of administration was assessed. Furthermore, PMNs were recruited into the tissue from the microvasculature-like channel, while retaining NETotic functionality. Taken together, we leveraged organ-on-chip technology to develop a novel open-top microfluidic platform, designed to replicate immunocompetent cervical (cancer) tissue using patient-specific primary cells and tumor spheroids. We also showcase its potential for evaluating chemotherapy and simulating immune cell perfusion.

5. Experimental Section

Design and Layer Preparation: The design of the microfluidic platform was created using AUTODESK AUTOCAD 2021. To fabricate the platforms multiple different types of polymer sheets (5 mm thick sheets of PMMA (Modular, Germany) for the media reservoir layers, 750 μm thick sheets of SEBS (Hexpol TPE AB, Sweden) for the tissue layers, and PET membranes with a pore size of 5 μm (Sabeu, Germany)) were processed utilizing laser-assisted structuring (Laser Cutter R5000 V1.0, Universal Laser Systems, USA). The dimensions and different views of the layers are depicted in Figure S1A–C, Supporting Information.

The bottom layers containing the media channels were structured in a SEBS/PC (It4ip, Belgium) hybrid via hot-embossing, whereby molds were produced based on previously introduced protocols,^[52] with minor adaptations—an SU-8 master mold was produced from a 4-inch silicon wafer (Siegart Wafer, Germany) via SU-8 50 (Kayaku Advanced Materials, Inc., Germany) based UV-lithography using patterned photomasks (KOPP-Desktopmedia, Germany) in an MA6 mask aligner (SÜSS Micro Tec, Germany) and mrDev 600 developer (MicroChemicals GmbH, Germany). A PDMS mold was subsequently fabricated by pouring a PDMS pre-polymer (Sylgard 184, Dow Corning, Germany) on the silicon mold, which was placed in a large circular petri dish, cured for 24 h at room temperature (RT) and afterward for 24 h at 80 °C. The resulting PDMS mold was placed into a custom-built steel tool and a two-component, high-temperature stable epoxy resin (EpoxAcast 670 HT, USA) was applied. The tool was left under vacuum for 24 h at RT and placed into an oven at 60 °C for 24 h, after which the mold could be removed from the tool. Subsequently, the mold was placed at 80 °C for 2 h, followed by 3 h at 130 °C. The mold was then gently cooled overnight by turning off the oven and opening the air vents.

The molds were employed for hot embossing the media channel structure into the thermoplastic elastomer SEBS and simultaneous fusion of SEBS to PC. Thereto, 11 \times 11 cm pieces of SEBS (250 μm thickness) and PC (175 μm thickness) were placed onto the mold and the polymer layers were pressed by a laminar roller. The construct was then flipped and placed onto a mirror-polished stainless-steel plate (TGA, Germany), which was spray-coated with a mold release agent (Weicon, Germany) beforehand. This construct was then placed into a 130 °C preheated hot press (LabEcon100, Fontijne, Netherlands). The mold was pressed with 6 kN at 130 °C for 10 min to structure the SEBS layer and bond it to the PC layer. The resulting SEBS/PC media layer was then assembled with the other chip parts.

Chip Assembly with Adapter Integration: The SEBS tissue layer was aligned and assembled onto the PMMA media reservoir layer. The PET membranes were cleaned by submersion into isopropanol (MIPU1025, MicroChemicals), dried for 30 s, and placed over the tissue holes. Subse-

quently, the SEBS/PC bottom layers were placed on top and aligned with the other layers. The stack of polymer layers was placed between two clean glass slides (Menzel, Germany) and sandwiched between two metal plates (each 700 g) pre-heated to 60 °C. The platform was subsequently thermally bonded at 80 °C in an oven (Memmert, Germany) for at least 12 h. The pressure on the chips equaled \approx 3.9, 1.9, and 1.3 kPa for one, two, and three chips, respectively. Tubing adapters were prepared by inserting a cannula (5 mm in length, outer diameter of 0.6 mm) derived from stainless steel plastic hub dispensing needles (Gauge 23, KDS2312P, Weller) into flexible plastic tubing (length \approx 8 mm, inner diameter of 0.5 mm, AAD04103, VWR). The adapters were inserted with the tubing ahead into the in- and outlet ports of the chip. PDMS was applied at the interface between adapter and chip and cured for 1–2 h at 80 °C, sealing and stabilizing the connection. The platform was sterilized with EtOH (70%), washed with DI water, air-dried, and equilibrated in the incubator before cell seeding.

Cell Isolation and Culture: Human biopsies of the cervix uteri and whole blood were obtained from patients with unrelated diseases and healthy donors, respectively. Patients and donors gave informed consent as approved by the ethical committee of the Eberhard Karls University Tübingen (No. 495/2018/BO02 for the isolation of fibroblasts from cervix uteri and PBMCs and PMNs from whole blood).

The isolation process for primary human cervical fibroblasts was adapted from Deng et al. with minor modifications.^[53] Immediately after surgery and gross examination by the pathologist, biopsies were washed three times in phosphate-buffered saline (PBS, D8537, Sigma Aldrich) supplemented with penicillin-streptomycin (P/S, 100 U mL⁻¹ and 100 μg mL⁻¹, P06-07100, Pan Biotech). Excess connective tissue was removed and remaining epithelium with subepithelial stromal layer was cut into small stripes and digested overnight in dispase II (2 U mL⁻¹, 17105041, Gibco) in DMEM/F12 (12634010, Gibco) at 4 °C. Epithelia were removed and stromal layer was minced into small pieces of \approx 2 \times 2 mm and further digested with collagenase I (1 U Wuensch mL⁻¹, C1-22, Sigma Aldrich) in DMEM (41965039, Gibco) for 90 min at 37 °C on a rocker (Rocker 2D, IKA, Germany). Cell suspension was filtered through a 70 μm strainer (542170, Greiner Bio-one, Germany) and mixed with DMEM with fetal calve serum (FCS, 10%, SH30066.03, Cytavia). After an additional wash of the strainer with PBS, the cell suspension was centrifuged at 200 \times g for 5 min and plated in DMEM with FCS (10%). Cells were incubated at 37 °C with 5% CO₂ in a humidified atmosphere. Media was changed every 2–3 days and TrypLE Select (12563-029, Gibco) was used for detachment.

SiHa were provided by T. Ifner and F. Stubenrauch (Eberhard Karls University Tübingen, Germany) and cultured as described for primary cervical fibroblasts.

The procedure for isolating PMNs from whole blood was based on a previously published protocol, with minor adjustments.^[54] Whole blood was collected in ethylene diamine tetraacetic acid (EDTA) monovettes (02.1066.001, Sarstedt) and immediately diluted with the same volume of 2% dextran buffer (4.01 g mL⁻¹ dextran (31392, Sigma Aldrich, Germany), 0.9 g mL⁻¹ NaCl (A2942, AppliChem, Germany), in sterile water) and incubated for 10 min at RT. The supernatant was layered on top of Histopaque-107 separation medium for density gradient centrifugation (10771, Sigma Aldrich, Germany) in a ratio of 2:3 [v/v]. Samples were centrifuged at 400 \times g for 30 min without breaks and acceleration for experiments in 2D and 800 \times g for 20 min with acceleration at running profile 4 for chip perfusion. Blood plasma and separation medium were discarded, and the pellet was resuspended in erythrocyte lysis buffer (PL-29-L, C.C. Pro, Germany) and incubated for 5 min at RT. PBS was added to reduce osmotic pressure and cell suspension was centrifuged at 200 \times g for 5 min with maximum acceleration and deceleration. Supernatant was discarded and the pellet was resuspended in the desired medium or PBS.

Spheroid Generation: Spheroids were formed as described previously.^[90] In brief, wells of a 6-well microwell culture plate (AggreWell400, STEMCELL Technologies, USA) were replicated out of Hydrosil (101301, SILADENT, Germany) and glued to a PMMA holder. After sterilization with 70% EtOH, the structured side was remolded with agarose (3%) and transferred to a 24 well-plate, with the microwells pointing upward. DMEM with FCS (10%) was added before removal of air bubbles. Cervical fibroblasts or SiHa were detached with TrypLE,

Table 1. Conjugated antibodies for characterization of PMNs in flow cytometry measurements.

Antibody	Host species	Supplier	Catalog no.
CD45-AF700	Mouse	BioLegend	304024
CD66b-APC, REAfinity	Mouse	Miltenyi Biotec	130-117-692
CD11b-PE-Cy7	Mouse	BioLegend	301321
CD16-BV605	Mouse	BioLegend	302040

centrifuged at $200 \times g$ for 5 min, and resuspended in DMEM with FCS (10%). 480 000 cells were seeded into each well and were centrifuged at $200 \times g$ for 5 min and incubated at 37 °C with 5% CO₂ in a humidified atmosphere until use the next day.

Cell Seeding in Dextran-Hydrogel: The next day, 3-D Life RGD peptide (0.5 mM, Acetyl-Cys-Doa[®]-Doa-Gly-Arg-Gly-Asp-Ser-Pro-NH₂; Doa = 8-amino-3,6-dioxoactanoic acid, P10-3, Cellendes, Germany) was chemically crosslinked to 3-D Life SG-dextran (2.9 mM, M91-3, Cellendes, Germany) according to manufacturer's instructions. Spheroids were harvested by transferring them with a P1000 to a 5 mL Eppendorf tube and left to sediment by gravity.

Spheroids (final 100 000 spheroids per mL) and cervical fibroblasts (final 10e6 fibroblasts per mL) were mixed in dextran hydrogel and crosslinked with thiol-functionalized hyaluronic acid crosslinker CD-HyLink (2.4 mM, Cellendes, Germany), containing the metalloprotease (MMP)-cleavable peptide (Pro-Leu-Gly-Leu-Trp-Ala). 1.5 μL of this mix was seeded in each well of the CCoC and 50 μL of CnT-Prime Full Thickness 3D Airlift Medium (FTALS, CELLnTEC, Switzerland) was added into each reservoir. CCoC was sealed with Breath-Easy sealing membrane (Z380059, Sigma Aldrich) to reduce evaporation and keep a sterile environment.

Perfusion of the CCoC: Medical Tygon tubing (AAD04103, VWR, USA) was connected to the adapters at the ports. The tubing from the outlet led to reaction tubes as effluent collecting containers and the tubing into the inlet was connected to a syringe via a stainless-steel plastic hub dispensing needle (KDS2112P, Gauge 21, Weller, Germany). Media perfusion through the channel with FTALS was realized by pushing 20 μL h⁻¹ with an external syringe pumping system (LA-190, Landgraf Laborsysteme HLL GmbH, Germany).

PMN Perfusion: Tygon tubing was disconnected from the adapter and the cannula was removed. G23 Gauge dispensing needles were shortened to ≈8 mm length and inserted into the adapter as PMN reservoirs. PMNs were perfused for 5 h by withdrawing with 40 μL h⁻¹. Lids prepared from reaction tubes were added to maintain a sterile environment while allowing convenient refilling of the reservoirs.

Cisplatin Treatment: To investigate the effect of cisplatin on the viability of the CCoC, cisplatin (Z32120, Sigma Aldrich) was prepared as a stock (1.67 mM) in 0.9% saline and stored at 4 °C. 5 days post tissue-generation, cisplatin was perfused for 24 h as either a "low" dose of cisplatin at 4.6 μM in FTALS, or a "dynamic" treatment with an initial 1 h perfusion of 14.3 μM cisplatin followed by 23 h of "low" dose. When CCoCs were treated repeatedly, FTALS without cisplatin was used for on-chip culture in-between treatments.

5.5. Cell and tissue characterization
Tissue Retrieval: For independent analysis of each tissue of the CCoC platform, tissue was retrieved using a 4 mm biopsy punch (49401, pfm medical AG) without the plunger. Thereby, tissue including a protective ring of SEBS material around it could be transferred from the biopsy punch using a knee bent tweezer (PZ31, Hartenstein) to 96 well plates for further analysis.

Flow Cytometry: To characterize PMNs isolated from whole blood, 500 000 cells were washed twice with PBS (300 rpm, 5 min at 4 °C) and resuspended in staining buffer (PBS with 10% FCS, 2 mM EDTA). For each panel, unstained cells were prepared as control. Cells were resuspended in Fc blocking solution (20 μg mL⁻¹, 564219, BD Pharmingen) and incubated for 20 min at RT. After washing, cells were incubated with Zombie Aqua for 15 min at RT and subsequently stained with an antibody cocktail (Table 1) for 30 min at 4 °C in the dark. Cells were fixed in Fixation Buffer (88-8824,

eBioscience, Thermo Fisher Scientific) for a minimum of 20 min at RT, resuspended in Permeabilization Buffer (88-8824, eBioscience, Thermo Fisher Scientific) and incubated with intracellular antibody cocktail for a minimum of 30 min at RT. Cells were washed and resuspended in staining buffer and measured with BD LSRFortessa flow cytometer (BD Biosciences, USA). Data was analyzed using FlowJo software.

Live/Dead Staining: Samples were stained after tissue retrieval in a 96 well plate. Calcein AM green (2 μg mL⁻¹, C3099, Thermo Fisher Scientific) was added for staining viable cells in PBS and incubated at 37 °C for 20 min. Propidium iodide (50 μg mL⁻¹, P4170, Sigma Aldrich) was added for 5 min at 37 °C for labeling nuclei of dead cells. Samples were washed with PBS containing magnesium chloride and calcium chloride (PBS+, D8662, Sigma Aldrich) for 10 min and imaged via fluorescence microscopy.

Sytox Green Assay: The method was adapted from Linnemann et al.^[91] In brief, 62 500 PMNs per cm² were seeded in a 96 well plate in respective media with SYTOX green (1 μM, S7020, Thermo Fisher Scientific) and PMN stimulation was performed with Phorbol 12-myristate 13-acetate (PMA, 100 nM, ab120297, Abcam). Cells were lysed with 1% triton-X-100 (X100, Sigma Aldrich) as a reference for the maximum of dead cells. Fluorescence intensities were measured every hour using the Tristar 5 plate reader (Berthold, Germany) at 488 nm excitation and 523 nm emission. The fluorescence values of each replicate were normalized to the mean fluorescence intensity of triton X-100 lysed cells and multiplied by 100. The following media were tested: RPMI (21875, Gibco); RPMI with FCS (5%, SH30066, Cytavia); FTALS, FTALS with FCS (5%), endothelial cell growth medium (ECGM, C-22010; PromoCell) supplemented with FCS (5%), endothelial cell growth supplement (ECGS, 12 μg mL⁻¹, C-39210, PromoCell), epidermal growth factor (0.1 μg mL⁻¹, EGF, C-39210, Promocell), FGF (1 ng mL⁻¹) and heparin (90 μg mL⁻¹, all C-39210; PromoCell); RPMI and ECGM mixed 1:1 [v/v]; and proliferation media (PM, advanced DMEM/F12 (P04-41150, PAN-Biotech) supplemented with B27 (1%, 17504-044, Life Technologies), EGF (10 ng mL⁻¹, C-39210; PromoCell), fibroblast growth factor (FGF, 100 ng mL⁻¹, C-39210, PromoCell), forskolin (10 μM, 1099, Tocris), glutamax (1%, 35050061, Thermo Fisher Scientific), HEPES (12 mM, 15630056, Thermo Fisher Scientific), hydrocortisone (0.5 μg mL⁻¹, H0888, Sigma Aldrich), N-2 supplement (1%, 07152, STEMCELL Technologies), N-acetyl-L-cysteine (1.25 mM, A9165, Sigma Aldrich), nicotinamide (10 mM, N0636, Merck), noggin (100 ng mL⁻¹, 120-10C, Peprotech), ROCK inhibitor (10 μM, 72304, STEMCELL Technologies), TGFβ-kinase inhibitor IV (2 μM, 1614, Tocris) mixed 1:1 [v/v] with DMEM (41965039, Gibco).

TUNEL Assay: Apoptotic cells were detected with the Click-iT Plus TUNEL Assay Kits for In Situ Apoptosis Detection (C10619, Thermo Fisher Scientific) according to the manufacturer's instructions. Incubation times were increased as follows: samples were fixed for 30 min, permeabilized for 40 min, TdT reaction buffer incubated for 20–30 min, TdT reaction mix incubated between 2 h and overnight, washed three times for 30–90 min, the reaction cocktail incubated for 1–2.5 h, and was washed three times for 30–60 min. For a positive dead control, samples were perfused for 24 h with 1% triton-100 on day 5–6 or incubated statically for 4 h on day 20.

LDH Assay: Lactate dehydrogenase (LDH)-release into the media was detected according to the manufacturer's instructions using the LDH-Glo Cytotoxicity Assay kit (J2381, Promega). Effluents were diluted 1:10 in FTALS and luminescence was measured in triplicates in an opaque 384 well plate (lumitrac 781075, Greiner Bio-One) using the Tristar 5 plate reader (Berthold, Germany).

Live Cell Labeling: For tracking experiments cells were stained with a cell tracker at 1:500 in PBS+ according to manufacturer's instructions. SiHa were stained prior to spheroid generation with Cell Tracker Green CMFDA (C7025, Thermo Fisher Scientific), fibroblasts prior to hydrogel embedding with CellTracker Blue CMAC (C2110, Thermo Fisher Scientific), and PMN prior to perfusion with CellTracker Deep Red (C34565, Thermo Fisher Scientific).

Immunofluorescent Cell Staining: For antibody staining of PMNs in 2D, glass coverslips were cleaned with absolute ethanol and dried. Thereafter, glass coverslips were placed on the bottom of the wells of a 48-well plate, coated with poly-D-lysine (PDL, 1%, P7280, Sigma Aldrich) in PBS for

Table 2. Primary antibodies for immunofluorescent stainings.

Primary/conjugate antibody	Figure	Dilution, primary/conjugated antibody	Supplier, catalog number	Secondary antibody	Dilution, secondary antibody	Supplier, catalog number
CD3	6B	1:50, 4 °C for 2 days	Abcam, ab135372	Goat anti-rabbit—Alexa Fluor 488	1:100, 6 h at RT	Thermo Fisher Scientific, A-11008
CD66b (3D)	6B,C	1:50, 4 °C for 2 days	Miltenyi Biotec, 130-108-019	Goat anti-human—Alexa Fluor 555	1:100, 6 h at RT	Thermo Fisher Scientific, A-21433
CD66b (2D)	S2A, Supporting Information	1:200, overnight at 4 °C	Miltenyi Biotec, 130-108-019	Goat anti-human—Alexa Fluor 555	1:500, 45 min at RT	Thermo Fisher Scientific, A-21433
Cytokeratin-FITC	3C, 4C	1:50, 2 h at 37 °C	Miltenyi Biotec, 130-118-964			
Fibronectin	2B	1:200, overnight at 4 °C	Agilent, A0245	Donkey anti-rabbit—Alexa Fluor 647	1:500, 45 min at RT	Thermo Fisher Scientific, A-31573
H3cit (3D)	6C	1:200, 4 °C for 2 days	Abcam, ab281584	Goat anti-rabbit—Alexa Fluor 488	1:100, 6 h at RT	Thermo Fisher Scientific, A-11008
H3cit (2D)	S2A, Supporting Information	1:500, overnight at 4 °C	Abcam, ab281584	Goat anti-rabbit—Alexa Fluor 488	1:500, 45 min at RT	Thermo Fisher Scientific, A-11008
Ki67	4C	1:25, 2 h at 37 °C	Abcam, ab16667	Donkey anti-rabbit—Alexa Fluor 647	1:100, 1 h at 37 °C	Thermo Fisher Scientific, A-31573
NE (3D)	6B,C	1:50, 4 °C for 2 days	R&D systems, MAB91671	Goat anti-mouse—Alexa Fluor 647	1:100, 6 h at RT	Thermo Fisher Scientific, A-21235
NE (2D)	S6A Supporting Information	1:100, overnight at 4 °C	R&D systems, MAB91671	Goat anti-mouse—Alexa Fluor 647	1:500, 45 min at RT	Thermo Fisher Scientific, A-21235
MPO (3D)	6C	1:100, 4 °C for 2 days	Miltenyi Biotec, 130-122-342	Goat anti-human—Alexa Fluor 555	1:100, 6 h at RT	Thermo Fisher Scientific, A-21433
MPO (2D)	S2A, Supporting Information	1:200, overnight at 4 °C	Miltenyi Biotec, 130-122-342	Goat anti-human—Alexa Fluor 555	1:500, 45 min at RT	Thermo Fisher Scientific, A-21433
Vimentin-Alexa Fluor 405	3C, 4C	1:25, 2 h at 37 °C	R&D systems, IC2105V			
Vimentin	2B	1:200, 4 °C overnight	R&D systems, MAB2105	Goat anti-rat—Alexa Fluor 555	1:500, 45 min at RT	Thermo Fisher Scientific, A48263

5 min, washed with PBS and dried at RT. 200 000 PMNs per cm² were seeded in RPMI (21875, Gibco) with FCS (5%). PMA (100 nM) was added, well plate with cells was centrifuged for 5 min at 200 × g and incubated at 37 °C and 5% CO₂ in a humidified atmosphere. After 5 h, wells were carefully washed three times with PBS at 200 × g for 5 min, with 300 μL remaining in the wells after each wash to reduce cell loss. Cells were fixed using paraformaldehyde (PFA, 4%, 0335.1, Carl Roth in PBS) for 15 min at RT and washed with PBS as described before. 3D tissues and fibroblast monolayers were washed in PBS+ for 5–10 min and fixed with ROTI-Histofix (P087.4, Carl Roth) for 15–30 min, washed with PBS, and stored until further processing at 4 °C in PBS. For independent analysis, chip samples were retrieved and stained in a 96-well plate. For permeabilization and blocking of unspecific bindings, triton (0.1%, X100, Sigma Aldrich) and BSA (3%, A9647, Sigma Aldrich) in PBS were added for 30 min (monolayers) or 45–60 min (3D tissues) at RT. Primary antibodies (50 μL) were applied as summarized in Table 2 in background reducing antibody diluent (S302283-2, Agilent) and washed with IHC wash buffer (WL583C0500, DCS Innovative Diagnostik-Systeme) for 30 min on mono-layer samples and 7 h for staining of PMNs in Figure 6B,C at RT, and 1.5 h at 37 °C for staining of Figures 3C and 4C. Secondary antibodies (50 μL) were added if applicable as summarized in Table 2 and samples were washed in IHC wash buffer before storage at 4 °C until microscopic analysis.

Image Acquisition and Analyses: Images were obtained using the inverted fluorescent microscope (Axio Observer 7, Zeiss, Germany) and confocal Laser-Scanning-Microscope (LSM 880, Zeiss, Germany), as indicated. Images were processed by adjusting brightness and contrast using ZEN lite Software (Version 3.4, Zeiss), applying the same settings to all images within an experiment. For quantification of fluorescent intensities, the mean gray values of the entire tissue were determined using ImageJ2, with the detailed macros available in the Supporting Information (S1, Supporting Information).

Statistical Analysis: All data was analyzed using GraphPad Prism 9.3.1, bar graphs depict mean ± standard deviation (SD) with sample sizes as stated for each case individually. For testing statistical significance, one-way ANOVA with Holm-Sidak's multiple comparisons test was performed as stated in each graph. Significance is stated as values for $p > 0.05$, one asterisk for $p \leq 0.05$, two asterisks for $p \leq 0.01$, and three asterisks for $p \leq 0.001$.

Supporting Information

Supporting Information is available from the Wiley Online Library or from the author.

Acknowledgements

The authors thank Prof. Thomas Ifner and Prof. Frank Stubenrauch for providing the cell line SiHa, Dr. Eduardo Brás for his assistance with chip fabrication, Nicole Anderle and Dr. Claudia Teufel for flow cytometry analysis, Dr. Madalena Cipriano and Dr. Jan Hodapp for support with image analysis, and Cellendes GmbH for providing CD-HyLink. Graphical abstract and human silhouette in Figure 2 were created with BioRender.com. This research was supported by the German Federal Institute for Risk Assessment (BfR, 60-0102-01.P581) and the Innovative Medicines Initiative 2 Joint Undertaking under grant agreement no. 101007799 (Inno4Vac). This Joint Undertaking receives the support from the European Union's Horizon 2020 research and innovation programme and EFPIA.

Conflict of Interest

The authors declare no conflict of interest.

Data Availability Statement

The data that support the findings of this study are available from the corresponding author upon reasonable request.

Keywords

cancer-on-chip, cervical cancer, cisplatin, microphysiological systems, neutrophils, organ-on-chip

Received: August 17, 2023

Revised: November 4, 2023

Published online:

- [1] H. Sung, J. Ferlay, R. L. Siegel, M. Laversanne, I. Soerjomataram, A. Jemal, F. Bray, *Ca-Cancer J. Clin.* **2021**, *71*, 209.
- [2] J. M. M. Walboomers, M. V. Jacobs, M. M. Manos, F. X. Bosch, J. A. Kummer, K. V. Shah, P. J. F. Snijders, J. Peto, C. J. L. M. Meijer, N. Muñoz, *J. Pathol.* **1999**, *189*, 12.
- [3] H. W. Chesson, E. F. Dunne, S. Hariri, L. E. Markowitz, *Sex. Transm. Dis.* **2014**, *41*, 660.
- [4] A. C. Rodriguez, M. Schiffman, R. Herrero, A. Hildesheim, C. Bratti, M. E. Sherman, D. Solomon, D. Guillen, M. Alfaro, J. Morales, M. Hutchinson, H. Katki, L. Cheung, S. Wacholder, R. D. Burk, *J. Natl. Cancer Inst.* **2010**, *102*, 315.
- [5] WHO, Cervical Cancer Elimination Initiative, (accessed: August 2023). <https://www.who.int/initiatives/cervical-cancer-elimination-initiative>.
- [6] Z. Song, K. Zou, L. Zou, *Front. Oncol.* **2022**, *12*, 1045481.
- [7] C. Sun, A. J. Brown, A. Jhingran, M. Frumovitz, L. Ramondetta, D. C. Bodurka, *Int. J. Gynecol. Cancer* **2014**, *24*, 1077.
- [8] A. S. Linhares Moreira, T. M. Cunha, S. Esteves, *Diagn. Interv. Radiol.* **2020**, *26*, 403.
- [9] A. Obermair, R. Asher, R. Pareja, M. Frumovitz, A. Lopez, R. Moretti-Marques, G. Rendon, R. Ribeiro, A. Tsunoda, V. Behan, A. Buda, M. Q. Bernadini, H. Zhao, M. Vieira, J. Walker, N. M. Spirtos, S. Yao, N. Chetty, T. Zhu, D. Isla, M. Tamura, J. Nicklin, K. P. Robledo, V. Gebiski, R. L. Coleman, G. Salvo, P. T. Ramirez, *Am. J. Obstet. Gynecol.* **2020**, *222*, 249e1.
- [10] C. Federico, J. Sun, B. Muz, K. Alhallak, P. F. Cospser, N. Muhammad, A. Jeske, A. Hinger, S. Markovina, P. Grigsby, J. K. Schwarz, A. K. Azab, *Int. J. Radiat. Oncol., Biol., Phys.* **2021**, *109*, 1483.
- [11] Y. Shan, Z. Ding, Z. Cui, A. Chen, *J. Obstet. Gynaecol.* **2023**, *43*, 2181690.
- [12] M. Watson, M. Saraiya, V. Benard, S. S. Coughlin, L. Flowers, V. Cokkinides, M. Schwenn, Y. Huang, A. Giuliano, *Cancer* **2008**, *113*, 2855.
- [13] M. Spurgeon, P. Lambert, *Viruses* **2017**, *9*, 219.
- [14] K. P. Maniar, J.-J. Wei, *Global Libr. Women's Med.* **2017**, <https://doi.org/10.3843/GLOWM.10230>.
- [15] Y. Wang, M. He, G. Zhang, K. Cao, M. Yang, H. Zhang, H. Liu, *Cancer Med.* **2021**, *10*, 2380.
- [16] V. S. Lebleu, E. G. Neilson, *FASEB J.* **2020**, *34*, 3519.
- [17] R. Wiedner, *Cancers* **2023**, *15*, 2014.
- [18] T. Sato, *Gynecol. Oncol.* **2004**, *92*, 47.
- [19] K. C. Valkenburg, A. E. De Groot, K. J. Pienta, *Nat. Rev. Clin. Oncol.* **2018**, *15*, 366.
- [20] J. Zhu, C. B. Thompson, *Nat. Rev. Mol. Cell Biol.* **2019**, *20*, 436.
- [21] R. Mhaidly, F. Mechta-Grigoriou, *Semin. Immunol.* **2020**, *48*, 101417.
- [22] R. S. Joshi, S. S. Kanugula, S. Sudhir, M. P. Pereira, S. Jain, M. K. Aghi, *Cancers* **2021**, *13*, 1399.
- [23] N. Fine, N. Tasevski, C. A. Mcculloch, H. C. Tenenbaum, M. Glogauer, *Front. Immunol.* **2020**, *11*, 571085.
- [24] E. Pérez-Figueroa, P. Álvarez-Carrasco, E. Ortega, C. Maldonado-Bernal, *Front. Immunol.* **2021**, *12*, 631821.
- [25] X.-Y. He, D. Ng, M. Egeblad, *Annu. Rev. Cancer Biol.* **2022**, *6*, 223.
- [26] Z. G. Fridlender, S. M. Albelda, *Carcinogenesis* **2012**, *33*, 949.

- [27] M. T. Masucci, M. Minopoli, M. V. Carriero, *Front. Oncol.* **2019**, *9*, 1146.
- [28] M. E. Shaul, Z. G. Fridlender, *Nat. Rev. Clin. Oncol.* **2019**, *16*, 601.
- [29] M. Wu, M. Ma, Z. Tan, H. Zheng, X. Liu, *Front. Immunol.* **2020**, *11*, 565165.
- [30] S. Xiong, L. Dong, L. Cheng, *J. Hematol. Oncol.* **2021**, *14*, 173.
- [31] C. C. Hedrick, I. Malanchi, *Nat. Rev. Immunol.* **2022**, *22*, 173.
- [32] K. R. Zahid, U. Raza, S. Tumbath, L. Jiang, W. Xu, X. Huang, *Front. Oncol.* **2022**, *12*, 975981.
- [33] A. Teixeira, S. Garasa, M. C. Ochoa, M. Villalba, I. Olivera, A. Cirella, I. Eguren-Santamaria, P. Berraondo, K. A. Schalper, C. E. De Andrea, M. F. Sanmamed, I. Melero, *Clin. Cancer Res.* **2021**, *27*, 2383.
- [34] W. Zheng, J. Wu, Y. Peng, J. Sun, P. Cheng, Q. Huang, *Cancers* **2022**, *14*, 4755.
- [35] D. Hirschhorn, S. Budhu, L. Kraehenbuehl, M. Gigoux, D. Schröder, A. Chow, J. M. Ricca, B. Gasmji, O. De Henau, L. M. B. Mangarin, Y. Li, L. Hamadene, A.-L. Flamar, H. Choi, C. A. Cortez, C. Liu, A. Holland, S. Schad, I. Schulze, A. Betof Warner, T. J. Hollmann, A. Arora, K. S. Panageas, G. A. Rizzuto, R. Duhon, A. D. Weinberg, C. N. Spencer, D. Ng, X.-Y. He, J. Albregues, et al., *Cell* **2023**, *186*, 1432.
- [36] P. C. Fernandes, C. B. Garcia, D. C. Micheli, F. Q. Cunha, E. F. C. Murta, B. M. Tavares-Murta, *Int. J. Gynecol. Cancer* **2007**, *17*, 1068.
- [37] A. Carus, M. Ladekar, H. Hager, B. S. Nedergaard, F. Donskov, *Br. J. Cancer* **2013**, *108*, 2116.
- [38] Y. Matsumoto, S. Mabuchi, K. Kozasa, H. Kuroda, T. Sasano, E. Yokoi, N. Komura, K. Sawada, T. Kimura, *Gynecol. Oncol.* **2017**, *145*, 469.
- [39] B. Yan, X. Dai, Q. Ma, X. Wu, *Front. Oncol.* **2021**, *11*, 659445.
- [40] V. Brinkmann, U. Reichard, C. Goosmann, B. Fauler, Y. Uhlemann, D. S. Weiss, Y. Weinrauch, A. Zychlinsky, *Science* **2004**, *303*, 1532.
- [41] S. Masuda, D. Nakazawa, H. Shida, A. Miyoshi, Y. Kusunoki, U. Tomaru, A. Ishizu, *Clin. Chim. Acta* **2016**, *459*, 89.
- [42] V. Brinkmann, *J. Innate Immun.* **2018**, *10*, 414.
- [43] H. Yang, M. H. Biermann, J. M. Brauner, Y. Liu, Y. Zhao, M. Herrmann, *Front. Immunol.* **2016**, *7*, 302.
- [44] M. H. Shahzad, L. Feng, X. Su, A. Brassard, I. Dhoparee-Doomah, L. E. Ferri, J. D. Spicer, J. J. Cools-Lartigue, *Cancers* **2022**, *14*, 1359.
- [45] Y. Fomenko, Y. Kolesnikova, I. Beynikova, L. Muravlyova, V. Sirota, R. Bakirova, *Open Access Maced. J. Med. Sci.* **2018**, *6*, 2097.
- [46] Á. Teixeira, S. Garasa, M. Gato, C. Alfaro, I. Migueliz, A. Cirella, C. De Andrea, M. C. Ochoa, I. Otano, I. Etxeberria, M. P. Andueza, C. P. Nieto, L. Resano, A. Azpilikueta, M. Allegretti, M. De Pizzol, M. Ponz-Sarvisé, A. Rouzaut, M. F. Sanmamed, K. Schalper, M. Carleton, M. Mellado, M. E. Rodriguez-Ruiz, P. Berraondo, J. L. Perez-Gracia, I. Melero, *Immunity* **2020**, *52*, 856.
- [47] J. T. Atkins, G. C. George, K. Hess, K. L. Marcelo-Lewis, Y. Yuan, G. Borthakur, S. Khozin, P. Lorusso, D. S. Hong, *Br. J. Cancer* **2020**, *123*, 1496.
- [48] L. I. Larmour, T. W. Jobling, C. E. Gargett, *Int. J. Gynecol. Cancer* **2015**, *25*, 1345.
- [49] I. Kutle, R. Polten, J. Hachenberg, R. Klapdor, M. Morgan, A. Schambach, *Cancers* **2023**, *15*, 2518.
- [50] C. Tecchio, A. Micheletti, M. A. Cassatella, *Front. Immunol.* **2014**, *5*, 508.
- [51] E. B. Eruslanov, S. Singhal, S. M. Albelda, *Trends Cancer* **2017**, *3*, 149.
- [52] S. Schneider, E. J. S. Brás, O. Schneider, K. Schlünder, P. Loskill, *Micromachines* **2021**, *12*, 575.
- [53] H. Deng, S. Mondal, S. Sur, C. D. Woodworth, *J. Cell. Physiol.* **2019**, *234*, 7683.
- [54] K. Bitschar, L. Staudenmaier, L. Klink, J. Focken, B. Sauer, B. Fehrenbacher, F. Herster, Z. Bittner, L. Bleul, M. Schaller, C. Wolz, A. N. R. Weber, A. Peschel, B. Schitteck, *J. Invest. Dermatol.* **2020**, *140*, 1054.
- [55] R. Burgos-Panadero, F. Lucantoni, E. Gamero-Sandemetro, L. D. L. Cruz-Merino, T. Álvaro, R. Noguera, *Cancer Lett.* **2019**, *461*, 112.
- [56] A. S. Nunes, A. S. Barros, E. C. Costa, A. F. Moreira, I. J. Correia, *Biotechnol. Bioeng.* **2019**, *116*, 206.
- [57] F. Friedl, I. Kimura, T. Osato, Y. Ito, *Proc. Soc. Exp. Biol. Med.* **1970**, *135*, 543.
- [58] E. Malmström, M. Sennström, A. Holmberg, H. Frielingsdorf, E. Eklund, L. Malmström, E. Tufvesson, M. F. Gomez, G. Westergren-Thorsson, G. Ekman-Ordeberg, A. Malmström, *Mol. Hum. Reprod.* **2007**, *13*, 333.
- [59] S. Ghosh, *Bioorg. Chem.* **2019**, *88*, 102925.
- [60] A. Katke, R. Nanda, B. Thejaswini, T. Pasha, G. Giri, G. Babu, Y. Pawar, *Rep. Pract. Oncol. Radiother.* **2021**, *26*, 948.
- [61] P. Rajkumar, B. S. Mathew, S. Das, R. Isaiah, S. John, R. Prabha, D. H. Fleming, *J. Clin. Diagn. Res.* **2016**, *10*, XC01.
- [62] A. Boussommier-Calleja, in *Bioengineering Innovative Solutions for Cancer* (Eds: S. Ladame, J. Y. H. Chang), Academic Press, Cambridge, MA **2020**, pp. 273-325.
- [63] G. Kamoshida, T. Kikuchi-Ueda, S. Nishida, S. Tansho-Nagakawa, H. Kikuchi, T. Ubagai, Y. Ono, *FEBS Open Bio* **2017**, *7*, 877.
- [64] E. Neubert, S. N. Senger-Sander, V. S. Mancke, J. Busse, E. Polo, S. E. F. Scheidmann, M. P. Schön, S. Kruss, L. Erpenbeck, *Front. Immunol.* **2019**, *10*, 00012.
- [65] G. Vazquez Rodriguez, A. Abrahamsson, L. D. E. Jensen, C. Dabrosin, *Cancer Immunol. Res.* **2017**, *5*, 234.
- [66] M. Piergiovanni, O. Cangar, S. B. Leite, L. Mian, A. Jenet, R. Corvi, M. Whelan, F. Taucer, A. Ganesh, *Stem Cell Rep.* **2021**, *16*, 2076.
- [67] A. Moruzzi, T. Shroff, S. Keller, P. Loskill, M. Cipriano, *Educ. Sci.* **2023**, *13*, 144.
- [68] K. Löhmussaar, R. Oka, J. Espejo Valle-Inclan, M. H. H. Smits, H. Wardak, J. Korving, H. Begthel, N. Proost, M. Van De Ven, O. W. Kranenburg, T. G. N. Jonges, R. P. Zweemer, S. Veersema, R. Van Bortel, H. Clevers, *Cell Stem Cell* **2021**, *28*, 1380.
- [69] H. S. Seol, J. H. Oh, E. Choi, S. Kim, H. Kim, E. J. Nam, *J. Gynecol. Oncol.* **2022**, *34*, e35.
- [70] M. D. L. Zuñiga Martinez, C. M. López Mendoza, J. Tenorio Salazar, A. M. García Carrancá, M. A. Cerbón Cervantes, L. E. Alcántara-Quintana, *Mol. Cell. Oncol.* **2022**, *9*, 2078628.
- [71] B. Desoize, *Crit. Rev. Oncol./Hematol.* **2000**, *36*, 193.
- [72] S. Tomás-Pérez, J. Oto, C. Aghababayan, R. Herranz, A. Cuadros-Lozano, E. González-Cantó, B. Mc Cormack, J. Arrés, M. Castaño, F. Cana, L. Martínez-Fernández, N. Santonja, R. Ramírez, A. Herreros-Pomares, S. Cañete-Mota, A. Lluca, J. Mari-Alexandre, P. Medina, J. Gilabert-Estellés, *Front. Immunol.* **2023**, *14*, 1111344.
- [73] A. K. Witkiewicz, T. C. Wright, A. Ferenczy, B. M. Ronnett, R. J. Kurman, in *Blaustein's Pathology of the Female Genital Tract* (Eds: R. J. Kurman, L. H. Ellenson, B. M. Ronnett), Springer, Boston, MA **2011**, pp. 253-303.
- [74] J. C. Villegas-Pineda, A. Ramírez-de-Arellano, L. J. Bueno-Urquiza, M. d. R. Lizarazo-Taborda, A. L. Pereira-Suárez, *Front. Oncol.* **2023**, *13*, 1106757.
- [75] M. Nagura, N. Matsumura, T. Baba, R. Murakami, B. Kharia, J. Hamanishi, K. Yamaguchi, K. Abiko, M. Koshiyama, M. Mandai, T. Murata, S. K. Murphy, I. Konishi, *Gynecol. Oncol.* **2015**, *136*, 104.
- [76] L. Xiao, H. Zhu, J. Shu, D. Gong, D. Zheng, J. Gao, *Arch. Gynecol. Obstet.* **2022**, *305*, 179.
- [77] T.-Y. Chu, J.-T. Yang, T.-H. Huang, H.-W. Liu, *Radiat. Res.* **2014**, *181*, 540.
- [78] L.-J. Liang, Y. Yang, W.-F. Wei, X.-G. Wu, R.-M. Yan, C.-F. Zhou, X.-J. Chen, S. Wu, W. Wang, L.-S. Fan, *Oncogenesis* **2021**, *10*, 30.
- [79] W. Xu, X. Hu, Z. Chen, X. Zheng, C. Zhang, G. Wang, Y. Chen, X. Zhou, X. Tang, L. Luo, X. Xu, W. Pan, *PLoS One* **2014**, *9*, e97306.
- [80] T. I. Maulana, E. Kromidas, L. Wallstabe, M. Cipriano, M. Alb, C. Zaupa, M. Hudecek, B. Fogal, P. Loskill, *Adv. Drug Delivery Rev.* **2021**, *173*, 281.

- [81] H. Munir, J. O. Jones, T. Janowitz, M. Hoffmann, M. Euler, C. P. Martins, S. J. Welsh, J. D. Shields, *Nat. Commun.* **2021**, *12*, 683.
- [82] J. G. Hengstler, A.-K. Sjögren, D. Zink, J. J. Hornberg, *Arch. Toxicol.* **2020**, *94*, 353.
- [83] A.-K. Sjögren, K. Breitholtz, E. Ahlberg, L. Milton, M. Forsgard, M. Persson, S. H. Stahl, M. J. Wilmer, J. J. Hornberg, *Arch. Toxicol.* **2018**, *92*, 3175.
- [84] S. Saesoo, S. Bunthot, W. Sajomsang, P. Gonil, S. Phunpee, P. Songkhum, K. Laohhasurayotin, T. Wutikhun, T. Yata, U. R. Ruktanonchai, N. Saengkrit, *J. Colloid Interface Sci.* **2016**, *480*, 240.
- [85] P. Khumkrong, K. Piboonprai, W. Chaichompoo, W. Pimtong, M. Khongkwo, K. Namdee, A. Jantimaporn, D. Japrun, U. Asawapirom, A. Suksamrarn, T. Iempridee, *Biomolecules* **2019**, *9*, 494.
- [86] A.-K. Daum, J. Dittmann, L. Jansen, S. Peters, U. Dahmen, J. I. Heger, F. Hoppe-Seyler, A. Gille, J. H. Clement, I. B. Runnebaum, M. Dürst, C. Backsch, *Am. J. Transl. Res.* **2021**, *13*, 10298.
- [87] O. Michnov, E. Solomayer, T. Fehm, F. Stubenrauch, T. Iftner, *Am. J. Cancer Res.* **2012**, *2*, 309.
- [88] Y. Maru, N. Tanaka, K. Ebisawa, A. Odaka, T. Sugiyama, M. Itami, Y. Hippo, *Cancer Sci.* **2019**, *110*, 2992.
- [89] J.-Y. Kim, K. Na, H.-S. Kim, *Anticancer Res.* **2017**, *37*, 2557.
- [90] O. Schneider, A. Moruzzi, S. Fuchs, A. Grobel, H. S. Schulze, T. Mayr, P. Loskill, *Mater. Today Bio* **2022**, *15*, 100280.
- [91] C. Linnemann, S. Venturelli, F. Konrad, A. K. Nussler, S. Ehnert, *EXCLI J.* **2020**, *19*, 1481.